Single Electron Reduction of NHC-CO2 and NHC-CO2-BR3 Adducts

Agustín Morales Aguilar

Université Toulouse 3 – Paul Sabatier

Laboratoire de Chimie de Coordination

Universitat Autònoma de Barcelona

Departament Química - Unitat Química Física

Single Electron Reduction of NHC-CO_2 and NHC-CO_2-BR_3 Adducts.

Agustín Morales Aguilar

Doctoral Thesis

Toulouse, 2023

A mis padres, Agustín y Mati

Table of contents.

Acknowledgments.

First and foremost, I would like to express my profound gratitude to my supervisors, Dr. Olivier Baslé, Prof. Dr. Agustí Lledós and Dr. Sébastien Bontemps, for their invaluable guidance, unwavering support, and remarkable patience throughout my doctoral journey. Olivier and Sébastien, you welcomed an excited but fearful Andalusian who was determined to take on new challenges. You gave me the freedom and the necessary support that has allowed me to make mistakes, to learn from them and finally to progress as a person and as an experimental chemist. Agustí, we met almost a year later (summer 2021) in person. But since then, we have not stopped talking and exchanging new ideas. When I arrived in Barcelona, I had no fear but respect as I was about to enter a world completely alien to me: the Computational Chemistry World. From the very first moment, you sat right next to me and gave me the tools I needed. After a lot of "Error Syntax" in the output files and a lot of discussions, I started to understand what was going on behind the scenes of a calculation and I have to admit that I enjoyed it a lot (I still do it). I am very thankful to have graduated from “Agustí Lledós' Computational School”. In short, Sébastien, Olivier and Agustí, thank you for all.

I extend my gratitude to the members of my PhD jury, for their insightful feedback and their constructive criticism. Each of you has provided a unique perspective that has enriched the quality of this work.

My heartfelt thanks also go out to my colleagues from team A and N and fellow researchers at LCC, whose stimulating discussions and camaraderie have created a vibrant intellectual environment that has greatly enriched my academic experience. To Juju, thank you very much for all the moments we shared in the lab. In a very short period of time, you became one of my best friends in Toulouse. Without you, the thesis would have been much harder. I wish you a lot of success in the future. To my colleagues in Barcelona, it was a pity that I could not enjoy with you much more. Thank you for all those funny moments, discussions in the bar, all the advice you gave me. I would repeat this stay a thousand and one times more. I will never forget you, Bernat, Anna, Estefanía, Andrés, Iker and Irina.

During my short but enriching internship at Solvay, I had the opportunity to gain valuable insight into the world of the chemical industry. I am grateful to the entire Solay team in Lyon for welcoming me into their workspace with open arms. Your warm hospitality, willingness to share knowledge, and inclusiveness made me feel like a valued member of the team from day one. I extend my sincere thanks to my internship supervisor, Dr. Raphael Wischert. I appreciate the time you took to provide feedback and answer my questions, which contribute significantly to my professional development. Additionally, I want to thank Dr. Philippe Marion and Dr. Matthieu Corbet for their mentorship and for taking the time to share their expertise with me. Your willingness to provide guidance and encouragement was invaluable. Lastly, I am grateful to the entire Solvay company for fostering a positive and dynamic work environment. Your dedication to innovation and excellence has left a lasting impression on me.

I wish to acknowledge the European Union's Horizon 2020 research and innovation programme for the financial funding under the Marie Skłodowska-Curie grant agreement No. 860322 that have made this research possible. I would also like to thank the Project Management Team and all beneficiaries and partners of the program for all the efforts made to ensure that the project comes to fruition. Thanks also to all the network colleagues with whom I have been able to exchange ideas and who have helped me to improve day by day. To the ESR fellows, during these three years you have become family. We have suffered, we have had fun and we have learned together. I can say that I have been very lucky to have met 14 wonderful people that I will never forget. I hope that our paths will cross again, and I wish you all the best! To Max and Paven, I'm going to miss all the visits you used to pay me in the office and those five-minute breaks. I'm glad we were able to have a great time together in Toulouse.

In closing, this manuscript represents the culmination of years of hard work, dedication, and the support of a remarkable community of individuals. While my name appears on the cover, this achievement is a testament to the collective efforts of many. I am humbled and grateful for the privilege of pursuing my passion, and I look forward to seeing you again in the years to come.

Thank you, from the bottom of my heart.

General Considerations.

This doctoral thesis focusses on the synthesis of NHC-CO_2-based adducts and the evaluation of their one-electron reduction through a combined theoretical and experimental study. Carbon dioxide is an attractive source of carbon due to its abundance as a molecule. Its use as a C1 synthon has awakened the interest of the scientific community, ranging from fundamental research to applied studies. However, carbon dioxide exhibits high kinetic and thermodynamic stability, making challenging its use as an organic reagent.

The one-electron reduction of carbon dioxide to $[CO_2]^{\bullet-}$ could enable its use as a carbon source. However, this approach is challenging due to the highly negative reduction potential of CO_2. In our study, we investigate i) the use of N-Heterocyclic Carbenes (NHC) to overcome this reduction potential and ii) whether the resulting one-electron reduced NHC-CO_2 adducts would mimic the reactivity of the free radical CO_2 anion. These two questions are addressed in this manuscript (Scheme 1).

The work conducted in this doctoral thesis is divided into five chapters. Chapter 1 provides a literature review of the topics covered in the manuscript. This chapter is divided into four main sections. In the first section, various methods reported in the literature for generating $[CO_2]^{\bullet-}$ from CO_2 or formate salts are discussed, followed by their reactivity toward open-shell species and others unsaturated species. The second part of this chapter focuses on the reduction of NHC-CO_2 adducts. In the third section, the synthesis of compounds of the form NHC-CO_2-BR_3 (BR_3: borane) designed in the Tamm group is described. Finally, in the last section of Chapter 1, the basis for calculating reduction potentials from a thermodynamic perspective is explained, along with some relevant examples where reduction potentials have been calculated using DFT with the direct approach. Chapter 2 describes a preliminary theoretical study on the one-electron reduction of NHC-CO_2-based adducts with the aim of understanding how these species behave after the addition of an electron. This study aims to guide us in selecting adducts that may have the most accessible reduction potential for subsequent synthesis.

In Chapter 3, the synthesis and characterisation of NHC-CO_2-based adducts selected in Chapter 2 are considered. Then, the reduction of the previously synthesized compounds by electrochemical and chemical means is described. In Chapter 4, a theoretical analysis is presented, first to validate the computational method based on previous experimental results, and then to rationalize various properties related to the one-electron reduction of NHC-CO_2 adducts using quantum chemistry tools. Chapter 5 contains the experimental details of this doctoral thesis.

The general conclusions and prospects of this doctoral thesis are found at the end of this work. This manuscript has been written in English. However, this initial summary and the general conclusions have also been translated into Spanish and French. The references used in each chapter are included at the end of each chapter and are numbered independently for each chapter. The compounds presented in Chapter 1 are numbered separately from the rest of the chapters. The compounds described in this doctoral thesis are summarized in the "Summary of Compounds" section.

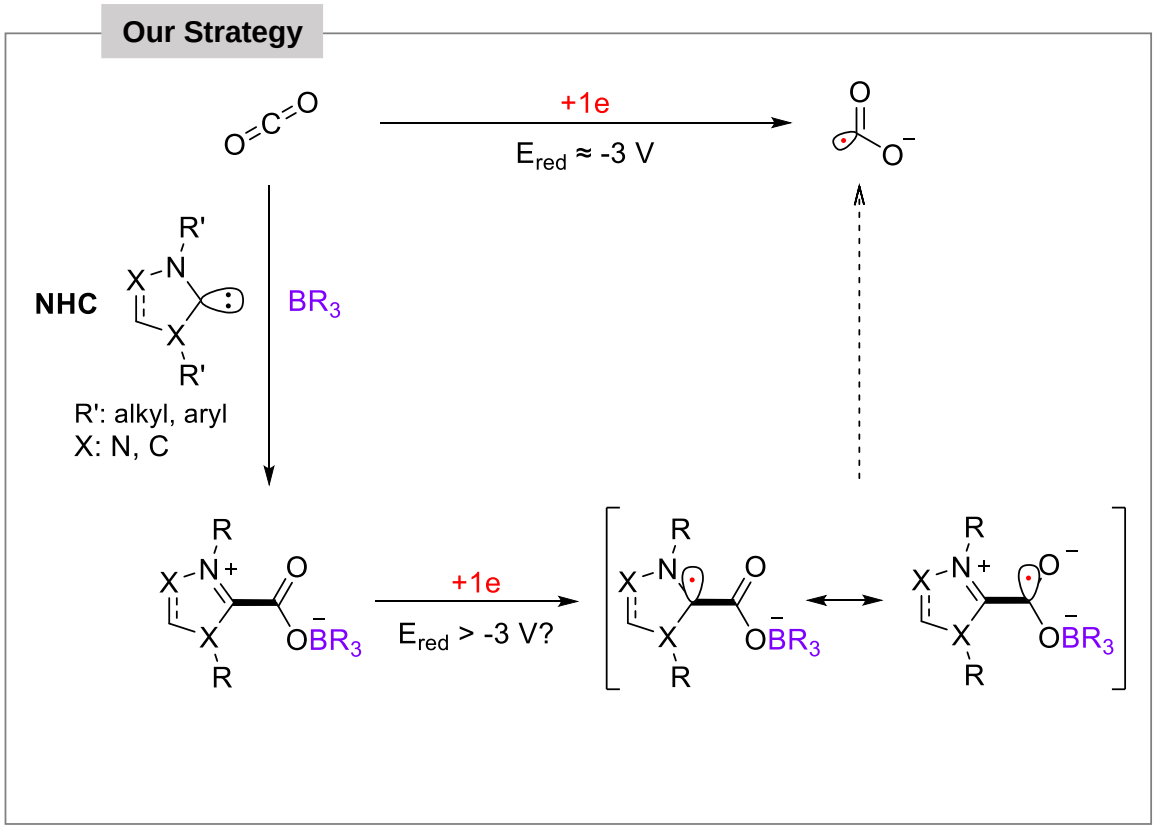

Scheme 1. Monoelectronic reduction of NHC-CO_2-based adducts.

Consideraciones Generales.

Esta tesis doctoral se centra en la síntesis de aductos NHC-CO_2 y la evaluación de su reducción a un electrón a través de un estudio combinado teórico y experimental. El dióxido de carbono es una fuente de carbono atractiva debido a su abundancia como molécula. Su uso como sintón C1 ha despertado interés en la comunidad científica, desde la investigación más fundamental hasta la más aplicada. Sin embargo, el dióxido de carbono presenta una alta estabilidad cinética y termodinámica que dificulta su uso como reactivo orgánico.

La reducción monoelectrónica del dióxido de carbono a $[CO_2]^{\bullet-}$ podría permitir su uso como fuente de carbono. Sin embargo, este enfoque es difícil debido al potencial de reducción altamente negativo del CO_2. En nuestro estudio, nos preguntamos i) sobre el uso de Carbenos N-Heterocíclicos (NHC, acrónimo en inglés) para superar este potencial de reducción y ii) si los aductos NHC-CO_2 reducidos monoelectrónicamente resultantes imitarían la reactividad del anión radical CO_2 libre. Estas dos cuestiones se abordan en este manuscrito (Esquema 1).

El trabajo realizado en esta tesis doctoral se divide en cinco capítulos. El Capítulo 1 proporciona una revisión bibliográfica de los temas a tratar en el manuscrito. Este capítulo se divide en cuatro secciones principales. En la primera sección, se discuten los diferentes métodos reportados en la literatura para generar $[CO_2]^{\bullet-}$ a partir de CO_2 o formiatos, seguidos de su reactividad hacia especies de capa abierta y otras especies insaturadas. La segunda parte de este capítulo se centra en la reducción de los aductos NHC-CO_2. En la tercera sección, se describe la síntesis de compuestos de la forma NHC-CO_2-BR_3 (BR_3: borano) diseñados en el grupo de Tamm. Finalmente, en la última sección del Capítulo 1, se explica la base del cálculo de potenciales de reducción desde un punto de vista termodinámico, así como algunos ejemplos relevantes donde los potenciales de reducción se han calculado mediante DFT utilizando el método directo. El Capítulo 2 describe un estudio teórico preliminar sobre la reducción monoelectrónica de aductos NHC-CO_2 con el objetivo de comprender cómo se comportan estas especies después de la adición de un electrón. Este estudio pretende orientarnos hacia la elección de aductos

que puedan tener el potencial de reducción más accesible para su síntesis posterior. En el Capítulo 3, se considera la síntesis y caracterización de los aductos a base de NHC-CO_2 seleccionados en el Capítulo 2. Luego, se describe la reducción de los compuestos previamente sintetizados mediante métodos electroquímicos y químicos. En el Capítulo 4, se presenta un análisis teórico en el que primero se busca validar el método computacional basado en los resultados experimentales previos, y luego se pretende racionalizar diferentes propiedades relacionadas con la monorreducción de los aductos a base de NHC-CO_2 utilizando herramientas de la química cuántica. El Capítulo 5 contiene los detalles experimentales de esta tesis doctoral.

Las conclusiones generales y las perspectivas de esta tesis doctoral se encuentran al final de este trabajo. Este manuscrito se ha redactado en inglés. Sin embargo, este resumen inicial y las conclusiones generales también se han traducido al español y al francés. Las referencias utilizadas en cada capítulo se incluyen al final de cada capítulo y se numeran de manera independiente para cada capítulo. Los compuestos presentados en el Capítulo 1 se numeran por separado del resto de los capítulos. Los compuestos descritos en esta tesis doctoral se resumen en la sección "Summary of compounds".

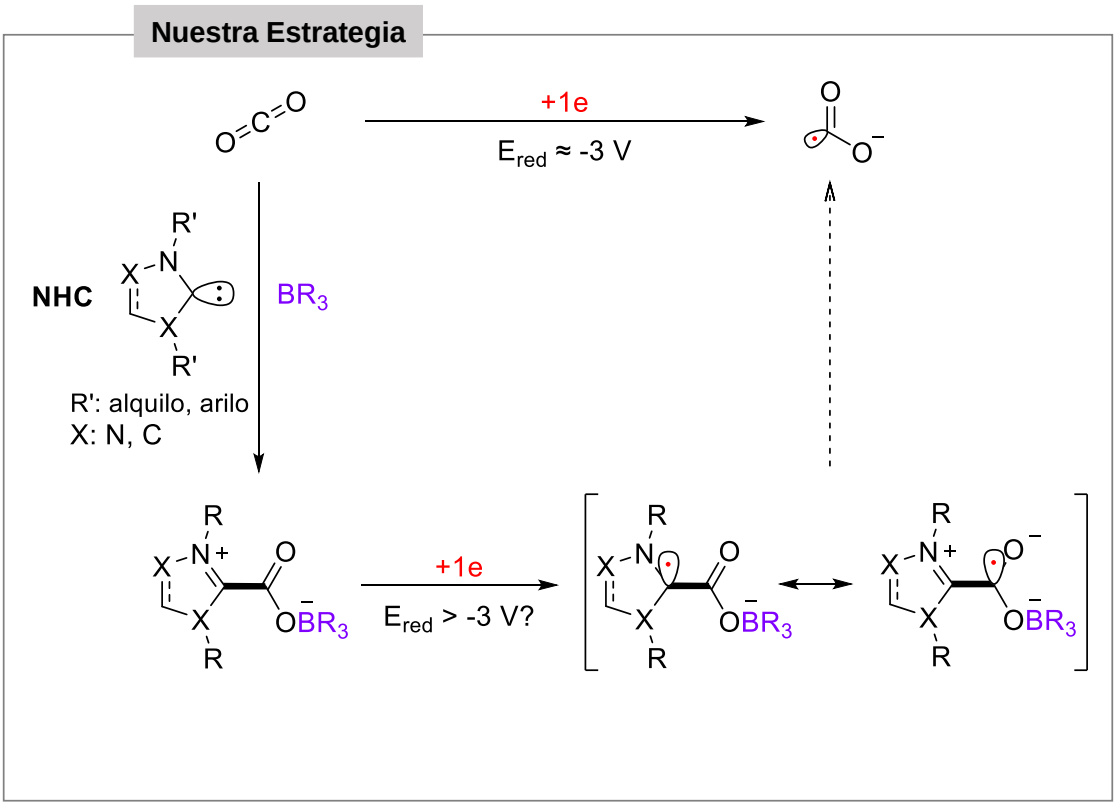

Esquema 1. Reducción monoelectrónica de las especies basadas en NHC-CO_2.

Considérations Générales.

Cette thèse doctorale concerne la synthèse d'adduits NHC-CO_2 et l'évaluation de leur réduction à un électron à travers une étude combinée théorique et expérimentale. Le dioxyde de carbone est une source de carbone attrayante car c'est une molécule abondante. Son utilisation en tant que synthone C1 suscite l'intérêt de la communauté scientifique, de la recherche la plus fondamentale à la plus appliquée. Cependant, le dioxyde de carbone présente une stabilité cinétique et thermodynamique élevée qui entrave son utilisation en tant que réactif organique.

La réduction monoélectronique du dioxyde de carbone en $[CO_2]^{\bullet-}$ pourrait permettre d'utiliser le CO_2 comme source de carbone. Cependant, cette approche est difficile car le potentiel de réduction du CO_2 est particulièrement négatif. Dans notre étude, nous nous sommes interrogé i) sur l'utilisation de Carbènes *N*-Hétérocycliques (NHC, acronyme en anglais) pour contourner ce potentiel de réduction et ii) si les adduits NHC-CO_2 monoréduits résultants de leur réduction imiteraient la réactivité de l'anion radical CO_2 libre. Ces deux questions seront abordées dans ce manuscrit (Schéma 1).

Le travail réalisé dans cette thèse doctoral a été divisé en cinq chapitres. Le Chapitre 1 fournit une revue bibliographique des sujets à aborder dans le manuscrit. Ce chapitre est divisé en quatre sections principales. Dans la première section, les différentes méthodes rapportées dans la littérature pour générer $[CO_2]^{\bullet-}$ à partir soit de CO_2, ou de sels de formiate, sont discutées, suivies de sa réactivité envers les espèces à couche ouverte et d'autres spèces insaturées. La deuxième partie de ce chapitre se concentre sur la réduction des adduits NHC-CO_2. Dans la troisième section, la synthèse de composés de la forme NHC-CO_2-BR_3 (BR_3: borane) conçus dans le groupe de Tamm est décrite. Enfin, dans la dernière section du Chapitre 1, la base du calcul des potentiels de réduction d'un point de vue thermodynamique est expliquée, ainsi que quelques exemples pertinents où les potentiels de réduction ont été calculés par DFT en utilisant l'approche directe. Le Chapitre 2 décrit une étude théorique préliminaire sur la réduction monoélectronique d'adduits NHC-CO_2 dans le but de comprendre comment ces espèces se comportent après l'ajout d'un électron. Cette étude vise à nous guider vers le choix

d'adduits qui pourraient présenter le potentiel de réduction le plus accessible pour leur synthèse ultérieure. Dans le Chapitre 3, la synthèse et la caractérisation des adduits à base de NHC-CO_2 sélectionnés dans le Chapitre 2 ont été envisagées. Ensuite, la réduction des composés précédemment synthétisés par des moyens électrochimiques et chimiques est décrite. Dans le Chapitre 4, une analyse théorique est présentée, dans laquelle il est d'abord prévu de valider la méthode computationnelle sur la base des résultats expérimentaux précédents, et ensuite de rationaliser différentes propriétés liées à la monoréduction des adduits à base de NHC-CO_2 en utilisant des outils basés sur la chimie quantique. Le Chapitre 5 comprend les détails expérimentaux de cette thèse doctorale

Les conclusions générales et les perspectives de cette thèse de doctorat se trouvent à la fin de ce travail. Ce manuscrit a été rédigé en anglais. Cependant, ce résumé initial et les conclusions générales ont également été traduits en espagnol et en français. Les références utilisées dans chaque chapitre ont été incluses à la fin de chaque chapitre et sont numérotées de manière indépendante pour chaque chapitre. Les composés présentés dans le Chapitre 1 sont numérotés séparément du reste des chapitres. Les composés décrits dans cette thèse de doctorat sont résumés dans la section "Summary of Compounds".

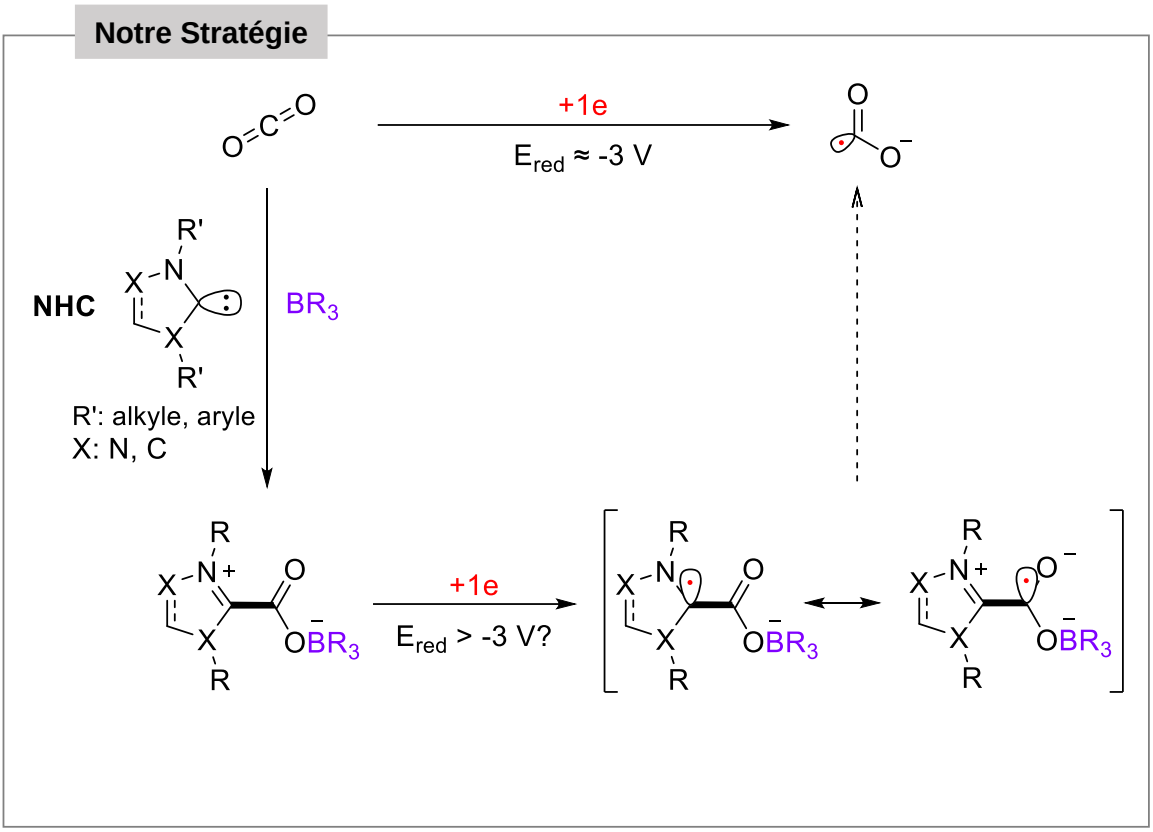

Schéma 1. Réduction monoélectronique des adduits à base de NHC-CO_2.

Summary of Compounds.

N-Alkyl groups

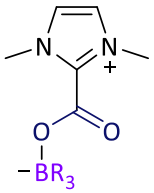

1: no BR_3
1-BH$_3$: BR_3 = BH_3
1-B(C$_6$F$_5$)$_3$: BR_3 = $B(C_6F_5)_3$
1-BCl$_3$: BR_3 = BCl_3

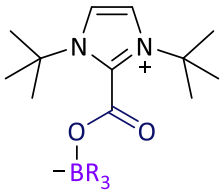

2: no BR_3
2-BH$_3$: BR_3 = BH_3
2-B(C$_6$F$_5$)$_3$: BR_3 = $B(C_6F_5)_3$
2-BCl$_3$: BR_3 = BCl_3

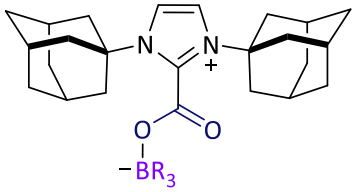

3: no BR_3
3-BH$_3$: BR_3 = BH_3
3-B(C$_6$F$_5$)$_3$: BR_3 = $B(C_6F_5)_3$
3-BCl$_3$: BR_3 = BCl_3

N-Aryl groups

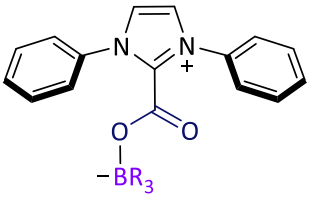

4: no BR_3
4-BH$_3$: BR_3 = BH_3
4-B(C$_6$F$_5$)$_3$: BR_3 = $B(C_6F_5)_3$
4-BCl$_3$: BR_3 = BCl_3

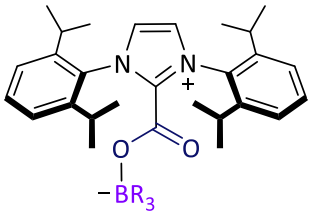

5: no BR_3
5-BH$_3$: BR_3 = BH_3
5-B(C$_6$F$_5$)$_3$: BR_3 = $B(C_6F_5)_3$
5-BCl$_3$: BR_3 = BCl_3

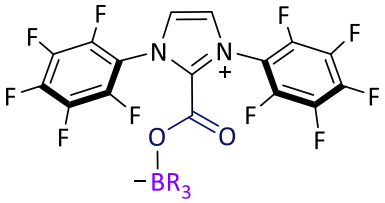

6: no BR_3
6-BH$_3$: BR_3 = BH_3
6-B(C$_6$F$_5$)$_3$: BR_3 = $B(C_6F_5)_3$
6-BCl$_3$: BR_3 = BCl_3

Enders and ^{Cy}CAAC-type NHCs

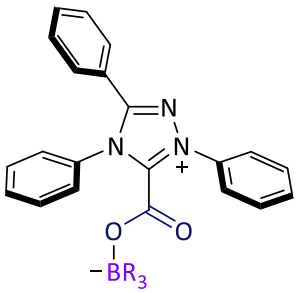

7: no BR_3
7-BH$_3$: BR_3 = BH_3
7-B(C$_6$F$_5$)$_3$: BR_3 = $B(C_6F_5)_3$
7-BCl$_3$: BR_3 = BCl_3

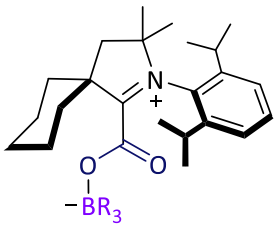

8: no BR_3
8-BH$_3$: BR_3 = BH_3
8-B(C$_6$F$_5$)$_3$: BR_3 = $B(C_6F_5)_3$
8-BCl$_3$: BR_3 = BCl_3

Scheme 2. Studied NHC-CO_2-based adducts in their neutral form.

N-Alkyl groups

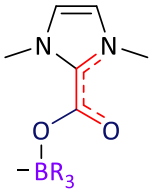

[1]$^{\bullet-}$: no BR_3
[1-BH$_3$]$^{\bullet-}$: BR_3 = BH_3
[1-B(C$_6$F$_5$)$_3$]$^{\bullet-}$: BR_3 = $B(C_6F_5)_3$
[1-BCl$_3$]$^{\bullet-}$: BR_3 = BCl_3

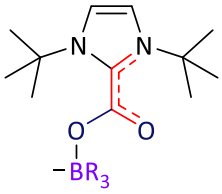

[2]$^{\bullet-}$: no BR_3
[2-BH$_3$]$^{\bullet-}$: BR_3 = BH_3
[2-B(C$_6$F$_5$)$_3$]$^{\bullet-}$: BR_3 = $B(C_6F_5)_3$
[2-BCl$_3$]$^{\bullet-}$: BR_3 = BCl_3

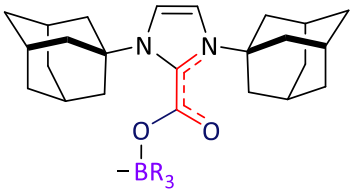

[3]$^{\bullet-}$: no BR_3
[3-BH$_3$]$^{\bullet-}$: BR_3 = BH_3
[3-B(C$_6$F$_5$)$_3$]$^{\bullet-}$: BR_3 = $B(C_6F_5)_3$
[3-BCl$_3$]$^{\bullet-}$: BR_3 = BCl_3

N-Aryl groups

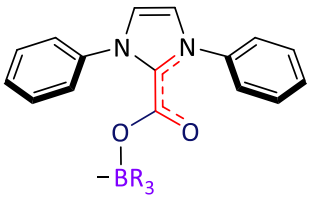

[4]$^{\bullet-}$: no BR_3
[4-BH$_3$]$^{\bullet-}$: BR_3 = BH_3
[4-B(C$_6$F$_5$)$_3$]$^{\bullet-}$: BR_3 = $B(C_6F_5)_3$
[4-BCl$_3$]$^{\bullet-}$: BR_3 = BCl_3

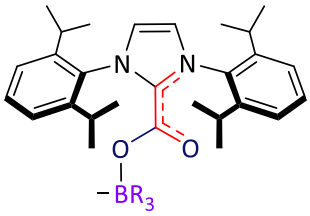

[5]$^{\bullet-}$: no BR_3
[5-BH$_3$]$^{\bullet-}$: BR_3 = BH_3
[5-B(C$_6$F$_5$)$_3$]$^{\bullet-}$: BR_3 = $B(C_6F_5)_3$
[5-BCl$_3$]$^{\bullet-}$: BR_3 = BCl_3

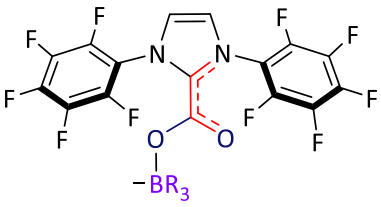

[6]$^{\bullet-}$: no BR_3
[6-BH$_3$]$^{\bullet-}$: BR_3 = BH_3
[6-B(C$_6$F$_5$)$_3$]$^{\bullet-}$: BR_3 = $B(C_6F_5)_3$
[6-BCl$_3$]$^{\bullet-}$: BR_3 = BCl_3

Enders and ^{Cy}CAAC-type NHCs

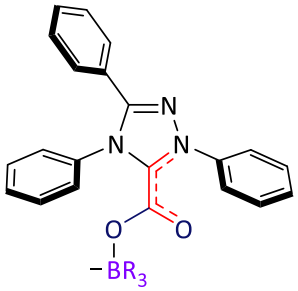

[7]$^{\bullet-}$: no BR_3
[7-BH$_3$]$^{\bullet-}$: BR_3 = BH_3
[7-B(C$_6$F$_5$)$_3$]$^{\bullet-}$: BR_3 = $B(C_6F_5)_3$
[7-BCl$_3$]$^{\bullet-}$: BR_3 = BCl_3

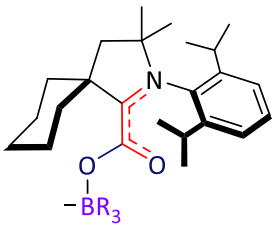

[8]$^{\bullet-}$: no BR_3
[8-BH$_3$]$^{\bullet-}$: BR_3 = BH_3
[8-B(C$_6$F$_5$)$_3$]$^{\bullet-}$: BR_3 = $B(C_6F_5)_3$
[8-BCl$_3$]$^{\bullet-}$: BR_3 = BCl_3

Scheme 3. Studied NHC-CO_2-based adducts in their monoreduced form.

Synthesised monoreduced adducts

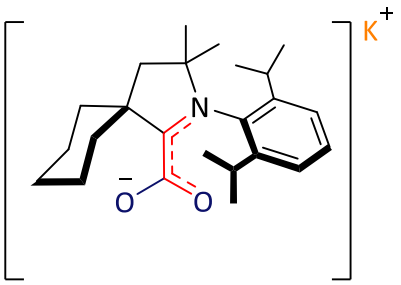

([8(K)]•)

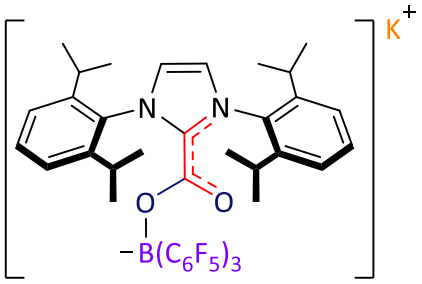

([5-B(C$_6$F$_5$)$_3$(K)]•)

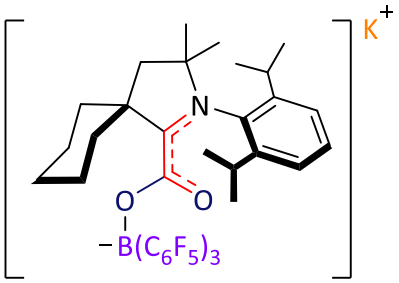

([8-B(C$_6$F$_5$)$_3$(K)]•)

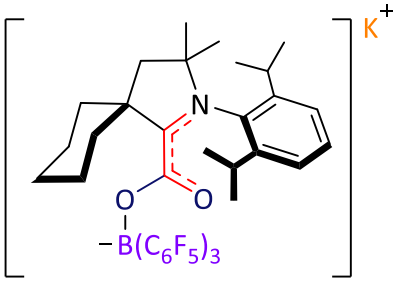

([8-B(C$_6$F$_5$)$_3$(Co)]•)

Scheme 4. Synthesised monoreduced NHC-CO_2-based adducts.

Chapter 1: Bibliographic Chapter

My PhD work concerns the synthesis of various NHC-CO_2-based adducts and the evaluation of their one-electron reduction chemistry by a combined experimental and theoretical study. In this first chapter, the topic of this work will be contextualised with examples reported in the literature. Firstly, the two pathways to generate a CO_2 radical anion, $[CO_2]^{\bullet-}$, will be described and secondly, we will cope with its reactivity towards open-shell and unsaturated species, eventually repeating information. The second part will deal with the one-electron reduction of NHC-CO_2-based adducts by electrochemical and chemical means. Later in the discussion, the synthesis of NHC-CO_2-BR_3 (BR_3: borane) reported in the literature will be exposed. To conclude, we will end up with the basis of estimation of theoretical reduction potential from the standpoint of thermodynamics.

1.1. Generation of CO_2 radical anion and formation of C-C bonds.

This subchapter concerns the generation of CO_2 radical anion, $[CO_2]^{\bullet-}$, and its use in C-C bond formation (Scheme 1). As shown in the scheme below, the generation of CO_2 radical anion can proceed from two main sources, CO_2 gas (1.1.1.1.) or from a formate salt (1.1.1.2.) under electrochemical and photochemical means (left, Scheme 1). It has been proven that it can later either react with open-shell via radical radical-radical coupling (1.1.2.1.) or towards alkene derivatives (1.1.2.2.) (right, Scheme 1).

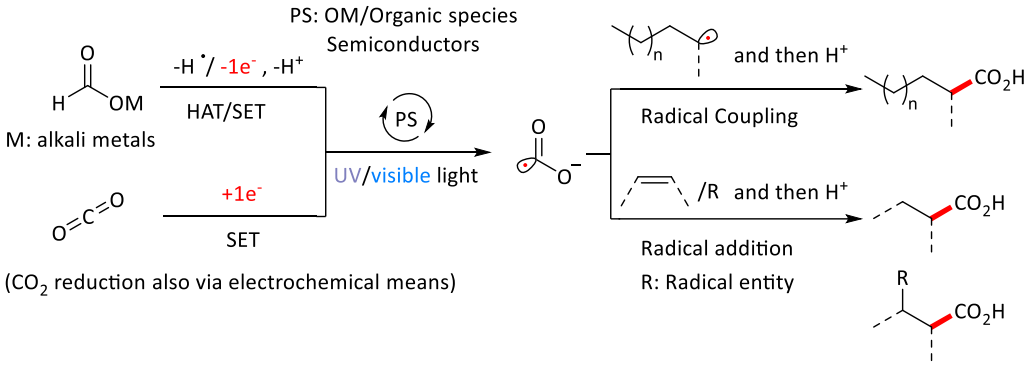

Scheme 1. Generation of CO_2 radical anion $[CO_2]^{\bullet-}$ and its use in C-C bond formation.

In section 1.1.1. "Generation of CO_2 radical anion, $[CO_2]^{\bullet-}$.", the schemes and discussions are oriented towards the reaction step in which the CO_2 radical anion is generated which means, that only chemical species involved in this step will appear on the schemes and discussions. In order to avoid the information reiteration in the schemes, the complete reactions will be discussed in detailed in section 1.1.2 "Reactivity of CO_2 radical anion.".

1.1.1. Generation of CO_2 radical anion, $[CO_2]^{\bullet-}$.

This section describes the different carbon-sources employed for the generation of the CO_2 radical anion, $[CO_2]^{\bullet-}$. In fact, the generation of $[CO_2]^{\bullet-}$ can be achieved through the direct single-electron reduction of carbon dioxide (1.1.1.1.), but also through hydrogen atom abstraction (HAT) or single electron oxidation of a formate salt (1.1.1.2.).

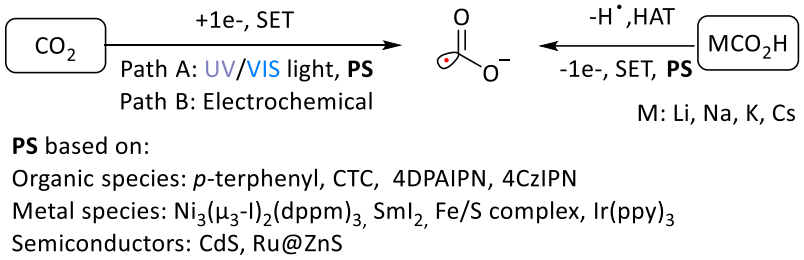

Scheme 2. Generation of CO_2 radical anion.

1.1.1.1. Generation of CO_2 radical anion from CO_2 gas.

The direct one-electron reduction of carbon dioxide is the most straightforward process to generate CO_2 radical anion, $[CO_2]^{\bullet-}$. Nevertheless, this approach is rather challenging since it operates at particularly negative potentials of E_{red} = −2.2 V in DMF, −2.3 V in CH_3CN versus SCE, -3 V in CH_3CN versus $Fc^{+/0}$ and -1.9 V versus SHE in aqueous solution at pH 7.[1,2,3,4]

1.1.1.1.1. Electrochemical conditions.

In 2019, Mellah and co-workers reported the formation of CO_2 radical anion from CO_2[5] gas and solid dry ice[6] through the *in situ* electrogenerated Sm(II) species (Scheme 3A). They observed that the use of dry ice significantly improves the yield. One year later, the

Zare's group[7] described the reduction of CO_2 upon reduction of the substrate (Scheme 3B). The latter plays the role of electron transfer agent affording the CO_2 radical anion. The direct formation of CO_2 radical anion with a sacrificial electrode in the absence of any mediator has also been reported (Scheme 3C).[8,9,10]

A) Electroreduction of CO_2 on a samarium anode

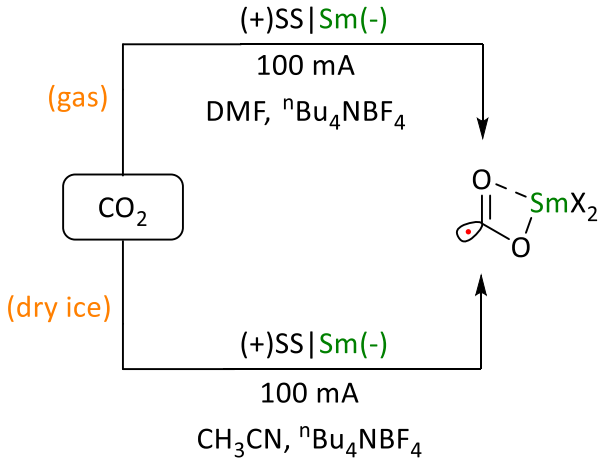

B) Electroreduction of CO_2 on a modified Glassy Carbon Electrode (GCE)

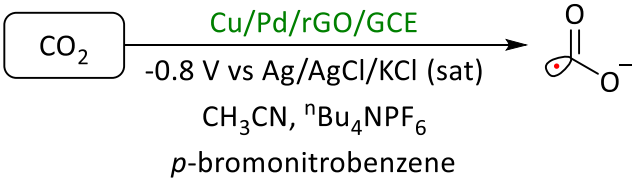

C) Electroreduction of CO_2 in the presence of a sacrificial electrode

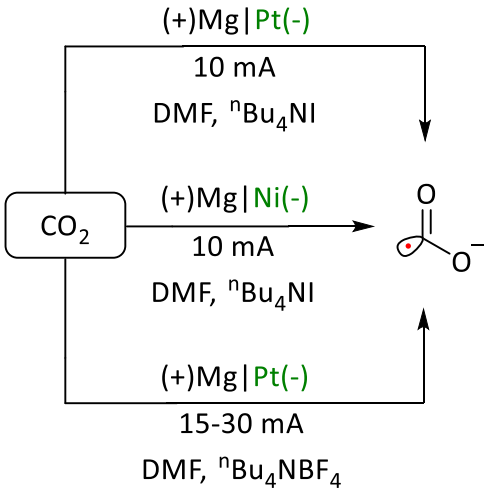

Scheme 3. Electroreduction of CO_2 on a Sm-based electrode (A), modified GCE (B) and in a presence of a Mg-based sacrificial electrode (C).

1.1.1.1.2. Photochemical conditions.

a) Using photoactive organic species.

In the literature, the use of organic dye species such as *p*-terphenyl as a photocatalyst to achieve this transformation using ultraviolet (UV) light has been reported.[11,12,13] As a key example, Jamison[11] and co-workers developed a photocatalytic system operating under flow chemistry for the carboxylation of styrene in less than 10 minutes, the hydrocarboxylated products were obtained with yields up to 87% and in a highly selective manner (<3% dicarboxylated product). According to the proposed mechanism, the reduction step proceeds as follows: upon irradiation of the *p*-terphenyl species, it produces a singlet excited state which undergoes a single-electron transfer (SET) with a sacrificial reductant amine, PMP, that would afford the mono-reduced form of the photocatalyst. At this point, the reduced photocatalyst (PC) exhibits a reduction potential which is reducing enough ($E°_{red}$ = −2.63 V vs SCE in DMF)[14] to generate $[CO_2]^{\bullet-}$ from carbon dioxide (Scheme 4).

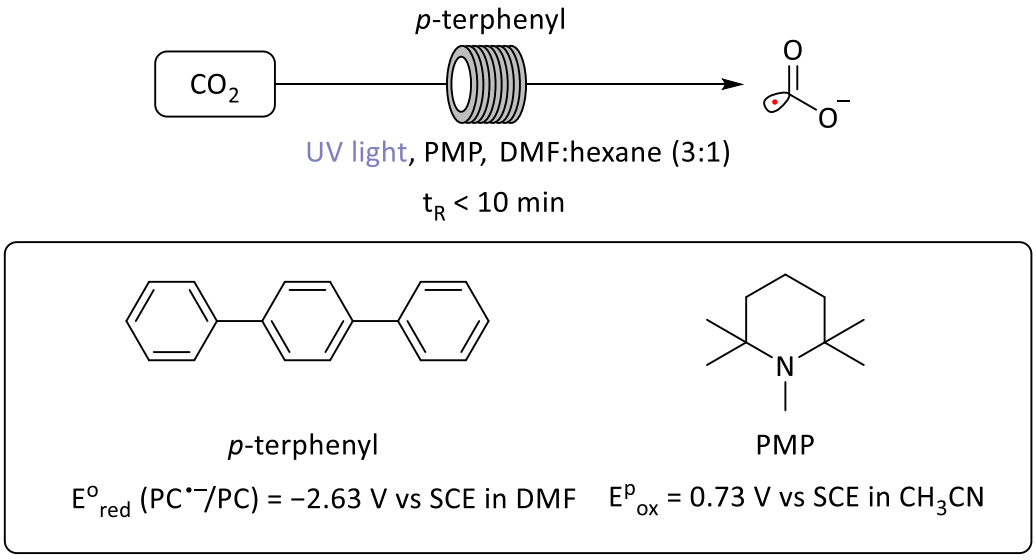

Scheme 4. Photoreduction of CO_2 to CO_2 radical anion using *p*-terphenyl under UV light.

Another recent example reported by the group of Yu[15] disclosed a strategy to perform an anti-Markovnikov hydrocarboxylation of activated alkenes (acrylates and styrene derivatives) with yields up to 73%. Their methodology is based on the formation of a thiolate-arene charge transfer complexes (CTC)[16,17,18,19], a photoactive species generated *in situ* between the thiolate and substrate. The initial step of the mechanism can take place under two different paths. Upon formation and irradiation of the CTC complex with

visible light, it produces a triplet state that enables the transfer of one electron to the CO_2 molecule resulting in the $[CO_2]^{\bullet-}$ formation. (Scheme 5).

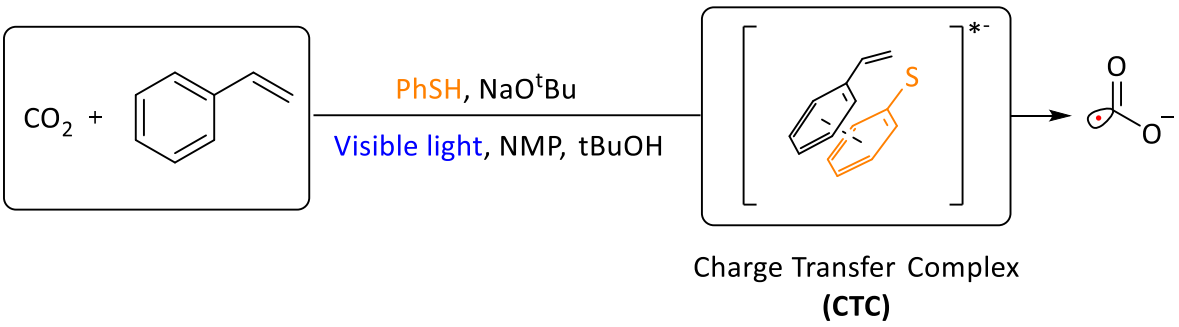

Scheme 5. Photoreduction of CO_2 using CTCs under visible light.

b) Using metal-based complexes.

The generation of CO_2 radical anion has also been reported using transition metal complexes. Works from Kubiak[20] and Ogawa[21] independently illustrated the possibility of photoreducing CO_2 into CO_2 radical anion using an inorganic Ni-based complex, $[Ni_3(\mu_3\text{-}I)_2(dppm)_3]$, and Sm-based salts ($SmI_2$/Sm) respectively. In the case of Kubiak's group, the carboxyl radical was generated by the oxidation of the Ni-based species upon irradiation using visible light (Scheme 6A). In the case of Ogawa, the Sm-based salt reduces both species, the substrate, and the carbon dioxide. They suggested that carbon dioxide coordinates to the samarium salt and subsequently, the CO_2 radical anion is formed through photoinduced electron transfer under visible light (Scheme 6B).

A) Photoreduction of CO_2 using a Ni-based complex

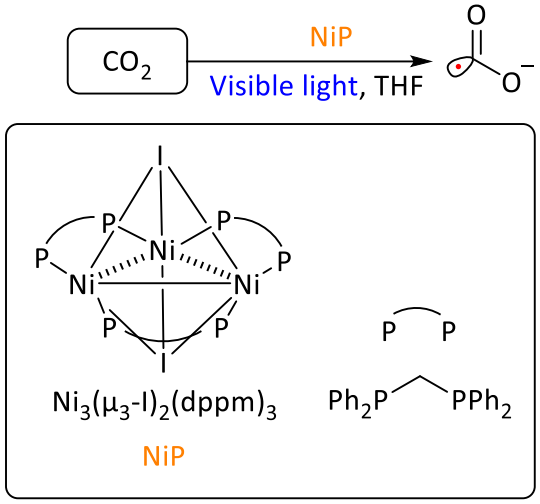

B) Photoreduction of CO_2 using a Sm-based salt

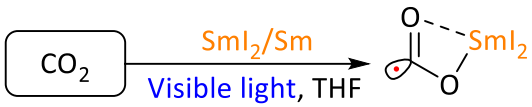

Scheme 6. Photoreduction of CO_2 using a Ni-based complex (A) and a Sm-based salt (B).

In contrast to the latter, Yu[22] and co-workers achieved this transformation based on a Fe/S cluster to yield thiocarboxylates *via* difunctionalization of olefins. Using catalytic amount of $FeCl_3$ (5 mol%) in the presence of a thiolate and a base (KO^tBu) in the medium, it affords the final product quantitatively. They hypothesised that an iron-sulphur cluster is generated and reduces CO_2 upon irradiation with visible light (Scheme 7A). Up to this date, the exact composition of the active species is still unknown. The same group disclosed in another work that a Ir-based photocatalyst (fac-Ir(ppy)$_3$) in very low catalyst loading (0.5-1 %mol) can also be used to have access to the highly reactive CO_2 radical anion in the carboxylation of unactivated alkenes context (Scheme 7B).[23,24]

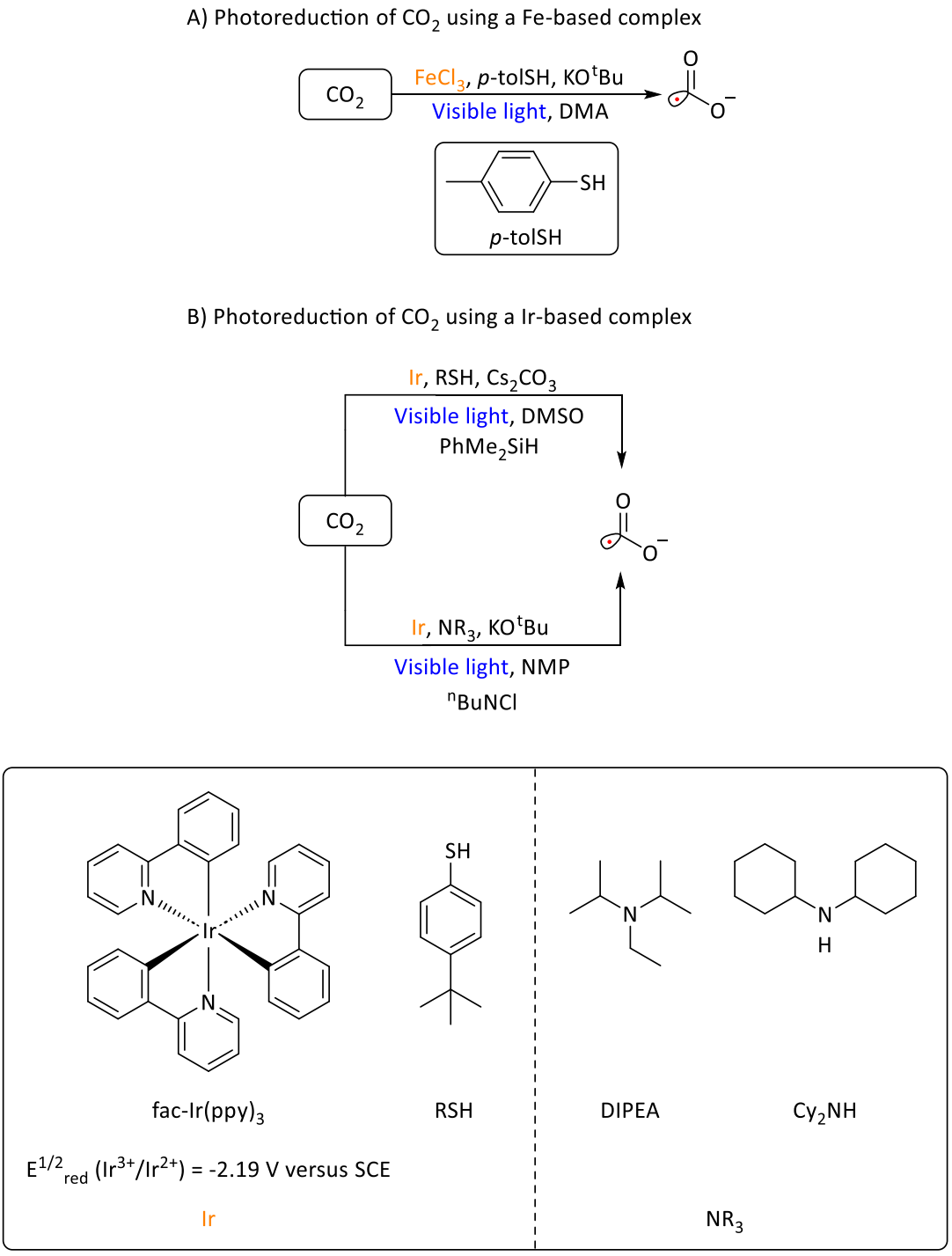

Scheme 7. Photoreduction of CO_2 using a Fe-based (A) and Ir-based (B) complexes.

c) Using a photoactive semiconductor.

The one-electron reduction of CO_2 to generate the CO_2 radical anion has been also achieved using photoactive semiconductors based on quantum dots, for instance, on CdS[25,26] crystallites in the presence of a sacrificial electron donor, triethylamine, using

visible light (upper, Scheme 8). These semiconductor nanoparticles exhibit composition- and size-dependent photophysical properties.[27] Another example based on ZnS deposited on Ru nanoparticles was described to enable the one-electron reduction of CO_2 (Ru@ZnS)[28,29] using UV light at its conduction band upon irradiation (down, Scheme 8).

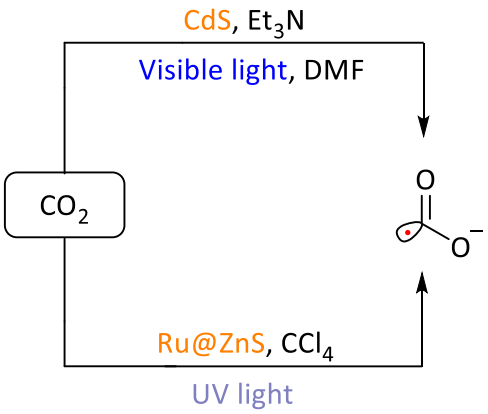

Scheme 8. Photoreduction of CO_2 using photoactive semiconductors.

1.1.1.2. Generation of CO_2 radical anion from a formate salt.

In order to circumvent the access to highly reducing potentials required to generate the CO_2 radical anion, formate salts were used in place of CO_2. In fact, the carbon dioxide radical anion can be generated *via* hydrogen atom transfer (HAT) from the formate with a suitable HAT abstractor agent or via single electron oxidation.

The generation of the CO_2 radical anion from formate can proceed *via* two main pathways, as previously cited, either *via* hydrogen atom transfer (HAT) using *N*-,*S*-based H-abstractors (HAT agents) or *via* its oxidation through a single electron transfer (SET). By definition, the hydrogen atom transfer[30] is a chemical transformation which consists of the movement of a proton and an electron (formally, a hydrogen atom) between two chemical species in a kinetic step. The species $Z^{\bullet}$ abstracts one hydrogen atom from the formate salt to form the new Z-H bond and the CO_2 radical anion (Scheme 9A). Thiol derivatives and tertiary amines are used as precursors to generate the active species (thiyl radical and amine radical cation, respectively) that would perform the HAT process in formate salts (formate $C(sp^2)$–H BDE = 86 kcal/mol[31]). BDE stands for "Bond Dissociation Energy". It is the maximum vibrational energy that a molecule can have prior

to its decomposition into the ground electronic stated of the constituent atoms.[32] This HAT event is essentially thermoneutral in the case of transformations where S-derivatives are involved as H-abstractors[33,34,35,36] (thiol S–H BDE = 88–90 kcal/mol)[36]. Similar behaviour can be observed in the case of N-derivatives[37,38,39], the H-abstraction is also favourable (tertiary N-H^+ BDE = 91 kcal/mol)[40]. The formate salt, whose potential is at 0.94 V vs SCE in DMSO, can also be oxidised by a suitable oxidising agent *via* SET (scheme 9B). This latter example will be presented later in the discussion.

A)

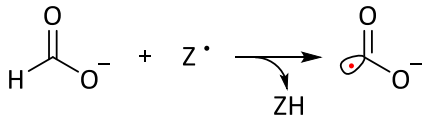

formate $C(sp^2)$–H BDE = 86 kcal/mol

B)

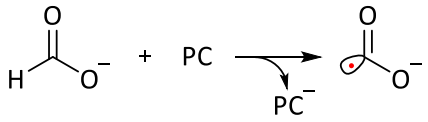

$E^{1/2}_{red}$ (HCO_2Cs) = 0.94 V vs SCE in DMSO

Scheme 9. A) Hydrogen Atom Transfer (HAT). B) Single Electron Transfer (SET) for a formate salt.

The formate species which have been employed in the literature are restricted to alkali formate species based on lithium, sodium, potassium, and caesium (right, Scheme 2). The choice of alkali counterion of the formate salt is not trivial as it has an impact on the formation of the carbon dioxide radical anion. As key examples, the work from the groups of Wickens[33] (upper, Scheme 10) and Li[41] (down, Scheme 10) independently described the hydrocarboxylation of activated alkenes using formate salts with different alkali counterions. In both cases, they observed that the use of potassium formate allowed them to access the desired product in excellent yields. Changing potassium to sodium and lithium was detrimental for the reaction yield. The use of caesium formate exhibited a rather similar yield compared to lithium and sodium formate species and the rate increased. The Wickens and Li attributed these differences to the solubility of these formate salts in DMSO, which would limit the formation of the carbon dioxide radical anion.

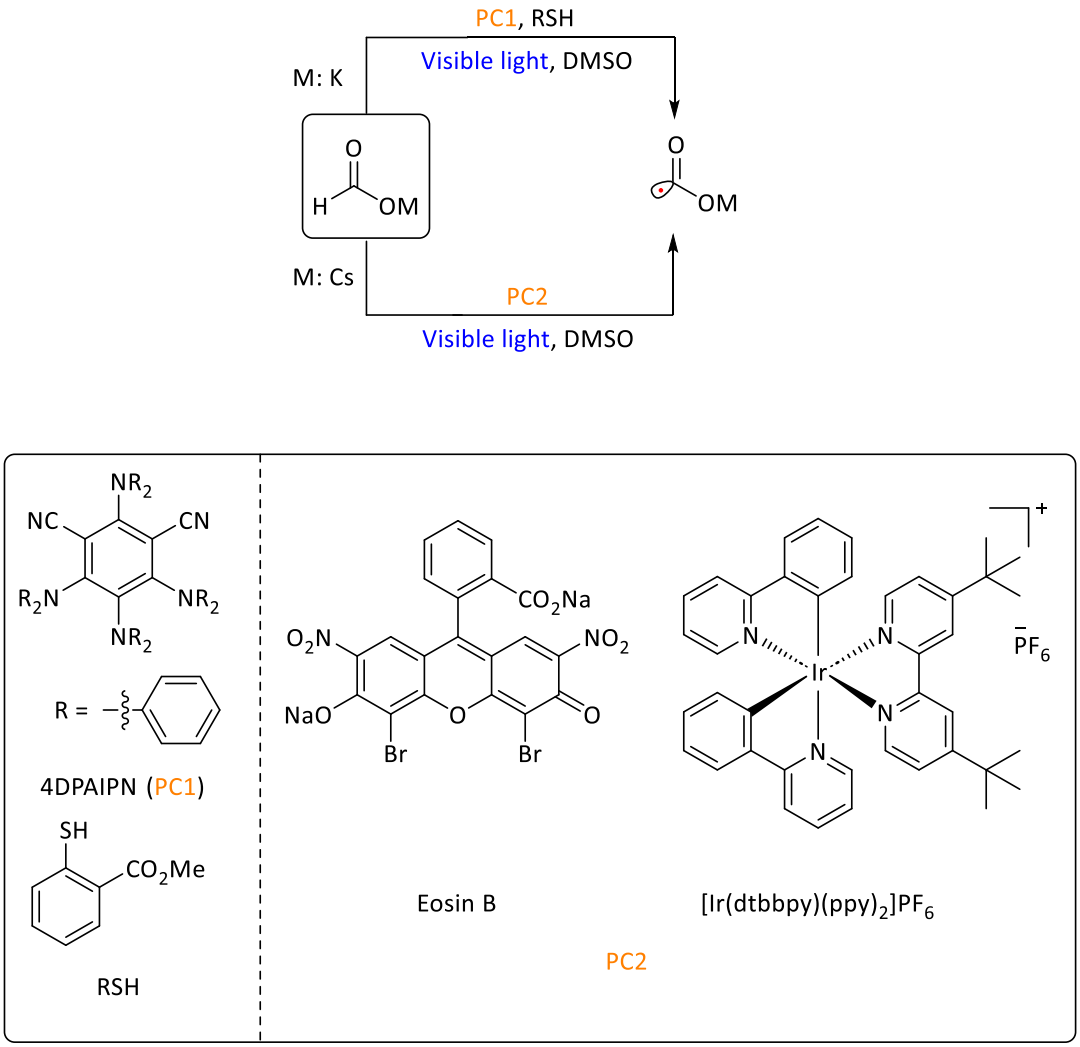

Scheme 10. Generation of CO_2 radical anion from formate.

In the case of the use of thiol as a HAT precursor for the generation of CO_2 radical anion, reports point out the use of this species as a co-catalyst. The thiyl radical is recycled during the reaction. The catalytical charge only goes up to 2 mol% in which the reaction is assisted by an additional photoactive species.[33,34] According to Wickens' reports[33,34], the thiyl radical is generated *via* the reductive quenching of the single excited state from the organic photocatalyst (4DPAIPN, PC1) with the thiol/thiolate (upper, Scheme 10). In another report from the same group[35], they envisaged the formation of the carbon dioxide radical anion in the absence of any additional photoactive species. The catalytical charge of thiol is increased up to 20 mol%. This significant increase in the thiol amount is related to the need of generating disulfide products. Under irradiation with visible light, the thiol undergoes a dehydrogenative homocoupling with a second thiol molecule to yield the disulfide product. To prove the hypothesis, they replace it by disulfide. Upon

its replacement by disulfide, the yield of the hydrocarboxylated product remained unaltered (Scheme 11).

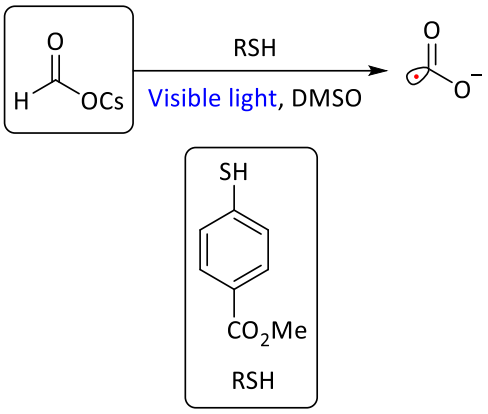

Scheme 11. Formation of CO_2 radical anion using only thiol derivatives under visible light.

Respect to the *N*-based precursors, DABCO is exclusively used as a HAT-agent precursor in the generation of the CO_2 radical anion.[37,38,39] The active species is generated *via* the oxidation of the tertiary amine yielding an amine radical cation as previously mentioned. It is observed that a large amount of DABCO is needed to carry out hydrocarboxylation reactions (around 50% mol).[37,38] In one example related to the topic reported by Xi[39] in which they described the carboxylation of benzyl halides with CO_2 and a formate salt, a stoichiometric amount of DABCO respect to the formate salt was required. Both reagents were employed in a large excess respect to the benzyl halide. In this work, the carboxylating agent was free CO_2 molecule. A DABCO molecule is oxidised by the excited state of the Ir-based photocatalyst resulting into the active (oxidised) form of DABCO capable of performing the HAT in the formate species. The role of the CO_2 radical anion in this example was to act as a reductant of the substrate and to yield its monoreduced form (Scheme 12). Previous to this work, Jui and co-workers showcased the new role of CO_2 radical anion as a reducing agent in the reduction of aryl chlorides and the effectiveness of *S*-based species (99%) respect to the DABCO (68%) as a HAT agents.[36] Due to the scope of this PhD, the use of carbon dioxide radical anion as a reducing agent will not be further discussed.

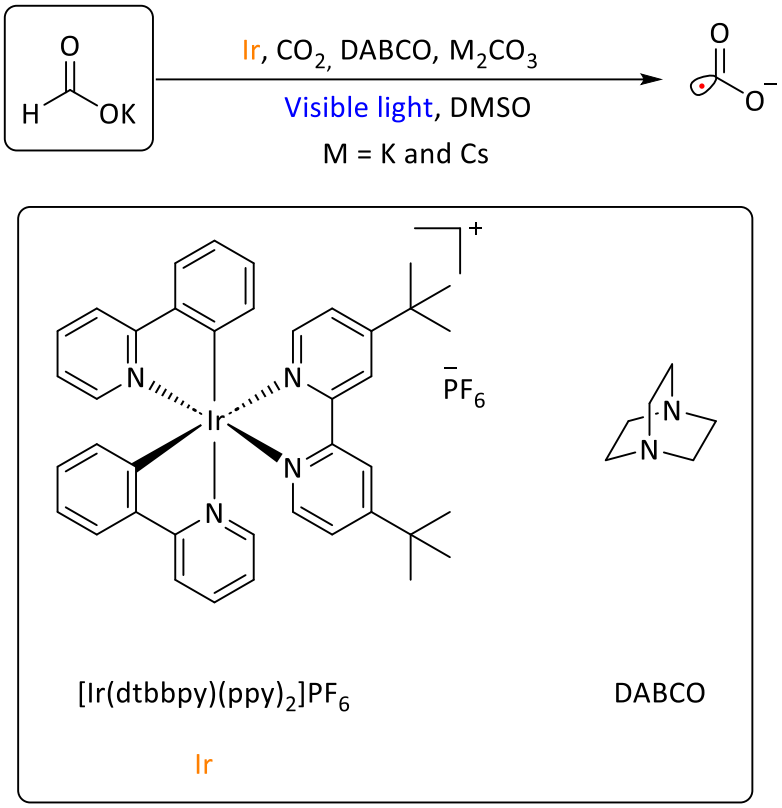

Scheme 12. Formation of CO_2 radical anion *via* HAT with *N*-based HAT agents.

Carbon dioxide radical anion can also be generated from a formate salt *via* SET. The single electron transfer (SET) is a process through which an electron is transferred from a chemical entity to another (Scheme 9A). As representative example, the group of Li[41] described the hydrocarboxylation of activated alkenes in the absence of HAT agent. According to this work, the caesium formate is oxidised to a formyloxyl radical intermediate *via* SET with the excited state of either Eosin B or $[Ir(dtbbpy)(ppy)_2]PF_6$ (1% mol) upon irradiation at 100°C. Then, it undergoes an H-abstraction with another formate molecule to yield the carboxyl radical and formic acid (path A, Scheme 13). Another plausible path is the photoexcitation of the reduced form of the photocatalyst. At that stage, it exhibits a reducing enough character to enable the reduction of alkenes (path B, Scheme 13). Subsequently, the reduced alkene reacts with the CO_2 originally formed from the decomposition of formyloxyl radical. Nevertheless, according to the authors this latter path is expressed in a minor degree. It seems the absence of any HAT agent requires harsher conditions compared to previous examples. They had to perform the reaction at high temperatures (100°C) and formate salt in excess (10 equivalents) in order to obtain similar yields to the work of Wickens[33]. Besides the absence of HAT agent,

they cannot rule out the possible presence of sulphur derivatives generated from the decomposition of DMSO under these conditions that may lead the reaction through a HAT process as in previous described reports.[41] Based on the previous described works, we can state that the use of a HAT agent and a photocatalyst makes accessible the generation of the CO_2 radical anion under mild conditions from formate salts.

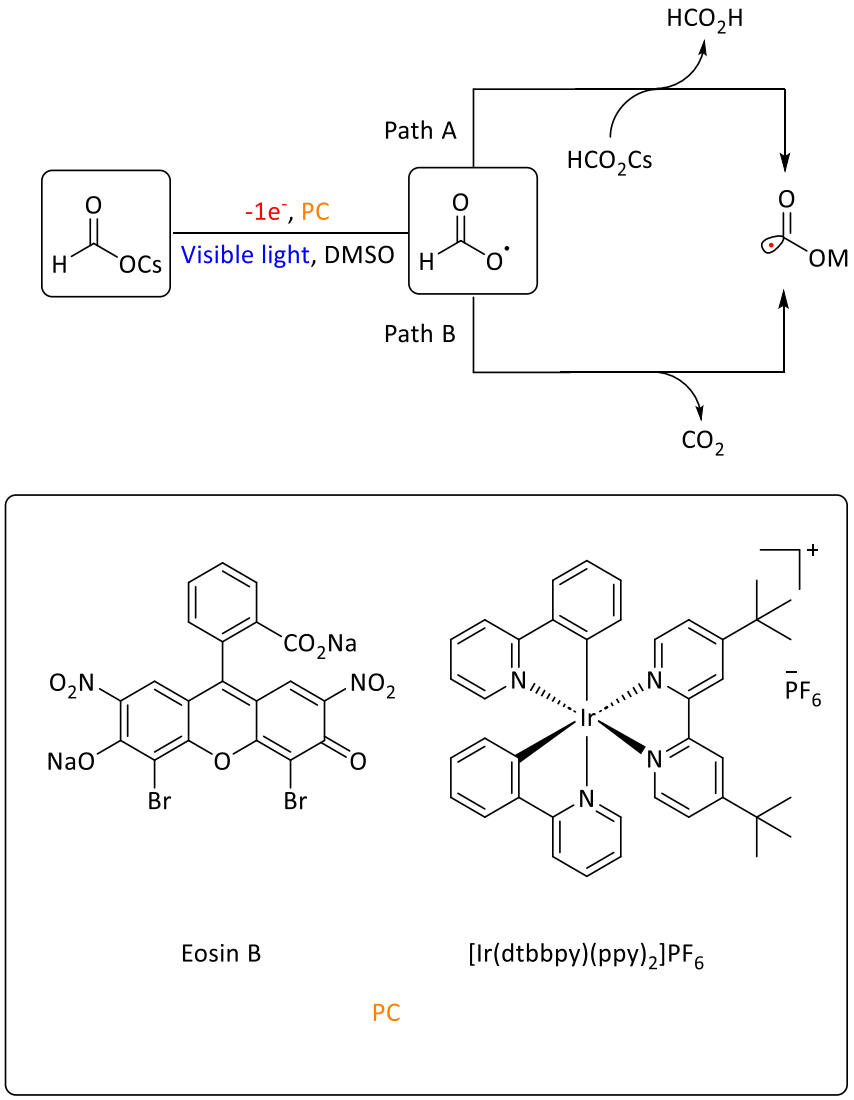

Scheme 13. Generation of CO_2 radical anion from the oxidation of caesium formate.

1.1.2. Reactivity of CO_2 radical anion.

In this section, the discussion will be focussed on the transformations related to the substrate and the experimental conditions in which the C-C bond formation takes place with the participation of CO_2 radical anion. Upon the formation of the carboxyl radical,

it can react either with open-shell species (1.1.2.1.) (Scheme 14A) or unsaturated species (1.1.2.2.) (Scheme 14B).

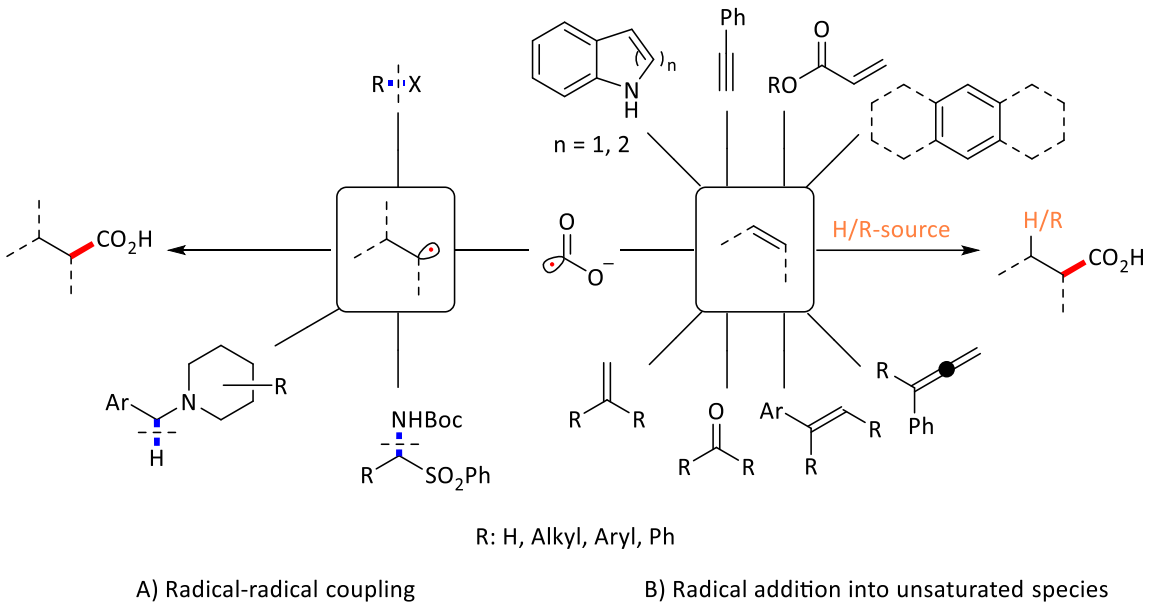

Scheme 14. Reactivity of the monoreduced form of CO_2 with open-shell (A) and unsaturated species (B).

1.1.2.1. Reactivity of CO_2 radical anion with open-shell species *via* radical-radical coupling.

The use of open-shell species generated *via* photochemical conditions to form C-C bonds with $[CO_2]^{\bullet-}$ is very scarce in the literature. In 2017, Jamison[13] and co-workers disclosed a photoredox strategy for the synthesis of α-amino acids using UV-light in continuous flow through the carboxylation of C(sp^3)-H bond from tertiary benzylic amines (*N*-benzylpiperidine derivatives) in a presence of a base, KCO_2CF_3. The open-shell species are generated as follows: upon irradiation of the photocatalyst, its single-excited state undergoes a reductive quenching with the amine affording the formation of the oxidised amine along with the reduced photocatalyst. Then, the amine cation is deprotonated by a base yielding the α-amino radical. After the formation of the carbon dioxide radical anion *via* SET with the reduced photocatalyst, the new C-C bond is formed through radical-radical coupling to produce the α-amino acids with yields up to 99% and 52:1 regioselectivity in only 10 minutes (Scheme 15).

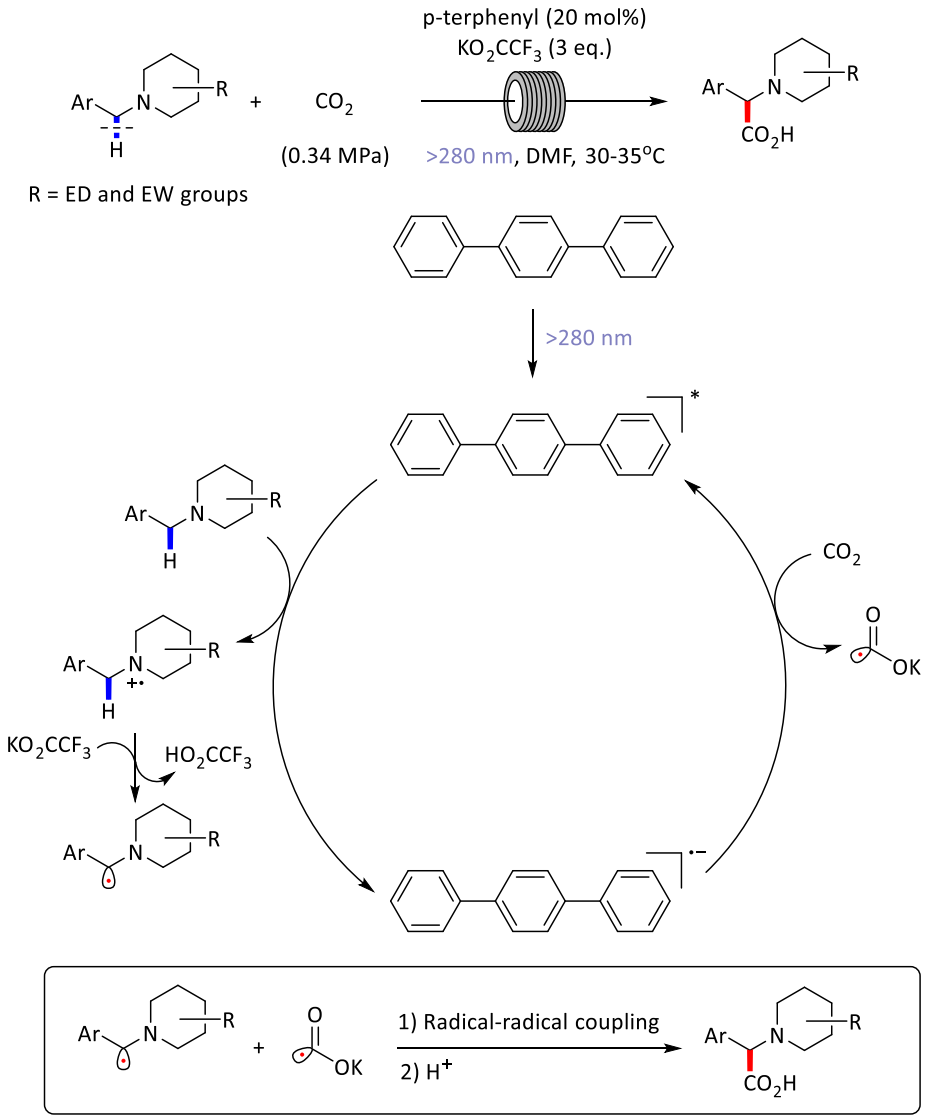

Scheme 15. Photoredox activation of carbon dioxide for amino acid synthesis in continuous flow by Jamison's group.

As previously discussed, pioneering work from Yanagida[25] demonstrated the photofixation of CO_2 into benzophenone catalysed by colloidal microcrystallites constituted by CdS under visible light in the presence of a sacrificial amine (Scheme 16A). Despite quantitative conversion of benzophenone, these nanostructures are more active towards the synthesis of benzopinacol (**2**) (79% in methanol) and benzohydrol (**3**) (88% in acetonitrile) in which the CO_2 is not involved. In the optimal experimental conditions for the product of interest (**1**), the reaction only yielded 12% of **1** in DMF, along with **2** and **3** in similar yields (**2**, 24%; **3**, 10% in DMF). This transformation is very dependent on the used solvent, in all cases it consisted of saturated-CO_2 solutions (Scheme 16A and

16B). Five years later, the same group enlarged the scope to other aromatic ketones and benzyl halides on the surface based on the previous technology.[26] Using other aryl ketones such as acetophenone, they could improve the yield towards the carboxylic acid product (**4**) (34%) pre-irradiating the reaction system for 1 h and increasing the reaction time up to 5h (**5**, 25%; **6**, 4%). Both substrates are reduced, CO_2 and the aryl ketones, and then coupled. Once the benzyl halides are reduced, they undergo a C-X bond (X = Cl, Br) mesolytic cleavage resulting into the corresponding halide anion a benzyl radical species which subsequently couples with the CO_2 radical anion in similar yields (X = Cl, 34%; X = Br, 16%) (Scheme 16B).

A) Photofixation of CO_2 into benzophenone catalysed by CdS microcrystallites

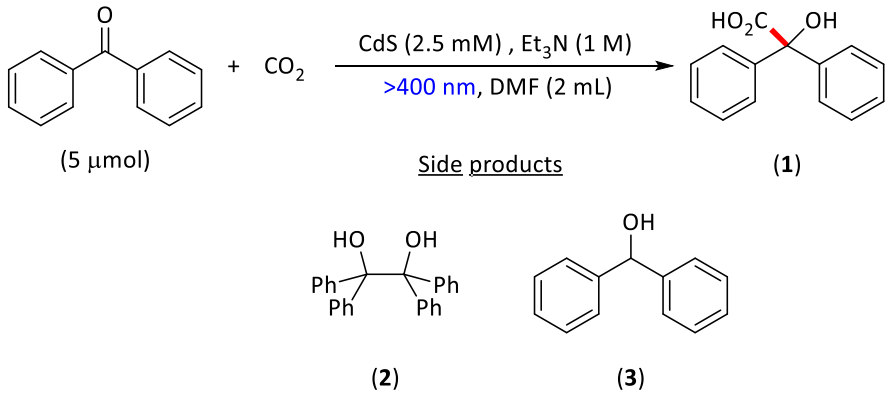

B) Photofixation of CO_2 into acetophenone and benzyl halides catalysed by CdS microcrystallites

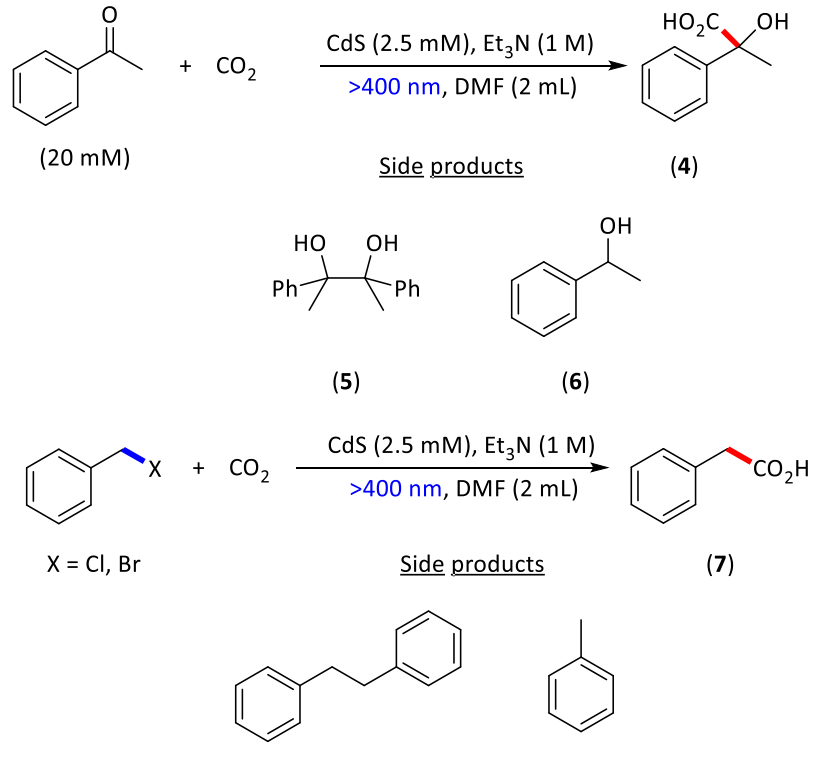

Scheme 16. Photofixation of CO_2 into benzophenone (A) and other aryl ketones and benzyl halides using CdS microcrystalites (B).

In 2014, the group of Macyk[28] reported the photocatalytic carboxylation of acetylacetone at ZnS deposited in Ru-based nanoparticles (Ru-NP) under UV light. Nevertheless, they observed very low yields (<1%) of the desired product (Scheme 17A). Only the group of Ogawa[21] described the reductive carboxylation using non-activated alkyl halides such as, docosanyl bromide (**8**) with CO_2 using a photoinduced Sm-mixed system under visible light with yields up to 76%. In this work both species are reduced, alkyl halide and CO_2 as in previous examples (Scheme 17B).

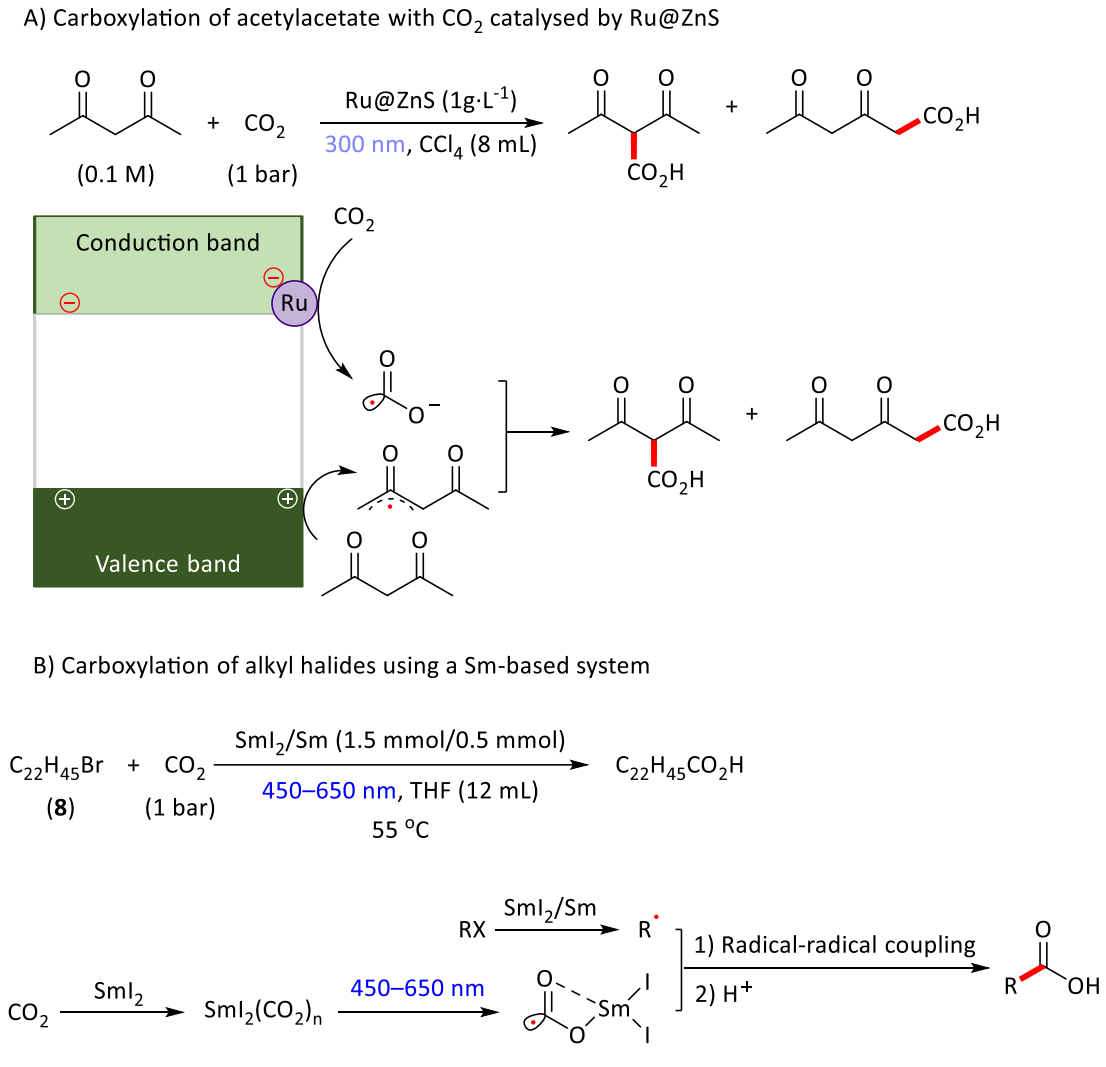

Scheme 17. Carboxylation of acetylacetate (A) and alkyl halides (B) with CO_2.

In 2006, Barba[42] and co-workers observed that carboxylated derivatives could be produced through the carboxyl radical generated under electrochemical conditions. In

the same direction that the work reported by Ogawa, Mellah and co-workers described the formation of C-C bonds using aryl[5] and benzyl halides[6] and CO_2 through the in *situ* electrogenerated Sm(II) species. This methodology was applied to a large scope of aryl derivatives from moderate to excellent yield and with a good chemical tolerance (Scheme 18A and 18B). Very recently, *N*-Boc-α-aminosulfones were studied as radical precursors in the C-CO_2 bond formation by Senboku and co-workers.[43] They proposed that upon reduction, these species undergo a reductive C-S bond cleavage at 0°C affording the benzyl radical that would react with the CO_2 radical anion to yield protected α-aminoacids from moderate to excellent yields (up to 87%) . Another possibility is the reduction of the benzyl radical to the anion that would react with the CO_2 *via* nucleophilic attack. Nevertheless, they are still working on the mechanism (Scheme 18C).

A) Carboxylation of aryl halides with CO_2 by electrogenerated SmX_2

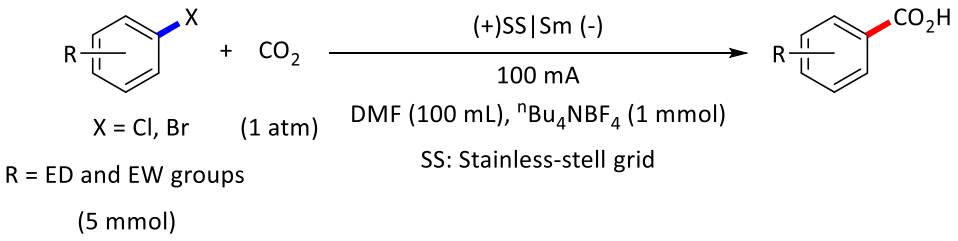

B) Carboxylation of benzyl halides with CO_2 by electrogenerated SmX_2

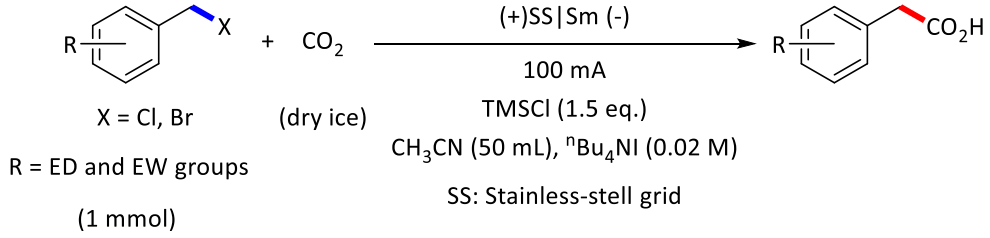

C) Electrochemical carboxylation of *N*-Boc-α-aminosulfones with CO_2

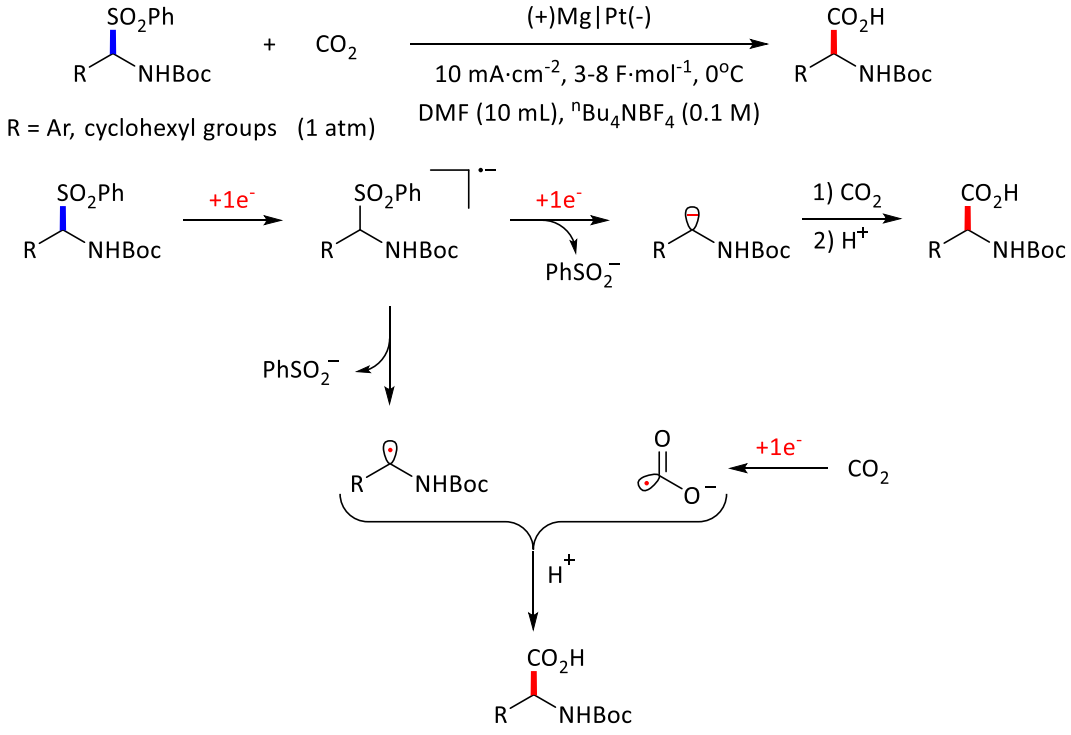

Scheme 18. Carboxylation of aryl (A) and benzyl (B) halides by electrogenerated SmX_2. Electrochemical carboxylation of *N*-Boc-α-aminosulfones (C).

1.1.2.2. Reactivity of CO_2 radical anion towards alkene derivatives.

The reactivity of CO_2 radical anion towards unsaturated species has been vastly reported compared to reaction in which open-shell species are involved. As a pioneering example, Kubiak[20] reported in the mid-90's the dicarboxylation of cyclohexene using stoichiometric amount of a Ni-based photoactive species. Upon irradiation, the excited state of the Ni-based complex enables the generation of the free CO_2 radical anion, which later undergoes a radical addition with a cyclohexene molecule yielding a generate a Giese-type species (**9**) (Scheme 19). Then, **9** reacts with a free molecule of CO_2 (reverse Kolbe reaction) and it is subsequently reduced by a second photoexcited Ni-based complex yielding 1,2-dichlohexanedicarboxylate molecule.

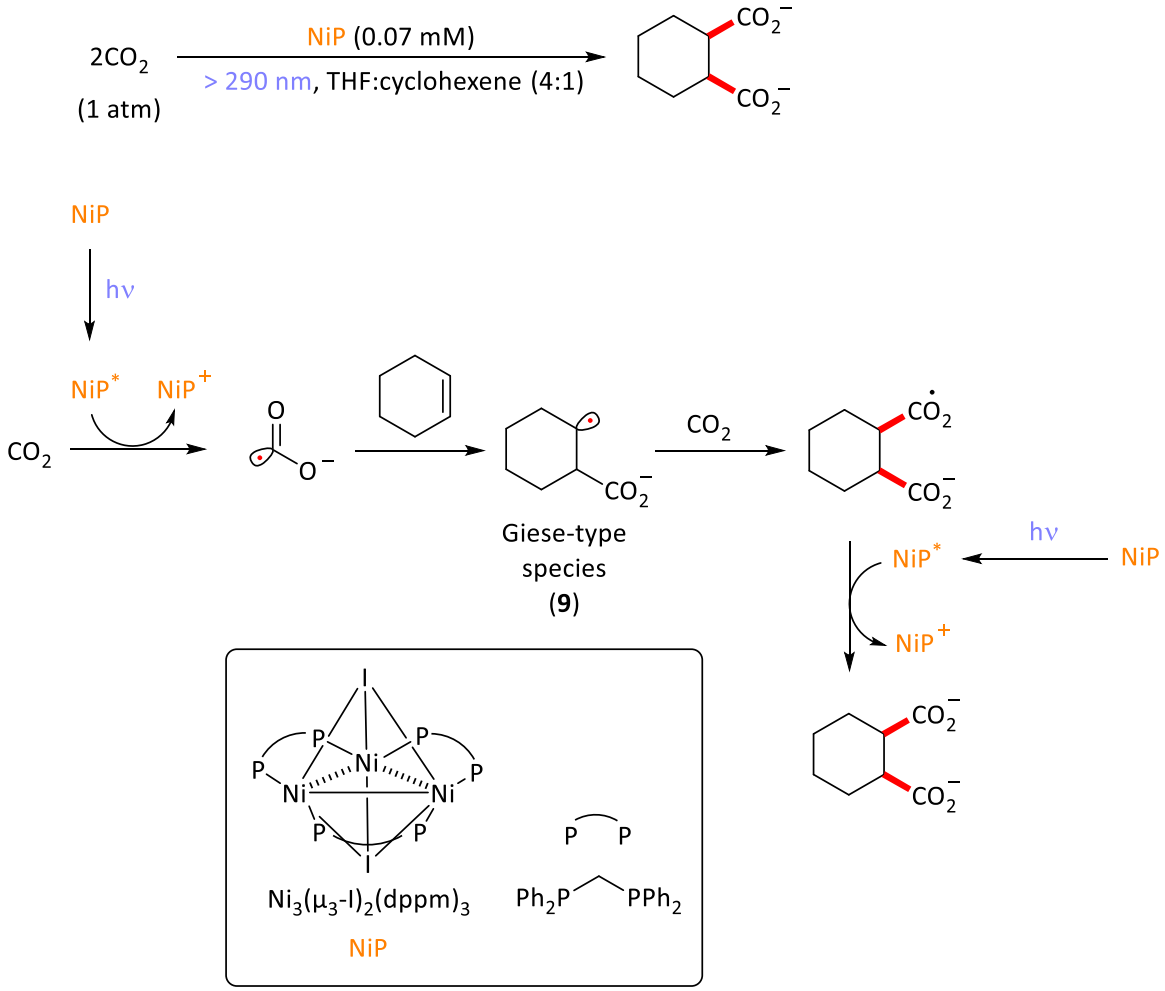

Scheme 19. Capture of CO_2 radical anion previously generated *via* SET with a photoactive Ni-based complex.

In the same vein, Yu[23] and co-workers recently disclosed a strategy using the vastly employed photocatalyst, fac-Ir(ppy)$_3$, to promote the carboxylation of a large scope of

unactivated alkenes with moderate to good yields (Scheme 20). Upon the first carboxylation of the alkene, the radical generated undergoes an intramolecular HAT process to afford a more stable benzyl radical. It can either react with another carboxyl radical to yield dicarboxylate derivatives or be reduced by the reduced photocatalyst to afford an anion. This reactive species undergoes a nucleophilic attack to another molecule of CO_2 to yield the dicarboxylated product. This strategy based on HAT-intramolecular process can also disrupted by the impossibility of forming the benzyl radical and lead to the β-hydrocarboxylation. In another report based on the previous methodology, they enlarge the substrate scope to activated alkenes, allenes and hetero(arenes)[44] affording the desired product in good yields.

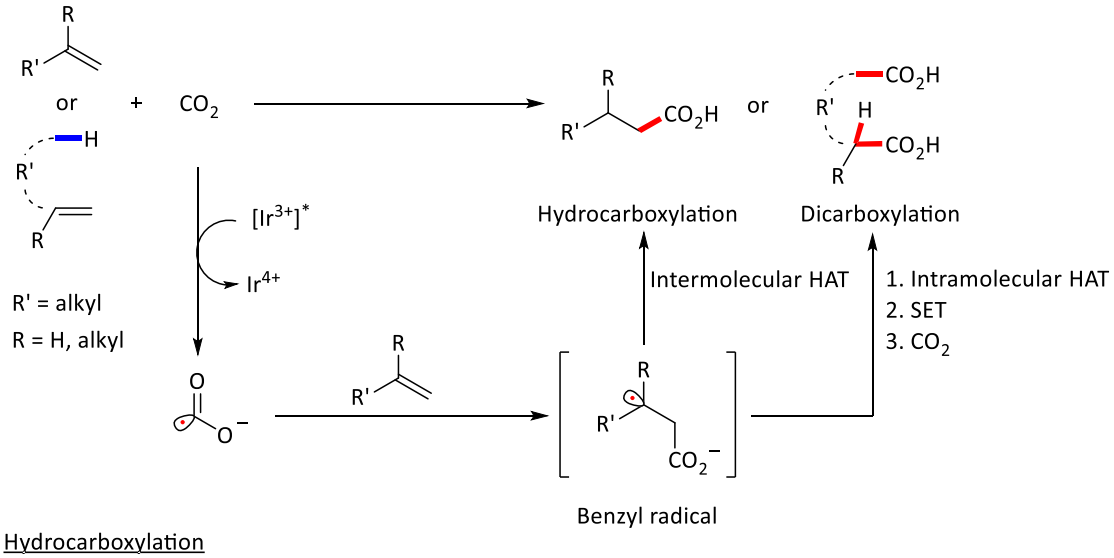

Hydrocarboxylation

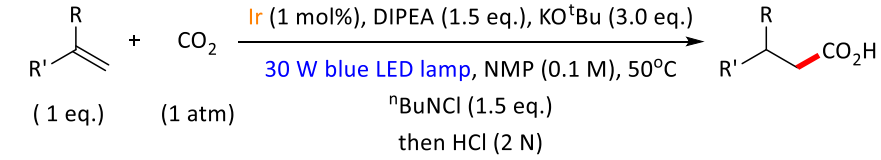

Dicarboxylation

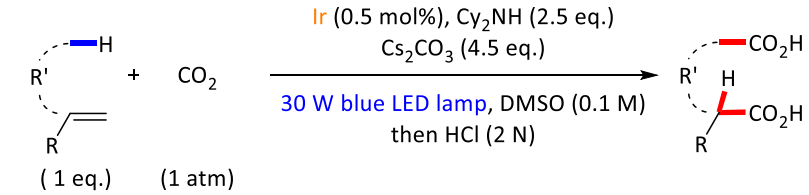

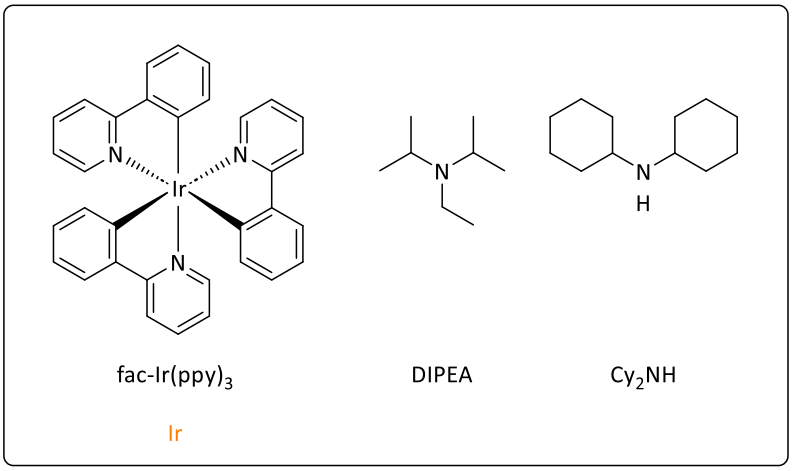

Scheme 20. Dicarboxylation and hydrocarboxylation of unactivatede alkenes using an Ir-based complex with CO_2.

In contrast to the previous example, the same group[44] employed an organic-based photocatalyst, 4CzIPN, with a higher catalytical loading (Scheme 21). As a mechanistic proposal, they suggested that the excited state of the 4CzIPN (4CzIPN*) undergoes a SET

with the amine to give the strong reductant capable of reducing the alkene to its radical anion. At this stage, two paths could take place. In path a, the resulting alkene radical anion could react with the CO_2 to generate a more stable benzyl radical. This intermediate then further undergoes a second SET to yield the benzylic anion, which then reacts with a second molecule of CO_2 *via* nucleophilic attack resulting in the formation of the desired product. In the case of path b, they also considered the possibility of the electron transfer from the alkene radical anion to the CO_2 molecule giving access to the CO_2 radical anion that would react with the benzyl radical and yield the dicarboxylate species. Yet, path b seems to be less favoured as no oxalate formation (from the CO_2 radical anion homocoupling) was observed in the reaction (Scheme 21).

As in other examples, the dicarboxylation of unsaturated species such as alkenes[45], arenes[46] and heterocycles[9] can occur through electrochemical means to produce dicarboxylic derivatives in good to excellent yields. Besides alkene derivatives, the formation of new C-C bonds with alkynes can also take place. As a key example, Jiang[47] and co-workers disclosed in 2010 a methodology to yield tricarboxylates (**12**) that would derive into anhydrides (**14**) upon hydrolysis in the presence of common metal salts under electrochemical means with yields up to 83% for compound **14** (R = Me, R’ = H). The dicarboxylic derivatives were also present in a significant amount, up to 27% for compound **13** (R = R’ = H). Internal alkynes were also tested (**10**, R = H, R’ = Ph) and the yield of compound **14** (R = H, R’ = Ph) (68%) was similar to the terminal alkyne homologous (**10**, R = H, R’ = H) (70%). The use of internal alkynes (**10**, R = H, R’ = Ph) were detrimental for the access of compound **13** (12%) as well as the use of alkynes bearing electro-withdrawing groups (**10**, R = NO_2, R’ = H) (7%). They could observe that the electrode material also exhibited a large impact on the electrocarboxylation reaction (Scheme 22).

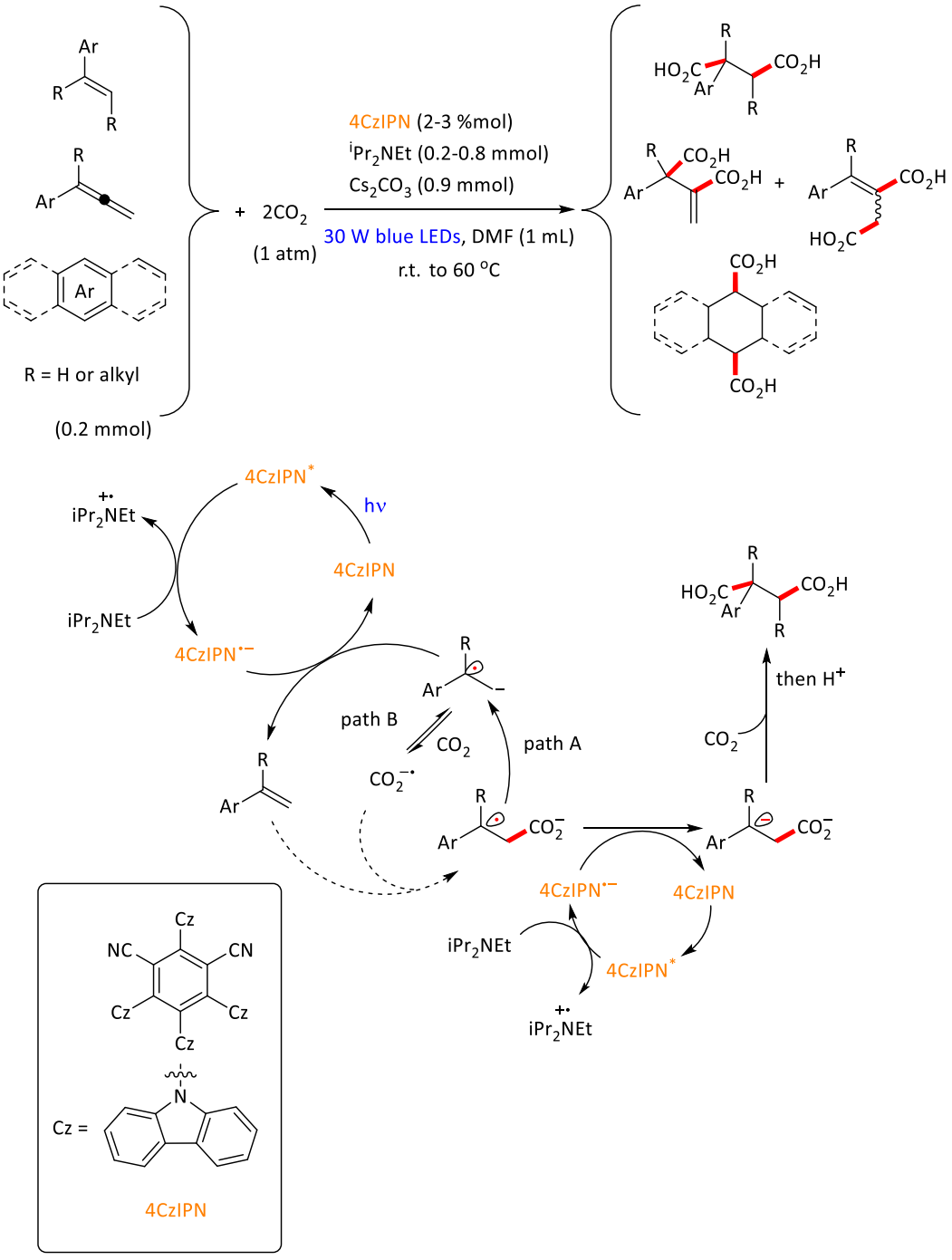

Scheme 21. Dicarboxylation of activated alkenes, dienes and hetero(arenes) with CO_2 using 4CzIPN as a photocatalyst under visible light.

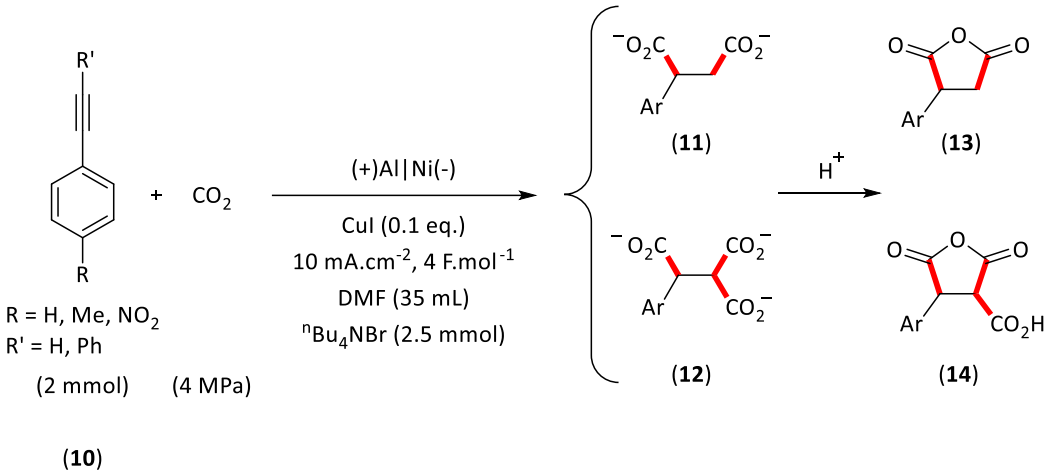

Scheme 22. Electrocarboxylation of alkynes with CO_2.

The β-hydrocarboxylation of unsaturated species is largely explored in the literature. As representative example, Li and colleagues described the β-selective hydrocarboxylation of substituted alkenes using Eosin B or an Ir-based photocatalyst (Scheme 23). Two plausible mechanisms were suggested by the authors. In path A, the excited state of the photocatalyst oxidises the formate salt to formyloxyl radical which is capable of trapping the hydrogen of formate salts and provide CO_2 radical anion and formic acid. Then, the $[CO_2]^{\bullet-}$ undergoes a radical addition to the alkene resulting in a Giese-type species (**15**) that will be reduced to the corresponding anion (**16**). The latter species is protonated yielding the desired product. In path B, the reduced form of the catalyst may be excited again and further reduce the alkenes to alkenyl radical anion which could react with the *in situ* generated CO_2 from the formate salt. Finally, the resulting functionalised alkenyl radical anion (**15**) is reduced and protonated as in path A to yield the desired carboxylate product.

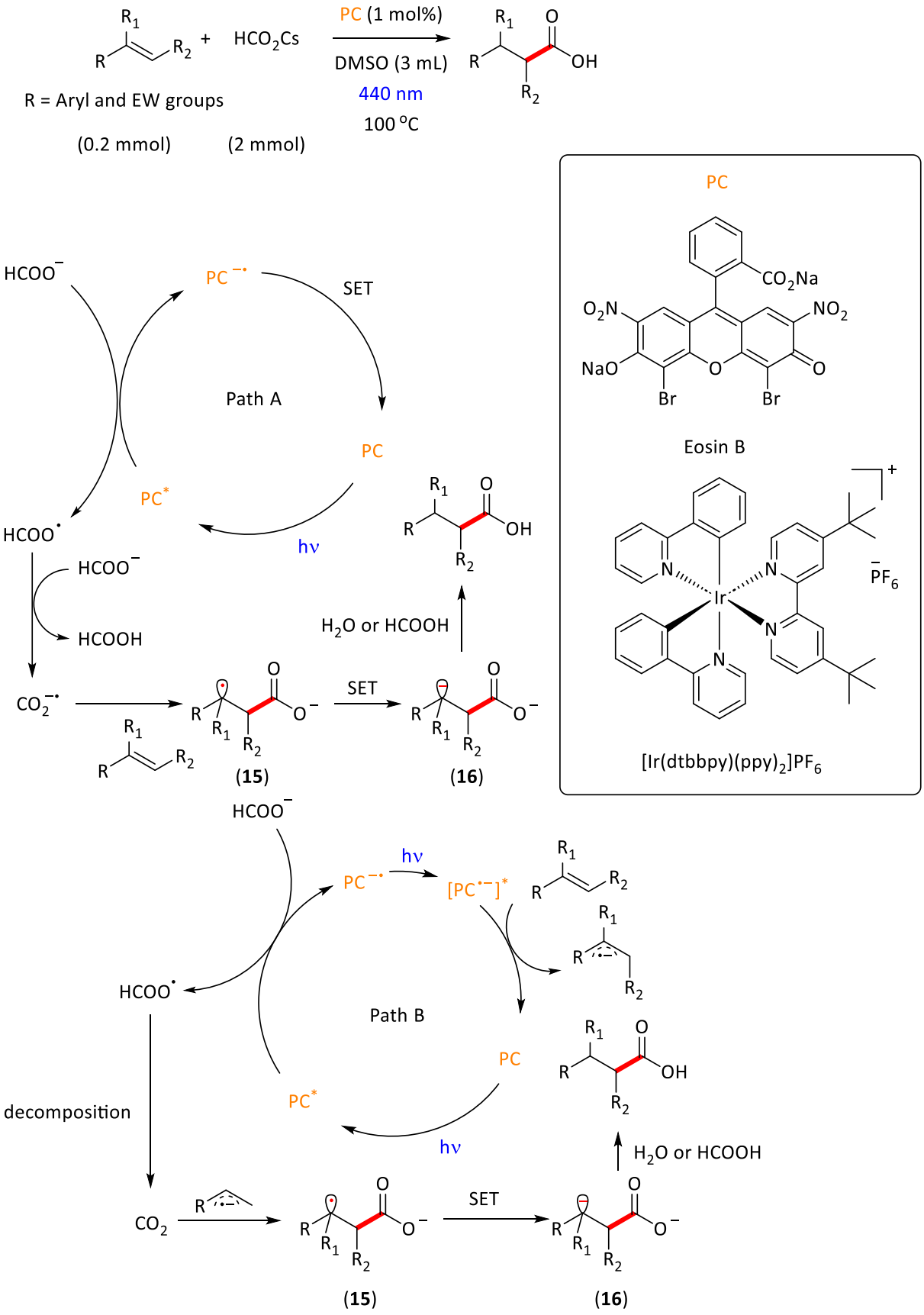

Scheme 23. Hydrocarboxylation of alkenes derivatives with formate salts catalysed by either an organic or an Ir-based photocatalyst .

As another key example, the group of Jamison[11] reported the β-selective hydrocarboxylation of terminal and α,β-substituted styrenes using CO_2 at atmospheric pressure under UV-light based on flow chemistry (Scheme 24). Following this strategy, they could have access to a large array of styrene derivatives with a good chemical tolerance. Based on deuterium-labelling and control experiments, they proposed a general mechanism for this transformation. Upon photoexcitation of the organic photocatalyst, *p*-terphenyl, its excited singlet state, [*p*-terphenyl]*, undergoes a single electron transfer (SET) with a sacrificial reductant agent, an amine, to provide very strong reductant *p*-terphenyl radical anion (E^o_{red} = –2.63 V vs SCE in DMF)[14]. At this stage, the *p*-terphenyl radical anion would further reduce CO_2 to its radical anion *via* SET as explained in the previous section. Then, the CO_2 radical anion undergoes a radical addition at β-position of styrene and produces a stable Giese-type intermediate (**17**) that it is reduced again to afford the benzylic anion (**18**). This species is protonated by a proton source species giving the hydrocarboxylated product with yields up to 88%. It was observed that the use of an excess of water (19 equivalents) was an important key factor to obtain the product of high yields. However, a too large excess of water was detrimental to the reaction due to homogeneity issues.

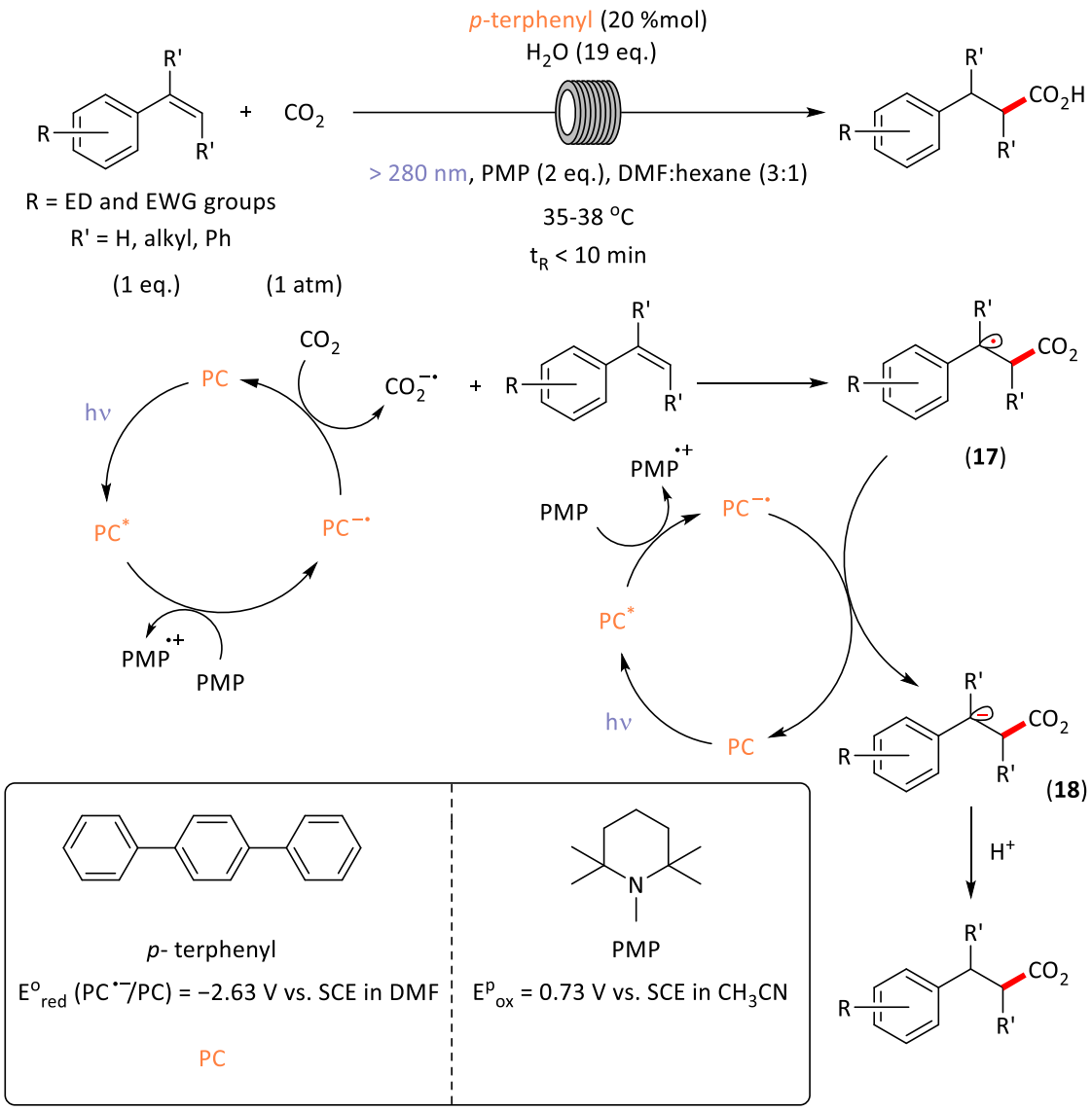

Scheme 24. Hydrocarboxylation of styrene derivatives with CO_2 catalysed by *p*-terphenyl in continous flow.

In 2020, Malkov and Buckley[48] described a selective *β*-hydrocarboxylation of broad scope of styrene derivates in organic solvent by electrochemical means (Scheme 25). Under experimental conditions, the *β*-hydrocarboxylation product (**19**) is obtained with yields up to 70% along with the dicarboxylation product (**20**). Nevertheless, the ratio between both products favours the formation of **19** (**19**:**20**, 8:1). Owing to the similarity of potentials between CO_2 and styrene, they suggested that two mechanisms can take place in parallel, either the reduction of CO_2 and subsequent addition to styrene (path A, Scheme 25) or the reduction of styrene and nucleophilic attack towards the CO_2 (path B, Scheme 25) (Scheme 25A). In the same vein, Nam[8] and Jiang[45] independently

described the electrosynthesis of carboxylates of styrene derivatives in water. In the example of the group of Nam, the ratio between hydrocarboxylation (**21**) and dicarboxylation product (**22**) can be tuned with the proton source (R-OH). For instance, **22** is favoured respect to **21** (**21**:**22**, 7:93) using methanol as proton source (Scheme 25B). In the case of Jiang and co-workers, they studied the influence of the electrode material in the formation of the dicarboxylation product (**23**). They could observe yields up to 89% under optimal conditions (Scheme 25C). As in the previous example reported by Malkov, the reaction can also undergo under two mechanisms in parallel.

A) Hydrocarboxylation and dicarboxylation of subtituted styrenes by electrochemical means

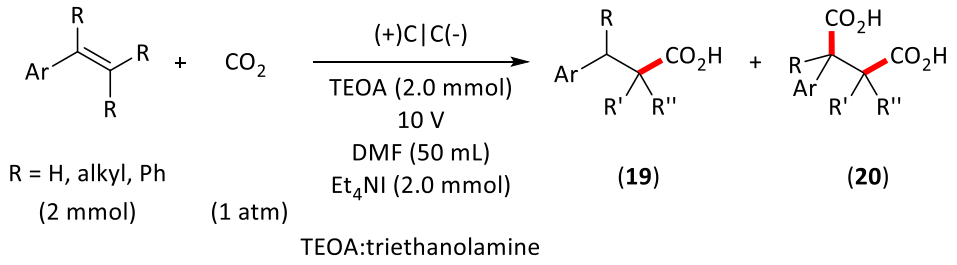

Path A) Reduction of CO_2 and subsequent addition to the unsaturated species

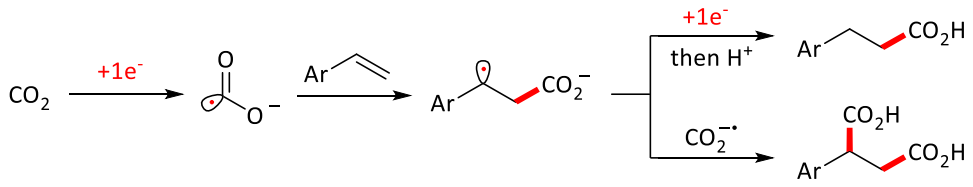

Path B) Reduction of the unsaturated species and nucleophilic attack towards CO_2

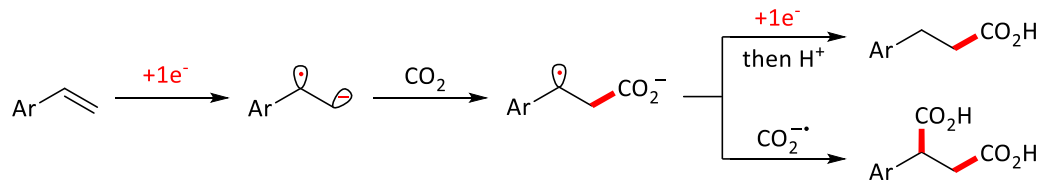

B) Electrochemical hydrocarboxylation/dicarboxylation of styrene derivatives

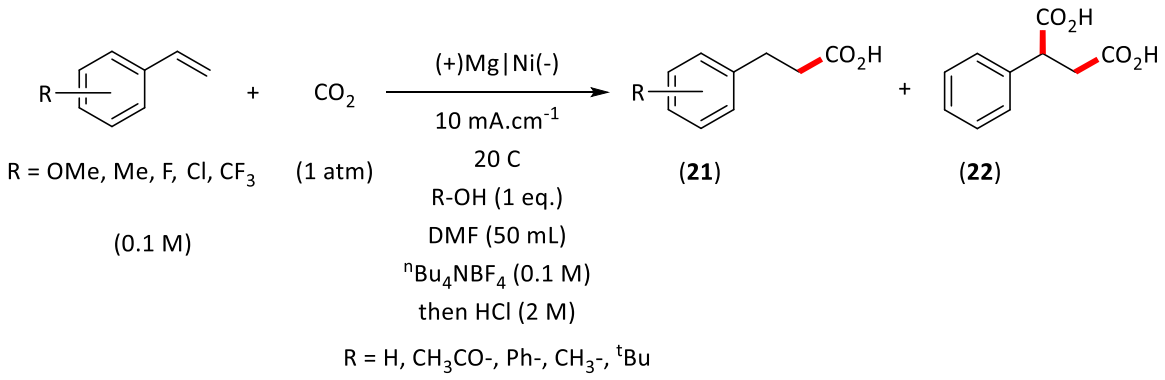

C) Dicarboxylation of styrene derivatives under electrochemical means

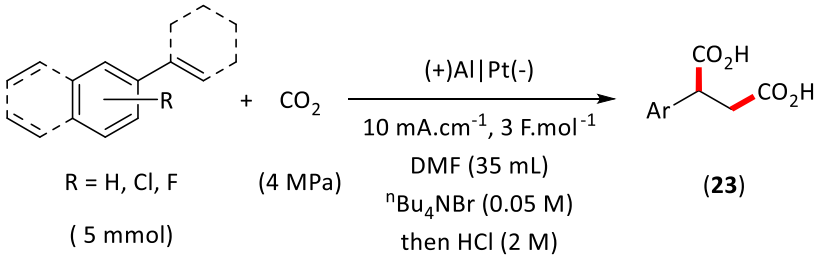

Scheme 25. Hydrocarboxylation and dicarboxylation of styrene derivatives with CO_2 under electrochemical means.

In 2021, Romo[12] and co-workers performed the β-selective hydrocarboxylation of α,β-unsaturated esters using the previous methodology developed by Jamison[11]. In this

work, they employed a bulkier $(TMS)_3SiH$ as a H-atom source compared to the ones tested by Jamison and it significantly improved the yield. The use of an amine with a more hindered N-alkyl group (Et) inhibits the formation of dimers that clogged the flow line. Besides the technical improvements in the existent methodology, they also describe how to synthesize β-lactones (**24**) from the resulting carboxylate species (Scheme 26A). A year later, Malkov and Buckley[49] envisioned the β-selective hydrocarboxylation of α,β-unsaturated esters by electrochemical means. They studied the mechanism of hydrocarboxylation, and they suggested that two different pathways might occur depending on the reduction potential of the substrate (Scheme 26B). According to a study from Jui's group[36], the CO_2 radical anion present an ambiphilic behaviour. It undergoes a hydrocarboxylation with Michael acceptors whose reduction potential is more negative than in the case of CO_2 (CO_2 radical anion plays the role of carboxylating agent). The substrates with a less negative reduction potentials than CO_2 would undergo a reduction with the $[CO_2]^{\bullet-}$ (CO_2 radical anion plays the role of reductant). This does not fully explain the behaviour in some substrates; thus, the two pathways could be operative. Accordingly, the mechanism is still under investigation.

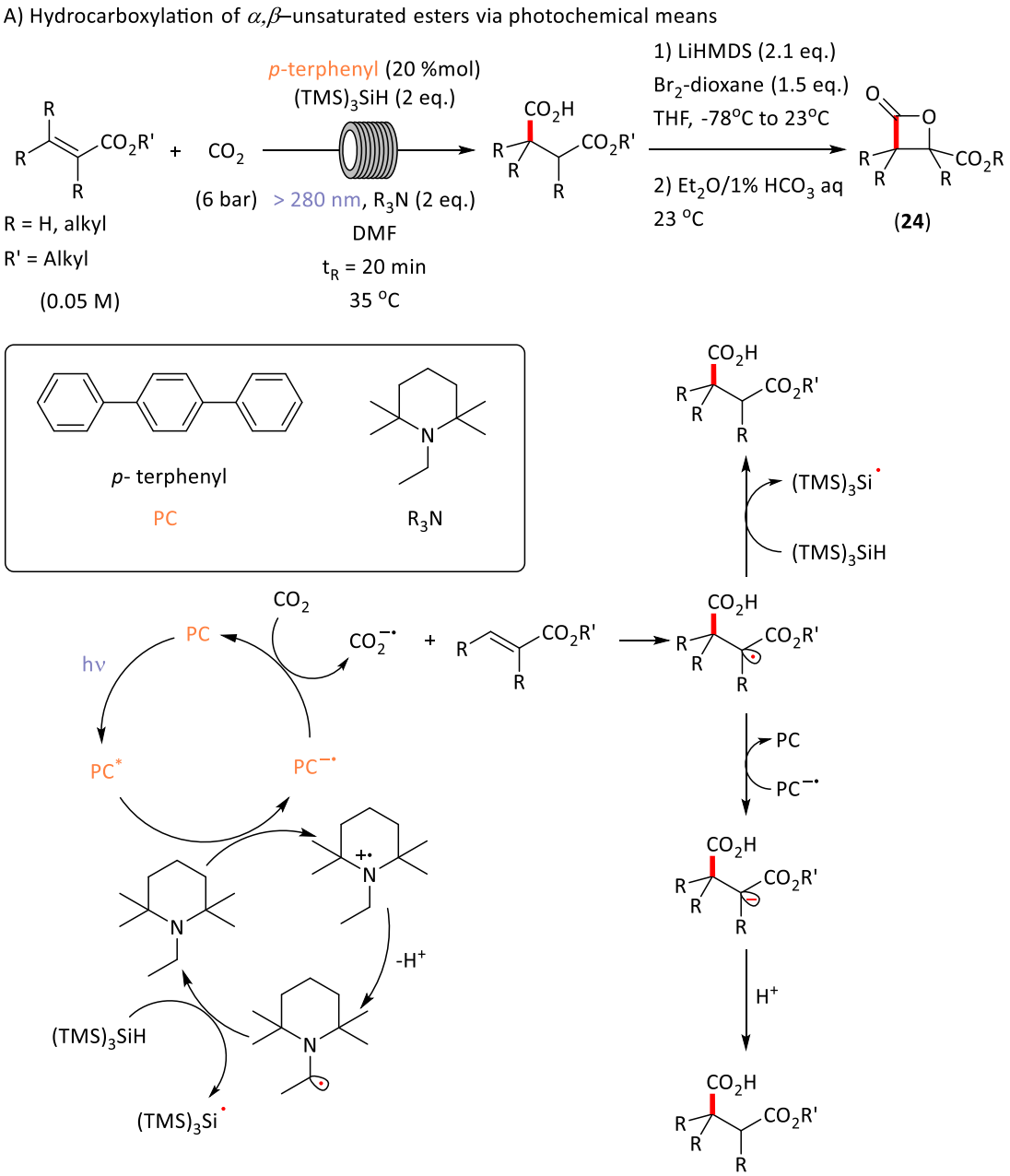

Scheme 26. Hydrocarboxylation of α,β-unsaturated esters with CO_2 *via* photochemical (A) and electrochemical means (B).

In 2017, Yu[22] and co-workers described an iron-promoted process to synthesize β-thioacids using styrenes and acrylates with CO_2 under visible light. In this study, they investigated the initiation of the difunctionalization of the alkene. Based on the observed regioselectivity and control experiments, they proposed that difunctionalization of the alkene begins with the C-C bond formation. Firstly, the CO_2 would be reduced by the excited state of Fe/S complex *via* SET. Then, the thiyl radical generated *via* the reductive quenching of the oxidised Fe/S complex further reacts with the C-centred radical *via* radical-radical coupling achieving the thiocarboxylic acid (**25**) with yields up to 94% that can be used lately in other synthetic applications (Scheme 27A). Three years later, the same group[15] described an organocatalytic approach for the hydrocarboxylation of acrylates and styrene derivatives under visible light through the formation of a charge-transfer complex (CTC) (**26**) in good yields, up to 73%. In this work, they employed sterically hindered thiols which are responsible of the excellent chemio- and regioselectivity. Based on experimental and computational results, Yu and co-workers stated that two possible pathways might proceed in parallel. Upon irradiation of the CTC, formed between the styrene/acrylate and the thiolate, either the CO_2 or the substrate is reduced. In both pathways, the same Giese-type intermediate (**27**) is generated that might undergo a HAT to yield the carboxylate product (Scheme 27B).

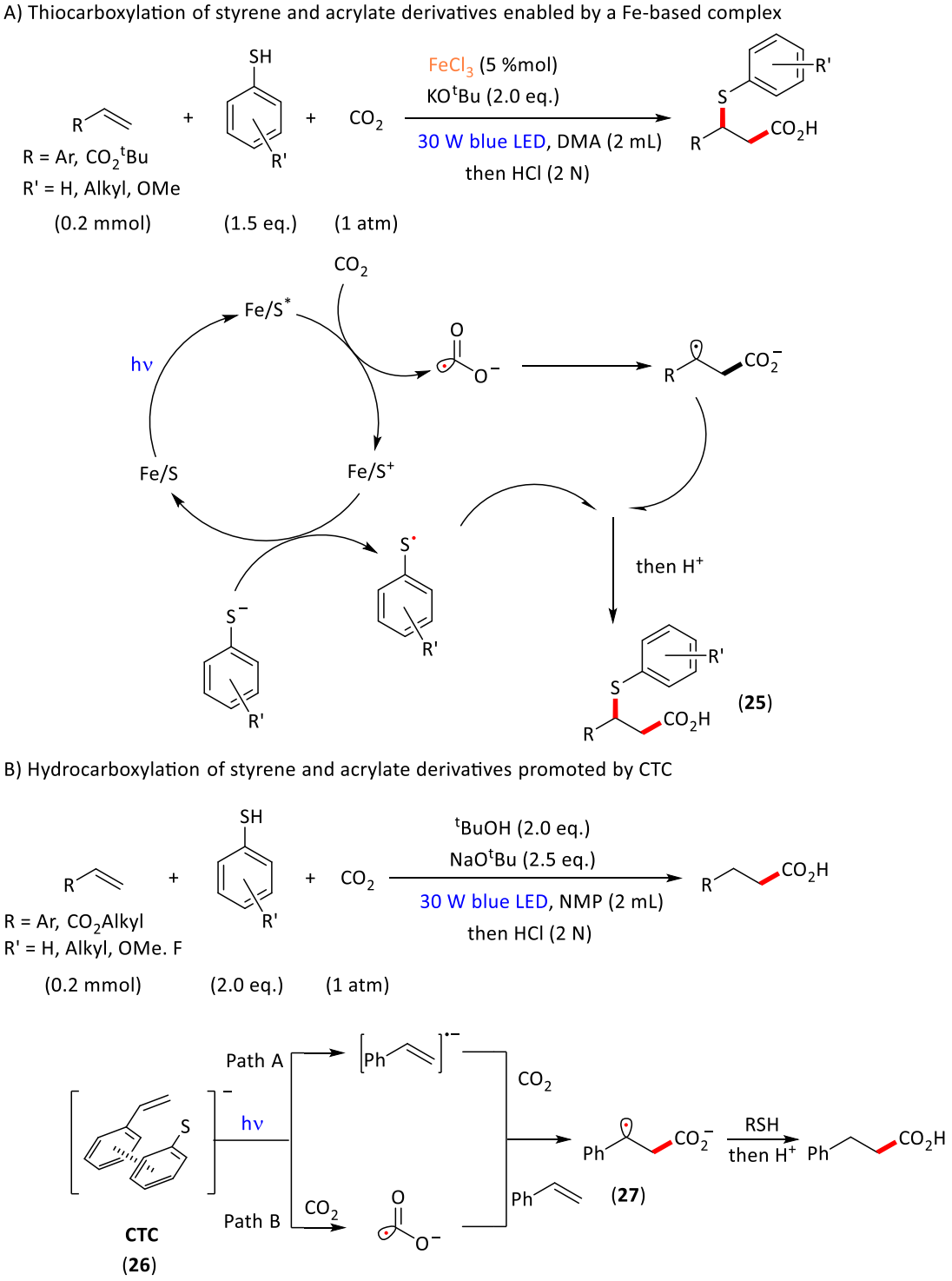

Scheme 27. A) Thiocarboxylation of styrene and acrylate derivatives enabled by a Fe-based complex. B) Hydrocarboxylation of styrene and acrylate derivatives promoted by a CTC complex.

In 2023, the same group reported the arylcarboxylation of unactivated alkenes.[24] Based on control studies, they noticed that the presence of a silane improves the reaction yield

up to 83% (absence of silane = 62%). They proposed a possible mechanism for this transformation. The excited state of the Ir-based photocatalyst upon irradiation can be quenched by a thiolate to yield a thiyl radical along with the reduced form of the photocatalyst (Ir^{2+}), which can then reduce CO_2 to form carbon dioxide radical anion. With the presence of the silane, another CO_2 radical anion formation pathway may occur which might explain the relative increase in the yield of hydrocarboxylation product (**28**). The silane reacts with the CO_2 resulting in the formation of a formate salt, that can undergo a HAT with the thiyl radical to generate the CO_2 radical anion. Then, it undergoes a radical addition to the alkene resulting in the formation of an alkyl carbon radical (**29**) which is trapped *via* cyclisation with the arene (**30**). Finally, the carboxylate (**28**) is yielded upon rearomatisation with the aid of the thiol (Scheme 28).

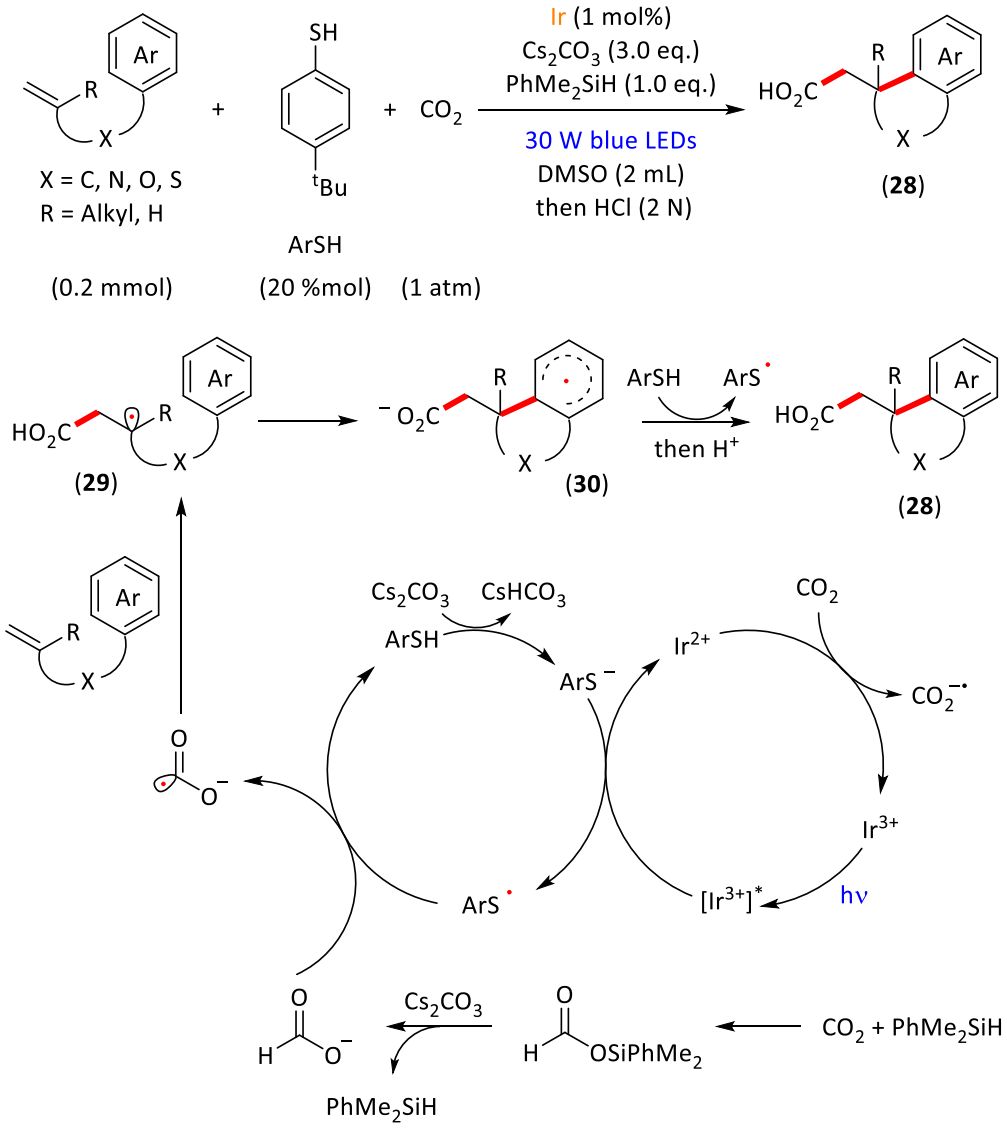

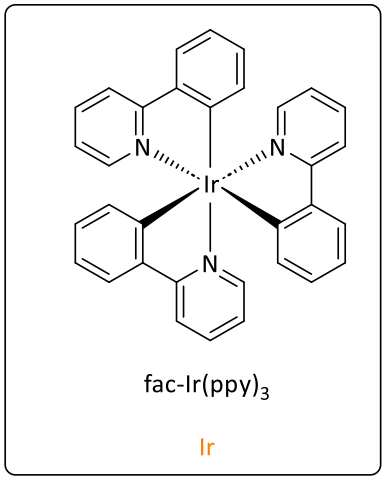

Scheme 28. Arylcarboxylation of unactivated alkenes with CO_2 using an Ir-based photocatalyst.

1.2. Reduction of NHC-CO_2-based species.

In this section, examples about the reduction of NHC-CO_2-based species are described (Scheme 29). Upon reduction of these adducts, it can result into the formation of formate (Scheme 29A) and methane (Scheme 29B) in the presence of a proton source. In the absence of any proton source, its radical anion (product of the one-electron reduction) is generated either *via* electrochemical (Scheme 29C) and chemical means (Scheme 29D).

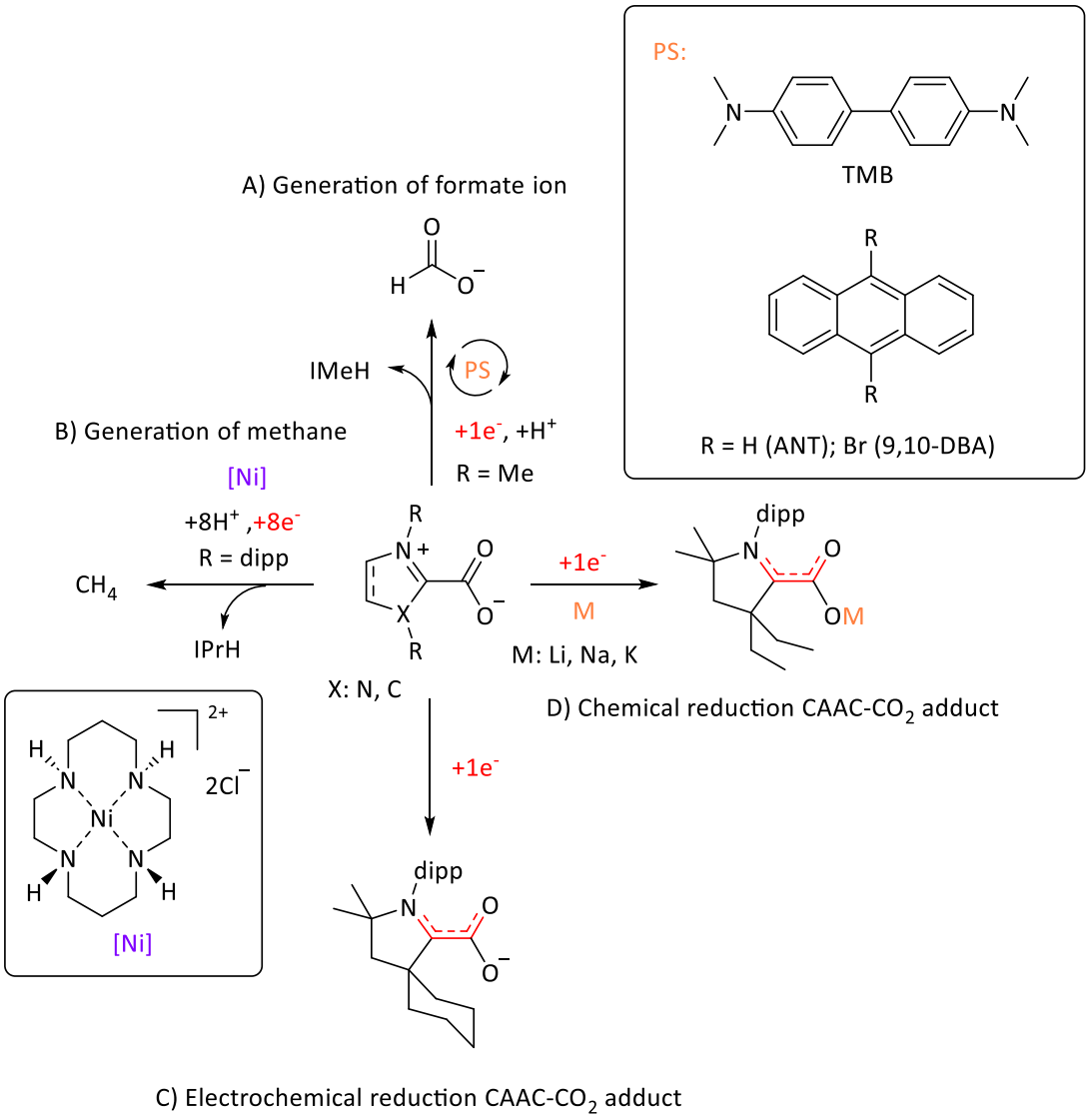

Scheme 29. Reduction of NHC-CO_2-based adducts. A) Generation of the formate ion. B) Generation of methane. C) Electrochemical reduction of CAAC-CO_2 adduct. D) Chemical reduction of CAAC-CO_2 adduct.

Examples of one-electron reduction of NHC-CO_2-based adducts are limited in the literature. In 2015, the group of Falvey[50] demonstrated that the net photochemical reduction of CO_2 can occur in the presence of IMe-CO_2 (**31**) through the photolysis of an excited state donor under ultraviolet light (350 nm) (Scheme 30). The authors proposed the following mechanism based on fluorescence quenching and photolysis experiments: the NHC-CO_2 adduct (**31**) quenches the excited state of the photosensitiser (PS: TMB, ANT and 9,10-DBA) previously generated upon irradiation at 350 nm and affords the monoreduced NHC-CO_2 adduct and the oxidised form of PS. Subsequently, the reduced form of adduct **31** undergoes an heterolytic dissociation which results in the release of CO_2 radical anion along with the free *N*-Heterocyclic Carbene (NHC). Based on their observation, they proposed that the generated CO_2 radical anion can follow two pathways in parallel: a net disproportionation to afford the formate ion (**32**) and a free CO_2 molecule (path A, Scheme 30) and, the homocoupling of $[CO_2]^{\bullet-}$ to yield oxalate species (path B, Scheme 30). The formation of formate was detected in a higher degree (47 %) than the oxalate species (<6 %) which seems to indicate that path A is favoured over path B. To shed more light on the generation of the carboxyl radical, they tried to measure the one-electron reduction of the IMe-CO_2 adduct *via* cyclic voltammetry. Despite several attempts, they could not have access to it. Owing to the impossibility of this measurement, they estimated that the reduction potential of IMe-CO_2 adduct (**31**) might be similar to the corresponding imidazolium cation (around -1.8 V vs Saturated Calomel Electrode (SCE) in DMF[51]).

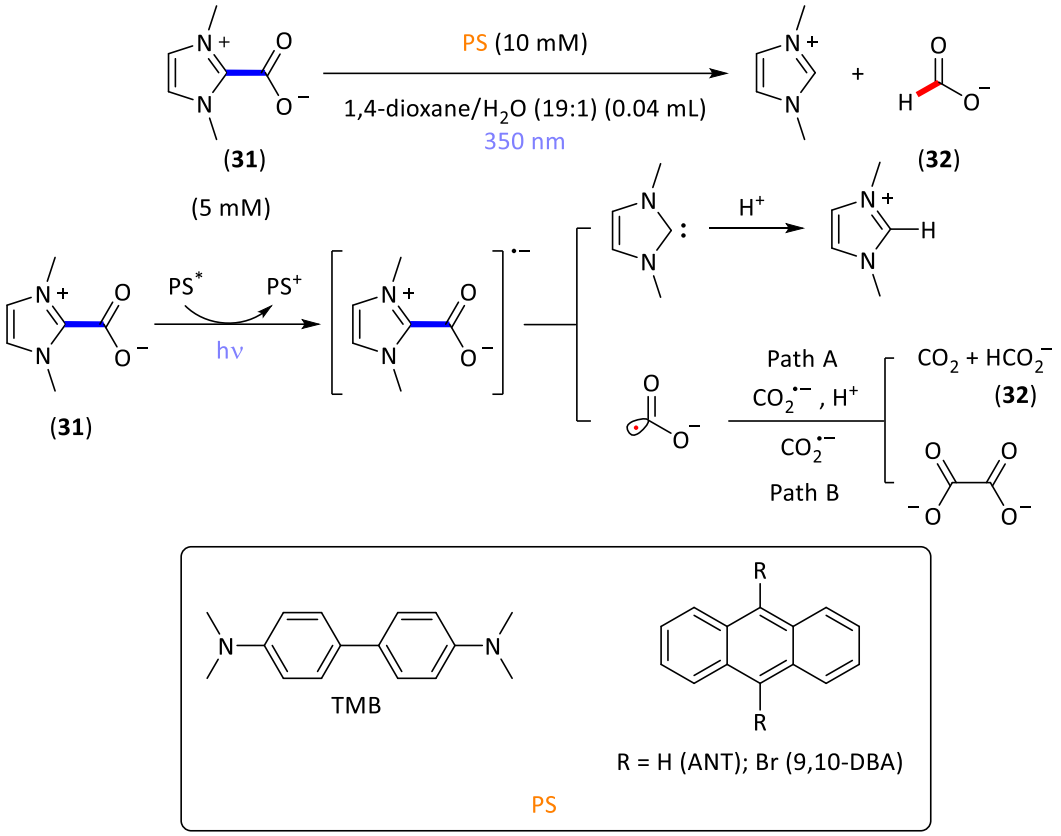

Scheme 30. Photogeneration of formate anion from a NHC-CO_2 adduct.

In the same year, Koval[52] and co-workers described the electrochemical 8-electron reduction of a preactivated CO_2 in an NHC-CO_2 adduct (IPr-CO_2) (**33**) to methane in the presence of a Ni-based complex and a proton source (CF_3CH_2OH) (Scheme 31). Based on isotopic labelling experiments, they could confirm that the carbon-source for the generation of methane (**34**) was the preactivated CO_2. After different electrolysis studies, they observed that the use of the preactivated CO_2 (in the form of NHC-CO_2 adduct) was essential to yield methane. In fact, in the absence of NHC, a mixture of dihydrogen and CO is produced from CO_2. The use of both forms of CO_2, preactivated and the free molecule, slightly increases the amount of methane generated. The reduction potential measurement of NHC-CO_2-based adducts (IMe-CO_2[50] and IPr-CO_2[52]) in the absence of any additives were still undone at that time.

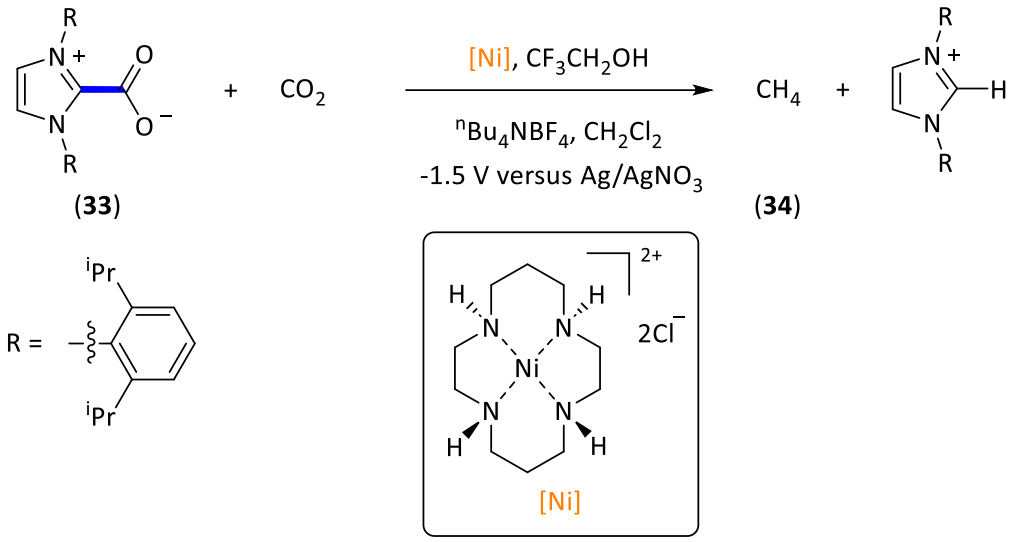

Scheme 31. Generation of methane though the reduction of a NHC-CO_2 adduct.

Three years later, Machan and Gilliard[53] in a joint work studied the electrochemical one-electron reduction of a NHC-CO_2 adduct using cyclic(alkyl)amino carbene (^{Cy}CAAC) (Scheme 32A). They could identify a reduction potential of -2.08 V and -2.15 vs. $Fc^{+/0}$ in MeCN and THF respectively. According to their DFT study, they estimate significant structural differences between the neutral and monoreduced form of ^{Cy}CAAC-CO_2 adduct. They estimated that the CO_2 moiety is placed perpendicular in respect to the ^{Cy}CAAC moiety in the neutral adduct, while it would rotate to a coplanar position in the reduced form. The additional electron would be mainly located at the π-vacant orbital of the carbenic carbon of the NHC. The spin density would also be located at the nitrogen and both oxygen atoms but, to a lesser degree in respect to the carbenic carbon. None was observed at the carbon atom of the CO_2 moiety. Very recently, the same groups described the chemical reduction of ^{Et}CAAC-CO_2 adducts using alkali metals (M = Li, Na, K) resulting in the formation of monoreduced CAAC-CO_2 metallic clusters (**35**) (Scheme 32B).[54] As predicted by DFT in the precedent work, they experimentally observed that CO_2 was placed in a coplanar position in respect to the CAAC moiety upon reduction. The spin density mainly resides at the carbenic carbon, followed by the nitrogen and the oxygen atoms as in the previous work.[53] However, a small portion of the spin density was also placed at the carbon of the CO_2 moiety. Depending on the Lewis acidity of the metal cation generated upon reduction of the adduct (Li^+, Na^+, K^+), the spin density was either enhanced or detrimental to the different atoms from the monoreduced adduct.

Increasing the Lewis acidity of alkali cation, the spin density at the C of the CO_2 was enhanced (from 4 % (Li^+) to 8 %(K^+)).

A) Electrochemical reduction of ^{Cy}CAAC-CO_2

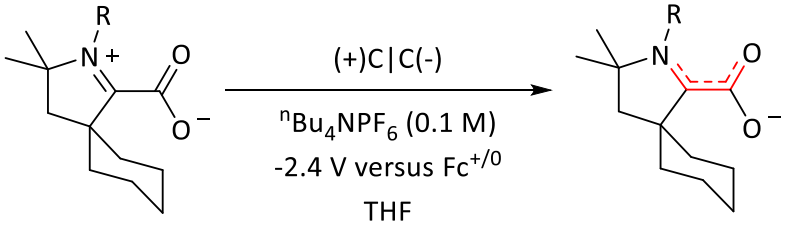

(5 mM)

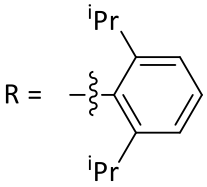

$E^{1/2}_{red}$ (^{Cy}CAAC-CO_2)

-2.08 V vs Fc$^{+/0}$ in CH_3CN

-2.15 V vs Fc$^{+/0}$ in THF

B) Chemical reduction of ^{Cy}CAAC-CO_2 enabled by alkali metals

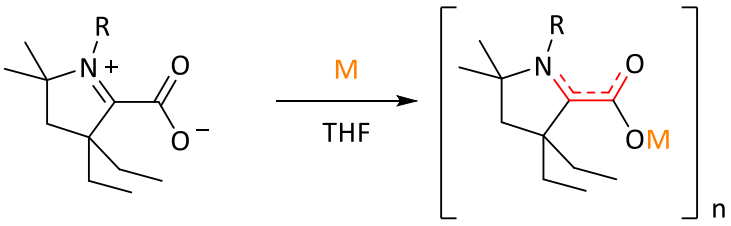

M: Li (2 eq.), Na (4 eq.) or K (4 eq.)

n= 2 or 4

(**35**)

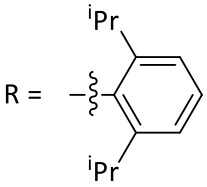

Scheme 32. Electrochemical (A) and chemical (B) reduction of ^{Cy}CAAC-CO_2.

1.3. Synthesis of NHC-CO_2-BR_3 adducts.

In this subsection, examples of NHC-CO_2-based adducts bearing a borane (BR_3) as a Lewis acid will be described.

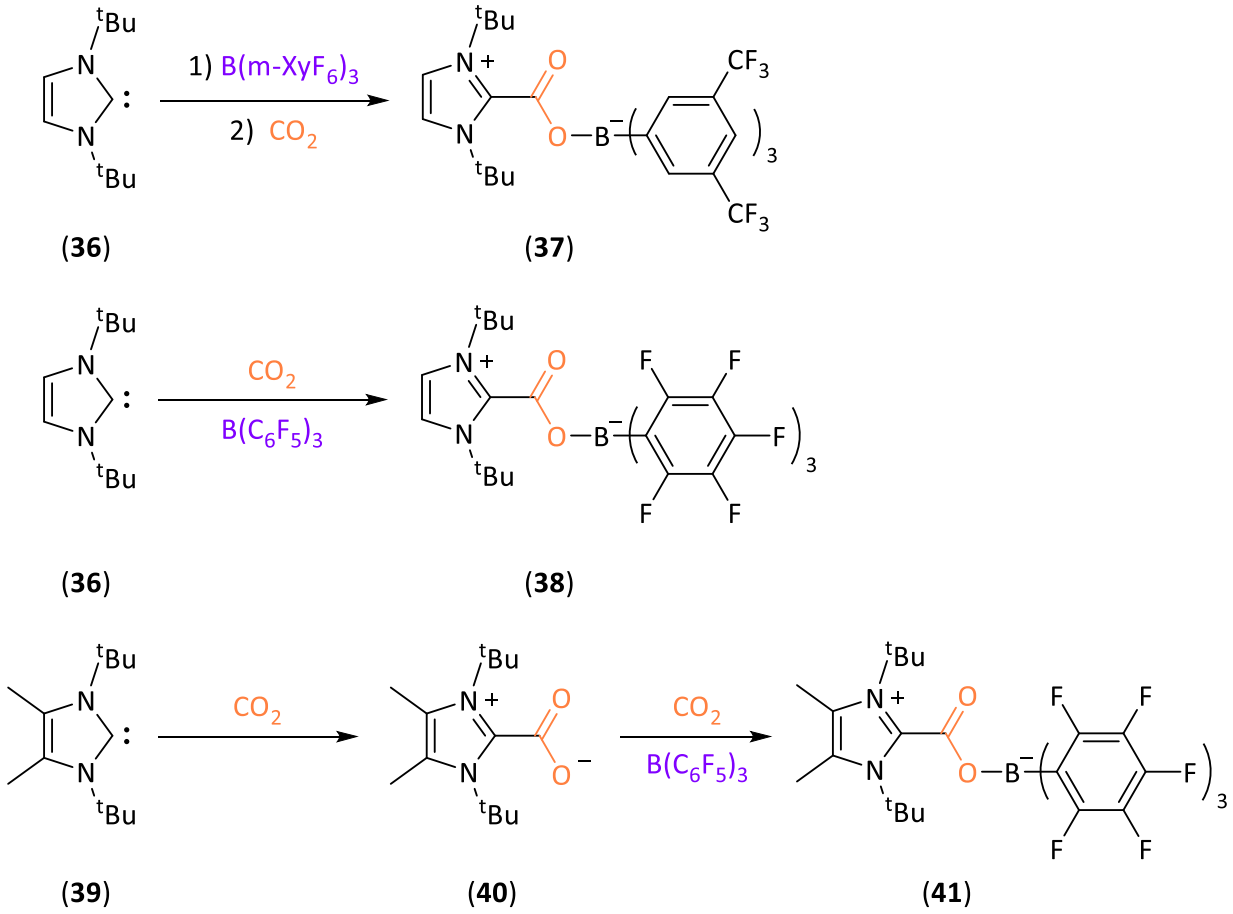

(**36**) (**37**)

(**36**) (**38**)

(**39**) (**40**) (**41**)

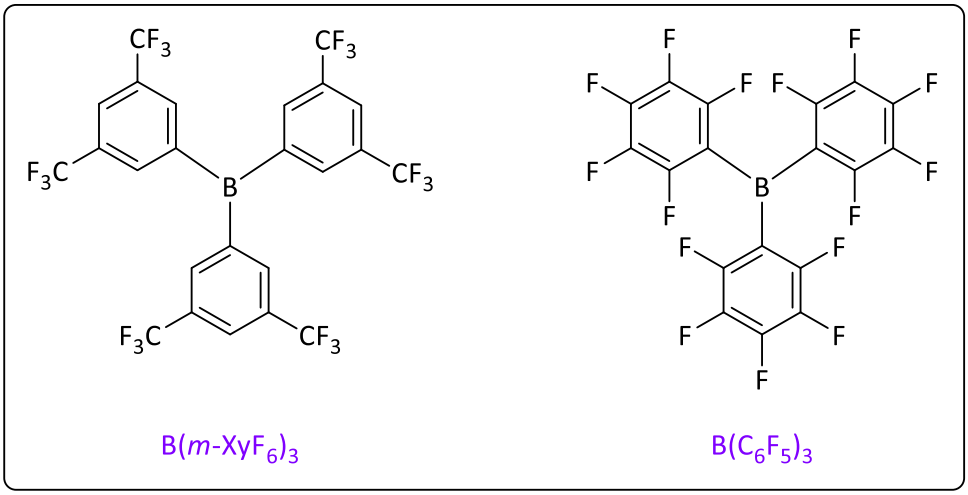

Scheme 33. Formation of NHC-CO_2-BR_3 adducts

In the last decade, Tamm and colleagues described three examples[55,56] of NHC-CO_2-BR_3 adducts (**37**, **39** and **42**) in the context of the FLP (Frustrated Lewis Pairs) chemistry. These systems consist of two parts, a bulky classical diaminocarbene bearing tert-butyl groups as a *N*-substituents (either (**38**) or (**40**)), and a hindered boron-based Lewis acid, tris[3,5-bis(trifluoromethyl(phenyl]borane (abbreviated as B(*m*-XyF_6)$_3$) (upper, scheme 33) and tris(pentafluorophenyl)borane (B(C_6F_5)$_3$) (down, scheme 33).

In 2012, they isolated a carbene-borane adduct (**42**) constituted by a I^{t}Bu carbene (**36**) and B(m-XyF_6)$_3$ (Scheme 34).[55] The singularity of this Lewis acid-base adduct is its ability to partially dissociate in solution. This dynamic behaviour could lead to the CO_2 bending, the THF ring-opening and C(sp)-H breaking of acetylene under the FLP-type chemistry. In the absence of CO_2, the addition of stoichiometric amount of carbene and borane afforded the carbene borane I^{t}Bu-B(m-XyF_6)$_3$ pair (**42**) in a high yield (95%). Heating under reflux in toluene led to the formation of an abnormal adduct interacting with the borane through an internal rearrangement (**43**). On the other hand, bubbling of CO_2 into a benzene solution of the I^{t}Bu-B(m-XyF_6)$_3$ Lewis pair (**42**) enabled the formation of the desired I^{t}Bu-CO_2-B(m-XyF_6)$_3$ adduct (**37**) in a 66% yield.

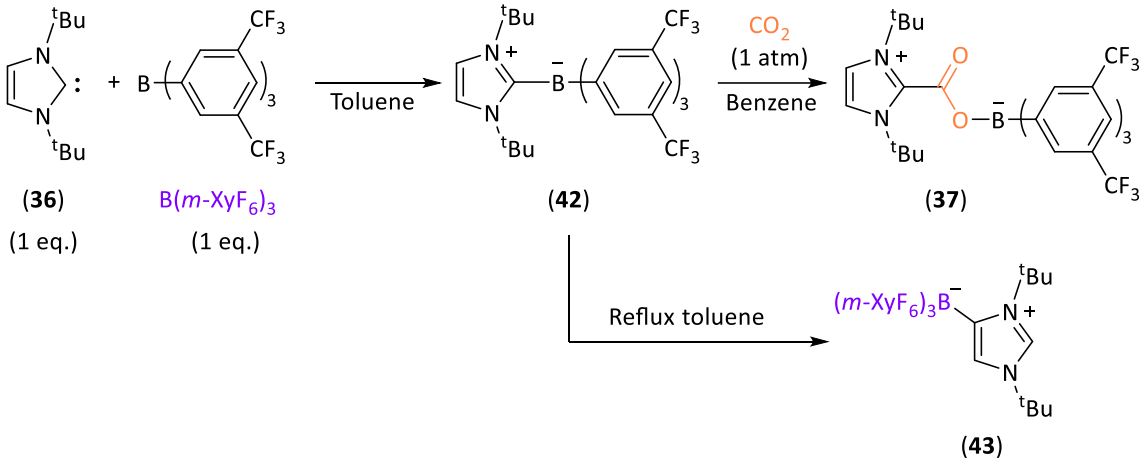

Scheme 34. Formation of I^{t}Bu-CO_2-B(m-XyF_6)$_3$ adduct from a normal Lewis adduct.

Previously, the same group confirmed that the equimolar combination of I^{t}Bu and B(C_6F_5)$_3$ was active towards the dihydrogen heterolytic splitting following a FLP-type reactivity.[57] In the absence of dihydrogen, they only could observe the irreversible formation of the abnormal adduct (**44**) (Scheme 35A). In this work, they studied the reactivity of this system towards CO_2 and N_2O activation in the form of NHC-based

adducts (Scheme 35B).[56] Besides I^{t}Bu carbene (**36**), a NHC-CO_2 adduct (**40**) constituted by an equivalent carbene with a methylated backbone was also tested in order to preclude the possible abnormal adduct formation. Both NHC-CO_2-$B(C_6F_5)_3$ adducts were obtained in good yields (R = H (**39**), 89%; R = CH_3 (**42**), 68%).

A) Heterolytic dihydrogen activation by a frustrated carbene–borane Lewis pair

In the absence of dihydrogen

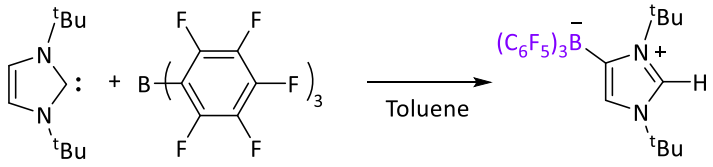

(**36**) (1 eq.) + $B(C_6F_5)_3$ (1 eq.) → (**44**)

In the presence of dihydrogen

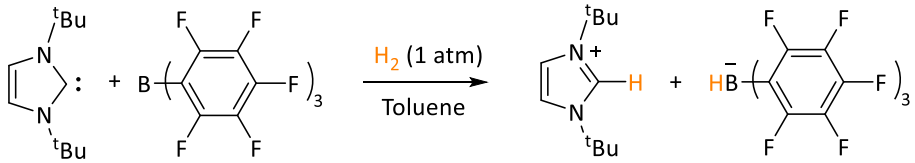

(**36**) (1 eq.) + $B(C_6F_5)_3$ (1 eq.)

B) CO_2 activation by a frustrated carbene-borane Lewis pair

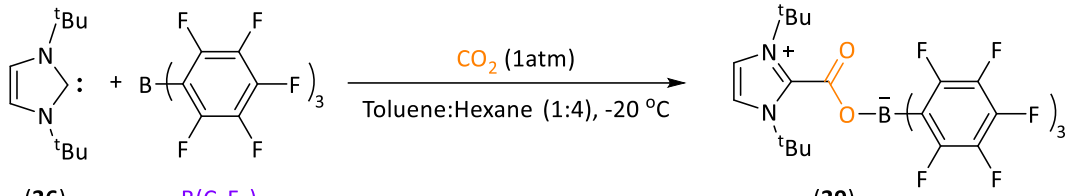

(**36**) (1 eq.) + $B(C_6F_5)_3$ (1 eq.) → (**39**)

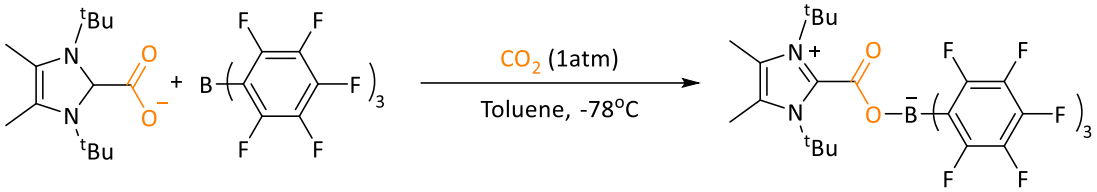

(**49**) (1 eq.) + $B(C_6F_5)_3$ (1 eq.) → (**42**)

Scheme 35. Dihydrogen (A) and CO_2 (B) activation by a frustrated carbene-borane Lewis pair.

1.4. Reduction potentials: Concepts and applications.

This subchapter, which concerns an introduction about the origin of redox potential from a thermodynamic standpoint, is divided into two sections. The definition of redox potential as well as its basis (1.4.1.) will be described and then, examples about the estimation of reduction potentials *via* DFT means based on the direct approach will also be discussed (1.4.2.).

1.4.1. Definition of redox potential and its origin.

Reduction-oxidation (redox) reactions are largely present in a wide array of chemical transformations. The propensity of the chemical species to either gain or lose electrons during the electron transfer is dictated by the redox potential of the reaction. Depending on the direction of this electron transfer, it can be either the reduction potential (the species of interest acquires electrons) or oxidation potential (lose electrons). In thermodynamic terms, the redox potential in a chemical reaction refers to the thermodynamic feasibility of electrons to be transferred from one chemical species to another. All chemical reactions in nature are governed by the chemical potential of each species involved in the reaction, defined by the Greek letter, μ. By definition, the chemical potential of the component J of a mixture in solution is defined as the partial molar Gibbs energy (Equation 1).

$$\mu_J = \left(\frac{\partial G}{\partial n_J}\right)_{P,T,n_{i\neq j}} \qquad Eq.1$$

Applying the definition of the chemical potential into the Gibbs equation, it results:

$$\mu_J = \mu^o + RTln(a_J) \qquad Eq.2$$

where μ^o refers to the chemical potential at its standard state, R and T are the gas constant and the temperature respectively and, a_J is the activity of component J in solution.

Considering the following simplified reduction reaction,

$$O\ (solution) + ze^-\ (gas) \rightarrow R\ (solution);\ E_{red}(O/R) \qquad Eq.3$$

where *O* (oxidised form of J) is reduced by *z* electrons to yield *R* (reduced form of J) in solution. This half-reaction (O/R redox couple) presents associated a reduction potential, E_{red} (O/R). Instead of chemical potential, the electrochemical potential must be considered in electrochemical reactions, and it is represented by $\bar{\mu}$. The chemical potential of charged species (electrochemical potential) consists of the sum of its chemical potential at the neutral state and the electric potential contribution (Equation 4). By definition, its electric contribution (second term) is the work of adding a charge ze to a region where the potential is ϕ (Equation 5). The parameter z refers to the stoichiometric number of electrons transferred in the reaction and F to the Faraday constant. The maximum of the non-expansion work (electrical work is this case) is equals to the Gibbs free energy difference.[58]

$$\bar{\mu} = \mu + ze\Phi \qquad Eq.4$$

$$w_e = ze\Phi;\ w_e = zF\Phi \qquad Eq.5$$

$$w_{e,max} = \Delta G \qquad Eq.6$$

Combining eq. 7 and eq. 8,

$$\Delta G = zF\Phi \qquad Eq.7$$

The potential ϕ turns into the E_{red}(O/R) which is the absolute potential associated to the gain of one electron by the oxidised form of J resulting in the reduced form of J. At this point, we can relate the reduction potential associated with a redox half-reaction to its thermodynamic feasibility, ΔG_{red} (Equation 8).

$$\Delta G_{red} = zFE_{abs,red}(O/R) \qquad Eq.8$$

On the other hand, applying Equation 3 into Equation 2 results into the molar Gibbs energy of the chemical reaction (Equation 9),

$$\Delta G_{red} = \Delta G^{o}_{red} + lnQ = \Delta G^{o}_{red} + RTln\left(\frac{a_R}{a_O}\right) \qquad Eq.9$$

where Q is the reaction coefficient resulted by the activities relation between reduced and oxidised form of the involved chemical species, J. In equilibrium, Q is equal 1 therefore,

$$Q = 1;\ \Delta G_{red} = \Delta G^{o}_{red} = zFE_{abs,red}(O/R) \qquad Eq.10$$

$$E_{abs,red} = \frac{\Delta G^{o}_{red}}{zF} \qquad Eq.11$$

To predict a theoretical reduction potential to subsequently compare it to an experimental reduction potential, another important aspect must be considered. Upon the obtention of the Gibbs energy associated with the half-reaction, it is translated into the absolute reduction potential of the reaction using the Equation 11. Experimentally, the absolute reduction potential cannot be achieved. It is always measured respect to either a reference electrode or a redox couple which possess another absolute reduction potential. Taking as reference the absolute reduction potential of the electrode/redox couple, the reduction potential of the half reaction of interest can be compared to the estimated theoretical reduction potential (Equation 12).

$$E^{o}_{red}(O/R\ vs.RE) = E^{o}_{abs,red}(O/R) - E^{o}_{abs,red}(RE) \qquad Eq.12$$

E^{o}_{red} (O/R vs. RE) refers to the reduction potential of the half reaction respect to the reference electrode. The $E^{o}_{abs,red}$ (RE) is the absolute reduction potential of the reference electrode (RE) or the redox couple used as a reference. The most widely used are the standard hydrogen electrode (SHE) and the saturated calomel electrode (SCE). A more detailed discussion based on the theory behind the calculation of reduction potentials *via* DFT (Density Functional Theory) can be found in Chapter II, subsection 2.1.6. "Determination of theoretical reduction potentials *via* DFT means.".

1.4.2. Examples of prediction of redox potential *via* DFT means using the direct approach.

In this section, representative examples using the direct approach that can be found in the literature in which the reduction potentials have been estimated *via* DFT will be discussed.

A pioneering work by Lledós and colleagues in the early 2000s reported the oxidation potential of inorganic complexes constituted with $\{Pt_2S_2\}$ cores. These potentials were consistent with the experimental data using as a functional, B3LYP, with an absolute error lower than 0.3 V.[59] In 2015, Nicewicz and colleagues described the experimental

potential for large collection of organic substrates (180 organic molecules) and evaluate the accuracy of M062X and B3LYP functional in their estimation. The observed the B3LYP could slightly offer a better performance. Nonetheless, both functionals show deviations in defined cases. In this data set, B3LYP underestimated the potentials associated to the reduction process whereas M062X overestimated the oxidation one. At the end, both could assess electrochemical potentials in a reasonable manner with a standard deviation of 0.3 for both cases.[60]

In 2019, the group of Isegawa provided a detailed DFT mechanism for the reduction of CO_2 using an Mn-based electrocatalyst in the presence of $Mg(OTf)_2$ playing the role of Lewis acid. They predicted the reduction potential related to the two-electron reduction of the Mn-based complex with an error around 0.2 V.[61] In 2016, Pantazis and Krewald studied the redox behaviour of a Mn-based helicate cluster that could access to six consecutive total oxidation levels from $Mn(II)_5$ to $Mn(III)_5$. The evaluated a small collection of functionals in the prediction of reduction potentials. They could observe that TPSSh provided the smallest deviation, 0.13 V.[62]

In 2017, Puiatti and Perini and co-workers evaluated a large collection of DFT functionals in order treat organic anionic species. They studied how accurate different functional could predict the electron affinity as well as the reduction potential in an extensive and diverse dataset (62 molecules bearing as an ample diversity of chemical groups ranging potentials from 0 V to -3 V). Ther hybrid and meta-GGA functionals PBE0, B3PW91, M06 and TPSSh exhibited the lowest mean absolute deviation error at 0.13V.[63]

In 2019, Luo and co-workers disclosed a systematic study on redox properties in enamines. They calculated the oxidation potentials of a large group of secondary and tertiary enamines using different functionals. The one that predicted a oxidation potential closer to the measure one was M06-2X with a absolute error of 0.03 V.[64]

Very recently, Dean Toste and Head-Gordon studied a collection of redox-active molecules (quinoxaline derivatives) that could be affordable and high-performing as storage materials. In this work, they determine how accurate and precise a group of functionals were in the estimation of their reduction potentials with the aid of experimental reduction potentials. Once the computational protocol was validated, they

also predicted the reduction potentials for prospective new molecules. The employed functional that provided a smallest absolute error was TPSSh-D4 , 0.06 V.[65]

1.5. References.

(1) Koppenol, W. H.; Rush, J. D. Reduction Potential of the Carbon Dioxide/Carbon Dioxide Radical Anion: A Comparison with Other C1 Radicals. *J. Phys. Chem.* **1987**, *91* (16), 4429–4430. https://doi.org/10.1021/j100300a045.

(2) Lamy, E.; Nadjo, L.; Saveant, J. M. Standard Potential and Kinetic Parameters of the Electrochemical Reduction of Carbon Dioxide in Dimethylformamide. *J. Electroanal. Chem. Interfacial Electrochem.* **1977**, *78* (2), 403–407. https://doi.org/10.1016/S0022-0728(77)80143-5.

(3) Grills, D. C.; Matsubara, Y.; Kuwahara, Y.; Golisz, S. R.; Kurtz, D. A.; Mello, B. A. Electrocatalytic CO_2 Reduction with a Homogeneous Catalyst in Ionic Liquid: High Catalytic Activity at Low Overpotential. *J. Phys. Chem. Lett.* **2014**, *5* (11), 2033–2038. https://doi.org/10.1021/jz500759x.

(4) Wu, J.; Huang, Y.; Ye, W.; Li, Y. CO_2 Reduction: From the Electrochemical to Photochemical Approach. *Adv. Sci.* **2017**, *4* (11), 1700194. https://doi.org/10.1002/advs.201700194.

(5) Bazzi, S.; Le Duc, G.; Schulz, E.; Gosmini, C.; Mellah, M. CO_2 Activation by Electrogenerated Divalent Samarium for Aryl Halide Carboxylation. *Org. Biomol. Chem.* **2019**, *17* (37), 8546–8550. https://doi.org/10.1039/C9OB01752F.

(6) Bazzi, S.; Schulz, E.; Mellah, M. Electrogenerated Sm(II)-Catalyzed CO_2 Activation for Carboxylation of Benzyl Halides. *Org. Lett.* **2019**, *21* (24), 10033–10037. https://doi.org/10.1021/acs.orglett.9b03927.

(7) Mohammadzadeh, S.; Zare, H. R.; Khoshro, H.; Ghobadi, K.; Benvidi, A. The Electrochemical Behavior of 4-Nitrobenzyl Bromide and Its Catalytic Activity for Reduction of CO_2 in the Acetonitrile Solvent at the Cu/Pd/rGO/GCE Surface. *Electrochim. Acta* **2020**, *352*, 136483. https://doi.org/10.1016/j.electacta.2020.136483.

(8) Kim, Y.; Park, G. D.; Balamurugan, M.; Seo, J.; Min, B. K.; Nam, K. T. Electrochemical *b*-Selective Hydrocarboxylation of Styrene Using CO_2 and Water. *Adv. Sci.* **2020**, *7* (3), 1900137. https://doi.org/10.1002/advs.201900137.

(9) You, Y.; Kanna, W.; Takano, H.; Hayashi, H.; Maeda, S.; Mita, T. Electrochemical Dearomative Dicarboxylation of Heterocycles with Highly Negative Reduction Potentials. *J. Am. Chem. Soc.* **2022**, *144* (8), 3685–3695. https://doi.org/10.1021/jacs.1c13032.

(10) Wang, Y.; Tang, S.; Yang, G.; Wang, S.; Ma, D.; Qiu, Y. Electrocarboxylation of Aryl Epoxides with CO_2 for the Facile and Selective Synthesis of β-Hydroxy Acids. *Angew. Chem.* **2022**, *134* (38). https://doi.org/10.1002/ange.202207746.

(11) Seo, H.; Liu, A.; Jamison, T. F. Direct β-Selective Hydrocarboxylation of Styrenes with CO_2 Enabled by Continuous Flow Photoredox Catalysis. *J. Am. Chem. Soc.* **2017**, *139* (40), 13969–13972. https://doi.org/10.1021/jacs.7b05942.

(12) Kang, G.; Romo, D. Photocatalyzed, β-Selective Hydrocarboxylation of a,b-Unsaturated Esters with CO_2 under Flow for *b*-Lactone Synthesis. *ACS Catal.* **2021**, *11* (3), 1309–1315. https://doi.org/10.1021/acscatal.0c05050.

(13) Seo, H.; Katcher, M. H.; Jamison, T. F. Photoredox Activation of Carbon Dioxide for Amino Acid Synthesis in Continuous Flow. *Nat. Chem.* **2017**, *9* (5), 453–456. https://doi.org/10.1038/nchem.2690.

(14) Matsuoka, S.; Kohzuki, T.; Pac, C.; Ishida, A.; Takamuku, S.; Kusaba, M.; Nakashima, N.; Yanagida, S. Photocatalysis of Oligo(*p*-Phenylenes): Photochemical Reduction of Carbon Dioxide with Triethylamine. *J. Phys. Chem.* **1992**, *96* (11), 4437–4442. https://doi.org/10.1021/j100190a057.

(15) Huang, H.; Ye, J.-H.; Zhu, L.; Ran, C.-K.; Miao, M.; Wang, W.; Chen, H.; Zhou, W.-J.; Lan, Y.; Yu, B.; Yu, D.-G. Visible-Light-Driven Anti-Markovnikov Hydrocarboxylation of Acrylates and Styrenes with CO_2. *CCS Chem.* **2021**, *3* (6), 1746–1756. https://doi.org/10.31635/ccschem.020.202000374.

(16) Liu, B.; Lim, C.-H.; Miyake, G. M. Visible-Light-Promoted C–S Cross-Coupling *via* Intermolecular Charge Transfer. *J. Am. Chem. Soc.* **2017**, *139* (39), 13616–13619. https://doi.org/10.1021/jacs.7b07390.

(17) Liu, B.; Lim, C.-H.; Miyake, G. Transition-Metal-Free, Visible-Light-Promoted C–S Cross-Coupling through Intermolecular Charge Transfer. *Synlett* **2018**, *29* (19), 2449–2455. https://doi.org/10.1055/s-0037-1610230.

(18) Yang, M.; Cao, T.; Xu, T.; Liao, S. Visible-Light-Induced Deaminative Thioesterification of Amino Acid Derived Katritzky Salts via Electron Donor–Acceptor Complex Formation. *Org. Lett.* **2019**, *21* (21), 8673–8678. https://doi.org/10.1021/acs.orglett.9b03284.

(19) Li, G.; Yan, Q.; Gan, Z.; Li, Q.; Dou, X.; Yang, D. Photocatalyst-Free Visible-Light-Promoted C(Sp^2)–S Coupling: A Strategy for the Preparation of *S* -Aryl Dithiocarbamates. *Org. Lett.* **2019**, *21* (19), 7938–7942. https://doi.org/10.1021/acs.orglett.9b02921.

(20) Morgenstern, D. A.; Wittrig, R. E.; Fanwick, P. E.; Kubiak, C. P. Photoreduction of Carbon Dioxide to Its Radical Anion by Nickel Cluster $[Ni_3(\mu^3\text{-}I)_2(dppm)_3]$: Formation of Two Carbon-Carbon Bonds via Addition of Carbon Dioxide Radical Anion to Cyclohexene. *J. Am. Chem. Soc.* **1993**, *115* (14), 6470–6471. https://doi.org/10.1021/ja00067a096.

(21) Nomoto, A.; Kojo, Y.; Shiino, G.; Tomisaka, Y.; Mitani, I.; Tatsumi, M.; Ogawa, A. Reductive Carboxylation of Alkyl Halides with CO_2 by Use of Photoinduced SmI_2/Sm Reduction System. *Tetrahedron Lett.* **2010**, *51* (50), 6580–6583. https://doi.org/10.1016/j.tetlet.2010.10.028.

(22) Ye, J.-H.; Miao, M.; Huang, H.; Yan, S.-S.; Yin, Z.-B.; Zhou, W.-J.; Yu, D.-G. Visible-Light-Driven Iron-Promoted Thiocarboxylation of Styrenes and Acrylates with CO_2. *Angew. Chem. Int. Ed.* **2017**, *56* (48), 15416–15420. https://doi.org/10.1002/anie.201707862.

(23) Song, L.; Wang, W.; Yue, J.-P.; Jiang, Y.-X.; Wei, M.-K.; Zhang, H.-P.; Yan, S.-S.; Liao, L.-L.; Yu, D.-G. Visible-Light Photocatalytic Di- and Hydro-Carboxylation of Unactivated Alkenes with CO_2. *Nat. Catal.* **2022**, *5* (9), 832–838. https://doi.org/10.1038/s41929-022-00841-z.

(24) Zhang, W.; Chen, Z.; Jiang, Y.-X.; Liao, L.-L.; Wang, W.; Ye, J.-H.; Yu, D.-G. Arylcarboxylation of Unactivated Alkenes with CO_2 via Visible-Light Photoredox Catalysis. *Nat. Commun.* **2023**, *14* (1), 3529. https://doi.org/10.1038/s41467-023-39240-8.

(25) Kanemoto, M.; Ankyu, H.; Wada, Y.; Yanagida, S. Visible-Light Induced Photofixation of CO_2 into Benzophenone Catalyzed by Colloidal CdS Microcrystallites. *Chem. Lett.* **1992**, *21* (11), 2113–2114. https://doi.org/10.1246/cl.1992.2113.

(26) Fujiwara, H.; Kanemoto, M.; Ankyu, H.; Murakoshi, K.; Wada, Y.; Yanagida, S. Visible-Light Induced Photofixation of Carbon Dioxide into Aromatic Ketones and Benzyl Halides Catalysed by CdS Nanocrystallites 1. *J. Chem. Soc. Perkin Trans. 2* **1997**, No. 2, 317–322. https://doi.org/10.1039/a604515d.

(27) Maxwell, T.; Campos, M. G. N.; Smith, S.; Doomra, M.; Thwin, Z.; Santra, S. Chapter 15 - Quantum Dots. In *Nanoparticles for Biomedical Applications*; Chung, E. J., Leon, L., Rinaldi, C., Eds.; Micro and Nano Technologies; Elsevier, **2020**; pp 243–265. https://doi.org/10.1016/B978-0-12-816662-8.00015-1.

(28) Baran, T.; Dibenedetto, A.; Aresta, M.; Kruczała, K.; Macyk, W. Photocatalytic Carboxylation of Organic Substrates with Carbon Dioxide at Zinc Sulfide with Deposited Ruthenium Nanoparticles. *ChemPlusChem* **2014**, *79* (5), 708–715. https://doi.org/10.1002/cplu.201300438.

(29) Aresta, M.; Dibenedetto, A.; Baran, T.; Wojtyła, S.; Macyk, W. Solar Energy Utilization in the Direct Photocarboxylation of 2,3-Dihydrofuran Using CO_2. *Faraday Discuss.* **2015**, *183*, 413–427. https://doi.org/10.1039/C5FD00040H.

(30) Capaldo, L.; Ravelli, D. Hydrogen Atom Transfer (HAT): A Versatile Strategy for Substrate Activation in Photocatalyzed Organic Synthesis: Hydrogen Atom Transfer (HAT): A Versatile Strategy for Substrate Activation in Photocatalyzed Organic Synthesis. *Eur. J. Org. Chem.* **2017**, *2017* (15), 2056–2071. https://doi.org/10.1002/ejoc.201601485.

(31) Grills, D. C.; Lymar, S. V. Radiolytic Formation of the Carbon Dioxide Radical Anion in Acetonitrile Revealed by Transient IR Spectroscopy. *Phys. Chem. Chem. Phys.* **2018**, *20* (15), 10011–10017. https://doi.org/10.1039/C8CP00977E.

(32) Minkin, V. I. Glossary of Terms Used in Theoretical Organic Chemistry. *Pure Appl. Chem.* **1999**, *71* (10), 1919–1981. https://doi.org/doi:10.1351/pac199971101919.

(33) Alektiar, S. N.; Wickens, Z. K. Photoinduced Hydrocarboxylation via Thiol-Catalyzed Delivery of Formate Across Activated Alkenes. *J. Am. Chem. Soc.* **2021**, *143* (33), 13022–13028. https://doi.org/10.1021/jacs.1c07562.

(34) Mikhael, M.; Alektiar, S.; Yeung, C.; Wickens, Z. *Translating Planar Heterocycles into 3D Analogs via Photoinduced Hydrocarboxylation*; preprint; Chemistry, **2022**. https://doi.org/10.26434/chemrxiv-2022-md8rg.

(35) Alektiar, S. N.; Han, J.; Dang, Y.; Rubel, C. Z.; Wickens, Z. K. Radical Hydrocarboxylation of Unactivated Alkenes via Photocatalytic Formate Activation. *J. Am. Chem. Soc.* **2023**, *145* (20), 10991–10997. https://doi.org/10.1021/jacs.3c03671.

(36) Hendy, C. M.; Smith, G. C.; Xu, Z.; Lian, T.; Jui, N. T. Radical Chain Reduction via Carbon Dioxide Radical Anion ($CO_2^{\bullet-}$). *J. Am. Chem. Soc.* **2021**, jacs.1c04427. https://doi.org/10.1021/jacs.1c04427.

(37) Wang, H.; Gao, Y.; Zhou, C.; Li, G. Visible-Light-Driven Reductive Carboarylation of Styrenes with CO_2 and Aryl Halides. *J. Am. Chem. Soc.* **2020**, *142* (18), 8122–8129. https://doi.org/10.1021/jacs.0c03144.

(38) Zhou, C.; Wang, X.; Yang, L.; Fu, L.; Li, G. Visible-Light-Driven Regioselective Carbocarboxylation of 1,3-Dienes with Organic Halides and CO_2. *Green Chem.* **2022**, *24* (16), 6100–6107. https://doi.org/10.1039/D2GC01256A.

(39) Hang, W.; Li, D.; Zou, S.; Xi, C. Visible-Light-Driven Reductive Carboxylation of Benzyl Bromides with Carbon Dioxide Using Formate as Terminal Reductant. *J. Org. Chem.* **2023**, *88* (8), 5007–5014. https://doi.org/10.1021/acs.joc.2c01840.

(40) Liu, W.-Z.; Bordwell, F. G. Gas-Phase and Solution-Phase Homolytic Bond Dissociation Energies of H−N^+ Bonds in the Conjugate Acids of Nitrogen Bases. *J. Org. Chem.* **1996**, *61* (14), 4778–4783. https://doi.org/10.1021/jo950933r.

(41) Huang, Y.; Hou, J.; Zhan, L.-W.; Zhang, Q.; Tang, W.-Y.; Li, B.-D. Photoredox Activation of Formate Salts: Hydrocarboxylation of Alkenes *via* Carboxyl Group Transfer. *ACS Catal.* **2021**, *11* (24), 15004–15012. https://doi.org/10.1021/acscatal.1c04684.

(42) Otero, M. D.; Batanero, B.; Barba, F. CO_2 Anion–Radical in Organic Carboxylations. *Tetrahedron Lett.* **2006**, *47* (13), 2171–2173. https://doi.org/10.1016/j.tetlet.2006.01.113.

(43) Senboku, H.; Minemura, Y.; Suzuki, Y.; Matsuno, H.; Takakuwa, M. Synthesis of *N*-Boc-*α*-Amino Acids from Carbon Dioxide by Electrochemical Carboxylation of *N*-Boc-*α*-Aminosulfones. *J. Org. Chem.* **2021**, *86* (22), 16077–16083. https://doi.org/10.1021/acs.joc.1c01516.

(44) Ju, T.; Zhou, Y.-Q.; Cao, K.-G.; Fu, Q.; Ye, J.-H.; Sun, G.-Q.; Liu, X.-F.; Chen, L.; Liao, L.-L.; Yu, D.-G. Dicarboxylation of Alkenes, Allenes and (Hetero)Arenes with CO_2 via Visible-Light Photoredox Catalysis. *Nat. Catal.* **2021**, *4* (4), 304–311. https://doi.org/10.1038/s41929-021-00594-1.

(45) Yuan, G.-Q.; Jiang, H.-F.; Lin, C.; Liao, S.-J. Efficient Electrochemical Synthesis of 2-Arylsuccinic Acids from CO_2 and Aryl-Substituted Alkenes with Nickel as the Cathode. *Electrochim. Acta* **2008**, *53* (5), 2170–2176. https://doi.org/10.1016/j.electacta.2007.09.023.

(46) Zhao, Z.; Liu, Y.; Wang, S.; Tang, S.; Ma, D.; Zhu, Z.; Guo, C.; Qiu, Y. Site-Selective Electrochemical C−H Carboxylation of Arenes with CO_2. *Angew. Chem. Int. Ed.* **2023**, *62* (3), e202214710. https://doi.org/10.1002/anie.202214710.

(47) Li, C.; Yuan, G.; Jiang, H. Electrocarboxylation of Alkynes with Carbon Dioxide in the Presence of Metal Salt Catalysts. *Chin. J. Chem.* **2010**, *28* (9), 1685–1689. https://doi.org/10.1002/cjoc.201090285.

(48) Alkayal, A.; Tabas, V.; Montanaro, S.; Wright, I. A.; Malkov, A. V.; Buckley, B. R. Harnessing Applied Potential: Selective β-Hydrocarboxylation of Substituted Olefins. *J. Am. Chem. Soc.* **2020**, *142* (4), 1780–1785. https://doi.org/10.1021/jacs.9b13305.

(49) Sheta, A. M.; Alkayal, A.; Mashaly, M. A.; Said, S. B.; Elmorsy, S. S.; Malkov, A. V.; Buckley, B. R. Selective Electrosynthetic Hydrocarboxylation of α,β-Unsaturated Esters with Carbon Dioxide. *Angew. Chem.* **2021**, *133* (40), 22003–22008.

(50) Denning, D. M.; Thum, M. D.; Falvey, D. E. Photochemical Reduction of CO_2 Using 1,3-Dimethylimidazolylidene. *Org. Lett.* **2015**, *17* (17), 4152–4155. https://doi.org/10.1021/acs.orglett.5b01891.

(51) De Robillard, G.; Devillers, C. H.; Kunz, D.; Cattey, H.; Digard, E.; Andrieu, J. Electrosynthesis of Imidazolium Carboxylates. *Org. Lett.* **2013**, *15* (17), 4410–4413. https://doi.org/10.1021/ol401949f.

(52) Luca, O. R.; McCrory, C. C. L.; Dalleska, N. F.; Koval, C. A. The Selective Electrochemical Conversion of Preactivated CO_2 to Methane. *J. Electrochem. Soc.* **2015**, *162* (7), H473–H476. https://doi.org/10.1149/2.0371507jes.

(53) Lieske, L. E.; Freeman, L. A.; Wang, G.; Dickie, D. A.; Gilliard, R. J.; Machan, C. W. Metal-Free Electrochemical Reduction of Carbon Dioxide Mediated by

Cyclic(Alkyl)(Amino) Carbenes. *Chem. - Eur. J.* **2019**, *25* (24), 6098–6101. https://doi.org/10.1002/chem.201900316.

(54) Freeman, L. A.; Obi, A. D.; Machost, H. R.; Molino, A.; Nichols, A. W.; Dickie, D. A.; Wilson, D. J. D.; Machan, C. W.; Gilliard, R. J. Soluble, Crystalline, and Thermally Stable Alkali CO_2^- and Carbonite (CO_2^{2-}) Clusters Supported by Cyclic(Alkyl)(Amino) Carbenes. *Chem. Sci.* **2021**, *12* (10), 3544–3550. https://doi.org/10.1039/D0SC06851A.

(55) Kolychev, E. L.; Bannenberg, T.; Freytag, M.; Daniliuc, C. G.; Jones, P. G.; Tamm, M. Reactivity of a Frustrated Lewis Pair and Small-Molecule Activation by an Isolable Arduengo Carbene-B{3,5-$(CF_3)_2C_6H_3$}$_3$ Complex. *Chem. - Eur. J.* **2012**, *18* (52), 16938–16946. https://doi.org/10.1002/chem.201202840.

(56) Theuergarten, E.; Bannenberg, T.; Walter, M. D.; Holschumacher, D.; Freytag, M.; Daniliuc, C. G.; Jones, P. G.; Tamm, M. Computational and Experimental Investigations of CO_2 and N_2O Fixation by Sterically Demanding *N*-Heterocyclic Carbenes (NHC) and NHC/Borane FLP Systems. *J. Chem. Soc. Dalton Trans.* **2014**, *43* (4), 1651–1662. https://doi.org/10.1039/c3dt52742e.

(57) Holschumacher, D.; Bannenberg, T.; Hrib, C. G.; Jones, P. G.; Tamm, M. Heterolytic Dihydrogen Activation by a Frustrated Carbene–Borane Lewis Pair. *Angew. Chem. Int. Ed.* **2008**, *47* (39), 7428–7432. https://doi.org/10.1002/anie.200802705.

(58) Atkins, P. W.; De Paula, J. *Atkins' Physical Chemistry*, 8th ed.; W.H. Freeman: New York, **2006**.

(59) Mas-Ballesté, R.; Capdevila, M.; González-Duarte, P.; Hamidi, M.; Lledós, A.; Mégret, C.; Montauzon, D. D. Electrochemical and Theoretical Study of the Redox Properties of Transition Metal Complexes with (Pt_2S_2) Cores. *J. Chem. Soc. Dalton Trans.* **2004**, *4* (5), 706–712. https://doi.org/10.1039/b315509a.

(60) Roth, H. G.; Romero, N. A.; Nicewicz, D. A. Experimental and Calculated Electrochemical Potentials of Common Organic Molecules for Applications to Single-Electron Redox Chemistry. *Synlett* **2016**, *27* (5), 714–723. https://doi.org/10.1055/s-0035-1561297.

(61) Isegawa, M.; Sharma, A. K. CO_2 Reduction by a Mn Electrocatalyst in the Presence of a Lewis Acid: A DFT Study on the Reaction Mechanism. *Sustain. Energy Fuels* **2019**, *3* (7), 1730–1738. https://doi.org/10.1039/C9SE00213H.

(62) Krewald, V.; Pantazis, D. A. Understanding and Tuning the Properties of Redox-Accumulating Manganese Helicates. *Dalton Trans.* **2016**, *45* (47), 18900–18908. https://doi.org/10.1039/C6DT02800D.

(63) Borioni, J. L.; Puiatti, M.; Vera, D. M. A.; Pierini, A. B. In Search of the Best DFT Functional for Dealing with Organic Anionic Species. *Phys. Chem. Chem. Phys.* **2017**, *19* (13), 9189–9198. https://doi.org/10.1039/C6CP06163J.

(64) Li, Y.; Wang, D.; Zhang, L.; Luo, S. Redox Property of Enamines. *J. Org. Chem.* **2019**, *84* (18), 12071–12090. https://doi.org/10.1021/acs.joc.9b02003.

(65) Zhang, W.; Walser-Kuntz, R.; Tracy, J. S.; Schramm, T. K.; Shee, J.; Head-Gordon, M.; Chen, G.; Helms, B. A.; Sanford, M. S.; Toste, F. D. Indolo[2,3-b]Quinoxaline as a Low Reduction Potential and High Stability Anolyte Scaffold for Nonaqueous Redox Flow Batteries. *J. Am. Chem. Soc.* **2023**, *145* (34), 18877–18887. https://doi.org/10.1021/jacs.3c05210.

Chapter 2: An in silico study to explore the monoelectronic reduction of NHC-CO_2-based adducts.

This chapter aims at compiling all the research design choices related to the computational determination of reduction potentials in NHC-based adducts. The chapter integrates the core of this research project and has been divided into two defined subsections. Firstly, the computational methodology that was followed will be described (2.1.) and subsequently, the assessed results will be presented and discussed (2.2.).

2.1. Methodology.

In this section, the computational details related to our theoretical study is given. In addition to that, theoretical concepts are also discussed: a brief preamble of the origin of the Density Functional Theory (DFT), functionals and basis set commonly used as well as the solvent model. The methodology section concludes with a discussion related with the determination of theoretical reduction potentials.

2.1.1. Computational details.

In order to understand prior to the experiments how NHC-CO_2-based species behave after the addition of one electron, we envisaged a preliminary *in silico* study that aims at guiding us towards the choice of adduct/s that may exhibit most accessible reduction potential for its further synthesis. This computationally integrated strategy would allow us to effectively save material and time resources. For this study, a collection of diverse diaminocarbene adducts differing by *N*-substituents along with other types of NHC-CO_2-based species (**1**-**8**) were evaluated in order to make the study as general as possible (Scheme 1).

N-Alkyl groups

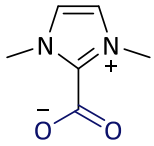

(**1**)

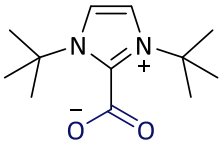

(**2**)

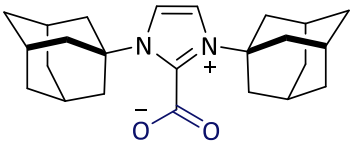

(**3**)

N-Aryl groups

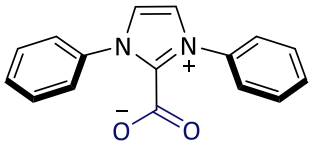

(**4**)

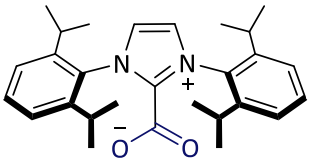

(**5**)

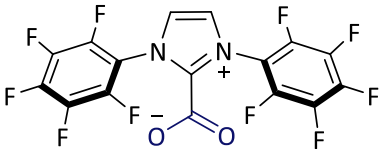

(**6**)

Enders and ^{Cy}CAAC-type NHCs

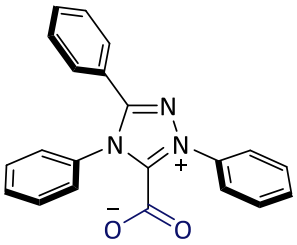

(**7**)

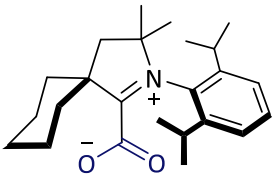

(**8**)

Scheme 1. Studied NHC-CO_2 adducts

The DFT calculations were carried out using Gaussian16 software.[1] Geometry optimizations were performed using both functionals hybrid functionals B3LYP[2,3,4] and M06-2X[5] combined with the Grimme's D3 correction to consider dispersion effects.[6] The optimisations were carried out in solution (solvents= acetonitrile, ε = 35.688 ; dichloromethane, ε = 8.93) using the SMD continuum model[7] with BS1 as a basis set. BS1 uses the 6-311-G++(d,p) basis set for all the atoms.[8,9] All energies in solution were corrected by single-point calculations with a larger basis set (BS2) including def2TZVP basis set for all atoms.[10]

Gibbs energies in solution were calculated at 298.15 K adding to the energies in solution, obtained with single-point calculations using BS2, the thermal and entropic corrections obtained from frequency calculations with BS1. Frequencies calculations were

performed with the aim at characterising the stationary points, either minima or transition states. All energies in solution were corrected by single-point calculations with a larger basis set (BS2) including def2TZVP basis set for all atoms.[10]

To adjust the Gibbs energies from 1 atm to 1 mol/L standard state in solution, a correction of RTln(cs/cg) was added ($\Delta G^{1\ atm \rightarrow 1\ M}$). The value 1.9 kcal·mol^{-1} was added to energies of all species, c_s is the standard molar concentration in solution (1 mol·L^{-1}), c_g is the standard molar concentration in gas phase (0.0446 mol·L^{-1}), and R is the gas constant (8.314 J·mol^{-1}·K^{-1}). All reported energies in the following discussion correspond to both functional Gibbs energies in solution at 298.15K in kcal·mol^{-1}, if not otherwise specified, calculated using the formula:

$$G = E(BS2) + G(BS1) - E(BS1) + \Delta G^{1\ atm \rightarrow 1\ M} \qquad Eq.1$$

Structure visualization was performed with Chemcraft[11], IboView[12], CYLview software[13]. The orbital related calculations were performed using ORCA 5.0.4 suite of programmes[14] with the functional M06-2X.[5] It was combined with Grimme's D3 correction considering the original damping function (D3ZERO)[6] including def2TZVP basis set for all atoms.[10]

The EPR calculations were carried out using ORCA 5.0.4 suite of programmes[14] with the functional M06-2X[5] including 6-311G(d,p)[15] basis set for all atoms in solution (solvent= tetrahydrofuran, ε = 7.4257) using the SMD continuum model. The EPR simulations were performed by EasySpin, an open-source MATLAB toolbox.[16]

2.1.2. Preamble to the Density Functional Theory (DFT).

The density functional theory is one of the most popular methods used in computational chemistry in which the energy of a many-electron system can be estimated from its electron density distribution, ρ(r). The basis of DFT were established by the physicists Pierre Hohenberg and Walter Kohn in two theorems (Hohenberg-Kohn theorems).[17]

1. The energy of the electronic ground state of a many-electron system can be calculated as a functional (a generalisation of a function) of its electron density distribution that solely depends on three spatial coordinates (x,y,z), E[ρ(r)]. The energy is expressed by the equation

$$E[\rho(r)] = F[\rho(r)] + \int \rho(r)v(r)dr \qquad Eq.2$$

where F[(ρ(r)] is a universal functional that contains the kinetics energy, and the electron-electron interaction and v(r) corresponds to the external potential. There is a one-to-one relationship between the electron density and the external potential. This means that the electron density in the ground state contains the information of an electronic system.

2. A variational principle for the density ρ(r) exist which means that any approximate density, expressed as ρ' would return a higher energy than the correct ground state density, E[ρ'] > E[ρ], would.[18] There minimum energy provided will be ruled by the ground state electron density distribution which will be the exact solution of the electronic Schrödinger equation. So far, the exact expression for the density functional is unknown.

Despite approximate functionals have been developed, they do not accurately provide the kinetic energy part of the energy, that as aforementioned, it integrates F[(ρ(r)] (Equation 2). An alternative approach was proposed by Walter Kohn and Lu Jeu Sham (Kohn-Sham theory). This concept is based on choosing as an input a fictious non-interacting reference system built from a set of orbitals (Kohn-Sham orbitals, Eq. 3) such that a major part of the kinetic energy can be computed to good accuracy. These non-interacting electrons have for their overall ground-state density the same density as some real system of interest where the electrons do interact (note that since the density determines the position and atomic numbers of the nuclei, these quantities are necessarily identical in the non-interacting and in the real systems).[19] Following this procedure, as much information as possible is computed in an exact manner and only a small part of the total energy is defined by an approximate functional[20] (see next section 2.1.3 "Functionals.").

$$\rho_{approx} = \sum_{i=1}^{Nelec} |\Phi_i|^2 \qquad Eq.3$$

2.1.3. Functionals.

The choice of the functional in DFT is not an easy task. The hunt of a *magical* functional that describe each system and assesses its energies in an accurate manner at low computation cost has attracted the attention of the scientific community along the way. In the last decade, the group of Swart, Bickelhaupt and Duran have conducted different surveys and annuals poll for density functionals with the main aim of ranking them up in terms of popularity in the community.[21]

The DFT determination of reduction potentials in NHC-CO_2-based adducts could not be found in the literature. As a theoretical approach towards the determination of theoretical reduction potentials, a calibration of functional must be done first in order to check the dependence of computed results with the functional. As aforedescribed, the functionals that were evaluated in the estimation of reduction potentials for NHC-based adducts were, B3LYP and M06-2X, both of them with the Grimme's correction. Both functionals have been largely employed in order to determine the redox potentials in organic substrates,[22,23,24,25,26,27,28,29] therefore we thought that it might be also applicable in NHC-CO_2-based systems.

In order to better understand how functionals are classified from the simplest to the most complex ones, computational scientists usually use as quite bright analogy, the Jacob's ladder. In a very brief manner, the biblical patriarch Jacob dreamt of ladder that leads to heaven.[30] Nevertheless, each religion and culture has adopted this concept to their own vision. In the DFT field, the simplest functional (or level of theory) would occupy the lowest rung of that ladder whilst the highly parametrised would stay in the highest ones, the closest to the heaven of the chemical accuracy (DFT calculations has associated the same error as the best experimental measurement).[31] In the literature, most of the authors agrees that this ladder is constituted by four rungs: the local density approximation (LDA), generalized gradient approximations (GGA), meta-GGAs and finally, the hybrid density functional that would be placed on the forth rung. Very lately, it appeared a higher level of theory (fifth rung) which are the random-phase approximation (RPA) and doubly hybrid approximation (DHA) (Scheme 2).[20]

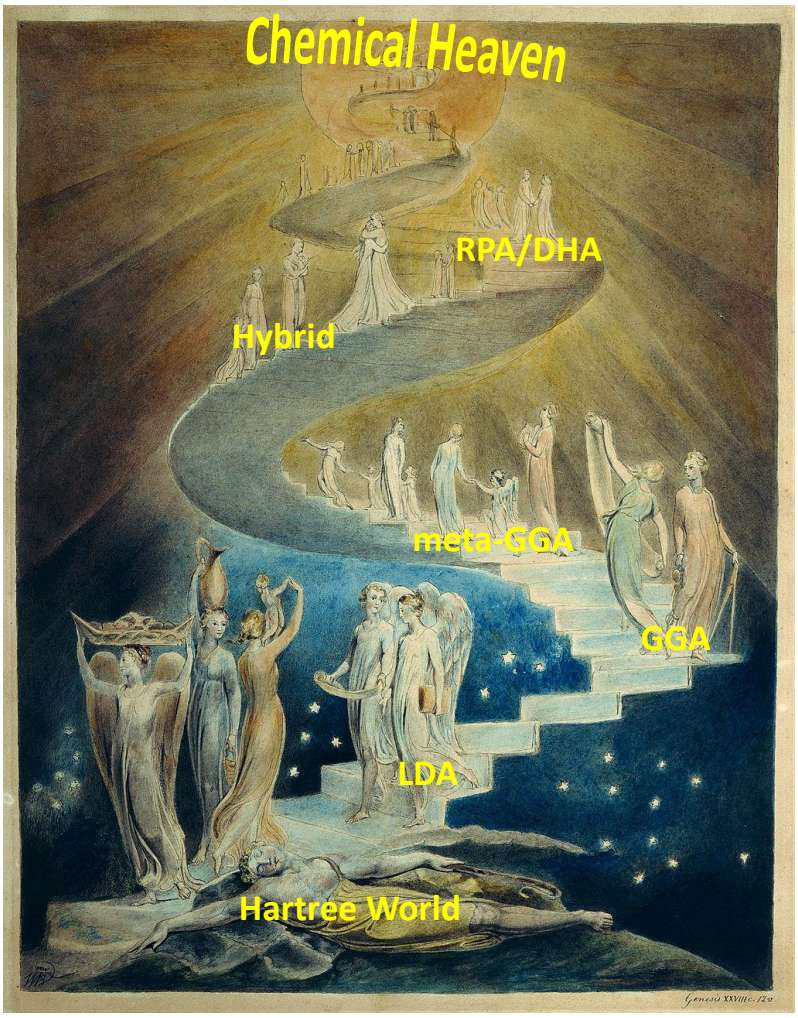

Scheme 2. The Jacob's ladder of DFT inspired in "Jacob's Ladder" by William Blake (c. 1800, British Museum, London).

1) The lowest rung, local density approximation (LDA).[32] This level of theory is the simplest in DFT. The LDA was developed by Kohn and Sham and the exchange correlation energy solely relies on the density at a given point (local density). For this reason, the use of this functional could lead to large errors (around 30 kcal·mol^{-1}) which are not acceptable in chemical transformations. Nevetheless, this level of theory is currently used in the solid-state physics field. Some examples include Perdew-Wang 91 (PW91) and Ceperley-Alder (CA) functionals.
2) Second rung, generalized density gradient approximation (GGA).[33] In contrast to LDA, GGA considers the gradient at each point along with the density. Popular-based GGA functionals are PBE[34] and BLYP[35,36].

3) Third rung, meta-GGA. Additionally, to the parametrization of LDA and GGA, it also depends on kinetic energy density (density hessian). As function, TPSS can be highlighted.[37]
4) Forth rung, hybrid approximation. The two functionals that were used in our study, B3LYP and M06-2X belongs to this level of theory. These functionals integrate a portion of exact exchange energy that has been previously calculated based on the Hartree-Fock theory (H-F theory) which significantly improves the calculation of different molecular properties.

   B3LYP, which stands for "Becke, 3-parameter, Lee-Yang-Parr" is a very popular functional in the scientific community.[38] It was the first functional constituted by a portion of exact exchange energy ever created. The exchange-correlation energy of this functional (E_{XC}^{B3LYP}) could be represented as in Equation 4.

$$E_{XC}^{B3LYP} = (1-a)E_X^{LSDA} + aE_X^{HF} + b\Delta E_X^B + (1-c)E_C^{LSDA} + cE_C^{LYP} \qquad Eq.4$$

   In Eq. 4, a = 0.2, b = 0.72 and c = 0.81. These parameters constituted the "3-parameter" of B3LYP. E_X^{LSDA} and E_C^{LSDA} corresponds to local spin density approximation to the exchange and the correlation functional. E_X^B refers to Becke88 exchange functional. Finally, E_C^{LYP} is related to the correlation functional LYP. The percentage of Hartree-Fock exchange is 20%.

   The case of M06-2X belongs to the Minnesota functionals family. They have been conceptualised by Truhlar's group.[5] This rather recent functional compared to B3LYP is a high-nonlocal functional with double amount of nonlocal exchange (2X). According to the authors, it has been exclusively parametrised for nonmetals. In this case, the percentage of Hartree-Fock exchange is 54%.

   As previously showed with different examples, M06-2X and B3LYP could be perfect candidates to test due to their performance in main-group thermochemistry and the accurate assessment of reduction potentials in organic molecules.

5) Fifth rung, RPA and DHA.[39] In addition to the occupied KS orbitals, the unoccupied orbitals are considered too. This level of theory is the one that is closer to the longed chemical accuracy. However, the application of these methods is not straightforward. As known, DFT is based on the electron density therefore it could be disrupting to think that the level of theory includes these electronically unoccupied orbitals. There are two elegant approaches, RPA which stands for random-phase approximation (RPA) and doubly hybrid approximation (DHA). The application of these methods comes with a high computational cost compared to the precedent approximations although, some progress has been done in this aspect. As example, RPA has been used to compute models containing up to 1500 atoms in only one hour whereas the same calculation could last several months if a lower level of theory is employed.[40]

2.1.4. Basis sets.

In this section, the definition of basis set and orbital-type functions are described and in the latter instance, the classification of them focussing on the minimal and split-valance basis are discussed.

2.1.4.1. Definition of basis set and orbital-type functions.

The basis sets, also known as basis functions, are a collection of one-particle functions centred on an atom that mimic the solutions of hydrogen atom (orbitals). In the computational chemistry field, the basis set are usually constituted by atomic orbitals which result in the linear combination of atomic orbitals (LCAO) approximation. Mathematically, higher the number of atomic orbitals comprised on a LCAO, better is the description of the system is achieved. For example, the hydrogen atom could have more orbitals, besides the 1s. This would enable a more flexible representation of the molecular orbitals. These general atomic orbitals are known as the basis functions. Based on the LCAO, the problem of solving the molecular orbitals is significantly reduced as only the coefficients of the basis functions must be determined by a self-consistent field (SCF) calculation. There are two different orbitals that have been widely used, Slater-type orbitals and Gaussian-type orbitals:

a) **Slater-type orbitals (STO).**[41] The orbital functions are generally expressed as in Equation 5,

$$\Phi_{abc}^{STO}(x,y,z) = Nx^a y^b z^c e^{-\zeta r} \qquad Eq.5$$

where N is the normalization constant; a, b, c are parameters which control the angular momentum and the orbital exponent, the Greek letter zeta (ζ,) which determine the width of the orbital, small zeta values resulting into functions with a diffuse character and vice versa. These orbital functions exhibit a radial dependence of the H-atom solutions therefore it closely matches more hydrogenic orbitals. Nevertheless, the use of these functions is very time consuming therefore is recommended to use the Gaussian-type orbitals.

b) **Gaussian-type orbitals (GTO).**[42] The use of these orbital functions is preferred with respect to STOs as they enable a more efficient molecular integral computation. This fact lays on the Gaussian Product Theorem (GPT). It states that the product of two Gaussian function will result in a third Gaussian function around a shift centre. The single Gaussian-type functions (primitive) usually present significant errors compared to STOs, in particular close to the nucleus. In order to minimise these errors, linear combinations of normalised Gaussian-type orbitals, name as contracted GTOs, are employed to mimic the behaviour of STOs near to the nucleus. The basis function is much improved when it is constituted by several GTOs. They are generally defined as expressed in Equation 6.

$$\Phi_{abc}^{GTO}(x,y,z) = Nx^a y^b z^c e^{-\zeta r^2} \qquad Eq.6$$

2.1.4.2. Classification of basis sets.

The more commonly used basis sets in computational chemistry are classified in multiple groups. Due to the extension in their classification, minimal and split-valence basis set will be only discussed below.

a) **Minimal basis set**. This is the simplest basis set. Every occupied atomic orbital is represented using a single basis function. One of the most common minimal basis sets is the STO-nG.[43] It is constituted by a single Slater-type Orbital (STO) built up with a linear combination of a finite number (n) of Gaussian-type Orbital which

varies from 1 to 6. As example, STO-3G. Higher the number of Gaussian-type functions, the accuracy of the energy increases as well as the computational cost.

b) **Split-Valence basis set.**[44] In this case, the basis set is minimal for the inner (core) orbitals and the valence orbitals is split. This basis set is constituted by more than one basis function for each occupied atomic orbitals: double zeta (DZ), triple zeta (TZ), quadruple (QZ) and so on. Pople proposed a notation to better identify the composition of the split-valence basis set. Each basis set can be usually represented in the X-YZG manner. X stands for the number of primitive GTOs in the core of each AO. Y and Z refers to a linear combination of Y and Z GTOs at the valence orbitals. As example 3-21G, this basis set is constituted by three primitives for the core (STO-3G) and each valence orbital consists of basis function (two GTOs for contracted valence orbitals and one for extended valence orbitals).

Additional functions can also be introduced into the basis sets: polarisation, and diffusion functions. For example, the atomic orbitals that constitute the molecular orbitals of an arbitrary molecule get polarised during a reaction. Additional orbital-type functions (p, d, f) can be added in order to reflect that polarisation process. As example, 6-31G(d). In this basis set d-type orbitals have been added to all atoms but hydrogen. In the case of 6-31G(d,p), p-type functions were added to H atoms, d-type to all atoms (Z(atomic number)>2) except hydrogen.

In the case of the diffuse functions, they are fundamental in the description of systems in which part of its electronic density is relatively dispersed as in anions, lone pair and single electrons (radicals) for instance. This is indicated by the "+" symbol (Pople's notation). As example, 6-31+G, it exhibits an additional p-type GTO with a low orbital exponent to induce flexibility in the system. This extra orbital is added to all atoms except for H. For addition diffuse functions into the H atoms, it is expressed as "++"

As aforementioned in subsection 2.1.1. "Computational details" in this chapter. 6-311++G(d,p) was the basis set employed for the optimization of the neutral and monoreduced NHC-CO_2-based species on this study. This basis set is constituted by one

set of core orbitals (6 GTO) for all atoms except for the H atom and three sets of valence orbitals (triple zeta) (3(1s) for H and 3x4(2s,2p) for the rest atoms). The symbol "++" indicates that two sets of diffuse valence orbital were added. One set (4 (2s,2p)) for atoms where Z>2 and another set for hydrogen (1(1s)). As polarisation functions, one set of five *d*-functions to the atoms where Z>2 and one set of three *p*-functions for the H atom.

After optimization of the structure, single point calculation with a more extensive basis set were done in order to obtain a more accurate energy. To do that, the used basis set was def2-TZVP.[10] It belongs to the Karlsruhe basis set family jointly by Weigend and Ahlrichs. In the case of def2-TZVP, it is the improved version of def-TZVP. Def stands for "default" and TZVP for "Valence triple-zeta polarization". In the systems of our study, the H atoms exhibits a set of three *s*- and one *p*-type polarization function and the rest of the atoms, five *s*-, three *p*-, two *d*- and one *f*-type orbitals. If it is compared to its forerunner, def-TZVP (five s-, three p- and one d-type orbitals). The set of polarization functions for H atoms is identical to def2-TZVP (three *s*- and one *p*-type orbitals). The main difference is the presence of *f*-type and the presence of one additional *d*-type functions (two in total). According to the authors, def2-TZVP bases are usually identical to def2-TZVPP (two sets of polarization functions) for *p*-elements, but no more details were cited on the work.

2.1.5. Solvent models.

The third key player in calculation in the solution-state phase is the solvent model. The use of a solvent model in calculations enables thermodynamic calculations that take place in solution as it is our case. There are three large families of solvent models: explicit, implicit (or continuum) and hybrid solvent model. Due to the discussion matter, the continuum implicit solvent model will be described in a more detailed manner.

The explicit solvent model consists of a solute molecule in a box solvated by as many solvent molecules as required to reproduce the density of the system (Scheme 3). This model provides a realistic description of the condensed phase environment, and they can also simulate the dynamics of the solvent itself. Nonetheless, it is mandatory the use

of additional statistical methods to sample the large diversity of solvent configurations. The use of the explicit solvent model can easily result into costly calculations in computational resources.

In order reduced the computational costs, the hybrid implicit-explicit solvent model can be considered (Scheme 3). In this model, a selected number of explicit solvent molecules is included into the atomistic part of the calculation, along with the addition of the implicit continuum solvation to take into account the large-range electrostatic effect. The problem associated with this hybrid model is the difficulty to define the exact number and location of the solvent molecules over the solute which will derive, as in the previous solvent model (explicit solvent model), into a large diversity of solvent configurations.

The solvent model that was used in our study was the implicit (or continuum) solvent model. No explicit solvent molecules are present in the atomistic part of the calculation therefore, the solvent sampling is circumvented (Scheme 3). The solvent is considered as a bulk homogeneous polarizable medium, described by the dielectric solvent constant. Within the advantages of using this model is its computational efficiency compared to the latter described model. Nonetheless, the implicit solvent models do provide a "average" solvent effect derived from considering the solvent as a bulk and do not capture specific interactions with solvent molecules. If the solvent is involved in the system as a participant, an hybrid solvent model should be employed.[45]

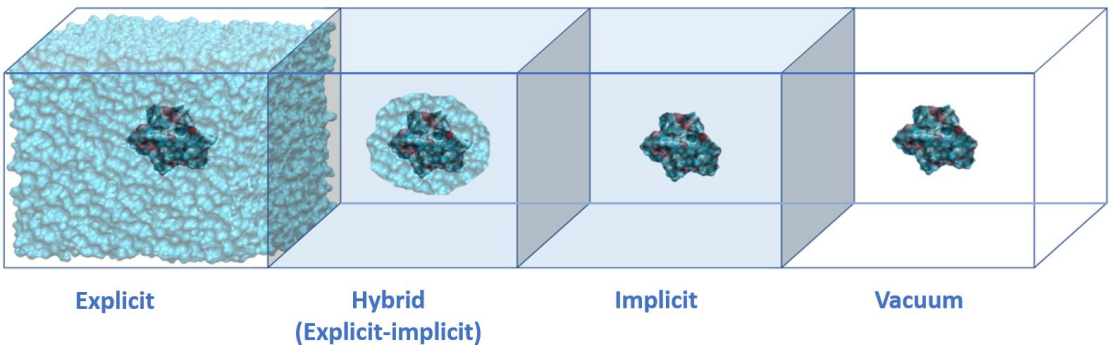

Scheme 3. Classification of solvent models.[45]

The implicit model is governed with three main physical parameters: cavity, electrostatic and non-electrostatic effects.

a) **Cavity**. Each solvent model exhibits a cavity treatment with different size and shape. Nevertheless, a general feature for all of them is that the cavity must

exhibit a physical meaning, and not simply a mathematical approach as the dipole-based model in which the cavity presented a spherical shape introduced by Onsager.[46] The cavity should contain within its boundaries the largest amount of charge distribution of the solute excluding any solvent. At this point, a dichotomy might appear between the computational cost and the accuracy and adjustment to the real world. The use of spherical cavities could give access to faster calculations nevertheless, the molecular shape is quite far to be either a sphere or an ellipsoid. In order to balance these two complementary counterparts, the molecular surface can be consisted as an interconnected superposition of spherical-shaped atoms whose radii[47] was close to van der Waals radii (Polarised Continuum solvent Model, PCM). Another radii choice has been proposed by Truhlar and co-workers, the intrinsic Coulombic atomic radii. This sort of radius is exclusive of the SMx solvent model (x = 4, 6, 8, D). The solvent model used in this work was SMD which stands for the solvent model based on density. It is also known as the universal solvent model due to its applicability to charged and uncharged solutes.[7] Due to the irregular shape of molecules, it is not unusual that a portion of solvent does not have full access to all local parts of the molecule. For this reason, two different sorts of surface considerations arose depending on the access or non-access of the solvent: the solvent-excluding (SES) and solvent accessible surface (SAS). In both cases, the solvent exhibits a van der Waals spheric shape. The SAS is built up though the rolling of the centre of the solvent sphere over the solute surface. SE is the region in which a same sized solvent sphere cannot penetrate. As another example, Fang[48] and co-workers proposed another solvent treatment approach. They envisage the electronic density of the solute as boundaries of the cavity. They named it as isodensity polarizable continuum model, IPCM. It is based on the isodensity-based SCRF radii.

b) **Electrostatic contributions**. Mathematically, the energy associated with a solution system can be indicated as follows,

$$E = \left\langle \psi^{pol} \middle| \hat{H} + \frac{\hat{V}}{2} \middle| \psi^{pol} \right\rangle \qquad Eq.7$$

where ψ^{pol} refers to the molecule in solution wavefunction, $\hat{H}$ and $\hat{V}$ the Hamilton operator in vacuo and the solute-solvent interaction operator, respectively. There is a ½ factor to consider the interaction energy decrease due to polarisation performed by the solvent.[49,50.51]

The electrostatic energy contribution depends on the generated cavity and appears due to the induced permanent dipole. In the case of PCM, the electrostatic contribution is calculated as follows,

$$E_{electrostatic} = \frac{1}{2}\sum_{j}\sum_{i}\frac{Q_j q_i}{R_j - r_i} \qquad Eq.8$$

The ½ factor is from equation 5, Q_j is the solute charge distribution estimated from quantum mechanics (QM) calculations and q_i the charge distribution in the cavity surface from the Poisson equation (equivalent to Equation 9). The difference between R_j and r_i refers to the distance between the cavity surface and the solute atoms.[49,50,52,53]

In the case of the SMD model[7], the electrostatic contributions are governed by IEF-PCM, the integral equation formalism. In this contribution, it is express as the solution of nonhomogeneous Poisson equation (NPE) by the IEF-PCM model using the Coulomb radii.[54,55,56,57]

The IPCM solvent model is ruled by the Poisson equation (Eq. 7), in which the electronic potential, ϕ, and charge density, ρ, is consider with the aim at resolving the polarized charge distribution q. ε_0 is the dielectric constant under vacuum.

$$\Delta\Phi = -\frac{\rho}{\varepsilon_0} \qquad Eq.9$$

c) **Non-electrostatic contributions**. These contributions are mainly constituted by three components: dispersion, cavitation, and repulsion energy. The dispersion related to solute-solvent is one of the important components of the solute-

solvent interaction.[51] Truhlar and co-workers[7] summed up all non-electrostatic contributions in the solvent model SMD in the following empirical equation,

$$G_{CDS} = \sum_{k}^{atoms} \sigma_k A_k[R,(R_k + r_S)] + \sigma^M \sum_{k}^{atoms} A_k[R,(R_k + r_S)] \qquad Eq.10$$

The equation 10 was named by the authors, "cavity-dispersion-solvent-structure Gibbs energy" where σ_k corresponds to the atomic surface tension of an arbitrary atom, k and σ^M, to the molecular surface tension. A_k refers to SAS area that is subject to the k atom geometry, R. The latter geometry is given the atomic van der Waals radii, R_k besides r_S, solvent radius.

Regarding the cavitation energy, several approaches exist that takes into account the shape of the solute and other different paraments related to the solvent itself.[50] As examples, Pierotti[58] and co-workers based their treatment in the scaled particle theory (SPT) previously disclosed by Reiss[59], and co-workers in which the cavity exhibit a hard spheric shape. The sphere could not be superposed. Based on the precedented subsection (a) "Cavity" of this chapter, the cavity was lately described as a collection of overlapping spheres.[7,45,53,55] This can be expressed using the following equation,

$$G_{cav} = \sum_{i}^{spheres} \frac{A_i}{4\pi R_i^2} \Delta G_{cav}(R_i) \qquad Eq.11$$

where A_i refers to the surface area of an arbitrary sphere, I, whose radius exposed to the solvent is R_i. $G_{cav}(R_i)$ is the cavitation energy associated with the sphere, I, calculated from the Pierotti's work[58] (Equation 12).

$$G_{cav}(R_i) = \sum_{j=0}^{3} K_j(P,T,\rho_S,R_S)(R_i + r_S)^j \qquad Eq.12$$

where K_j is a factor which depends on pressure (P), temperature (T) and the density of the solvent, ρ_S.

2.1.6. Determination of theoretical reduction potentials *via* DFT means.

In this subsection, the discussion previously introduced in the section 1.4. "Reduction potentials: Concepts and applications." in Chapter 1 is continued in a more detailed

manner. In Chapter 1, the determination of reduction potentials was envisaged from a thermodynamical point of view. We aim at describing the basis of the estimation of theoretical reduction potentials *via* DFT means.

2.1.6.1. Thermodynamic cycle for the calculation of potentials and implicit solvent models.

As illustrated in the section 1.4: "Reduction potentials: Concepts and applications." in Chapter 1, the only thermodynamic parameter required for the estimation of the theoretical reduction of an electrochemical half-reaction is the Gibbs energy in the standard state of the half reaction ($\Delta G°_{solution}$). Based on the Born-Haber cycle, thermodynamics cycles can also be employed for the estimation of absolute reduction potentials[60] (Scheme 4). Given the Equation 5, Chapter 1, the thermodynamic cycle would result in

$$O\ (solution) + ze^{-}\ (gas) \rightarrow R\ (solution);\ E_{red}(O/R) \qquad Eq.5\,, Chapter\ I$$

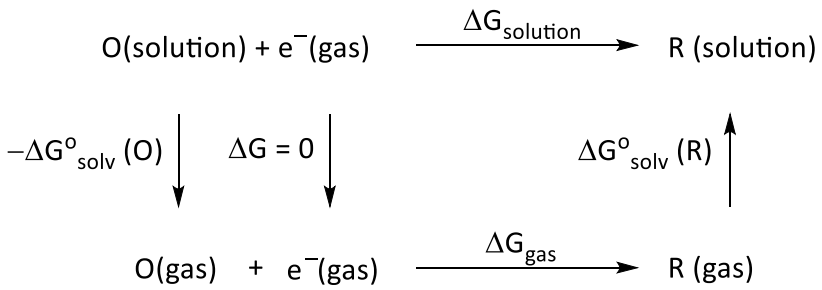

Scheme 4. Thermodynamic cycle for calculating an absolute reduction potential.

where $\Delta G°_{solv}$ is the Gibbs free energy of solvation of the chemical species, O and R.

$$\Delta G^{o}_{solution} = \Delta G^{o}_{gas} + \Delta G^{o}_{solv}(R) - \Delta G^{o}_{solv}(O) \quad Eq.13$$

As Equation 13 illustrates, the calculation of the Gibbs energy of the reduction reaction in solution can be decomposed in the Gibbs free energy of the reaction in the gas phase state and the solvation energies associated with each chemical species, O and R. Based on the previous thermodynamic cycle (Scheme 4), the use of continuum solvent model is commonly employed in the calculation of Gibbs solvation energies (previously discussed in subsection 2.1.5. "Solvation model.").

Considering as example the chemical reaction described above in Equation 5, Chapter 1 in standard conditions, it can be expressed in terms of Gibbs energy taking into account the Gibbs energy for each of the involved chemical species, $G^o(O)$, $G^o(R)$ and $G^o(e^-)$. If we focus our attention on the latter Gibbs energy, $G^o(e^-)$. The Gibbs energy associated with the electron is expressed in the gas-phase state and its value would depend on the choice of the statistical mechanical formalism. There are two different formalisms for the treatment of the electron in this context: the stationary electron convention (SEC) and the ion convention (IC). In the stationary electron convention, this subatomic particle is considered as an element. By convention, the Gibbs free energy and enthalpy are defined to be zero for the elements in their standard state. On the other hand, the ion convention considers that the formation of the enthalpy of the electron is defined by the heat capacity. The stationary electron convention will be assumed as convention for the electron treatment.

Following the thermodynamic cycle protocol, the deviations are still high with respect to the experimental measured reduction potentials (errors between 0.25 V-0.3 V).[61,62] The origin of these error was associated with the Gibbs free solvation energy of the participating species. Mathematically, most of the continuum models presents the following form,

$$\Delta G_{solvation} = \left\langle \psi^{pol} \middle| \hat{H} + \frac{\hat{V}}{2} \middle| \psi^{pol} \right\rangle + G_{nes} - E_{gas} \quad Eq.14$$

where ψ^{pol} refers to the molecule in solution (R and O) wavefunction, $\hat{H}$ and $\hat{V}$ the Hamilton operator in vacuo and the solute-solvent interaction operator (derived from Equation 7). In the context of calculation of theoretical reduction, the development of protocols that enable to directly predict the theoretical reduction potentials with a better accuracy without going through the separate calculation (gas-phase state and solvation energies) gained a significant interest in order to avoid the use of a thermodynamic cycle. The group of Mora-Diez, Cukrowski and Wetmore have calculated the Gibbs free energy in condensate-phase state based on the use ideal gas partition functions along with the rigid rotor harmonic oscillator and thermal and entropic corrections (Equation 15).[63,64,65,66,67] In the case of the Gibbs free energy of the gas-phase state, it correspond to the energy of the molecule (O and R) in that state in conjunction

with another thermal and entropic correction (G^{corr}_{gas} and G^{corr}_{soln}) (Equation 16). These thermal corrections relate to different contribution such as electronic, rotational, vibrational, and translational computed in gas phase (G^{corr}_{gas}) and in dielectric continuum, respectively.[68] In the same vein, Truhlar and Cramer[7] based on the SMD model found that the partition function related to the translation in the gas-phase state turns into the liberational energy in solution. This means that this contribution is cancelled in the solvation free energy independently to the behaviour of the solute as ideal gas in solution (Equation 17).

$$G^*_{solution} = \left\langle \psi^{pol} \middle| H' + \frac{V}{2} \middle| \psi^{pol} \right\rangle + G_{nes} + G^{corr}_{solution} \qquad Eq.15$$

$$G^*_{gas} = E_{gas} + G^{corr}_{gas} \qquad Eq.16$$

$$\Delta G^*_{solvation} = G^*_{solution} - G^*_{gas} \qquad Eq.17$$

The use of the equation 15 in SMD solvent model provides a possible solution to circumvent the use of a thermodynamic cycle and their incertitude related to the solvation energies. The group of Ho reopened the investigation and they could state that the direct calculation of free energies using as a solvent model, SMD is a reliable approximation to the thermodynamic cycle (Scheme 4).[68] There are numerous recent examples in which Gibbs energy associated with the half-reaction is calculated through the direct approach circumventing the separate calculation of the gas-phase state and the solvation energies. Representative examples were described in Chapter 1, subsection 1.4.2. “Examples of prediction of redox potential *via* DFT means using the direct approach.”.

2.2. Preliminary results.

After describing the methodology associated with our study, the preliminary results of the *in silico* study about the monoelectronic reduction of NHC-CO_2-based adducts, in particular, about the estimation of theoretical reduction potentials related to the NHC-CO_2-based adducts.

2.2.1. NHC-CO_2 adducts.

Firstly, we studied the influence of the *N*-Heterocyclic carbene (NHC) in the monoelectronic reduction of NHC-CO_2 adducts. In this work, we planned to estimate the reduction potential of a collection of diaminocarbene NHC-CO_2-based adducts bearing different *N*-groups along with other types of NHC-based species (**1**-**8**) (Scheme 1).

Based on the "direct approach", the Gibbs energy associated to the monoreduction of NHC-CO_2 adducts enables the estimation of an absolute reduction potential for each NHC-CO_2 adduct (**1**-**8**, Scheme 1). The next step is to reference it with respect to either a reference electrode or a redox couple. The most widely used reference electrodes are the standard hydrogen electrode (SHE) and the saturated calomel electrode (SCE). In the literature, the absolute reduction potential of SHE, E^{red}_{SHE}, has been theoretically determined by diverse means. Nevertheless, it can vary from 4.05 V to 4.44 V depending on the used parameters, such as proton Gibbs energy and surface potential among others.[69,70,71,72,73] The theoretical reduction potential of SCE is dependent on the SHE which may complicate the assessment of accurate reduction potentials. In order to circumvent any possible source of inaccuracies, we decided to find another alternative that did not depend on the SHE. Coote, Namazian and co-workers performed a study about the determination of the theoretical reduction potential of the redox couple, ferrocenium/ferrocene ($Fc^{+/0}$), in different non-aqueous solvents at different levels of theory. They reported reduction potentials at 4.988 V (acetonitrile), 4.927 V (dichloroethane) and 5.043 V (DMSO).[74] Other report from the group of Mikkelsen estimated its reduction potentials at 4.780 V in dichloromethane.[75] In this work, all absolute reduction potentials were referenced to ferrocene, 4.988 V (for acetonitrile) and 4.780 V (for dichloromethane).

Table 1. Theoretical reduction potential of **1**-**8** adducts versus $Fc^{+/0}$ in acetonitrile using M06-2X-D3 and B3LYP-D3 as a level of theory.

Compounds	M06-2X-D3		B3LYP-D3	
	ΔG_{red}/ kcal·mol^{-1}	E_{red} vs $Fc^{+/0}$/V	ΔG_{red}/ kcal·mol^{-1}	E_{red} vs $Fc^{+/0}$/V
Free CO_2	-49.2	-2.85	-46.1	-2.99
1	-38.3	-3.33	-38.6	-3.32
2	-34.6	-3.49	-35.1	-3.47
3	-34.5	-3.49	-34.1	-3.51
4	-48.0	-2.90	-48.2	-2.90
5	-44.8	-3.04	-44.9	-3.04
6	-58.9	-2.43	-59.3	-2.42
7	-51.8	-2.74	-52.4	-2.72
8	-58.1	-2.47	-55.5	-2.58

A clear tendency in the reduction potential of the adducts can observed using M06-2X-D3 functional. In NHC-CO_2-based systems whose *N*-substituents are alkyl groups such as methyl (**1**), tert-butyl (**2**) and adamantyl (**3**) groups, their reduction potential is more negative than the reduction of a free CO_2 molecule, around -3 V vs $Fc^{+/0}$ (Table 1). In the case of diaminocarbene-based adducts with aryl derivatives as *N*-substituents (**4**-**6**, Table 1), the reduction potential of these species is more favourable than the reduction potential in precedent NHC-CO_2 adducts (**1**-**3,** Table 1). Only adduct **6** has a reduction potential less negative than the case of free CO_2. The use of NHCs whose *N*-substituents are aryl groups gave access to more accessible reduction potentials than in the case of adducts with alkyl groups as *N*-substituents. In other particular cases such as Enders carbene and ^{Cy}CAAC adducts, the reduction is more accessible than in the case of free carbon dioxide (Table 1).

Then, the B3LYP-D3 functional was tested in the estimation of reduction potentials of NHC-CO_2-based adducts. The functional does not have a significant impact on the reduction potential calculations with respect to the results assessed with M06-2X-D3 (Table 1). The adduct that presented the less negative reduction potential using both functionals is adduct **6**. This might be explained by the presence of strong electron-

withdrawing *N*-substituents (perfluorinated groups). Within all NHC-CO_2 adducts, the compound **8** exhibits the largest difference between the potentials evaluated with both functionals, 0.11 V (2.6 kcal·mol^{-1}).

2.2.2. NHC-CO_2-BR_3 adducts.

Subsequently, the influence of the addition of a borane was studied. We questioned if a borane (BR_3) would favour the reduction of NHC-CO_2 adducts at less negative reduction potentials. We envisaged the use of three different boranes with different Lewis acidities: the simplest borane BH_3 and two more acidic ones, BCl_3 and tris(pentafluorophenyl)borane, $B(C_6F_5)_3$.

2.2.2.1. NHC-CO_2-BH_3 adducts.

Due to the simplicity of this borane, it was chosen as starting point of this study. It would allow the access to the corresponding reduction potential with a lower computational cost compared to other boranes. The corresponding adducts will be numbered as in Scheme 1 plus '-BH_3'. As example, the resulting adduct after the addition of BH_3 to **1**, it would be defined as **1-BH_3**.

N-Alkyl groups

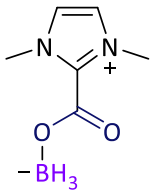

(**1-BH_3**)

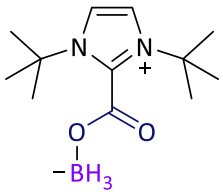

(**2-BH_3**)

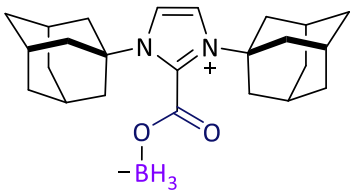

(**3-BH_3**)

M06-2X-D3	-2.65 (-53.9)	-2.89 (-48.3)	-2.90 (-48.1)
B3LYP-D3	-2.64 (-54.2)	-2.85 (-49.3)	-2.89 (-48.3)

N-Aryl groups

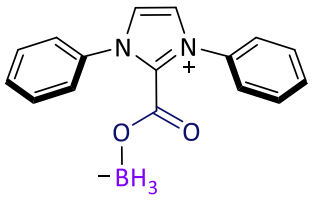

(**4-BH_3**)

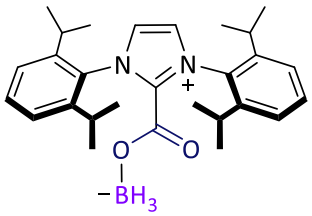

(**5-BH_3**)

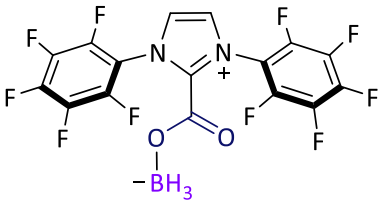

(**6-BH_3**)

M06-2X-D3	-2.36 (-60.5)	-2.37 (-60.3)	-1.86 (-72.1)
B3LYP-D3	-2.34 (-61.1)	-2.39 (-59.9)	-1.93 (-70.5)

Enders and ^{Cy}CAAC-type NHCs

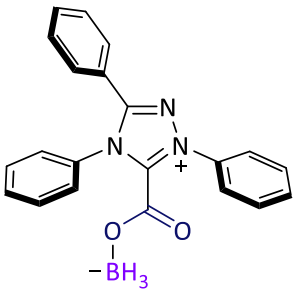

(**7-BH_3**)

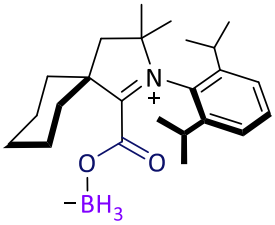

(**8-BH_3**)

M06-2X-D3	-2.05 (-67.8)	-1.87 (-71.9)
B3LYP-D3	-2.01 (-68.6)	-1.87 (-71.9)

Scheme 4. Studied NHC-CO_2-BH_3 adducts with their theoretical reduction potential and the reduction Gibbs energy (in brackets) in acetonitrile with M06-2X-D3 and B3LYP-D3 in blue and orange respectively. The potentials are in volts (V) versus $Fc^{+/0}$ and the Gibbs energies in kcal·mol^{-1}.

As shown in Scheme 2, the tendency in the reduction potential does not change with respect to adducts in the absence of any borane (**1**-**8**, Scheme 1). Even more importantly, the addition of a borane presents a beneficial impact in the monoelectronic reduction of NHC-CO_2 adducts (**1**-**8**, Scheme 1). With the addition of a borane, these adducts ((**1**-**8**)-$\mathbf{BH_3}$, Scheme 4) present a higher reduction potential (less negative) than NHC-CO_2 adducts (**1**-**8**, Scheme 1). At this stage, the reduction potential of adducts (**1**-**8**)-$\mathbf{BH_3}$ are less negative than in the case of the free CO_2 molecule. As in NHC-CO_2 adducts, both functionals, B3LYP-D3 and M06-2X-D3 report similar reduction potentials between them. The NHC-CO_2-BH_3 adduct which present the less negative reduction potential is **6-$\mathbf{BH_3}$**, followed closely by **8-$\mathbf{BH_3}$**. The largest difference between theoretical reduction potential estimated by both functional is **6-$\mathbf{BH_3}$** (0.07 V, 1.6 kcal·mol^{-1}).

2.2.2.2. NHC-CO_2-BCl_3 adducts.

As it was evidenced that it exists an impact in the reduction potentials of NHC-CO_2-based adducts, we also questioned if increasing the Lewis acidity of the borane could improve the obtained reduction potentials. The results are in Scheme 5.

N-Alkyl groups

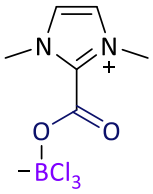

(**1-BCl_3**)

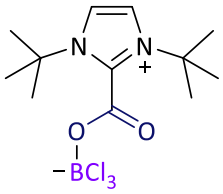

(**2-BCl_3**)

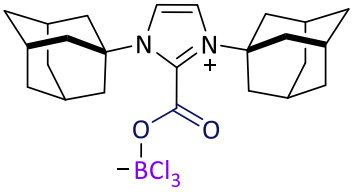

(**3-BCl_3**)

M06-2X-D3	-2.27 (-62.7)	-2.62 (-54.7)	-2.74 (-51.8)
B3LYP-D3	-2.24 (-63.3)	-2.58 (-55.4)	-2.68 (-53.2)

N-Aryl groups

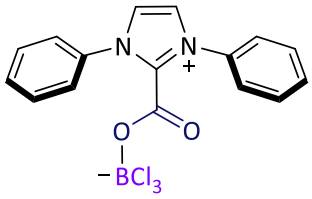

(**4-BCl_3**)

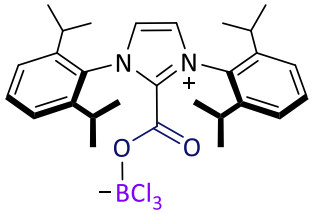

(**5-BCl_3**)

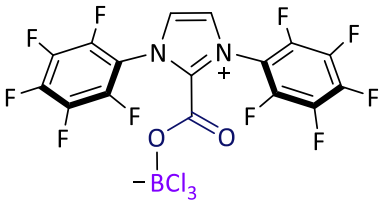

(**6-BCl_3**)

M06-2X-D3	-2.04 (-68.0)	-2.08 (-67.0)	-1.53 (-79.8)
B3LYP-D3	-2.06 (-67.6)	-2.08 (-67.0)	-1.60 (-78.2)

Enders and ^{Cy}CAAC-type NHCs

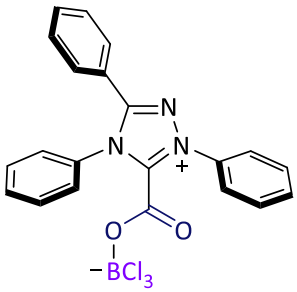

(**7-BCl_3**)

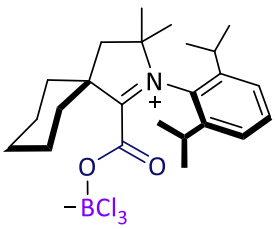

(**8-BCl_3**)

M06-2X-D3	-1.82 (-73.1)	-1.49 (-80.7)
B3LYP-D3	-1.79 (-73.8)	-1.57 (-78.8)

Scheme 5. Studied NHC-CO_2-BCl_3 adducts with their theoretical reduction potential and the reduction Gibbs energy (in brackets) in acetonitrile with M06-2X-D3 and B3LYP-D3 in blue and orange respectively. The potentials are in volts (V) and the Gibbs energies in kcal·mol^{-1}.

Increasing the Lewis acidity of the borane we can have access to even less negative reduction potentials (Scheme 5) than in the case of free CO_2, NHC-CO_2 (Table 1 and 2) and NHC-CO_2-BH_3 adduct (Scheme 4).

By changing the functional, the use of B3LYP-D3, as in previous examples, did not show a significant impact in the estimation of theoretical reduction potentials. If both functionals are compared (Scheme 5), the largest difference is 0.08 V (1.9 kcal·mol^{-1}) at the adduct **8-BCl_3**. The one that exhibits the less negative reduction potential is adduct **8-BCl_3** followed by **6-BCl_3**.

2.2.2.3. NHC-CO_2-$B(C_6F_5)_3$ adducts.

After the assessment of more accessible reduction potentials in NHC-CO_2-BR_3 adducts increasing the Lewis acidity of the borane ((**1**-**8**)-**BCl_3**). We got interested in the used of highly acidic boranes to experimentally synthesise adducts with these properties. Based on the literature, there is experimental proof that NHC-CO_2-$B(C_6F_5)_3$ adducts can be synthesised in moderate yields (Chapter 1, Section 1.3 "Synthesis of NHC-CO_2-BR_3 adducts."). We wondered if these (**1**-**8**)-**$B(C_6F_5)_3$** adducts exhibited a similar behaviour to their analogous adducts, (**1**-**8**)-**BCl_3**.

N-Alkyl groups

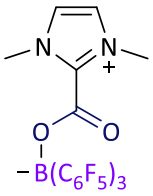

(1-B(C_6F_5)$_3$)

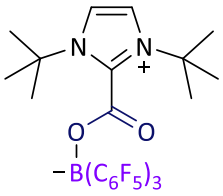

(2-B(C_6F_5)$_3$)

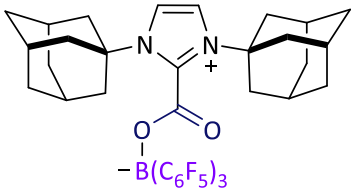

(3-B(C_6F_5)$_3$)

M06-2X-D3	-2.46 (-58.4)	-2.41 (-59.4)	-2.47 (-58.0)
B3LYP-D3	-2.45 (-58.6)	-2.46 (-58.2)	-2.53 (-56.7)

N-Aryl groups

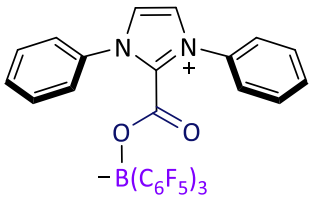

(4-B(C_6F_5)$_3$)

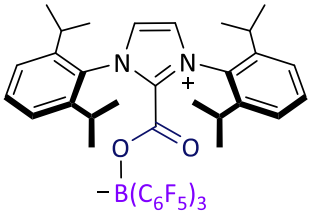

(5-B(C_6F_5)$_3$)

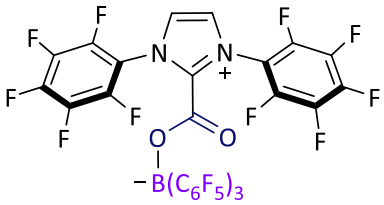

(6-B(C_6F_5)$_3$)

M06-2X-D3	-2.25 (-63.1)	-2.17 (-65.0)	-1.73 (-75.2)
B3LYP-D3	-2.37 (-60.3)	-2.28 (-62.5)	-1.72 (-75.4)

Enders and ^{Cy}CAAC-type NHCs

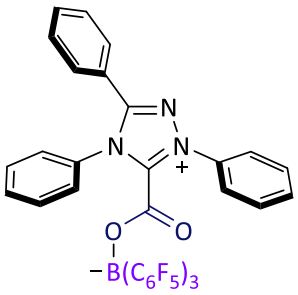

(7-B(C_6F_5)$_3$)

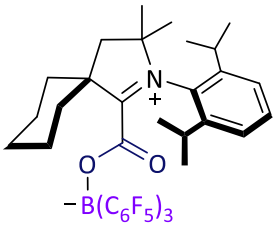

(8-B(C_6F_5)$_3$)

M06-2X-D3	-1.91 (-71.1)	-1.60 (-78.1)
B3LYP-D3	-1.98 (-69.4)	-1.75 (-74.7)

Scheme 4. Studied NHC-CO_2-B(C_6F_5)$_3$ adducts with their theoretical reduction potential and the reduction Gibbs energy (in brackets) in acetonitrile with M06-2X-D3 and B3LYP-D3 in blue and orange respectively. The potentials are in volts (V) and the Gibbs energies in kcal·mol^{-1}

As shown in Scheme 4, the reduction potential of NHC-CO_2-$B(C_6F_5)_3$ adducts (**1**-**8**)-**$B(C_6F_5)_3$** is slightly under the reduction potential of NHC-CO2-BCl_3. Despite this fact, the reduction potential of (**1**-**8**)-**$B(C_6F_5)_3$** are more accessible than in the case of NHC-CO_2 (**1**-**8**) adducts and free molecule of CO_2. The reduction potential in (**1**-**8**)-**$B(C_6F_5)_3$** adducts does not strongly depend on the choice of the functional, B3LYP-D3 and M06-2X-D3. Nevertheless, the reduction potential of the adduct **8-$B(C_6F_5)_3$** calculated using M06-2X-D3 as a functional significantly differs from the one calculated based on the B3LYP-D3. The difference is of 0.15 V (3.4 kcal·mol^{-1}) between both functionals. The adduct that exhibit the less negative reduction potential is **8-$B(C_6F_5)_3$** closely followed by **6-$B(C_6F_5)_3$**.

2.3. Conclusions

After this preliminary study about the estimation of reduction potentials in NHC-CO_2-based adducts, some conclusions can be drawn.

1. Within the studied functionals, M06-2X-D3 and B3LYP-D3 do generally provide similar reduction Gibbs energies (reduction potentials) for a same adduct.
2. The monoelectronic reduction of CO_2 is influenced by the addition of a *N*-Heterocyclic Carbene (NHC). The diaminocarbene NHC-CO_2 adducts whose *N*-substituents are aryl groups (**4**-**6**) have associated a reduction potential less negative than those bearing alkyl groups (**1**-**3**) as a *N*-substituents.
3. The addition of a Lewis acid, such as borane, is fundamental to have access to less negative reduction potentials than in the case of free CO_2. NHC-CO_2-BR_3 adducts possess a less negative reduction potentials than NHC-CO_2 adducts in the absence of a borane.
4. Increasing the Lewis acidity of the borane, more accessible reduction potentials can be obtained.
5. The most promising adducts regarding their theoretical reduction potentials are ^{Cy}CAAC-based adducts (**8-BCl_3** and **8-$B(C_6F_5)_3$**).

In the next chapter, “Chapter 3: Experimental approach towards the one-electron reduction in NHC-CO_2-BR_3 adducts”, we will tackle the synthesis of a selection of NHC-CO_2-BR_3 adducts and the measurement of their reduction potential. This would enable

us to compare the reduction potentials assessed by DFT means to the experimental reduction potentials and then, determine the accuracy of the methodology.

2.4. References

(1) Frisch, M. J.; Trucks, G. W.; Schlegel, H. B.; Scuseria, G. E.; Robb, M. A.; Cheeseman, J. R.; Scalmani, G.; Barone, V.; Petersson, G. A.; Nakatsuji, H.; Li, X.; Caricato, M.; Marenich, A. V.; Bloino, J.; Janesko, B. G.; Gomperts, R.; Mennucci, B.; Hratchian, H. P.; Ortiz, J. V.; Izmaylov, A. F.; Sonnenberg, J. L.; Williams; Ding, F.; Lipparini, F.; Egidi, F.; Goings, J.; Peng, B.; Petrone, A.; Henderson, T.; Ranasinghe, D.; Zakrzewski, V. G.; Gao, J.; Rega, N.; Zheng, G.; Liang, W.; Hada, M.; Ehara, M.; Toyota, K.; Fukuda, R.; Hasegawa, J.; Ishida, M.; Nakajima, T.; Honda, Y.; Kitao, O.; Nakai, H.; Vreven, T.; Throssell, K.; Montgomery, J. A., Jr; Peralta, J. E.; Ogliaro, F.; Bearpark, M. J.; Heyd, J. J.; Brothers, E. N.; Kudin, K. N.; Staroverov, V. N.; Keith, T. A.; Kobayashi, R.; Normand, J.; Raghavachari, K.; Rendell, A. P.; Burant, J. C.; Iyengar, S. S.; Tomasi, J.; Cossi, M.; Millam, J. M.; Klene, M.; Adamo, C.; Cammi, R.; Ochterski, J. W.; Martin, R. L.; Morokuma, K.; Farkas, O.; Foresman, J. B.; Fox, D. J. Gaussian 16 Rev. C.01, **2016**.

(2) Becke, A. D. Density-Functional Thermochemistry. III. The Role of Exact Exchange. *J. Chem. Phys.* **1993**, *98* (7), 5648–5652. https://doi.org/10.1063/1.464913.

(3) Raghavachari, K. Perspective on “Density Functional Thermochemistry. III. The Role of Exact Exchange.” *Theor. Chem. Acc. Theory Comput. Model. Theor. Chim. Acta* **2000**, *103* (3–4), 361–363. https://doi.org/10.1007/s002149900065.

(4) Miehlich, B.; Savin, A.; Stoll, H.; Preuss, H. Results Obtained with the Correlation Energy Density Functionals of Becke and Lee, Yang and Parr. *Chem. Phys. Lett.* **1989**, *157* (3), 200–206. https://doi.org/10.1016/0009-2614(89)87234-3.

(5) Zhao, Y.; Truhlar, D. G. The M06 Suite of Density Functionals for Main Group Thermochemistry, Thermochemical Kinetics, Noncovalent Interactions, Excited States, and Transition Elements: Two New Functionals and Systematic Testing of Four M06-Class Functionals and 12 Other Functionals. *Theor. Chem. Acc.* **2008**, *120* (1–3), 215–241. https://doi.org/10.1007/s00214-007-0310-x.

(6) Grimme, S.; Antony, J.; Ehrlich, S.; Krieg, H. A Consistent and Accurate *Ab Initio* Parametrization of Density Functional Dispersion Correction (DFT-D) for the 94 Elements H-Pu. *J. Chem. Phys.* **2010**, *132* (15), 154104. https://doi.org/10.1063/1.3382344.

(7) Marenich, A. V.; Cramer, C. J.; Truhlar, D. G. Universal Solvation Model Based on Solute Electron Density and on a Continuum Model of the Solvent Defined by the Bulk Dielectric Constant and Atomic Surface Tensions. *J. Phys. Chem. B* **2009**, *113* (18), 6378–6396. https://doi.org/10.1021/jp810292n.

(8) Clark, T.; Chandrasekhar, J.; Spitznagel, G. W.; Schleyer, P. V. R. Efficient Diffuse Function-Augmented Basis Sets for Anion Calculations. III. The 3-21+G Basis Set for First-Row Elements, Li-F. *J. Comput. Chem.* **1983**, *4* (3), 294–301. https://doi.org/10.1002/jcc.540040303.

(9) Pietro, W. J.; Francl, M. M.; Hehre, W. J.; DeFrees, D. J.; Pople, J. A.; Binkley, J. S. Self-Consistent Molecular Orbital Methods. 24. Supplemented Small Split-Valence Basis Sets for Second-Row Elements. *J. Am. Chem. Soc.* **1982**, *104* (19), 5039–5048. https://doi.org/10.1021/ja00383a007.

(10) Weigend, F.; Ahlrichs, R. Balanced Basis Sets of Split Valence, Triple Zeta Valence and Quadruple Zeta Valence Quality for H to Rn: Design and Assessment of Accuracy. *Phys. Chem. Chem. Phys.* **2005**, *7* (18), 3297. https://doi.org/10.1039/b508541a.

(11) *Chemcraft, Graphical software for visualization of quantum chemistry*. https://www.computationshemcraftprog.com.

(12) Knizia, G. *IboView, A program for chemical analysis*. http://iboview.org/index.html.

(13) Legault, C. Y. *CYLview, Visualization and analysis software for computational chemistry*. https://www.cylview.org/index.html.

(14) Neese, F. Software Update: The ORCA Program System—Version 5.0. *WIREs Comput. Mol. Sci.* **2022**, *12* (5), e1606. https://doi.org/10.1002/wcms.1606.

(15) Krishnan, R.; Binkley, J. S.; Seeger, R.; Pople, J. A. Self-consistent Molecular Orbital Methods. XX. A Basis Set for Correlated Wave Functions. *J. Chem. Phys.* **2008**, *72* (1), 650–654. https://doi.org/10.1063/1.438955.

(16) Stoll, S.; Schweiger, A. EasySpin, a Comprehensive Software Package for Spectral Simulation and Analysis in EPR. *J. Magn. Reson.* **2006**, *178* (1), 42–55. https://doi.org/10.1016/j.jmr.2005.08.013.

(17) Hohenberg, P.; Kohn, W. Inhomogeneous Electron Gas. *Phys. Rev.* **1964**, *136* (3B), B864–B871. https://doi.org/10.1103/PhysRev.136.B864.

(18) Harvey, J. *Computational Chemistry*; Oxford University Press, **2018**.

(19) Cramer, C. J. *Essentials of Computational Chemistry: Theories and Models*, 2nd ed.; Wiley: Chichester, West Sussex, England ; Hoboken, NJ, **2004**.

(20) Koch, W.; Holthausen, M. C. *A Chemist's Guide to Density Functional Theory*, 1st ed.; Wiley, **2001**. https://doi.org/10.1002/3527600043.

(21) Armstrong, G. *Five years of polling the computational chemistry community*. Chemistry Community. https://chemistrycommunity.nature.com/posts/46468-five-years-of-polling-the-computational-chemistry-community (accessed 2023-08-09).

(22) Roth, H. G.; Romero, N. A.; Nicewicz, D. A. Experimental and Calculated Electrochemical Potentials of Common Organic Molecules for Applications to Single-Electron Redox Chemistry. *Synlett* **2016**, *27* (5), 714–723. https://doi.org/10.1055/s-0035-1561297.

(23) Méndez-Hernández, D. D.; Gillmore, J. G.; Montano, L. A.; Gust, D.; Moore, T. A.; Moore, A. L.; Mujica, V. Building and Testing Correlations for the Estimation of One-Electron Reduction Potentials of a Diverse Set of Organic Molecules. *J. Phys. Org. Chem.* **2015**, *28* (5), 320–328. https://doi.org/10.1002/poc.3413.

(24) Wang, D.; Huang, S.; Wang, C.; Yue, Y.; Zhang, Q. Computational Prediction for Oxidation and Reduction Potentials of Organic Molecules Used in Organic Light-Emitting Diodes. *Org. Electron.* **2019**, *64*, 216–222. https://doi.org/10.1016/j.orgel.2018.10.038.

(25) Lee, Jae-Beom; Hwang, Sungu. Density Functional Theoretical Study on the Reduction Potentials of Catechols in Water. *Bull. Korean Chem. Soc.* **2012**, *33* (11), 3889–3890. https://doi.org/10.5012/BKCS.2012.33.11.3889.

(26) Prata-Duque, A.; Pinto, T.; Serpa, C.; Caridade, P. *Performance of Functionals and Basis Sets in DFT Calculation of Organic Compounds Redox Potentials*; preprint; Preprints, **2022**. https://doi.org/10.22541/au.165820504.41485770/v1.

(27) Bhattarai, S.; Mareta, P.; Crawford, P. W.; Kessler, J. M.; Ragain, C. M. Improved Computational Prediction of the Electrochemical Reduction Potential of Twenty 3-Aryl-Quinoxaline-2-Carbonitrile 1,4-Di-N-Oxide Derivatives. *Computation* **2023**, *11* (1), 9. https://doi.org/10.3390/computation11010009.

(28) Zandler, M. E.; D'Souza, F. The Remarkable Ability of B3LYP/3-21G(*) Calculations to Describe Geometry, Spectral and Electrochemical Properties of Molecular and Supramolecular Porphyrin–Fullerene Conjugates. *Comptes Rendus Chim.* **2006**, *9* (7–8), 960–981. https://doi.org/10.1016/j.crci.2005.12.008.

(29) Martínez-Cifuentes, M.; Salazar, R.; Ramírez-Rodríguez, O.; Weiss-López, B.; Araya-Maturana, R. Experimental and Theoretical Reduction Potentials of Some Biologically Active Ortho-Carbonyl Para-Quinones. *Molecules* **2017**, *22* (4), 577. https://doi.org/10.3390/molecules22040577.

(30) *The Holy Bible*; Genesis 28:10–19.

(31) Car, R. Fixing Jacob's Ladder. *Nat. Chem.* **2016**, *8* (9), 820–821. https://doi.org/10.1038/nchem.2605.

(32) Kohn, W.; Sham, L. J. Self-Consistent Equations Including Exchange and Correlation Effects. *Phys. Rev.* **1965**, *140* (4A), A1133–A1138. https://doi.org/10.1103/PhysRev.140.A1133.

(33) Solomon, E. I.; Scott, R. A.; King, R. B. *Computational Inorganic and Bioinorganic Chemistry*; **2009**.

(34) Perdew, J. P.; Burke, K.; Ernzerhof, M. Generalized Gradient Approximation Made Simple. *Phys. Rev. Lett.* **1996**, *77* (18).

(35) Becke, A. D. Density-Functional Exchange-Energy Approximation with Correct Asymptotic Behavior. *Phys. Rev. A* **1988**, *38* (6), 3098–3100. https://doi.org/10.1103/PhysRevA.38.3098.

(36) Lee, C.; Yang, W.; Parr, R. G. Development of the Colle-Salvetti Correlation-Energy Formula into a Functional of the Electron Density. *Phys. Rev. B* **1988**, *37* (2), 785–789. https://doi.org/10.1103/PhysRevB.37.785.

(37) Tao, J.; Perdew, J. P.; Staroverov, V. N.; Scuseria, G. E. Climbing the Density Functional Ladder: Nonempirical Meta–Generalized Gradient Approximation Designed for Molecules and Solids. *Phys. Rev. Lett.* **2003**, *91* (14), 146401. https://doi.org/10.1103/PhysRevLett.91.146401.

(38) Stephens, P. J.; Devlin, F. J.; Ashvar, C. S.; Chabalowski, C. F.; Frisch, M. J. Theoretical Calculation of Vibrational Circular Dichroism Spectra. *Faraday Discuss.* **1994**, *99*, 103. https://doi.org/10.1039/fd9949900103.

(39) Zhang, I. Y.; Xu, X. On the Top Rung of Jacob's Ladder of Density Functional Theory: Toward Resolving the Dilemma of SIE and NCE. *WIREs Comput. Mol. Sci.* **2021**, *11* (1). https://doi.org/10.1002/wcms.1490.

(40) Del Ben, M.; Schütt, O.; Wentz, T.; Messmer, P.; Hutter, J.; VandeVondele, J. Enabling Simulation at the Fifth Rung of DFT: Large Scale RPA Calculations with Excellent Time to Solution. *Comput. Phys. Commun.* **2015**, *187*, 120–129. https://doi.org/10.1016/j.cpc.2014.10.021.

(41) Slater, J. C. Atomic Shielding Constants. *Phys. Rev.* **1930**, *36* (1), 57–64. https://doi.org/10.1103/PhysRev.36.57.

(42) Electronic Wave Functions - I. A General Method of Calculation for the Stationary States of Any Molecular System. *Proc. R. Soc. Lond. Ser. Math. Phys. Sci.* **1950**, *200* (1063), 542–554. https://doi.org/10.1098/rspa.1950.0036.

(43) Stewart, R. F. Small Gaussian Expansions of Slater-Type Orbitals. *J. Chem. Phys.* **2003**, *52* (1), 431–438. https://doi.org/10.1063/1.1672702.

(44) Ditchfield, R.; Hehre, W. J.; Pople, J. A. Self-Consistent Molecular-Orbital Methods. IX. An Extended Gaussian-Type Basis for Molecular-Orbital Studies of Organic Molecules. *J. Chem. Phys.* **2003**, *54* (2), 724–728. https://doi.org/10.1063/1.1674902.

(45) Norjmaa, G.; Ujaque, G.; Lledós, A. Beyond Continuum Solvent Models in Computational Homogeneous Catalysis. *Top. Catal.* **2022**, *65* (1–4), 118–140. https://doi.org/10.1007/s11244-021-01520-2.

(46) Onsager, L. Electric Moments of Molecules in Liquids. *J. Am. Chem. Soc.* **1936**, *58* (8), 1486–1493. https://doi.org/10.1021/ja01299a050.

(47) Bondi, A. Van Der Waals Volumes and Radii. *J. Phys. Chem.* **1964**, *68* (3), 441–451. https://doi.org/10.1021/j100785a001.

(48) Tao, J.-Y.; Mu, W.-H.; Chass, G. A.; Tang, T.-H.; Fang, D.-C. Balancing the Atomic Waistline: Isodensity-Based Scrf Radii for Main-Group Elements and Transition Metals. *Int. J. Quantum Chem.* **2013**, *113* (7), 975–984. https://doi.org/10.1002/qua.24065.

(49) Herbert, J. M. Dielectric Continuum Methods for Quantum Chemistry. *WIREs Comput. Mol. Sci.* **2021**, *11* (4). https://doi.org/10.1002/wcms.1519.

(50) Tomasi, J.; Persico, M. Molecular Interactions in Solution: An Overview of Methods Based on Continuous Distributions of the Solvent. *Chem. Rev.* **1994**, *94* (7), 2027–2094. https://doi.org/10.1021/cr00031a013.

(51) Liu, S.-C.; Zhu, X.-R.; Liu, D.-Y.; Fang, D.-C. DFT Calculations in Solution Systems: Solvation Energy, Dispersion Energy and Entropy. *Phys. Chem. Chem. Phys.* **2023**, *25* (2), 913–931. https://doi.org/10.1039/D2CP04720A.

(52) Rashin, A. A.; Honig, B. Reevaluation of the Born Model of Ion Hydration. *J. Phys. Chem.* **1985**, *89* (26), 5588–5593. https://doi.org/10.1021/j100272a006.

(53) Tomasi, J.; Mennucci, B.; Cammi, R. Quantum Mechanical Continuum Solvation Models. *Chem. Rev.* **2005**, *105* (8), 2999–3094. https://doi.org/10.1021/cr9904009.

(54) Cancès, E.; Mennucci, B.; Tomasi, J. A New Integral Equation Formalism for the Polarizable Continuum Model: Theoretical Background and Applications to Isotropic and Anisotropic Dielectrics. *J. Chem. Phys.* **1997**, *107* (8), 3032–3041. https://doi.org/10.1063/1.474659.

(55) Mennucci, B.; Tomasi, J. Continuum Solvation Models: A New Approach to the Problem of Solute's Charge Distribution and Cavity Boundaries. *J. Chem. Phys.* **1997**, *106* (12), 5151–5158. https://doi.org/10.1063/1.473558.

(56) Mennucci, B.; Cancès, E.; Tomasi, J. Evaluation of Solvent Effects in Isotropic and Anisotropic Dielectrics and in Ionic Solutions with a Unified Integral Equation Method: Theoretical Bases, Computational Implementation, and Numerical Applications. *J. Phys. Chem. B* **1997**, *101* (49), 10506–10517. https://doi.org/10.1021/jp971959k.

(57) Tomasi, J.; Mennucci, B.; Cancès, E. The IEF Version of the PCM Solvation Method: An Overview of a New Method Addressed to Study Molecular Solutes at the QM Ab Initio Level. *J. Mol. Struct. THEOCHEM* **1999**, *464* (1–3), 211–226. https://doi.org/10.1016/S0166-1280(98)00553-3.

(58) Pierotti, R. A. A Scaled Particle Theory of Aqueous and Nonaqueous Solutions. *Chem. Rev.* **1976**, *76* (6), 717–726. https://doi.org/10.1021/cr60304a002.

(59) Reiss, H.; Tully-Smith, D. M. Further Development of Scaled Particle Theory for Rigid Spheres: Application of the Statistical Thermodynamics of Curved Surfaces. *J. Chem. Phys.* **1971**, *55* (4), 1674–1689. https://doi.org/10.1063/1.1676297.

(60) Ho, J.; Coote, M.; Cramer, C.; Truhlar, D. Theoretical Calculation of Reduction Potentials; 2015; pp 229–259. https://doi.org/10.1201/b19122-8.

(61) Guerard, J. J.; Arey, J. S. Critical Evaluation of Implicit Solvent Models for Predicting Aqueous Oxidation Potentials of Neutral Organic Compounds. *J. Chem. Theory Comput.* **2013**, *9* (11), 5046–5058. https://doi.org/10.1021/ct4004433.

(62) Marenich, A. V.; Ho, J.; Coote, M. L.; Cramer, C. J.; Truhlar, D. G. Computational Electrochemistry: Prediction of Liquid-Phase Reduction Potentials. *Phys. Chem. Chem. Phys.* **2014**, *16* (29), 15068–15106. https://doi.org/10.1039/c4cp01572j.

(63) Govender, K. K.; Cukrowski, I. Density Functional Theory and Isodesmic Reaction Based Prediction of Four Stepwise Protonation Constants, as Log $K_H^{(n)}$, for Nitrilotriacetic Acid. The Importance of a Kind and Protonated Form of a Reference Molecule Used. *J. Phys. Chem. A* **2010**, *114* (4), 1868–1878. https://doi.org/10.1021/jp9092964.

(64) Govender, K. K.; Cukrowski, I. Density Functional Theory in Prediction of Four Stepwise Protonation Constants for Nitrilotripropanoic Acid (NTPA). *J. Phys. Chem. A* **2009**, *113* (15), 3639–3647. https://doi.org/10.1021/jp811044b.

(65) Brown, T. N.; Mora-Diez, N. Computational Determination of Aqueous pK_a Values of Protonated Benzimidazoles (Part 1). *J. Phys. Chem. B* **2006**, *110* (18), 9270–9279. https://doi.org/10.1021/jp055084i.

(66) Brown, T. N.; Mora-Diez, N. Computational Determination of Aqueous pK_a Values of Protonated Benzimidazoles (Part 2). *J. Phys. Chem. B* **2006**, *110* (41), 20546–20554. https://doi.org/10.1021/jp0639501.

(67) Przybylski, J. L.; Wetmore, S. D. Designing an Appropriate Computational Model for DNA Nucleoside Hydrolysis: A Case Study of 2'-Deoxyuridine. *J. Phys. Chem. B* **2009**, *113* (18), 6533–6542. https://doi.org/10.1021/jp810472q.

(68) Ho, J. Are Thermodynamic Cycles Necessary for Continuum Solvent Calculation of pK $_a$ s and Reduction Potentials? *Phys. Chem. Chem. Phys.* **2015**, *17* (4), 2859–2868. https://doi.org/10.1039/C4CP04538F.

(69) Trasatti, S. The Absolute Electrode Potential: An Explanatory Note: (Recommendations **1986**). https://doi.org/10.1515/iupac.58.0011.

(70) Fawcett, W. R. The Ionic Work Function and Its Role in Estimating Absolute Electrode Potentials. *Langmuir* **2008**, *24* (17), 9868–9875. https://doi.org/10.1021/la7038976.

(71) Kelly, C. P.; Cramer, C. J.; Truhlar, D. G. Aqueous Solvation Free Energies of Ions and Ion−Water Clusters Based on an Accurate Value for the Absolute Aqueous Solvation Free Energy of the Proton. *J. Phys. Chem. B* **2006**, *110* (32), 16066–16081. https://doi.org/10.1021/jp063552y.

(72) Kelly, C. P.; Cramer, C. J.; Truhlar, D. G. Single-Ion Solvation Free Energies and the Normal Hydrogen Electrode Potential in Methanol, Acetonitrile, and Dimethyl Sulfoxide. *J. Phys. Chem. B* **2007**, *111* (2), 408–422. https://doi.org/10.1021/jp065403l.

(73) Isse, A. A.; Gennaro, A. Absolute Potential of the Standard Hydrogen Electrode and the Problem of Interconversion of Potentials in Different Solvents. *J. Phys. Chem. B* **2010**, *114* (23), 7894–7899. https://doi.org/10.1021/jp100402x.

(74) Namazian, M.; Lin, C. Y.; Coote, M. L. Benchmark Calculations of Absolute Reduction Potential of Ferricinium/Ferrocene Couple in Nonaqueous Solutions. *J. Chem. Theory Comput.* **2010**, *6* (9), 2721–2725. https://doi.org/10.1021/ct1003252.

(75) Ree, N.; Andersen, C. L.; Kilde, M. D.; Hammerich, O.; Nielsen, M. B.; Mikkelsen, K. V. The Quest for Determining One-Electron Redox Potentials of Azulene-1-Carbonitriles by Calculation. *Phys. Chem. Chem. Phys.* **2018**, *20* (11), 7438–7446. https://doi.org/10.1039/C7CP08687C.

Chapter 3: Experimental approach towards the one-electron reduction in NHC-CO_2-BR_3 adducts.

This chapter comprises the experimental core of this research project. It has been divided into three well-defined subsections. Firstly, the synthesis and characterisation of NHC-CO_2-BR_3 (BR_3 = borane) adducts (3.1.). Upon their synthesis, the determination of their experimental reduction will be exposed (3.2.). Finally, the chapter will conclude with the assessment of monoreduced species by chemical means and their corresponding characterisation (3.3.).

3.1. Synthesis and characterisation of NHC-CO_2-BR_3 adducts.

3.1.1. Context.

Chapter 2 describes an exploratory study whose final aim was to understand how NHC-CO_2-based species behave upon the addition of one single electron, avoiding the synthesis of a large collection of NHC-CO_2-based adducts. Nevertheless, to validate whether the followed computational methodology accurately describes the reduction in NHC-CO_2-based adducts, a significantly more reduced collection of NHC-based adducts was experimentally tested. Based on the theoretical results, the DFT analysis points towards the synthesis of NHC-CO_2-BR_3 adducts to have access to less negative reduction potentials (more favourable) in contrast to NHC-CO_2 adducts. According to DFT analysis, the addition of boranes that present a higher Lewis acidity (such as BCl_3 and $B(C_6F_5)_3$) in NHC-CO_2-based adducts should favour the one-electron reduction (less negative reduction potentials) than in cases where the borane is less acidic (such as BH_3) or inexistent (NHC-CO_2 adducts).

In the literature, reports (Chapter 1, section 1.3. "Synthesis of NHC-CO_2-BR_3 adducts") confirmed the possibility to experimentally isolate NHC-CO_2-BR_3 adducts in which the NHC and the highly acidic borane are hindered inspired in a FLP (Frustrated Lewis Pair) approach in the presence of CO_2. Inspired by Tamm's work[1], we envisaged the synthesis of NHC-CO_2-$B(C_6F_5)_3$ adducts. In order to confirm if our theoretical methodology is suitable for the prediction of reduction potentials in NHC-based adducts regardless the electronic properties of the NHC, the choice of the NHC was not restricted to solely one

sort of NHC. We synthesised I^tBu-CO_2-$B(C_6F_5)_3$ (**2-B(C_6F_5)$_3$**, previously reported by Tamm[1]) and IAd-CO_2-$B(C_6F_5)_3$ (**3-B(C_6F_5)$_3$**) whose *N*-substituents are alkyl groups (tert-butyl groups and adamantyl groups respectively), IPr-CO_2-$B(C_6F_5)_3$ (**5-B(C_6F_5)$_3$**) with substituted aryl rings as *N*-tethered groups and finally ^{Cy}CAAC-CO_2-$B(C_6F_5)_3$ (**8-B(C_6F_5)$_3$**) inspired by previous works of Machan and Gilliard groups (^{Cy}CAAC-CO_2, **8**).[2] This would allow us to test our theoretical methodology in a diverse group of NHC-based systems.

3.1.2. Synthesis of NHC-CO_2-$B(C_6F_5)_3$ adducts (2-, 3-, 5-, 8-B(C_6F_5)$_3$).

In order to synthesise the previous adducts, we envisioned two different routes: either from free *N*-Heterocyclic Carbene (NHC) (**3'**) or from pre-synthesised NHC-CO_2 adducts (**2**, **5** and **8**) giving rise to poor to excellent yields (Scheme 1). As aforementioned, Tamm and colleagues disclosed the synthesis of I^tBu-CO_2-$B(C_6F_5)_3$ (**2-B(C_6F_5)$_3$**) based on a reaction with free carbene, I^tBu, and borane, $B(C_6F_5)_3$ under a CO_2 atmosphere provided *via* a balloon with 89 % yield. In order to determine if better yields could be obtained using an imidazolium carboxylate precursor, we attempted to perform the same reaction using I^tBu-CO_2 (**2**) instead of employing the free carbene, I^tBu, maintaining the rest of experimental parameters. We could not observe an improvement in the yield of the reaction (65 %). Upon recrystallisation, the yield decreased to 20 % (Scheme 1A). For the synthesis of analogous adduct bearing adamantyl groups as *N*-substituents (**3-B(C_6F_5)$_3$**), we increased the CO_2 pressure up to 2 atm thanks to a Fischer-Porter system. The reaction proceeded with 66%. No recrystallization was required (Scheme 1B). As for compound **2-B(C_6F_5)$_3$**, the synthesis of adduct **5-B(C_6F_5)$_3$** was performed employing the precoordinated-CO_2 precursor but at a lower temperature, -78 °C. The yield of the reaction was 29%, slightly higher than in **2-B(C_6F_5)$_3$** (20 %). This might be resulting from the slightly better solubility of the carboxylate precursor in toluene, IPr-CO_2 (**5**) than ItBu-CO_2 (**2**) (Scheme 1C). In the case of adduct ^{Cy}CAAC-CO_2-$B(C_6F_5)_3$ adduct, the synthesis was performed in CH_2Cl_2 due to its proven solubility and stability reported in the Machan's and Gilliard's work.[2] The reaction proceeded at room temperature under CO_2 atmosphere (2 atm) in a Fisher-Porter yielding 89 % of compound **8-B(C_6F_5)$_3$** without the need for recrystallization (Scheme 1D).

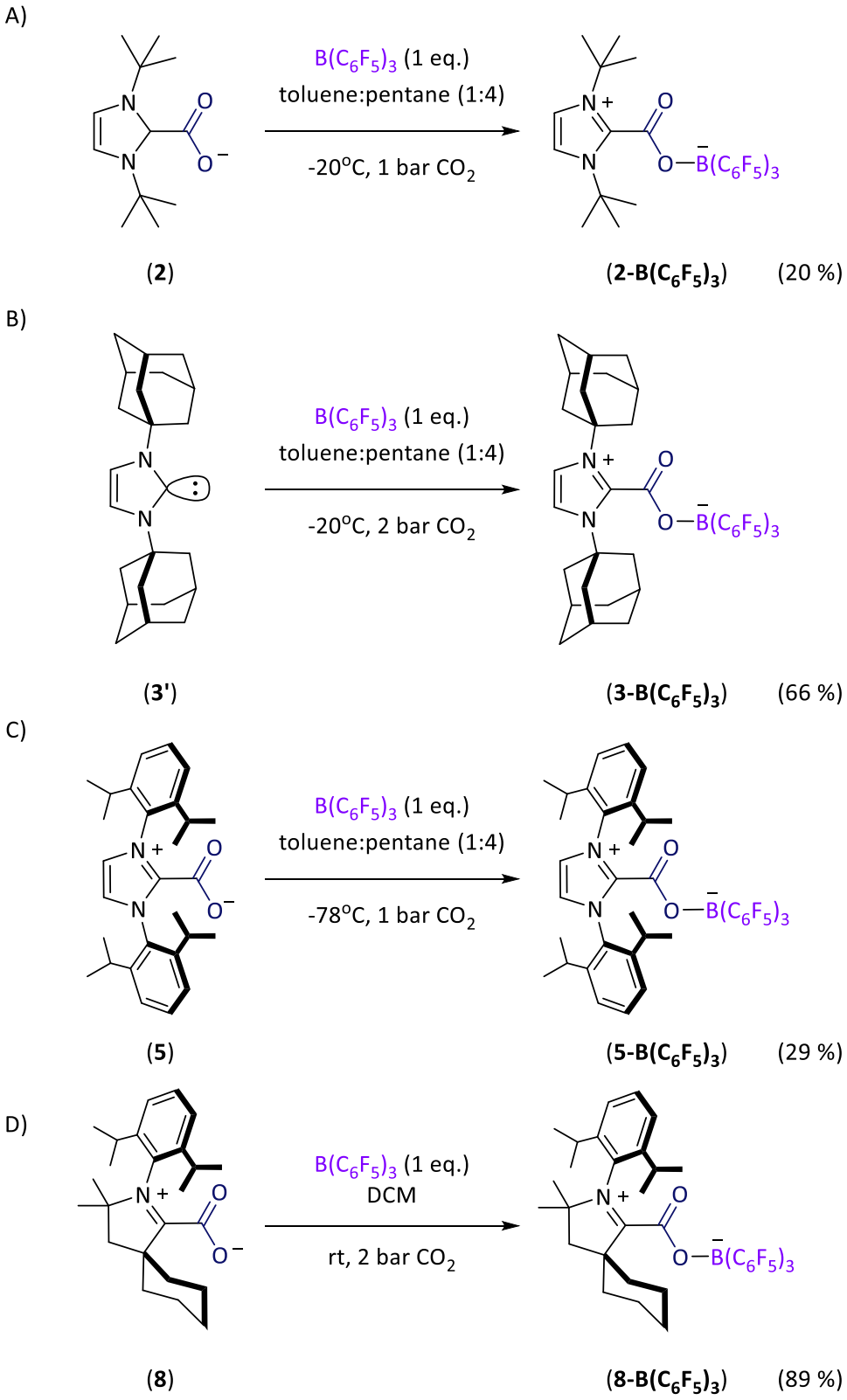

Scheme 1. Synthesised NHC-CO_2-$B(C_6F_5)_3$ adducts.

3.1.3. Characterisation of NHC-CO_2-$B(C_6F_5)_3$ adducts (2-, 3-, 5-, 8-$B(C_6F_5)_3$).

In the ^{13}C NMR spectra, the signal ascribed to the C from the CO_2 moiety appears at the following chemical shifts: δ = 156.0 ppm (**2-$B(C_6F_5)_3$**), δ = 161.1 ppm (**3-$B(C_6F_5)_3$**), δ = 152.8 ppm (**5-$B(C_6F_5)_3$**) and δ = 158.0 ppm (**8-$B(C_6F_5)_3$**) which are fairly similar to each other. These values are strongly shifted to downfield (by roughly 32 ppm) respect to free CO_2 (δ = 125.3 ppm, CD_2Cl_2).[3] The reason behind this large change in the chemical shift is the de-shielding phenomenon at the C atom from the carboxyl moiety, originating from the elimination of the rotationally symmetric π-system at the central C atom and its hybridization change (from C(sp) to C(sp^2)).[1] Another relevant proof of the desired NHC-CO_2-$B(C_6F_5)_3$ adducts was achieved by the ^{11}B NMR spectroscopy which evidenced characteristic signals at chemical shifts: δ = -3.9 ppm (**2-$B(C_6F_5)_3$**), δ = -3.8 ppm (**3-$B(C_6F_5)_3$**), δ = -3.4 ppm (**5-$B(C_6F_5)_3$**) and δ = -2.9 ppm (**8-$B(C_6F_5)_3$**) attesting to the tetrahedral coordination sphere around of the B atom from the $B(C_6F_5)_3$, and in agreement with the literature date for the previously reported analogous structures.[1,4] It is also important to note that the free $B(C_6F_5)_3$ exhibits a singlet signal at 59.3 ppm in in ^{11}B NMR in CD_2Cl_2.

Transparent single crystals suitable for X-Ray Diffraction (XRD) analysis of all synthesised adducts (**3-**, **5-**, **8-$B(C_6F_5)_3$**) were obtained from saturated CH_2Cl_2-pentane solutions at -36°C. The ORTEP diagrams are represented in Figures 1-3. The X-Ray diffraction analysis of **2-$B(C_6F_5)_3$** was previously reported by Tamm and colleagues.[1] As observed in Table 1, the B-O bond lengths in adducts (**3-**, **5-**, **8-$B(C_6F_5)_3$**) are slightly longer that the adduct previously reported by Tamm[1]. The same effect is associated to the distances of C=O and C-O bonds. The C-C bond lengths between the NHC and the CO_2 moiety in **3-**, **8-$B(C_6F_5)_3$** adducts are also slightly larger in respect to **2-$B(C_6F_5)_3$**. The adduct **5-$B(C_6F_5)_3$** exhibits the shortest distance (1.507(2) Å) within all synthesised adducts. This bond distance is associated with the steric hindrance originated from the *N*-substituents. The adduct **5-$B(C_6F_5)_3$** seems to present a lower steric bulkiness in respect to the other synthesised NHC-CO_2-$B(C_6F_5)_3$ adducts. Surprisingly, the dihedral (torsion) angles between the planes of the NHC and the CO_2 moieties (D(NHC-CO_2)) tends to set in a perpendicular position (**2-$B(C_6F_5)_3$**: 80.5(2)°, **3-$B(C_6F_5)_3$**: 76.7(3)° and **8-$B(C_6F_5)_3$**: 79.2(2)°) whilst **5-$B(C_6F_5)_3$** adduct is close to a coplanar position (7.3(2)°). A higher congestion at the carbenic

carbon "pocket" seems to favour the positioning of CO_2 moiety in a perpendicular position respect to the NHC. In all cases, the carboxylic group shows a trigonal planar coordination environment with angles around 130° (**2-B(C_6F_5)$_3$**: 130.1(2) °, **3-B(C_6F_5)$_3$**: 129.9(2) °, **3-B(C_6F_5)$_3$**: 128.8(1) ° and **8-B(C_6F_5)$_3$**: 129.3(1) °).

Table 1. Structural parameters of NHC-CO_2-B(C_6F_5)$_3$ (**2-**, **3-**, **5-**, **8-B(C_6F_5)$_3$**)

Structural parameters	**2-B(C_6F_5)$_3$**[1]	**3-B(C_6F_5)$_3$**	**5-B(C_6F_5)$_3$**	**8-B(C_6F_5)$_3$**
d(C=O)/Å	1.2972(19)	1.207(3)	1.2074(18)	1.2070(17)
d(C-O)/Å	1.2024(19)	1.298(3)	1.2980(17)	1.2977(17)
d(O-B)/Å	1.535(2)	1.540(3)	1.5363(18)	1.5492(18)
d($C_{carbenic}$-CO_2)/Å	1.516(2)	1.523(3)	1.5071(19)	1.5247(19)
a(CO_2)/°	130.09(15)	129.96(19)	128.78(13)	129.31(13)
D(NHC-CO_2)/°	80.5(2)	76.7(3)	7.3(2)	79.2(2)

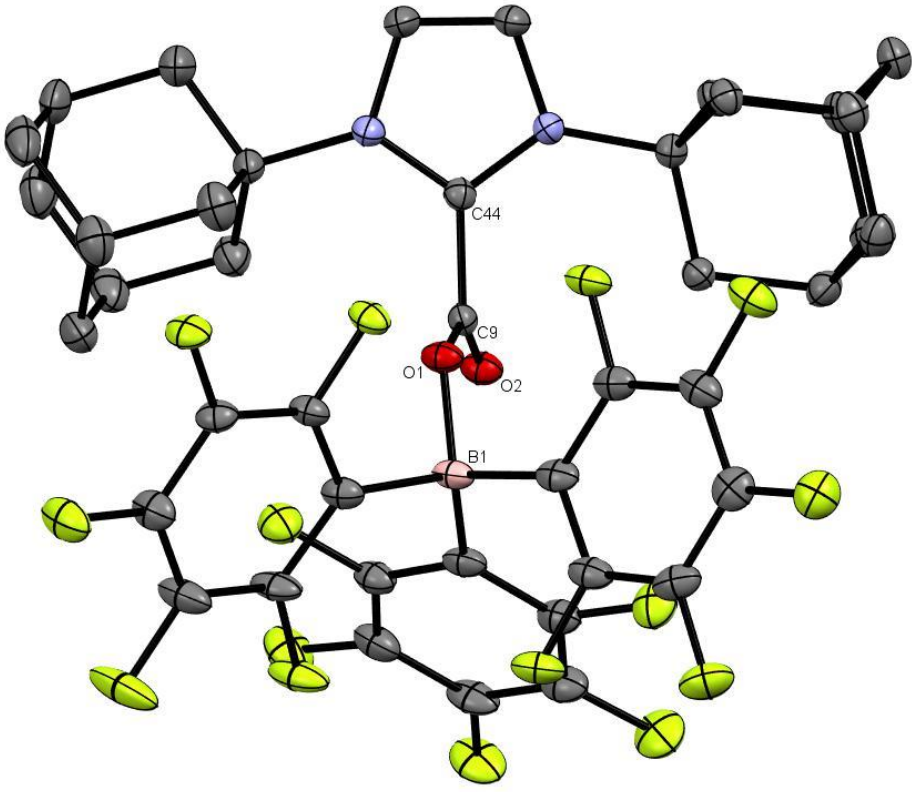

Figure 1. ORTEP diagram of compound **3-B(C_6F_5)$_3$**; for the sake of clarity hydrogen atoms are excluded, while thermal ellipsoids are set at 50% probability.

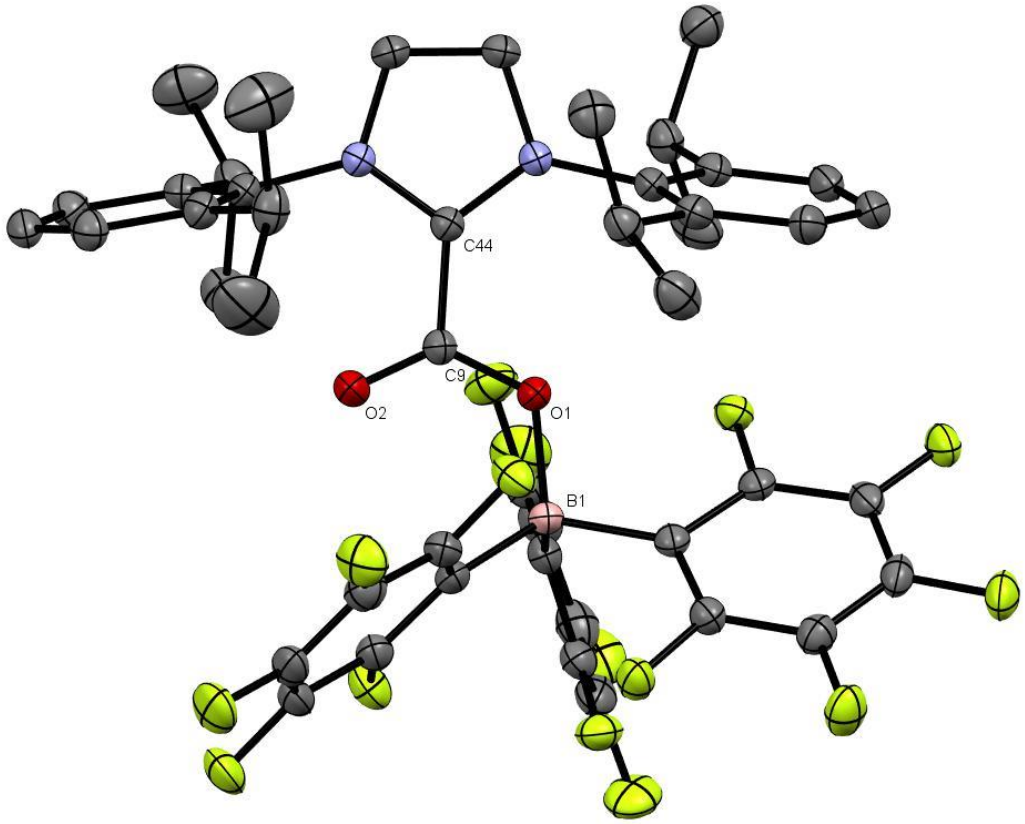

Figure 2. ORTEP diagram of compound **5-B(C_6F_5)$_3$**; for the sake of clarity hydrogen atoms are excluded, while thermal ellipsoids are set at 50% probability.

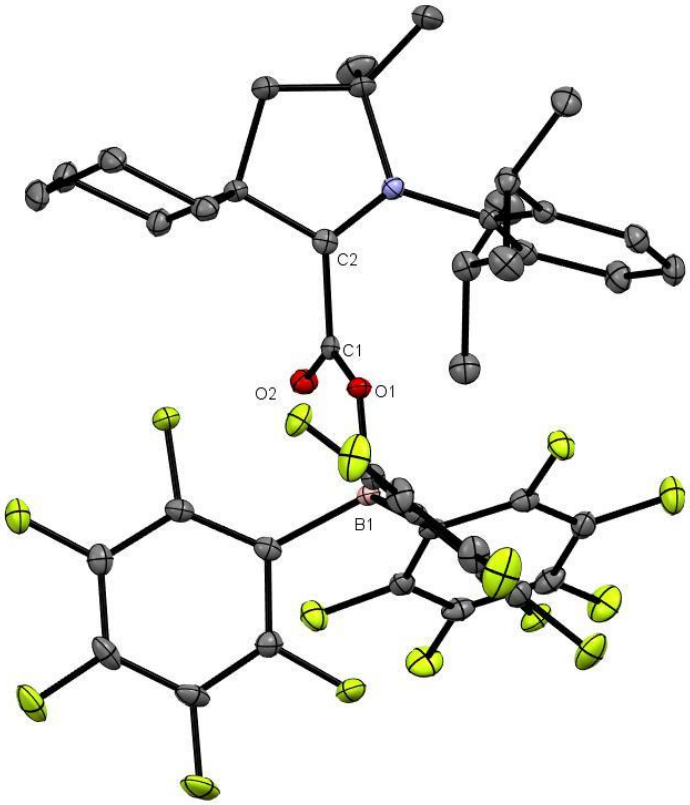

Figure 3. ORTEP diagram of compound **8-B(C_6F_5)$_3$**; for the sake of clarity hydrogen atoms are excluded, while thermal ellipsoids are set at 50% probability.

3.2. Measurement of reduction potentials in NHC-CO_2-B(C_6F_5)$_3$ adducts (2-, 3-, 5-, 8-B(C_6F_5)$_3$).

After the synthesis and characterisation of NHC-CO_2-B(C_6F_5)$_3$ (**2-**, **3-**, **5-**, **8-B(C_6F_5)$_3$**), we measured their reduction potential.

The measurements were performed by the cyclic voltammetry. Due to the compound stability in dichloromethane (the NMR spectra where registered in CH_2Cl_2), this solvent was employed in the measurement of the reduction potential of **2-**, **3-**, **5-**, **8-B(C_6F_5)$_3$** adducts. The active electrochemical window of dichloromethane (potential range accessible to an electrochemical system between which the solvent is neither oxidized nor reduced)[5] ranges from around -2 V to +2 V versus Saturated Calomel Electrode (SCE)[6]. Using as ferrocene ($Fe(Cp)_2$ symbolised as Fc) as a reference, the electrochemical window of dichloromethane is between -2.5 V and +1.5V. This potential range should be suitable for studying the reduction potentials of **2-**, **3-**, **5-** and **8-B(C_6F_5)$_3$**. As it will be

described in Chapter 4 in the subsection 4.1. "Which functional describes the reduction potential in NHC-CO_2-based adducts with a better accuracy and precision?", if our theoretical estimations are correct, the more negative limit of the reduction potential should be for compound **3-$B(C_6F_5)_3$** (M06-2X-D3: -2.30 V and B3LYP-D3: -2.36 V versus $Fc^{+/0}$ in dichloromethane) and the highest for compound **8-$B(C_6F_5)_3$** (M06-2X-D3: -1.29 V and B3LYP-D3: -1.58 V versus $Fc^{+/0}$ in dichloromethane). The supporting electrolyte, [n-Bu_4][PF_6] should be a good choice as it is highly soluble in dichloromethane, chemically and electrochemically inert in the experiment and is easy to purify (these three characteristics make a supporting electrolyte good for its use).[5] The electrode used as working electrode was the glassy carbon electrode (GCE) and SCE as a reference electrode. Nevertheless, the ferrocenium/ferrocene redox couple ($Fc^{+/0}$) was lately used as a reference instead of the SCE because the use of $Fc^{+/0}$ was more appropriate in the calculation of theoretical reduction potentials (see Chapter 2, section 2.2.1 "NHC-CO_2 adducts").[7] According to the literature, the reduction potential associated with the oxidation of the ferrocene to ferrocenium is 0.46 V versus SCE in dichloromethane. This relation between the potentials of SCE and ferrocene enables the expression of the reduction potentials of the adducts in respect to the ferrocene/ferrocenium redox couple.

After settling the experimental conditions, we tested the reproducibility of our system in the determination of the reduction potential of NHC-CO_2-based adducts. To our knowledge, it exists only one example in which the reduction potential of NHC-CO_2 adducts has been successfully determined. As previously mentioned in Chapter 1, subsection 1.2. "Reduction of NHC-CO_2-based species", Machan, Gilliard, and co-workers jointly reported the reduction potential of a ^{Cy}CAAC-CO_2 (**8**) at -2.08 V (in CH_3CN) and -2.15 V (in THF) versus $Fc^{+/0}$. We measured a reduction potential of ^{Cy}CAAC-CO_2 at -2.13 V versus $Fc^{+/0}$ in CH_2Cl_2 (Figure 4, purple curve). Compared to previous reduction potentials measured in MeCN and THF, we can observe that our system can provide a reduction potential in the same range. We then measured the reduction potentials of all studied adducts (**2-**, **3-**, **5-**, **8-$B(C_6F_5)_3$**). In the case of the adducts whose *N*-substituents were alkyl groups, tert-butyl (**2-$B(C_6F_5)_3$**) and adamantyl (**3-$B(C_6F_5)_3$**), they exhibited an irreversible behaviour with a reduction potential at -2.30 V (**2-$B(C_6F_5)_3$**) (Figure 4, orange

curve) and -2.44 V (**3-B(C_6F_5)$_3$**) (Figure 4, blue curve) versus $Fc^{+/0}$, respectively. This can be translated into the possible instability of the generated monoreduced NHC-CO_2-B(C_6F_5)$_3$. In both adducts (**2-B(C_6F_5)$_3$** and **3-B(C_6F_5)$_3$**), we applied an approximation to their obtained peak reduction potential (E^p_{red}) in order to assess an approximative half-wave reduction potential that will be later useful for comparison with the theoretical reduction potentials in order to evaluate the precision and accuracy of the employed functionals. More details regarding this approximation and the comparison between the experimental and the theoretical values will be given in Chapter 4, subsection 4.1.1. "Accuracy and precision of functionals". Upon the electroreduction of this adducts, a chemical transformation might by at play, that leads to either by-products or decomposition. In the case of compound **5-B(C_6F_5)$_3$**, which bears aryl derivatives as *N*-tethered groups, its reduction potential is at -2.08 V vs $Fc^{+/0}$ (Figure 4, brown curve). It is slightly less negative than in the previous cases (**2-** and **3-B(C_6F_5)$_3$**). In this example, this potential is associated to a pseudoreversible one-electron reduction in contrast to adducts **2-** and **3-B(C_6F_5)$_3$**. Finally, the compound **8-B(C_6F_5)$_3$** whose NHC moiety is based on a cyclic(alkyl)(amino) carbene (CAAC) exhibits a "duck-shaped" curve which is related to a reversible process. The reduction potential of this adduct was at -1.34 V vs $Fc^{+/0}$ (Figure 4, green curve). Within all synthesised adducts, **8-B(C_6F_5)$_3$** presented the most accessible reduction potential (less negative reduction potential). It is this example in which the one-electron reduction is more favoured than in other synthesised adducts (**8**, **2-**, **3-**, **5-B(C_6F_5)$_3$**). As predicted by our preliminary theoretical studies (Chapter 2), the presence of B(C_6F_5)$_3$ in an NHC-CO_2-B(C_6F_5)$_3$ adduct gives access to less negative reduction potentials. For instance, the addition of B(C_6F_5)$_3$ to the ^{Cy}CAAC-CO_2 (**8**) adduct results into a difference of 0.79 V respect to adduct **8**. The adduct **8-B(C_6F_5)$_3$** exhibits a reduction potential which is 0.79 V less negative than in the case of compound **8**.

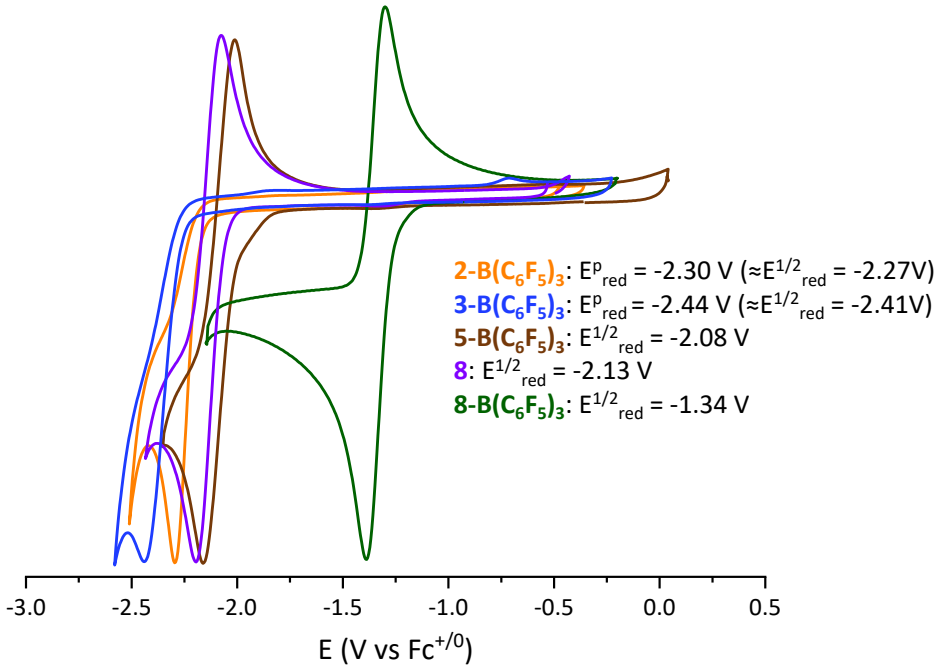

Figure 4. Normalised cyclic voltammogram of adducts **2-**, **3-**, **5-**, **8-B(C_6F_5)$_3$** at reducing potentials in CH_2Cl_2 versus $Fc^{+/0}$.

3.3. One electron reduction by chemical means: Synthesis and characterisation of monoreduced species.

After the synthesis and characterization of the previous compounds (**2-**, **3-**, **5-**, **8-B(C_6F_5)$_3$**), we envisioned the formation of the corresponding monoreduced species by chemical means. To our knowledge, only Machan and Gilliard groups[8] jointly reported the one-electron reduction of NHC-CO_2 adducts by chemical means.

Hitherto, the chemical reduction of NHC-CO_2-$B(C_6F_5)_3$ adducts remains inexistent in the literature. In our study, the chemical reactions were performed at room temperature in THF using a stoichiometric amount of KC_8 flakes, the reducing agent, in order to avoid the possibility of forming dianionic species. The potassium graphite (KC_8) is a string reducing agent, able to reduce benzenoids systems of low reduction potentials at -2.73 V versus SCE[9] in THF (-3.29 V versus $Fc^{+/0}$).[10] Therefore, the reduction of the studied adducts (**2-**, **3-**, **5-**, **8-B(C_6F_5)$_3$**) is thermodynamically favourable using KC_8. In the case of

2- and **3-B(C_6F_5)$_3$**, no change of colour was observed after 10 minutes upon addition of KC_8. The transparent solution turned into a black heterogeneous mixture after 12 hours (Scheme 2A and 2B). In contrast to latter, the colourless solution of **5-** and **8-B(C_6F_5)$_3$** immediately turned deep red (Scheme 2C) and yellow (Scheme 2D) respectively, upon the addition of the reductant reagent. The isolation of the adduct **[8-B(C_6F_5)$_3$(K)]$^\bullet$** *via* recrystallisation from a saturated THF-pentane solution yielded orange crystals at -37 °C suitable for X-ray diffraction analysis. In the case of **[8-B(C_6F_5)$_3$(K)]$^\bullet$**, the ^{Cy}CAAC moiety is completely planar (0.1 °) in respect to the CO_2 moiety unlike its neutral form (**8-B(C_6F_5)$_3$**) (79.2 °) (Table 2). There are other structural parameters that have been affected upon reduction such as the CO_2 angle and bond distances. Upon reduction, the carbon atom of the CO_2 shows a closer sp^2 hybridisation than in its neutral from. Furthermore, the C-O bonds are weakened whereas C-C bond between the NHC moiety and the CO_2 unit is strengthened (Table 2). The potassium ion coordinates to the free oxygen of the CO_2 moiety and interacts with the π-electronic system of the aryl ring and two THF molecules (Figure 5). Nevertheless, and despite several attempts, the isolation of adduct **[5-B(C_6F_5)$_3$(K)]$^\bullet$** as crystals was unsuccessful.

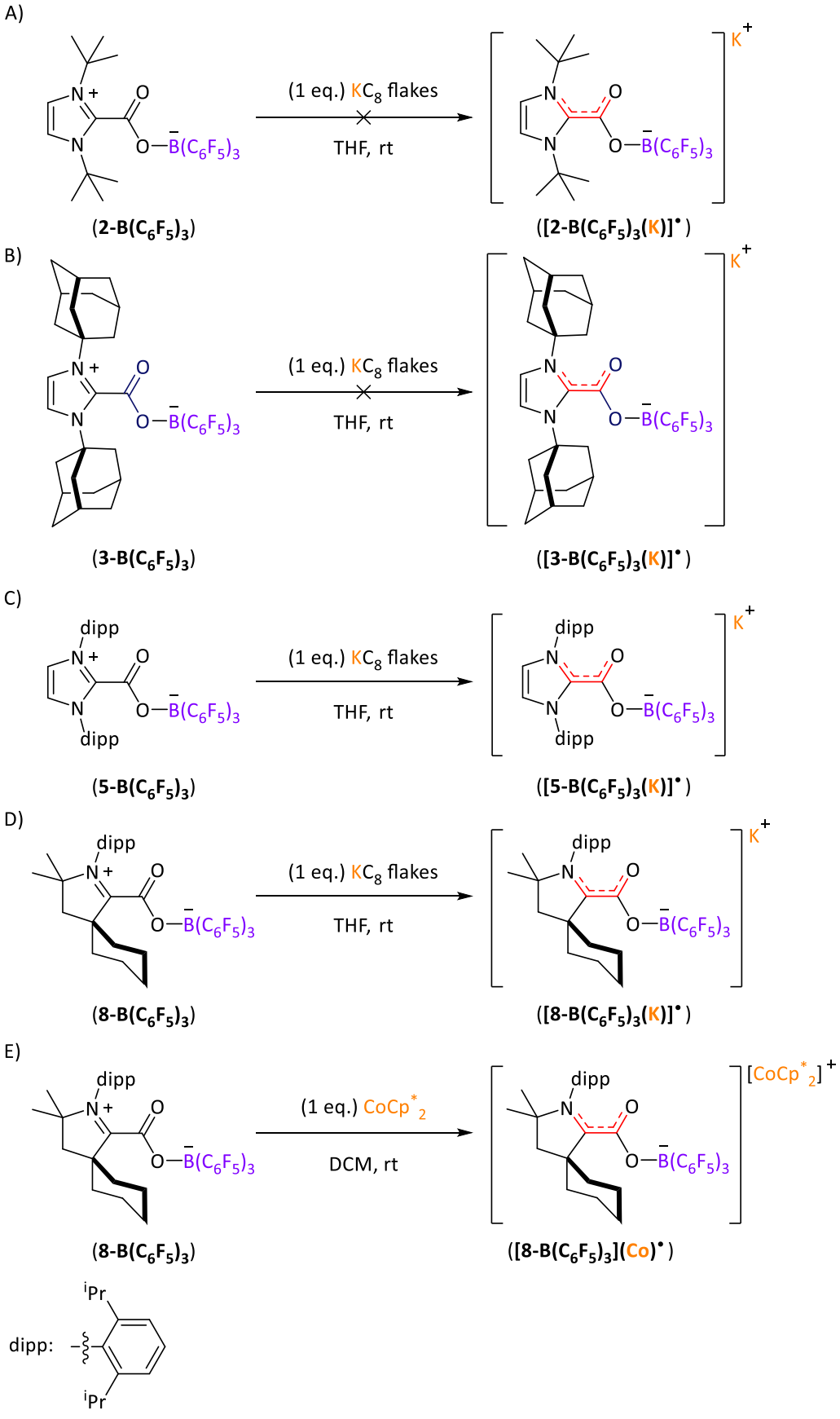

Scheme 2. Monoreduction of NHC-CO_2-$B(C_6F_5)_3$ adducts (**2-**, **3-**, **5-** and **8-B(C_6F_5)$_3$**).

Table 2. Structural parameters of ^{Cy}CAAC-CO_2-B(C_6F_5)$_3$ in its neutral (**8-B(C_6F_5)$_3$**) and monoreduced (**[8-B(C_6F_5)$_3$(K)]$^\bullet$**) form.

Structural parameters	**8-B(C_6F_5)$_3$**	**[8-B(C_6F_5)$_3$(K)]$^\bullet$**
d(C=O)/Å	1.2070(17)	1.241(3)
d(C-O(B))/Å	1.2977(17)	1.331(2)
d(O-B)/Å	1.5492(18)	1.486(3)
d($C_{carbenic}$-CO_2)/Å	1.5247(19)	1.433(3)
a(CO_2)/°	129.31 (13)	122.26(18)
D(NHC-CO_2)/°	79.2(2)	0.1(3)

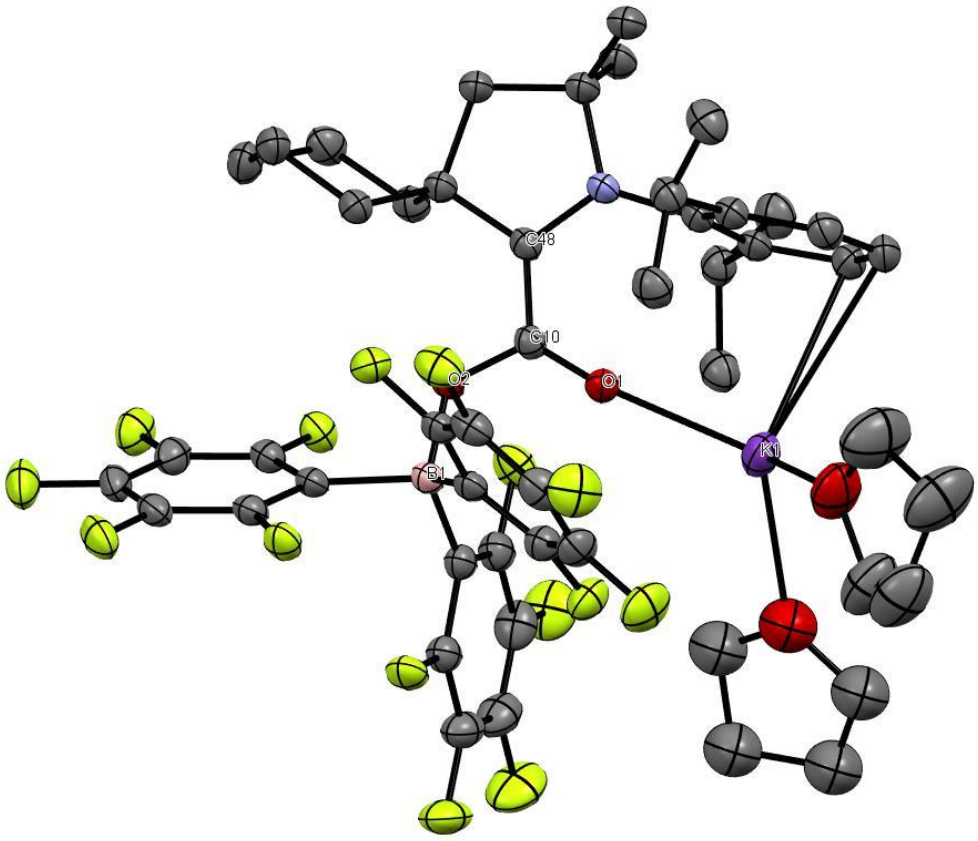

Figure 5. ORTEP diagram of compound **[8-B(C_6F_5)$_3$(K)]$^\bullet$**; for the sake of clarity hydrogen atoms and thermal ellipsoids are set at 50% probability.

In order to prove the formation and the electronic structure of the resulting monoreduced NHC-based systems, CW X-band EPR was performed to a diluted THF solutions (3.7 mM) at room temperature. As expected, we did not observe any signal

upon reduction in the case of adducts **2-** and **3-B(C_6F_5)$_3$** (Figure 6). The precedented cyclic voltammetry (CV) experiments presented in Figure 4 showed an irreversible redox behaviour in adducts **2-** and **3-B(C_6F_5)$_3$** in contrast with the other adducts (**5-** and **8-B(C_6F_5)$_3$**). The lack of reversibility in the CV curves is related to the instability of the monoreduced forms upon reduction.[11] Besides several attempts, this might explain the difficulties to measure an EPR signal for the respective monoreduced **[2-B(C_6F_5)$_3$(K)]$^\bullet$** and **[3-B(C_6F_5)$_3$(K)]$^\bullet$** adducts. For other adducts ([**5-B(C_6F_5)$_3$(K)]$^\bullet$** and **[8-B(C_6F_5)$_3$(K)]$^\bullet$**), an EPR signal could be obtained. In the case of the monoreduced CAAC-based adducts **[8(K)]$^\bullet$** (Figure 7, purple curve) and **[8-B(C_6F_5)$_3$(K)]$^\bullet$** (Figure 7, green curve)), the EPR signal consists of a triplet which corresponds to the coupling interaction between the unpaired electron and the nitrogen atom in the CAAC moiety. Considering the EPR coupling constant (a_N), the addition of $B(C_6F_5)_3$ presents a minor effect in the EPR coupling constant. It is slightly higher in adduct **[8(K)]$^\bullet$** than in **[8-B(C_6F_5)$_3$(K)]$^\bullet$** (Table 3). From this result, one can extrapolate that the spin density at the carbenic carbon is decreased with the addition of the borane. This fact might enable the localisation of spin density at the C from the CO_2 moiety. The discussion of the spin density in the monoreduced NHC-CO_2-based adducts will be discussed in Chapter 4.

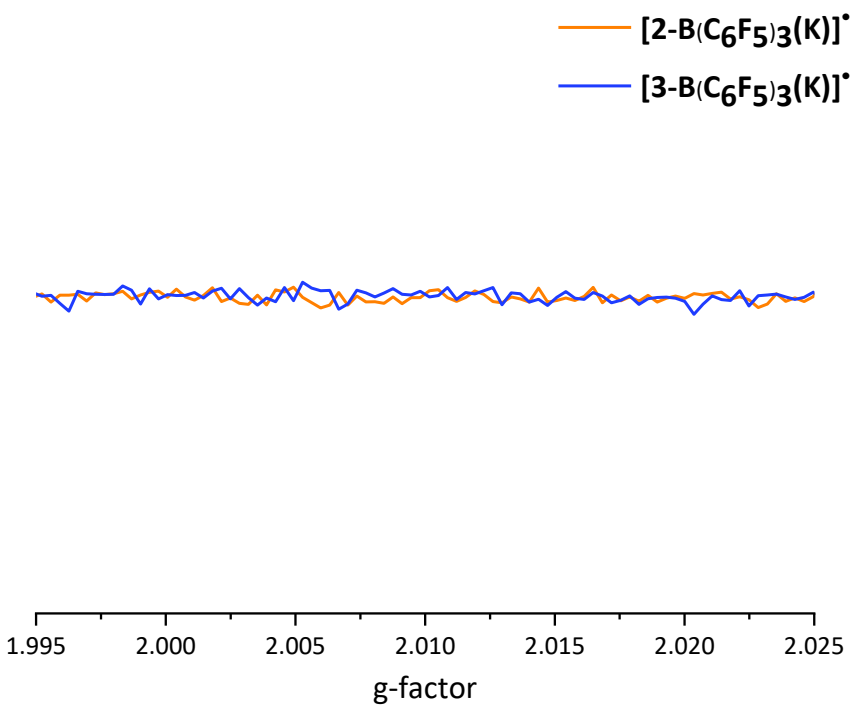

Figure 6. Continuous wave X-band EPR spectra of **[2-B(C$_6$F$_5$)$_3$(K)]•** and **[3-B(C$_6$F$_5$)$_3$(K)]•** taken on a 3.7 mM THF solution at rt.

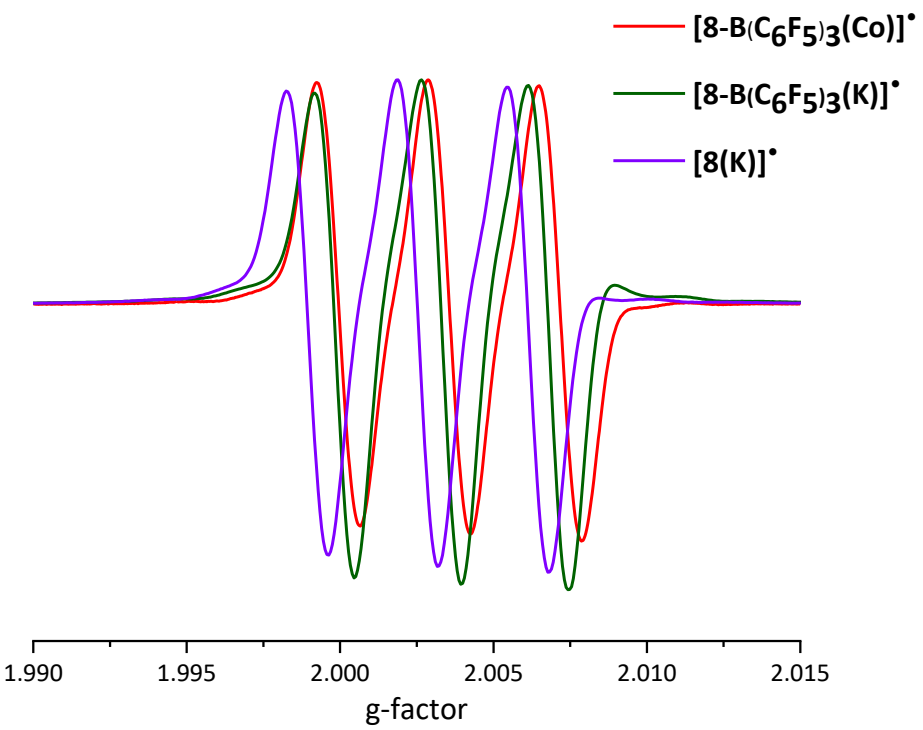

Figure 7. Continuous wave X-band EPR spectra of **[8(K)]•** and **[8-B(C_6F_5)$_3$(K)]•** taken on a 3.7 mM THF, and **[8-B(C_6F_5)$_3$(Co)]•** on 3.7 mM CH_2Cl_2 solution at rt.

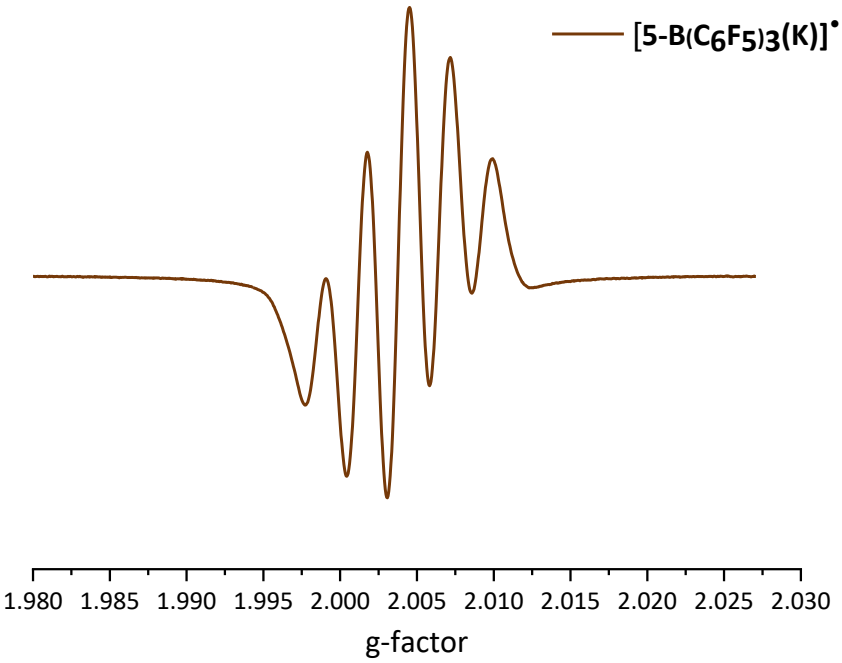

Figure 8. Continuous wave X-band EPR spectra of **[5-B(C$_6$F$_5$)$_3$(K)]$^{\bullet-}$** taken on a 3.7 mM THF solution at rt.

As aforementioned, there are only examples about chemical reduction in NHC-based system using very high reducing agents, alkali metals.[8] We also envisaged the use of a less reducing agent, decamethylcobaltocene (CoCp*$_2$), which still exhibits a less negative reduction potential (-1.94 V versus $Fc^{+/0}$ in CH_2Cl_2). Nevertheless, it is still thermodynamically capable of transferring one electron to the adduct **8-B(C$_6$F$_5$)$_3$** (-1.34 V versus $Fc^{+/0}$ in CH_2Cl_2) and generate the corresponding monoanionic radical, **[8-B(C$_6$F$_5$)$_3$(Co)]$^{\bullet}$** (Scheme 2E). The EPR experiment showed a very similar signal to the precedented measurement using KC_8 flakes as reductant (Figure 7, red curve and Table 3). The addition of B(C$_6$F$_5$)$_3$ enables the use of less harsh reducing agents to yield monoanionic radicals. In the case of the IPr-based adduct **[5-B(C$_6$F$_5$)$_3$(K)]$^{\bullet}$**, the EPR signal presented a quintet which corresponds to the interaction between the unpaired electron and the two equivalent nitrogen atoms from the NHC moiety (Figure 8). Regarding the coupling constant, it exhibits the lowest value within all studied adducts (4.45 G, Table 3). Following the precedented explanation for adduct **[8(K)]$^{\bullet}$** and **[8-B(C$_6$F$_5$)$_3$(K)]$^{\bullet}$**, one

can extrapolate that the spin density at the carbenic carbon is decreased with the addition of the borane and the change of NHC moiety. This fact might enable the localisation of spin density at the C from the CO_2 moiety. More details will be given in Chapter 4 section 4.3.3. "Spin density distribution and electron paramagnetic resonance (EPR)".

Table 3. EPR parameters of adducts **[8(K)]•**, **[5-B(C_6F_5)$_3$(K)]•**, **[5-B(C_6F_5)$_3$(K)]•**, **[8-B(C_6F_5)$_3$(Co)]•**.

	[5-B(C_6F_5)$_3$(K)]•	**[8(K)]•**	**[8-B(C_6F_5)$_3$(K)]•**	**[8-B(C_6F_5)$_3$(Co)]•**
g-factor	2.00375	2.00253	2.00347	2.00370
a_N/G	4.45	6.16	6.01	5.87

4.4. Conclusions.

After the synthesis of NHC-CO_2-B(C_6F_5)$_3$ adducts, determination of reduction potentials and the study of their related monoreduced species, some conclusions can be drawn.

1. Within all synthesised adducts, the diaminocarbene NHC-based adduct whose *N*-substituents are alkyl derivatives, **2-B(C_6F_5)$_3$** and **3-B(C_6F_5)$_3$** (tert-butyl and adamantyl groups, respectively) exhibit a more negative reduction potential than in the case of the NHC whose *N*-tethered groups are aryl derivatives (**5-B(C_6F_5)$_3$**). In terms of stability, in the case of **5-B(C_6F_5)$_3$** and **8-B(C_6F_5)$_3$**, they seem to exhibit a higher stability upon reduction than their analogous **2-B(C_6F_5)$_3$** and **3-B(C_6F_5)$_3$**.
2. The addition of B(C_6F_5)$_3$ to the adduct **8** is beneficial in the reduction process (increase the stability and the reduction potential). The cyclic voltammogram of **8-B(C_6F_5)$_3$** shows a text-book example of reversibility and a reduction potential of nearly one volt (0.79 V) more accessible than in the absence of any borane (**8**). The ^{Cy}CAAC-CO_2-B(C_6F_5)$_3$ (**8-B(C_6F_5)$_3$**) shows the less negative reduction potential within all synthesised adducts (-1.34 V versus $Fc^{0/+}$ in dichloromethane). Besides that, the addition of a B(C_6F_5)$_3$ enables the use of less harsh reducing agents to yield NHC-CO_2-based monoanionic radicals, **[8-B(C_6F_5)$_3$(Co)]•**.
3. The first EPR spectrum of a diamino-carbene-based **[5-B(C_6F_5)$_3$(K)]•** adduct has been registered thanks to stability that the borane offers to the NHC-CO_2 moiety.

In the next chapter, Chapter 4: "Theoretical analysis of the one-electron reduction in NHC-CO_2-based adducts", we evaluate based on computational techniques other parameters of interest that would ultimately allow us to rationalise how the NHC-based adducts behave after their one-electron reduction once the employed computational methodology is validated. Within these parameters, we can highlight the spin density distribution in monoreduced NHC-CO_2-based adducts, in particular, at the C from the CO_2 moiety and the orbital description of the neutral and monoreduced NHC-CO_2-based adducts among others.

4.5. References.

(1) Theuergarten, E.; Bannenberg, T.; Walter, M. D.; Holschumacher, D.; Freytag, M.; Daniliuc, C. G.; Jones, P. G.; Tamm, M. Computational and Experimental Investigations of CO_2 and N_2O Fixation by Sterically Demanding *N*-Heterocyclic Carbenes (NHC) and NHC/Borane FLP Systems. *J. Chem. Soc. Dalton Trans.* **2014**, *43* (4), 1651–1662. https://doi.org/10.1039/c3dt52742e.

(2) Lieske, L. E.; Freeman, L. A.; Wang, G.; Dickie, D. A.; Gilliard, R. J.; Machan, C. W. Metal-Free Electrochemical Reduction of Carbon Dioxide Mediated by Cyclic(Alkyl)(Amino) Carbenes. *Chem. - Eur. J.* **2019**, *25* (24), 6098–6101. https://doi.org/10.1002/chem.201900316.

(3) Fulmer, G. R.; Miller, A. J. M.; Sherden, N. H.; Gottlieb, H. E.; Nudelman, A.; Stoltz, B. M.; Bercaw, J. E.; Goldberg, K. I. NMR Chemical Shifts of Trace Impurities: Common Laboratory Solvents, Organics, and Gases in Deuterated Solvents Relevant to the Organometallic Chemist. *Organometallics* **2010**, *29* (9), 2176–2179. https://doi.org/10.1021/om100106e.

(4) Mömming, C. M.; Otten, E.; Kehr, G.; Fröhlich, R.; Grimme, S.; Stephan, D. W.; Erker, G. Reversible Metal-Free Carbon Dioxide Binding by Frustrated Lewis Pairs. *Angew. Chem. - Int. Ed.* **2009**, *48* (36), 6643–6646. https://doi.org/10.1002/anie.200901636.

(5) Leech, M. C.; Lam, K. A Practical Guide to Electrosynthesis. *Nat. Rev. Chem.* **2022**, *6* (4), 275–286. https://doi.org/10.1038/s41570-022-00372-y.

(6) Schotten, C.; Nicholls, T. P.; Bourne, R. A.; Kapur, N.; Nguyen, B. N.; Willans, C. E. Making Electrochemistry Easily Accessible to the Synthetic Chemist. *Green Chem.* **2020**, *22* (11), 3358–3375. https://doi.org/10.1039/D0GC01247E.

(7) Konezny, S. J.; Doherty, M. D.; Luca, O. R.; Crabtree, R. H.; Soloveichik, G. L.; Batista, V. S. Reduction of Systematic Uncertainty in DFT Redox Potentials of Transition-Metal Complexes. *J. Phys. Chem. C* **2012**, *116* (10), 6349–6356. https://doi.org/10.1021/jp300485t.

(8) Freeman, L. A.; Obi, A. D.; Machost, H. R.; Molino, A.; Nichols, A. W.; Dickie, D. A.; Wilson, D. J. D.; Machan, C. W.; Gilliard, R. J. Soluble, Crystalline, and Thermally Stable Alkali CO_2^- and Carbonite (CO_2^{2-}) Clusters Supported by Cyclic(Alkyl)(Amino) Carbenes. *Chem. Sci.* **2021**, *12* (10), 3544–3550. https://doi.org/10.1039/D0SC06851A.

(9) Ebert, L. B.; Mills, D. R.; Scanlon, J. C. The Interaction of Potassium with Graphite and Other Benzenoid Systems. *Mater. Res. Bull.* **1982**, *17* (10), 1319–1328. https://doi.org/10.1016/0025-5408(82)90168-4.

(10) Connelly, N. G.; Geiger, W. E. Chemical Redox Agents for Organometallic Chemistry. *Chem. Rev.* **1996**, *96* (2), 877–910. https://doi.org/10.1021/cr940053x.

(11) Elgrishi, N.; Rountree, K. J.; McCarthy, B. D.; Rountree, E. S.; Eisenhart, T. T.; Dempsey, J. L. A Practical Beginner's Guide to Cyclic Voltammetry. *J. Chem. Educ.* **2018**, *95* (2), 197–206. https://doi.org/10.1021/acs.jchemed.7b00361.

Chapter 4: Theoretical analysis of the one-electron reduction in NHC-CO_2-based adducts.

In this last chapter, we will firstly define which of the employed functional provide more accurate and precise reduction potentials in NHC-CO_2-based adducts, B3LYP-D3 or M06-2X-D3, with the aid of the experimental reduction potentials previously discussed in Chapter III. Once the functionals are benchmarked, other features related to NHC-CO_2-based species and their monoelectronic reduction will be disclosed such as how the structural parameters of all adducts influence the spin density distribution upon reduction, frontier orbital localisation and energy. Finally, the evolution of different parameters as their reduction potentials depending on the torsion angle between NHC and CO_2 moiety will also be described.

4.1. Which functional describes the reduction potential in NHC-CO_2-based adducts with a better accuracy and precision?

In this first section, we performed a study to conclude which of the tested functionals gives access to more accurate and precise reduction potentials based on the experimental reductions potentials described in the previous chapter (Chapter 3, section 3.2. "Measurement of reduction potentials in adducts NHC-CO_2-$B(C_6F_5)_3$ adducts (**2-**, **3-**, **5-**, **8-$B(C_6F_5)_3$**").

4.1.1. Accuracy and precision of functionals

In the previous chapter, the experimental reduction potential for all synthesised adducts (**8**, **2-**, **3-**, **5-**, **8-$B(C_6F_5)_3$**) was presented. In Chapter 3, we observed that compounds **2-$B(C_6F_5)_3$** and **3-$B(C_6F_5)_3$** exhibit an irreversible reduction wave. Their reduction potentials were defined as the peak potentials, E_p. In order to compare the experimental reduction potentials with the ones assessed by theoretical means (E^o_{red} that can be treated as $E^{1/2}_{red}$), an approximation was done consisting in subtracting 0.03 V, which resulted into an approximated half-wave reduction potential value, $E^{1/2}_{red}$ (**2-$B(C_6F_5)_3$**) = -2.41 V and

$E^{1/2}_{red}$ (**3-B(C_6F_5)$_3$**) = -2.27 V (Table 1). This value (0.03 V) originates from the peak-to-peak separation (ΔE_P, difference between the oxidation and reduction peak). An electrochemical curve is reversible only if ΔE_P between the oxidation and reduction peak is lower than 0.06 V at 25°C and the relation between oxidation and reduction intensities is close to the value one (i^{po}/i^{pr} = 1).[1] In organic solvents, the ΔE_P range could also be extended up to 0.1 V.

In Table 1, the experimental and the theoretical reduction potential along with their absolute error ($|\Delta E^{1/2}_{red}|$, Equation 1) are exposed for both functionals, M06-2X-D3 and B3LYP-D3. We can observe that the absolute maximal deviation (AMAX) observed is associated to adduct **8** in both functionals, 0.11 V (M06-2X-D3) and 0.24 V (B3LYP-D3). The mean absolute deviation (MAD, Equation 2) is 0.05 V and 0.09 V for M06-2X-D3 and B3LYP-D3, respectively. Based on the MAD, both functionals predict the reduction potentials of NHC-CO_2-based adducts with a good accuracy. Among the evaluated methods, both functionals gave MADs around 0.1 V (the usual value found in the literature as experimental error).[2]

$$\left|\Delta E_{1/2}\right| = \left|E_{1/2}^{theoretical} - E_{1/2}^{experimental}\right| \qquad (Eq.1)$$

$$MAD = N^{-1}\Sigma_{i=1}^{N}\left|\Delta E_{1/2,i}\right| \qquad (Eq.2)$$

Table 1. Theoretical reduction potential ($E^{1/2}_{red}$) of **2-B(C_6F_5)$_3$**, **3-B(C_6F_5)$_3$**, **5-B(C_6F_5)$_3$** and **8-B(C_6F_5)$_3$** versus $Fc^{+/0}$ redox couple in V for both functionals in dichloromethane. The deviation from the experimental reference ($|\Delta E^{1/2}_{red}|$) for each adduct is also given.

Density Functional	M06-2X-D3	B3LYP-D3	Experimental
$E^{1/2}_{red}$ (**2-B(C_6F_5)$_3$**)	-2.26	-2.30	-2.27
$\|\Delta E^{1/2}_{red}\|$ (**2-B(C_6F_5)$_3$**)	0.01	0.03	-
$E^{1/2}_{red}$ (**3-B(C_6F_5)$_3$**)	-2.30	-2.36	-2.41
$\|\Delta E^{1/2}_{red}\|$ (**3-B(C_6F_5)$_3$**)	0.11	0.05	-
$E^{1/2}_{red}$ (**5-B(C_6F_5)$_3$**)	-2.04	-2.10	-2.08
$\|\Delta E^{1/2}_{red}\|$ (**5-B(C_6F_5)$_3$**)	0.04	0.02	-
$E^{1/2}_{red}$ (**8-B(C_6F_5)$_3$**)	-1.29	-1.58	-1.34
$\|\Delta E^{1/2}_{red}\|$ (**8-B(C_6F_5)$_3$**)	0.05	0.24	-
MAD	0.05	0.09	-
AMAX	0.11	0.24	-

Additional statistical analysis was performed to confirm our choice of functional. Besides the MAD, the correlation between the computed absolute reduction potential versus the experimental one was also graphed (Figure 1). The parameters considered in this part of the study were the slope, the y-intercept and the corelation coefficient (R^2) (Table 2). The y-intercept should be equal to the value used to refer the absolute reduction potential to ferrocene (reference redox couple) $E^{o}_{abs,ox}$ ($Fc^{+/0}$) = 4.780 V.[2,3] This correlation is governed by Equation 12 from Chapter 1. As a reminder, it is as follows:

$$E^{o}_{red}(O/R\ vs.\ RE) = E^{o}_{abs,red}(O/R) - E^{o}_{abs,red}(RE) \qquad Eq.\,12, Chapter\ 1$$

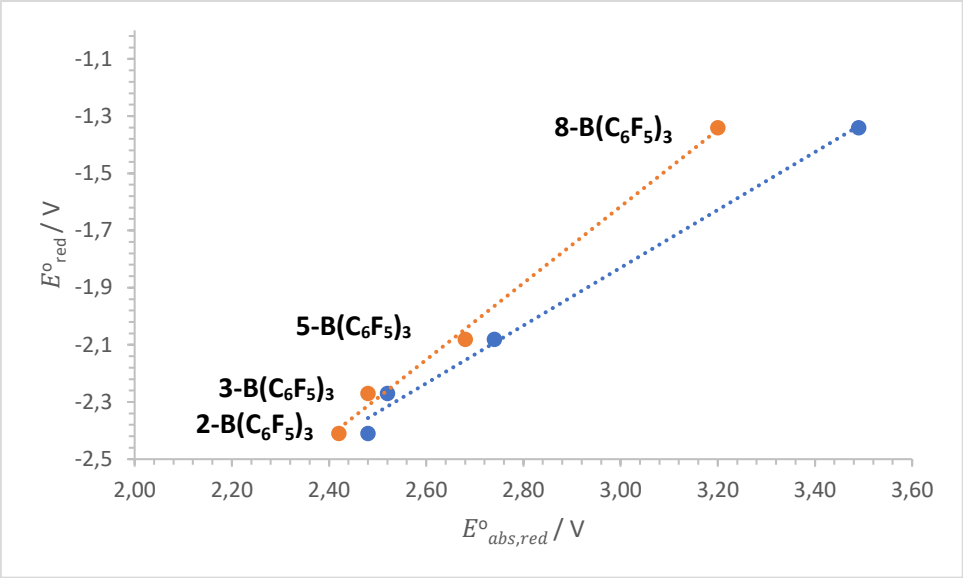

Figure 1. Correlation between the predicted absolute reduction potential ($E^{o}_{abs,red}$) and experimental reduction potential (E^{o}_{red}) of all synthesised adducts (**2-B(C$_6$F$_5$)$_3$**, **3-B(C$_6$F$_5$)$_3$**, **5-B(C$_6$F$_5$)$_3$** and **8-B(C$_6$F$_5$)$_3$**) for both tested functionals in dichloromethane. The blue line shows the tendency line for the functional M06-2X-D3 and the orange one, for B3LYP-D3. All values are expressed in volts (V).

Table 2. Coefficients of the tendency line equation for functionals M06-2X-D3 and B3LYP-D3 considering the synthesised adducts (**2-B(C$_6$F$_5$)$_3$**, **3-B(C$_6$F$_5$)$_3$**, **5-B(C$_6$F$_5$)$_3$** and **8-B(C$_6$F$_5$)$_3$**) in dichloromethane.

Equation Form		y = ax + b	
Density Functional	A (slope)	b (y-intercept)	R^2
M06-2X-D3	1.01	-4.86	0.992
B3LYP-D3	1.34	-5.63	0.995

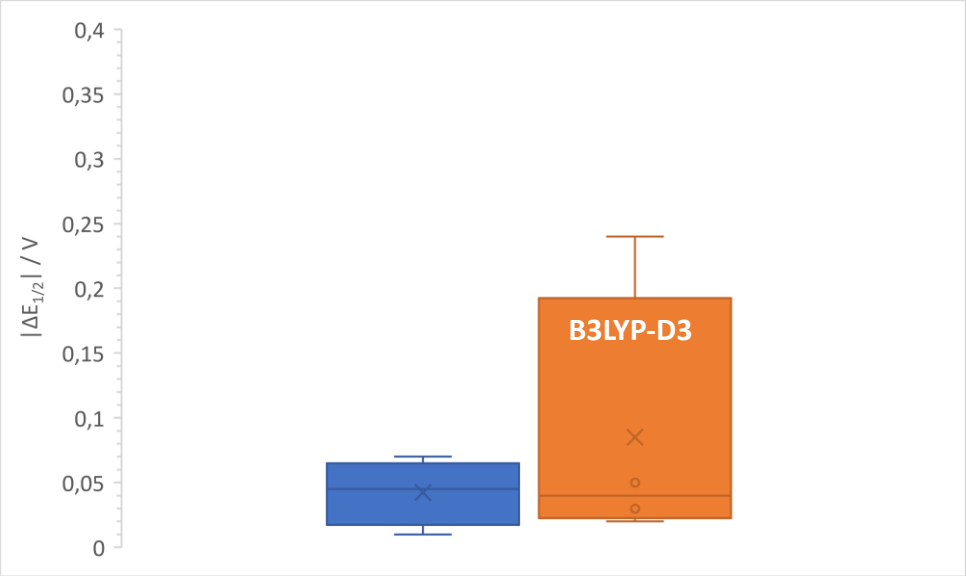

Figure 2. Difference between the biggest and the smallest deviations to measure the dispersion of the calculated reduction potentials in all synthesised NHC-CO_2-$B(C_6F_5)_3$ adducts (**2-$B(C_6F_5)_3$**, **3-$B(C_6F_5)_3$**, **5-$B(C_6F_5)_3$** and **8-$B(C_6F_5)_3$**.

By definition, a precise functional is the one that presents a lower range of dispersion (difference between the biggest and the smallest deviations) and MAD whereas the functionals with an ideal slope and y-intercept (1.00 and -4.78 respectively) are more accurate ones.[2] Considering all data (**2-$B(C_6F_5)_3$**, **3-$B(C_6F_5)_3$**, **5-$B(C_6F_5)_3$** and **8-$B(C_6F_5)_3$**), M06-2X-D3 seems to be a more precise functional (MAD: 0.05 V (Table 1) and with a lower dispersion (Figure 2) than B3LYP-D3 (MAD: 0.09 V) and also more accurate than B3LYP-D3 as its slope is closer to 1.00 and the y-intercept to -4.78 V (a: 1.01 and b: -4.86, Table 2).

The reduction potential of ^{Cy}CAAC-CO_2 (**8**) adduct was also calculated but it was not considered in the previous discussion. As shown in Table 3, the computed reduction potential does not agree with the experimental reduction potential in the case of adduct **8**. It seems this borane-free requires more exploration and it will be treated in section 4.6.2. "Influence of the NHC-CO_2 torsion angle on the reduction potentials" in this chapter.

Table 3. Theoretical reduction potential ($E^{1/2}_{red}$) of **8** versus $Fc^{+/0}$ redox couple in V for both functionals in dichloromethane. The deviation from the experimental reference ($|\Delta E^{1/2}_{red}|$) for adduct **8** is also given.

Density Functional	M06-2X-D3	B3LYP-D3	Experimental
$E^{1/2}_{red}$ (**8**)	-2.38	-2.49	-2.13
$\|\Delta E^{1/2}_{red}\|$ (**8**)	0.25	0.36	-

Based on the previous discussion, we can conclude that the hybrid functional M06-2X with the Grimme's correction (M06-2X-D3) provides a more precise and accurate reduction potential for NHC-CO_2-$B(C_6F_5)_3$ than B3LYP-D3. For this reason, the following discussion will be based on calculations in which M06-2X-D3 has been employed.

4.1.2. Theoretical reduction potentials in dichloromethane.

Having demonstrated that M06-2X-D3 is a functional that can predict reduction potentials high accuracy and precision versus the experiment, it was chosen to calculate the reduction potentials of all adducts described but this time, in dichloromethane. As a reminder, results from the preliminary study exposed in Chapter II were calculated in acetonitrile. Dichloromethane was employed to measure the reduction potentials of all synthesised adducts (**8**, **2-B(C_6F_5)$_3$**, **3-B(C_6F_5)$_3$**, **5-B(C_6F_5)$_3$** and **8-B(C_6F_5)$_3$**) (Chapter 3, section 3.2. "Measurement of reduction potentials in adducts NHC-CO_2-$B(C_6F_5)_3$ adducts (**2-**, **3-**, **5-**, **8-B(C_6F_5)$_3$**"). All the discussions and tendencies presented in Chapter 2 in acetonitrile do not differ from the ones in dichloromethane. The following theoretical reduction potentials are the ones that will be employed in the discussion of this chapter (Schemes 1-4).

N-Alkyl groups

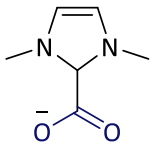

(**1**)

-3.25

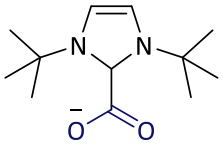

(**2**)

-3.42

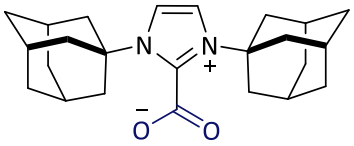

(**3**)

-3.44

N-Aryl groups

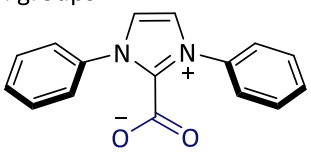

(**4**)

-2.84

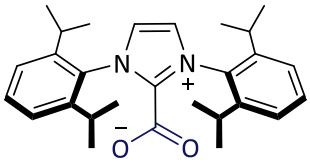

(**5**)

-3.00

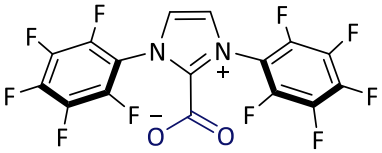

(**6**)

-2.30

Enders and ^{Cy}CAAC-type NHCs

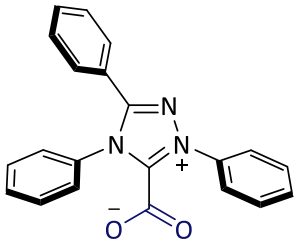

(**7**)

-2.65

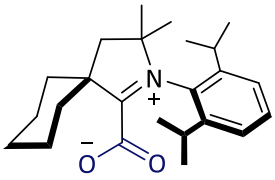

(**8**)

-2.38

Scheme 1. Studied NHC-CO_2 adducts with their theoretical reduction potential umderneath calculated in dichloromethane with the functional M06-2X-D3 (in blue). The potentials are expressed in volts (V) versus $Fc^{+/0}$.

N-Alkyl groups

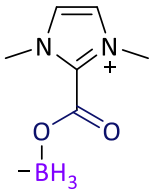

(**1-BH$_3$**)

-2.56

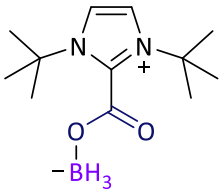

(**2-BH$_3$**)

-2.83

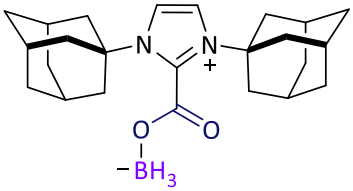

(**3-BH$_3$**)

-2.83

N-Aryl groups

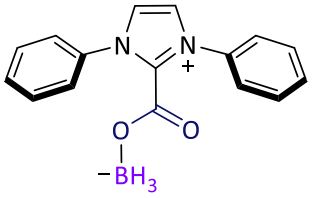

(**4-BH$_3$**)

-2.26

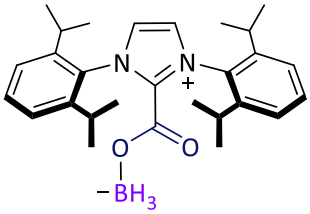

(**5-BH$_3$**)

-2.34

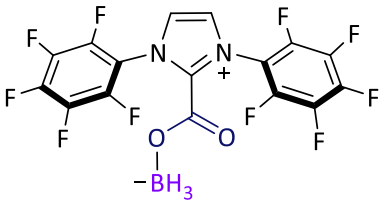

(**6-BH$_3$**)

-1.74

Enders and ^{Cy}CAAC-type NHCs

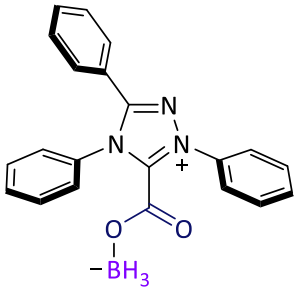

(**7-BH$_3$**)

-1.96

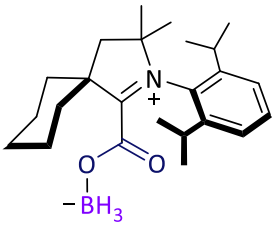

(**8-BH$_3$**)

-1.73

Scheme 2. Studied NHC-CO_2-BH_3 adducts with their theoretical reduction potential umderneath calculated in dichloromethane with the functional M06-2X-D3 (in blue). The potentials are expressed in volts (V) versus $Fc^{+/0}$.

N-Alkyl groups

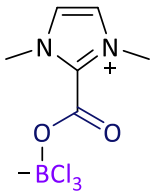

(**1-BCl_3**)

-2.17

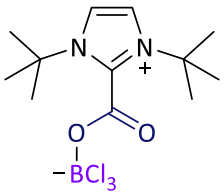

(**2-BCl_3**)

-2.50

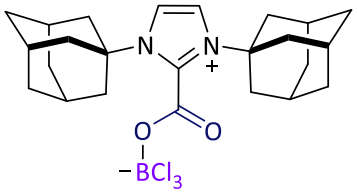

(**3-BCl_3**)

-2.64

N-Aryl groups

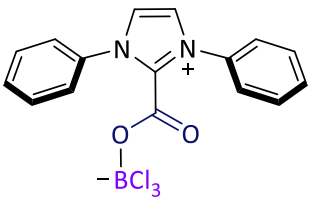

(**4-BCl_3**)

-1.94

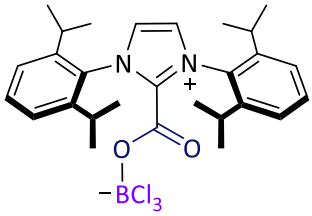

(**5-BCl_3**)

-1.93

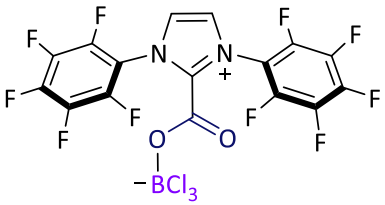

(**6-BCl_3**)

-1.41

Enders and ^{Cy}CAAC-type NHCs

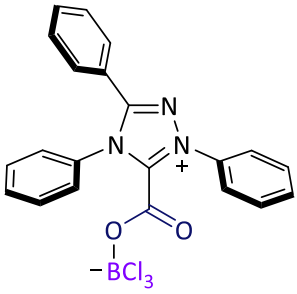

(**7-BCl_3**)

-1.66

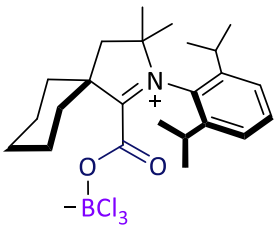

(**8-BCl_3**)

-1.38

Scheme 3. Studied NHC-CO_2-BCl_3 adducts with their theoretical reduction potential umderneath calculated in dichloromethane with the functional M06-2X-D3 (in blue). The potentials are expressed in volts (V) versus $Fc^{+/0}$.

N-Alkyl groups

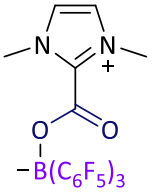

(**1-B(C_6F_5)$_3$**)

-2.28

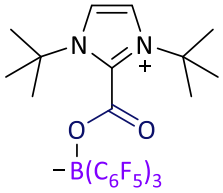

(**2-B(C_6F_5)$_3$**)

-2.26

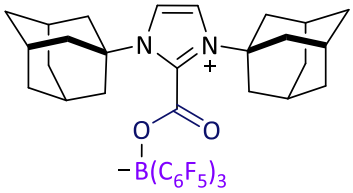

(**3-B(C_6F_5)$_3$**)

-2.30

N-Aryl groups

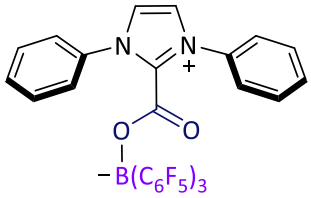

(**4-B(C_6F_5)$_3$**)

-2.29

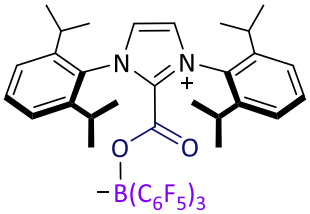

(**5-B(C_6F_5)$_3$**)

-2.04

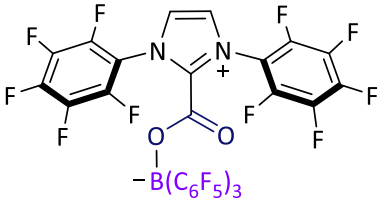

(**6-B(C_6F_5)$_3$**)

-1.55

Enders and ^{Cy}CAAC-type NHCs

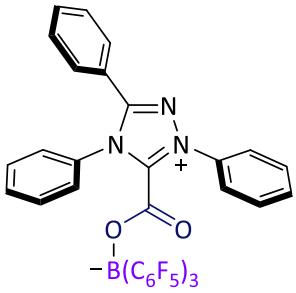

(**7-B(C_6F_5)$_3$**)

-1.79

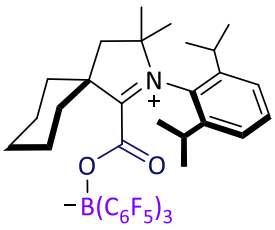

(**8-B(C_6F_5)$_3$**)

-1.29

Scheme 4. Studied NHC-CO_2-B(C_6F_5)$_3$ adducts with their theoretical reduction potential umderneath calculated in dichloromethane with the functional M06-2X-D3 (in blue). The potentials are expressed in volts (V) versus $Fc^{+/0}$.

4.2. Thermodynamic stability of NHC-CO_2 and NHC-CO_2-BR_3 adducts.

In this subsection, the stability of the studied NHC-CO_2-based adducts will be described. Firstly, the tendencies observed in NHC-CO_2 adducts depending on the nature of the NHC will be described and later, the impact of the Lewis acidity and bulkiness of borane will be also explained.

4.2.1. Influence of the nature of the NHC in the NHC-CO_2 stabilisation.

Before studying the monoelectronic reduction of NHC-CO_2-based adducts, it is fundamental to determine whether these adducts are thermodynamically stable or not. In the literature, this question has been already documented. In 2018, Xue and Ji jointly disclosed that the stability of the NHC-CO_2 adducts is mainly dictated by the basicity of the NHCs, based on a study with more than 90 examples of NHCs.[4] They observed that higher is the basicity (normally coinciding with stronger nucleophilicity) of the NHC, higher is the stability of the corresponding NHC-CO_2 adduct as it will result into a stronger bond between the NHC ring and the CO_2 moiety.

As shown in Scheme 5, the stability of different NHC-CO_2 adducts closely depends on the nature of NHC moiety. The binding energy of the NHC towards a linear free CO_2 molecule (ΔG) varies from -3.3 kcal·mol^{-1} to -19.5 kcal·mol^{-1} (a difference of 16.2 kcal·mol^{-1}). Based on the study from Louie's group in which they conclude that imidazolium carboxylates are more stable when the carboxylate moiety lie in the same plane as the NHC ring due to resonance stabilisation between the NHC and the carboxylate moiety.[5] We tried to rationalise these energy variations with structural parameters such as the dihedral (torsion) angle (D(NHC-CO_2)) between the NHC and the coordinate CO_2 moiety in NHC-CO_2-BR_3 adducts. But first, we verified this behaviour in NHC-CO_2 adducts.

Within the collection of imidazolium-based adducts (**1**-**6**), we studied adducts whose *N*-substituents are alkyl groups (a) and aryl derivatives (b):

a. Alkyl groups (**1**-**3**). The stability of the corresponding NHC-CO_2 adducts increases with the coplanarity between the NHC and the CO_2 moiety. Adduct **1** exhibits associated a Gibbs formation energy of -14.4 kcal.mol^{-1} which is slightly lower than in adducts **2** (-9.9 kcal·mol^{-1}) and **3** (-9.7 kcal·mol^{-1}). Adduct **1** is more stable than adduct **2** and **3**. The torsion angle of adduct **1** is also closer to the coplanarity (20.1 °) than adduct **2** (72.6 °) and **3** (84.2 °).
b. Aryl groups (**4**-**6**). In this category, we observed that adduct **6** whose torsion angle is at 11.3 ° is less stable (-5.8 kcal·mol^{-1}) compared to adduct **4** (-9.7 kcal·mol^{-1}, 60.2 °). The presence of strong electro-withdrawing perfluorophenyl groups in adduct **6** might be detrimental to the basicity of the carbene yielding a less stable adduct. This reveals that the stability of NHC-CO_2 adducts is not solely governed

by the hindrance factors but also by electronics. Finally, the adduct **5** is the most stable (-13.1 kcal·mol^{-1}) in this category with a small torsion angle, 28.2 °.

The *N*-Heterocyclic carbenes which constitute the adducts **7** and **8** exhibits electronic properties that differs from imidazolium-based adducts (**1**-**6**). For this reason, they have not been included in the previous discussion. The adduct **7** is constructed with an Enders carbene. It possesses the less negative stabilisation energy (-3.3 kcal·mol^{-1}). It has been reported that the pK_a of triazolium-based NHC precursors (the conjugated acid of the *N*-Heterocyclic Carbene) is lower than in imidazolium-based ones. In other words, the triazolium carbene exhibits a lower basicity than the imidazolium-based adduct.[4] For this reason, the resulting triazolium NHC-CO_2 adduct is expected to be less stable than imidazolium-based ones. The cyclic(alkyl)(amino) carbenes are known to be strong σ-donor which would results in the formation of strong NHC-CO_2 bonds (-19.5 kcal·mol^{-1}) despite its dihedral angle (85.5 °). Besides the torsion angle, other structural parameters such as the CO_2 angle and the C-C bond length between the NHC moiety and the CO_2 unit are also considered. In the case of the CO_2 angle, no significant difference is observed, it varies from 131.4 ° (**2**) to 133.6 ° (**7**). The average C-C bond in organic molecules has been reported at 1.53 Å.[6] In NHC-CO_2 adducts, it ranges from 1.533 Å (**4**) to 1.561 Å (**7**). Based on previous observations, the CO_2 unit in adduct **7** does not seem to be as coordinated as in others adducts therefore, we should also expect a smaller stabilisation energy (-3.3 kcal·mol^{-1}) than in other adducts. In next section (4.2.2. "Influence of the borane in the stability of NHC-CO_2-BR_3 adducts."), the discussion will be solely focussed on the dihedral angle as it is the most sensitive to the structural changes in NHC-CO_2-based adducts.

Reaction

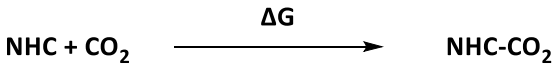

N-Alkyl groups

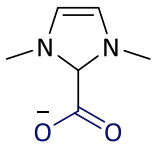

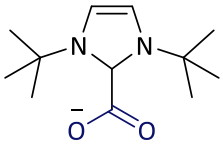

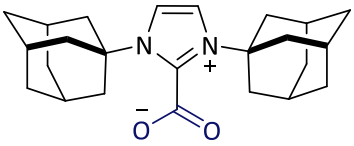

	(**1**)	(**2**)	(**3**)
ΔG:	-14.4	-9.9	-9.7
D(NHC-CO_2):	20.1	72.6	84.2

N-Aryl groups

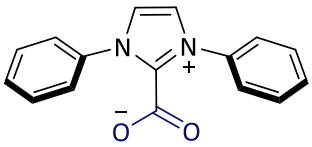

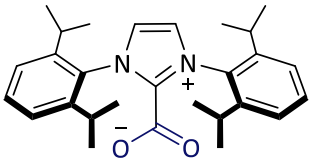

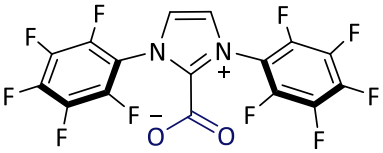

	(**4**)	(**5**)	(**6**)
ΔG:	-9.7	-13.1	-5.8
D(NHC-CO_2):	60.2	28.2	11.3

Enders and ^{Cy}CAAC-type NHCs

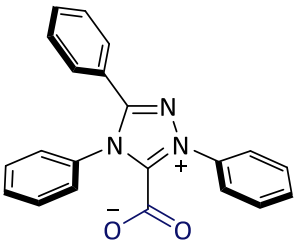

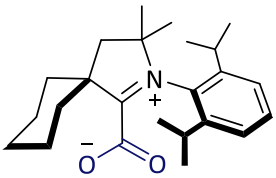

	(**7**)	(**8**)
ΔG:	-3.3	-19.5
D(NHC-CO_2):	60.8	85.2

Scheme 5. Gibbs formation energy of the studied NHC-CO_2 adducts (NHC binding energy) and dihedral (torsion) angle (D(NHC-CO_2)) between the NHC and the CO_2 moiety. The Gibbs energies are expressed in kcal·mol^{-1} and the dihedral angles in degrees (°).

4.2.2. Influence of the borane in the stability of NHC-CO_2-BR_3 adducts.

In this subsection, the influence of the acidity and bulkiness of the Lewis acids in the stability of NHC-based adducts will be exposed.

4.2.2.1. Use of BH_3 as reference Lewis acid.

Firstly, we tested whether the addition of a boron Lewis acid shows a beneficial impact on the stability of NHC-CO_2 adducts. As shown in Scheme 6, the addition of a BH_3 to NHC-CO_2 adduct exhibits a significant improvement in the stability of NHC-CO_2 adducts. The Gibbs energies vary between -23.7 kcal·mol^{-1} and -20.4 kcal·mol^{-1} (a difference of 3.3 kcal·mol^{-1}). In contrast to NHC-CO_2 adducts, the difference of Gibbs energy within all NHC-CO_2-BH_3 adducts is much lower. It seems that the formation energy of NHC-CO_2-BH_3 adducts tends to vary around -22 kcal·mol^{-1} regardless the NHC nature. All discussions exposed for the NHC-CO_2 adducts apply to NHC-CO_2-BH_3 adducts. Similar tendencies to the NHC-CO_2 adducts collection have been observed. In half of the adducts (**(1**, **4**, **5**, **7)-BH$_3$**), the CO_2 moiety tends to set in a position closer to the coplanarity respect to the NHC than NHC-CO_2 adducts (**1-8**). Nevertheless, their dihedral angle does not change significantly with the addition of BH_3. It seems that the torsion angle is mainly governed by the NHC ring. The largest difference in the torsion angle corresponds to adduct **1** and **1-BH$_3$**, 21.1 °. While in other cases where the NHC moiety exhibits a greater steric hindrance (**(2**, **3**, **6**, **8)-BH$_3$**), the torsion angle (D(NHC-CO_2)) barely varies.

Reaction

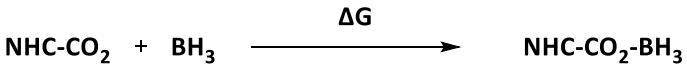

N-Alkyl groups

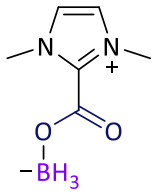

(**1-BH_3**)

ΔG: -23.1

D (NHC-CO_2): 0.0

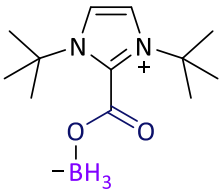

(**2-BH_3**)

ΔG: -23.7

D (NHC-CO_2): 73.9

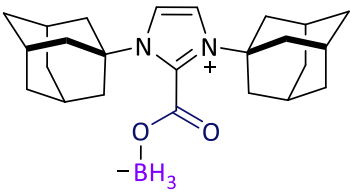

(**3-BH_3**)

ΔG: -23.8

D (NHC-CO_2): 82.5

N-Aryl groups

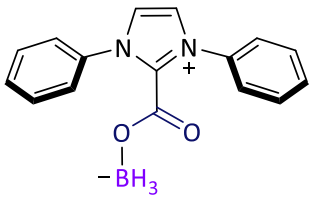

(**4-BH_3**)

ΔG: -22.0

D (NHC-CO_2): 45.8

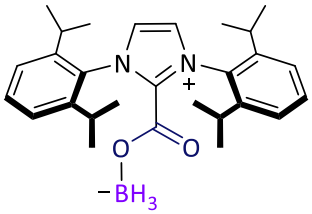

(**5-BH_3**)

ΔG: -23.5

D (NHC-CO_2): 11.5

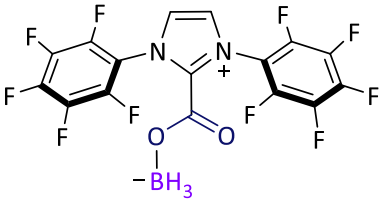

(**6-BH_3**)

ΔG: -20.4

D (NHC-CO_2): 10.9

Enders and ^{Cy}CAAC-type NHCs

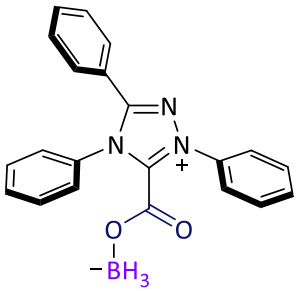

(**7-BH_3**)

ΔG: -20.5

D (NHC-CO_2): 46.5

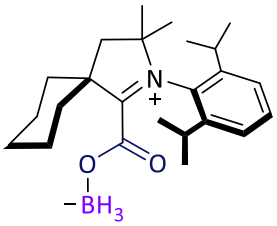

(**8-BH_3**)

ΔG: -22.6

D (NHC-CO_2): 89.1

Scheme 6. Gibbs formation energy of the studied NHC-CO_2-BH_3 adducts (NHC-CO_2 binding energy) and dihedral (torsion) angle (D(NHC-CO_2)) between the NHC and the CO_2

moiety. The Gibbs energies are expressed in kcal·mol^{-1} and the dihedral angles in degrees (°).

4.2.2.2. Use of boranes with a higher Lewis acidity, BCl_3.

Then, we tested the influence of the acidity of boranes in the stability of the adducts. In this study, we used BCl_3 which is known to exhibit a slightly higher Lewis acidity than in the case of BH_3.[7] As shown in Scheme 7, adducts constituted by a BCl_3 moiety ((**1**-**8**)-**BCl_3**) present a slightly lower Gibbs energy of formation. The adducts are more stable than in previous cases. The Gibbs energies vary between -25.1 kcal·mol^{-1} and -21.9 kcal·mol^{-1} (a difference of 3.2 kcal·mol^{-1}). The discussions used in previous examples applies to compounds (**1**-**8**)-**BCl_3**. There are no significant differences in the dihedral angle between NHC and CO_2 moiety respect to NHC-CO_2-BH_3 adducts. The largest difference in the torsion angle was observed in adduct **4-BCl_3**, only 8 ° difference compared to **8-BH_3**. Within all adducts ((**1**-**8**)-**BCl_3**), adduct **8-BCl_3** exhibited the lowest Gibbs energy of formation, -31.1 kcal·mol^{-1}.

Reaction

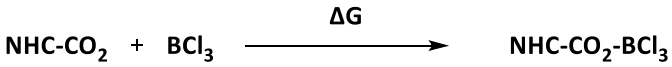

N-Alkyl groups

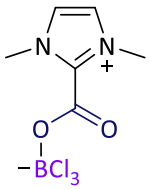

(**1-BCl_3**)

ΔG: -26.6

D (NHC-CO_2): 4.7

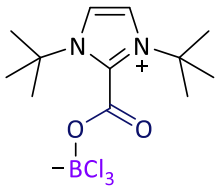

(**2-BCl_3**)

ΔG: -26.9

D (NHC-CO_2): 73.2

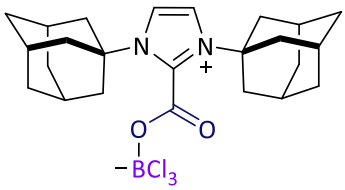

(**3-BCl_3**)

ΔG: -27.8

D (NHC-CO_2): 82.0

N-Aryl groups

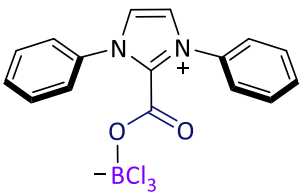

(**4-BCl_3**)

ΔG: -25.1

D (NHC-CO_2): 37.8

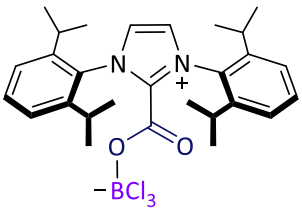

(**5-BCl_3**)

ΔG: -27.3

D (NHC-CO_2): 14.7

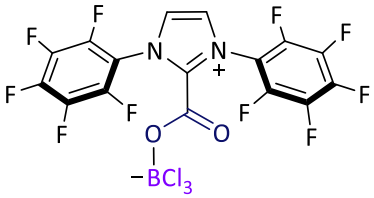

(**6-BCl_3**)

ΔG: -21.9

D (NHC-CO_2): 14.8

Enders and ^{Cy}CAAC-type NHCs

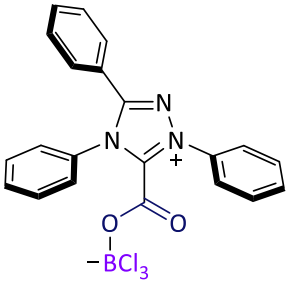

(**7-BCl_3**)

ΔG: -23.6

D (NHC-CO_2): 41.9

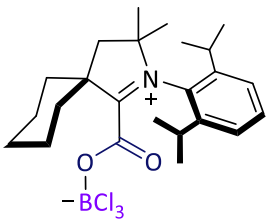

(**8-BCl_3**)

ΔG: -25.1

D (NHC-CO_2): 86.7

Scheme 7. Gibbs formation energy of the studied NHC-CO_2-BCl_3 adducts (NHC-CO_2 binding energy) and dihedral (torsion) angle (D(NHC-CO_2)) between the NHC and the CO_2 moiety. The Gibbs energies are expressed in kcal·mol^{-1} and the dihedral angles in degrees (°).

4.2.2.3. Use of more sterically hindered boranes, $B(C_6F_5)_3$.

We tested how the bulkiness of borane influence the formation of NHC-CO_2-$B(C_6F_5)_3$ adducts. It is expected that NHC-CO_2-$B(C_6F_5)_3$ adducts exhibit more favored Gibbs formation energies in cases where the *N*-substituents are less hindered than the others. The CO_2 moiety will be capable of position itself close to a coplanar position. As shown in Scheme 8, adducts constituted by a $B(C_6F_5)_3$ moiety ((**1**-**8**)-**$B(C_6F_5)_3$**) present a stabilisation energy equivalent to previous examples ((**1**-**8**)-**BCl_3**). The Gibbs energies are from -34.9 kcal·mol^{-1} and -20.5 kcal·mol^{-1} (a difference of 14.4 kcal·mol^{-1}). Compared to (**1**-**8)-BCl_3** adducts, the Gibbs energies of formation are more spread (it exists a larger difference between the lowest and higher energy). It means that the Gibbs energy of formation is more tuneable modifying the *N*-substituents that in other cases. Using a hindered borane instead a BH_3 or BCl_3, the torsion angles between the NHC and the CO_2 follows a tendency depending on the nature of the *N*-tethered groups. In adducts whose *N*-substituents are alkyl groups, the torsion angle is higher (**1-$B(C_6F_5)_3$**) or equivalent (**2-** and **3-$B(C_6F_5)_3$**) than adducts bearing BH_3 as a Lewis acid. In the case of aryl derivatives, the dihedral angle decreases (**4-$B(C_6F_5)_3$** and **6-$B(C_6F_5)_3$**) respect to **4-** and **6-BH_3**. In adduct **5-$B(C_6F_5)_3$**, no significant difference is observed compared to **5-BH_3**. However, the formation of **5-$B(C_6F_5)_3$** is 11.4 kcal·mol^{-1} more favoured than **5-BH_3**. The largest difference in the torsion angle was observed in adduct **1-$B(C_6F_5)_3$**, with 17.9 ° compared to **1-BH_3** (0.0 °). Within all adducts (**1-8-$B(C_6F_5)_3$**), compound **5-$B(C_6F_5)_3$** is the most stabilised, -34.9 kcal·mol^{-1}.

Reaction

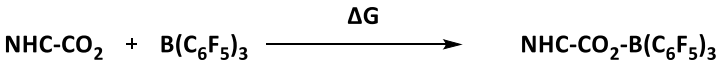

N-Alkyl groups

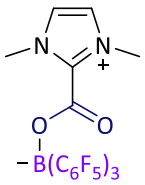

(**1-B(C_6F_5)$_3$**)

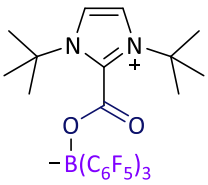

(**2-B(C_6F_5)$_3$**)

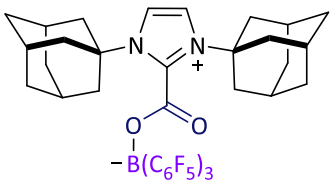

(**3-B(C_6F_5)$_3$**)

ΔG:	-23.0	-20.5	-22.7
D(NHC-CO_2):	17.9	71.8	83.8

N-Aryl groups

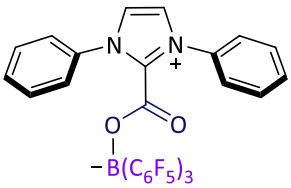

(**4-B(C_6F_5)$_3$**)

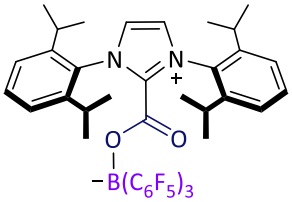

(**5-B(C_6F_5)$_3$**)

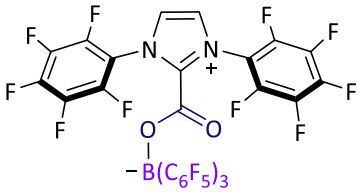

(**6-B(C_6F_5)$_3$**)

ΔG:	-25.8	-34.9	-21.2
D(NHC-CO_2):	35.7	19.3	0.7

Enders and ^{Cy}CAAC-type NHCs

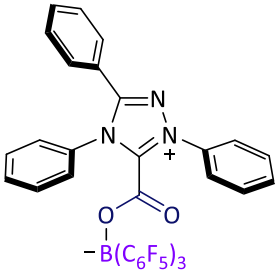

(**7-B(C_6F_5)$_3$**)

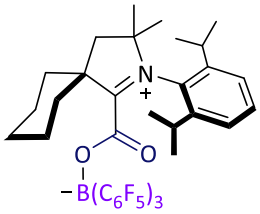

(**8-B(C_6F_5)$_3$**)

ΔG:	-23.1	-31.1
D(NHC-CO_2):	56.8	88.4

Scheme 8. Gibbs formation energy of the studied NHC-CO_2-B(C_6F_5)$_3$ adducts (NHC-CO_2 binding energy) and dihedral (torsion) angle (D(NHC-CO_2)) between the NHC and the CO_2 moiety. The Gibbs energies are expressed in kcal·mol^{-1} and the dihedral angles in degrees (°).

The formation of all synthesised adducts (**8**, **2-**, **3-**, **5-** and **8-B(C_6F_5)$_3$**) is thermodynamically favorable. Regarding the torsion angle in these adducts, the CO_2 moiety tends to set in a perpendicular position respect to the NHC ring except in compound **5-B(C_6F_5)$_3$.** In the latter adduct, the CO_2 sets in a coplanar position. It seems that carbene that constitutes the adduct **5-B(C_6F_5)$_3$** is less hindered than in other cases. As the CO_2 is set closer to the coplanarity with the NHC ring than other adducts, it presents a higher stabilisation energy (-34.9 kcal·mol^{-1}) respect to the others (**8**, **2-**, **3-** and **8-B(C_6F_5)$_3$**). As shown in Table 4, the dihedral angle of the computed adducts is in agreement with experimental one.

Table 4. Comparison between computed (in solution) and experimental (from XRD analysis) dihedral angles between NHC and CO_2 moiety (D(NHC-CO_2)) in synthesised compounds (**8**, **2-**, **3-**, **5-** and **8-B(C_6F_5)$_3$**) along with their Gibbs energy of formation (NHC-CO_2 adducts: NHC + CO_2 and NHC-CO_2-B(C_6F_5)$_3$: NHC-CO_2 + B(C_6F_5)$_3$).

Adducts	ΔG/kcal·mol^{-1}	Structural Parameters	
		D(NHC-CO_2) theoretical/°	D(NHC-CO_2) experimental/°
2-(B(C_6F_5)$_3$	-20.5	71.8	80.5(2)[8]
3-(B(C_6F_5)$_3$	-22.7	83.8	76.7(3)
5-(B(C_6F_5)$_3$	-34.9	19.3	7.3(2)
8	-19.5	85.2	77.9(4)[9]
8-(B(C_6F_5)$_3$	-31.1	88.4	79.2(2)

4.3. Spin density distribution in monoreduced NHC-CO_2 and NHC-CO_2-BR_3 adducts.

Besides the determination of reduction potentials of NHC-CO_2-based adducts, we interrogated whether the monoreduced NHC-based species mimic the CO_2 radical anion behaviour towards different substrates (Chapter 1, section 1.1.2 "Reactivity of CO_2 radical anion."). For this reason, we studied how the spin density (additional electron) is localised in their monoreduced species. Upon reduction of NHC-CO_2 adducts, the additional electron will localise, most likely, at the *p*-vacant orbital at the carbenic carbon (**I**, Scheme 5). By resonance, part of the spin density could also reside at the carbon from

the CO_2 moiety (**II**). We questioned if the addition of Lewis acid enhances the spin density at the carbon of the CO_2 moiety (**II-BR_3**, Scheme 9).

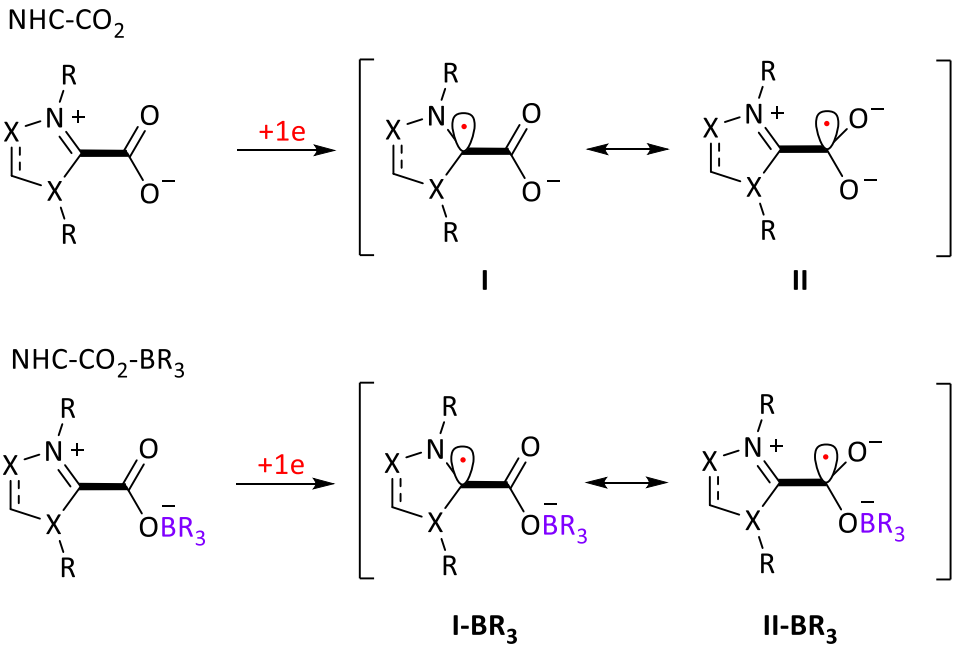

Scheme 9. Resonance structures in monoreduced NHC-CO_2-based adducts.

According to the literature, the free CO_2 radical anion exhibits a spin population of 68% at the carbon atom.[10] Using the theoretical methodology described in Chapter 2, we reported 81% of spin population at the C atom. In the following paragraphs, the spin density distribution focussing on the spin at the carbenic carbon and carbon from the CO_2 will be discussed (Table 6). The corresponding monoreduced adducts will be numbered as in Scheme 6. In order to refer to a monoreduced species, the notation used in precedented neutral examples will be in brackets with the symbol "·-" as exponent. As example, the adduct **1** upon reduction is denoted as **[1]$^{\bullet-}$**.

N-Alkyl groups

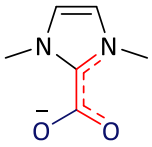

([**1**]$^{\bullet-}$)

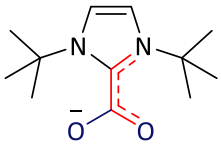

([**2**]$^{\bullet-}$)

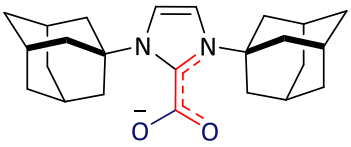

([**3**]$^{\bullet-}$)

D(NHC-CO_2)	9.5	17.1	46.2

N-Aryl groups

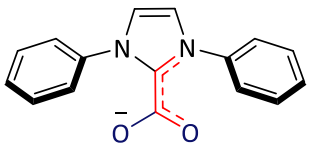

([**4**]$^{\bullet-}$)

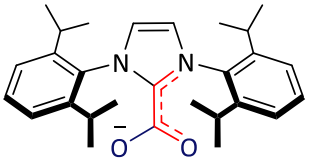

([**5**]$^{\bullet-}$)

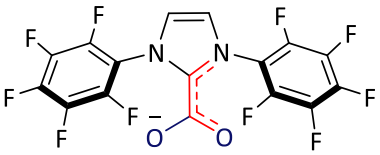

([**6**]$^{\bullet-}$)

D(NHC-CO_2)	23.6	2.2	11.7

Enders and ^{Cy}CAAC-type NHCs

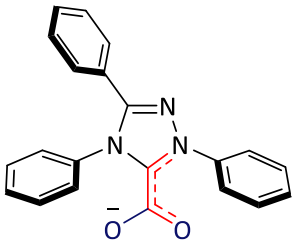

([**7**]$^{\bullet-}$)

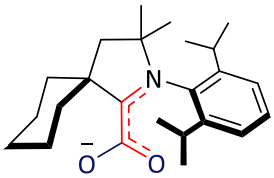

([**8**]$^{\bullet-}$)

D(NHC-CO_2)	74.6	10.1

Scheme 10. Studied mononoreduced species in the absence of a borane and the dihedral angle (D(NHC-CO2)). The dihedral angles are expressed in degrees (°).

4.3.1. Spin density in monoreduced NHC-CO_2 adducts ([**1**]$^{\bullet-}$-[**8**]$^{\bullet-}$) depending on the NHC structure.

In the absence of any borane, more than a half of the total spin density is mainly localized in the carbenic carbon, between 0.56 and 0.66. Except in the case of compound **[7]**$^{\bullet-}$ where it is almost inexistant at that position. A shared feature for all of them is that none exhibits spin density at the carbon of the CO_2 moiety. As in the previous section of this chapter: "Thermodynamic stability of NHC-CO_2 and NHC-CO_2-BR_3 adducts", the orientation of the CO_2 respect to the NHC ring should play an important role in the spin

density distribution. It is expected to observe higher spin density at the carbon atom from the CO_2 when the π-vacant orbital of the carbenic carbon aligns with a vacant orbital of the CO_2 (D(NHC-CO_2) is closer to 0 °). More insights regarding the orbital distribution will be exposed in section 4.4.2. "Localisation of the LUMO and SOMO orbital in NHC-CO_2-based adducts and their energy.". Nevertheless, in adducts **[1]**$^{\bullet-}$ (9.5 °), **[5]**$^{\bullet-}$ (2.2 °) and **[8]**$^{\bullet-}$ (10.1 °) despite their torsion angle close to the coplanarity (Scheme 10), no spin density is observed at the carbon from the CO_2 moiety. Besides the carbenic carbon, the spin density resides in a lesser degree on the nitrogen atoms (from 0.10 to 0.35) followed by the oxygen atoms from CO_2 (from 0.00 to 0.16). The adduct that exhibits the higher spin density at the CO_2 moiety is **[5]**$^{\bullet-}$ and **[8]**$^{\bullet-}$ with 0.16 and 0.15, respectively (Figure 3). In comparison with the free CO_2 radical anion, monoreduced NHC-CO_2 adducts does seem to be far from mimicking the spin density distribution of the free CO_2 radical anion. (Table 5)

Table 5. Spin density distribution in monoreduced NHC-CO_2 adducts (**[1]**$^{\bullet-}$**-[8]**$^{\bullet-}$) in comparison to the free CO_2 radical anion.

Compounds	CO_2 moiety			NHC moiety	
	C	O	Total Spin density (CO_2)	Carbenic C	N
Free [CO_2]$^{\bullet-}$	0.81	0.19	1.00	-	-
[1]$^{\bullet-}$	-0.10	0.14	0.04	0.62	0.21
[2]$^{\bullet-}$	-0.08	0.10	0.02	0.57	0.34
[3]$^{\bullet-}$	0.00	0.08	0.08	0.66	0.32
[4]$^{\bullet-}$	-0.02	0.10	0.08	0.59	0.14
[5]$^{\bullet-}$	0.00	0.16	0.16	0.56	0.19
[6]$^{\bullet-}$	-0.05	0.12	0.07	0.63	0.10
[7]$^{\bullet-}$	0.00	0.00	0.00	-0.03	0.35
[8]$^{\bullet-}$	0.00	0.15	0.15	0.61	0.22

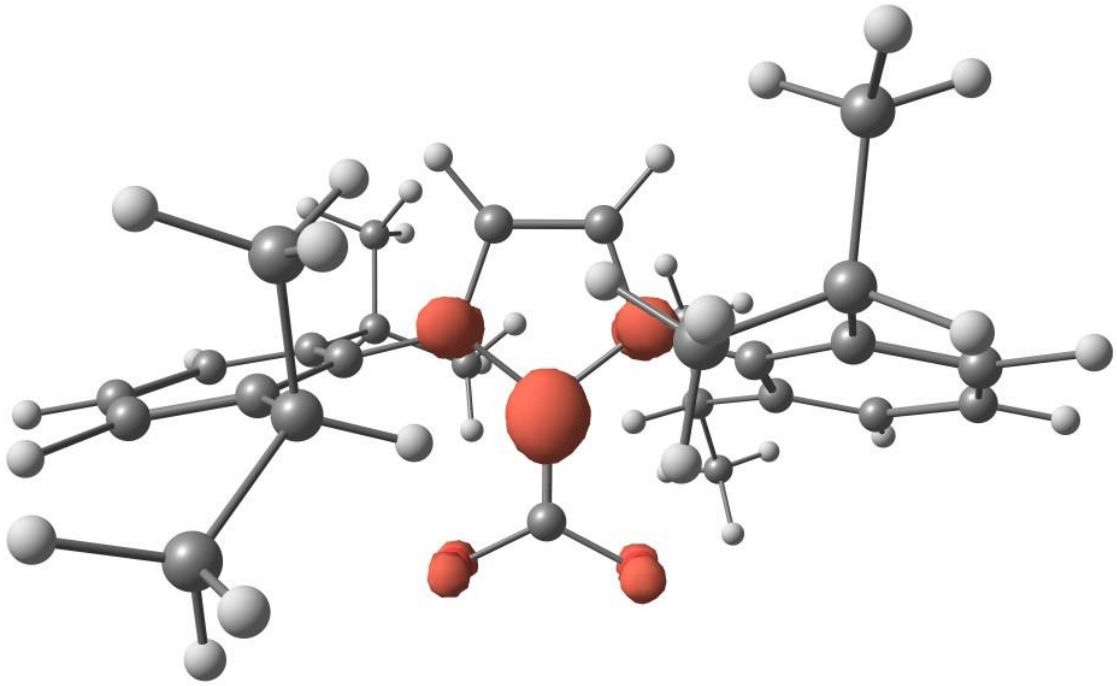

Figure 3. Spin density map of **[5]**$^{\bullet-}$ adduct. The isosurface value is 0.016.

4.3.2. Impact of a Lewis acid on the spin density distribution in monoreduced NHC-CO_2-BR_3 adducts.

In this part of the discussion, the influence of the boron Lewis acid in the spin density distribution of monoreduced NHC-CO_2-BR_3 will be discussed. As in previous discussions, we started with the description of NHC-CO2-BH_3 adducts to use it as a reference for further examples (3.2.1) and then, the influence of acidity (3.2.2) and bulkiness (3.2.3) of boranes in the spin density will be explained.

4.3.2.1. Use of BH_3 as a Lewis acid, [NHC-CO_2-BH_3]$^{\bullet-}$ adducts.

In the case of monoreduced NHC-CO_2-BH_3 adducts (**[1-BH_3]**$^{\bullet-}$-**[8-BH_3]**$^{\bullet-}$, Scheme 11), the addition of the BH_3 does not significantly modify the spin density at the C of the CO_2 unit. Nevertheless, some of the examples presents spin density at that position in contrast to monoreduced NHC-CO_2 adducts (**[1-BH_3]**$^{\bullet-}$ (0.07), **[4-BH_3]**$^{\bullet-}$ (0.05), **[5-BH_3]**$^{\bullet-}$ (0.06), **[8-BH_3]**$^{\bullet-}$ (0.01)) (Figure 4). The spin density at the carbenic position (from 0.39 to 0.65) as well as at the nitrogen atoms (from 0.17 to 0.34) does not significantly differs from NHC-CO_2 adducts. The boron atom does barely exhibit spin density (0.01). The main difference respect to monoreduced NHC-CO_2 is that the addition of BH_3 enables that part of the spin density resides at the C of the CO_2 adducts in some of the cases (Table 6).

N-Alkyl groups

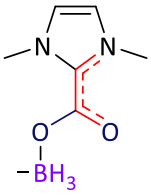

(**[1-BH_3]$^{\bullet-}$**)

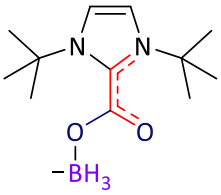

(**[2-BH_3]$^{\bullet-}$**)

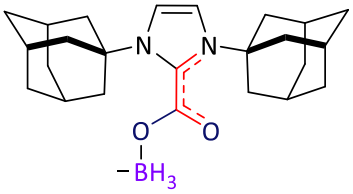

(**[3-BH_3]$^{\bullet-}$**)

D(NHC-CO_2)	7.4	21.9	1.1

N-Aryl groups

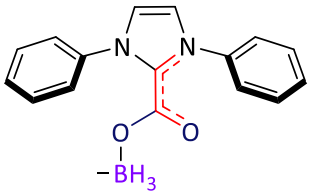

(**[4-BH_3]$^{\bullet-}$**)

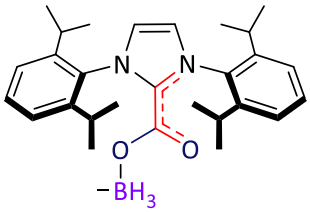

(**[5-BH_3]$^{\bullet-}$**)

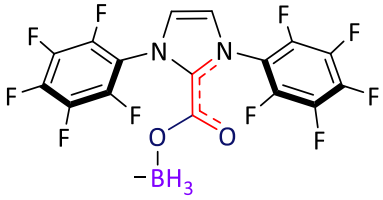

(**[6-BH_3]$^{\bullet-}$**)

D(NHC-CO_2)	21.6	1.0	11.6

Enders and ^{Cy}CAAC-type NHCs

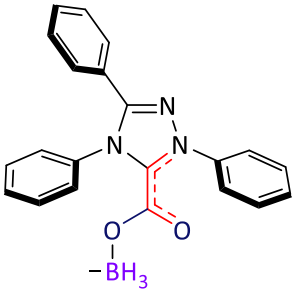

(**[7-BH_3]$^{\bullet-}$**)

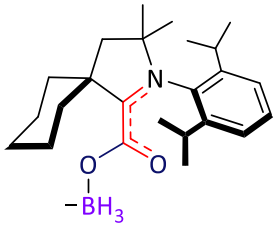

(**[8-BH_3]$^{\bullet-}$**)

D(NHC-CO_2)	23.1	7.2

Scheme 11. Studied mononoreduced NHC-CO_2-BH_3 adducts (**[1-BH_3]$^{\bullet-}$**-**[8-BH_3]$^{\bullet-}$**). The dihedral angles are expressed in degrees (°).

Table 6. Spin density distribution in monoreduced NHC-CO_2-BH_3 adducts (**[1-BH_3]$^{\bullet-}$**-**[8-BH_3]$^{\bullet-}$**) in comparison to the free CO_2 radical anion.

Compounds	CO_2 moiety				NHC moiety		BR_3 moiety
	C	O (C=O)	O (C-O)	Total Spin density (CO_2)	Carbenic C	N	B
Free [CO_2]$^{\bullet-}$	0.81	0.19		1.00	-	-	-
[1-BH_3]$^{\bullet-}$	0.07	0.14	0.04	0.25	0.39	0.30	0.01
[2-BH_3]$^{\bullet-}$	-0.02	0.11	0.11	0.20	0.60	0.34	0.00
[3-BH_3]$^{\bullet-}$	-0.09	0.12	0.02	0.04	0.51	0.33	0.01
[4-BH_3]$^{\bullet-}$	0.05	0.12	0.03	0.20	0.44	0.20	0.01
[5-BH_3]$^{\bullet-}$	0.06	0.15	0.03	0.24	0.44	0.22	0.00
[6-BH_3]$^{\bullet-}$	0.00	0.13	0.04	0.17	0.50	0.17	0.00
[7-BH_3]$^{\bullet-}$	-0.03	0.09	0.04	0.10	0.41	0.34	0.00
[8-BH_3]$^{\bullet-}$	0.01	0.13	0.02	0.16	0.65	0.22	0.01

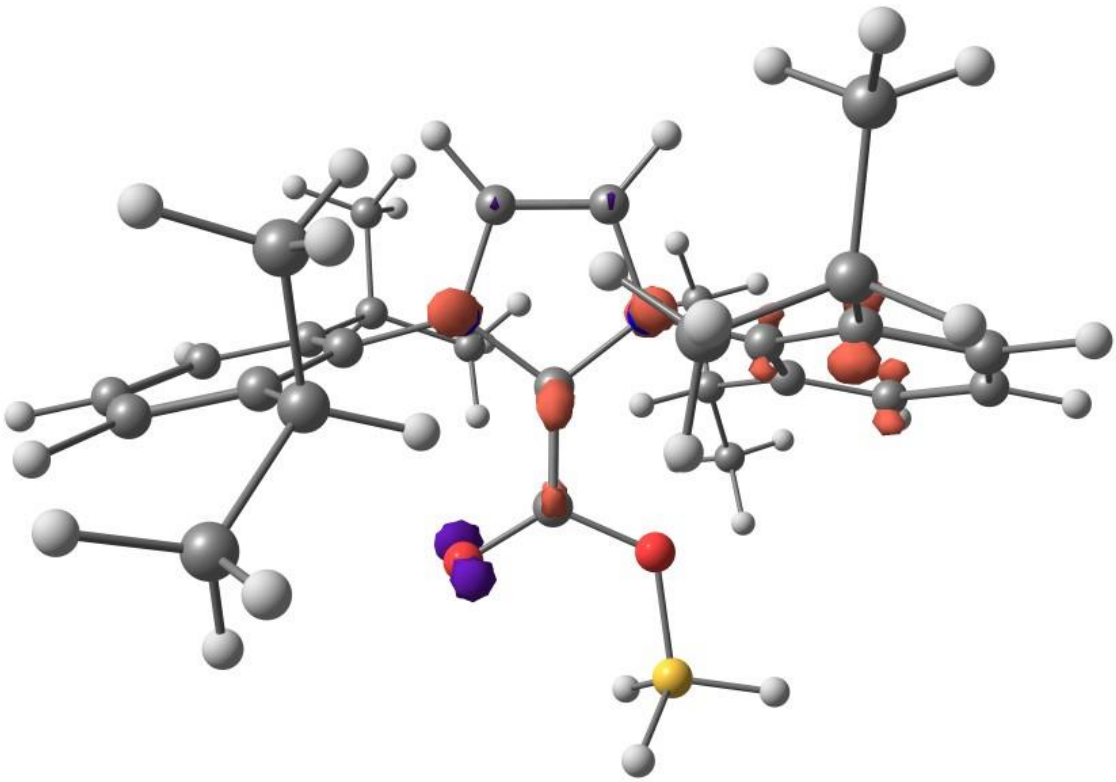

Figure 4. Spin density map of **[5-BH_3]$^{\bullet-}$** adduct. The isosurface value is 0.016.

4.3.2.2. Influence of the acidity in the spin density distribution, [NHC-CO_2-BCl_3]$^{\bullet-}$ adducts.

Using a boron Lewis acid with a higher Lewis acidity such as BCl_3, we observed that spin density can also reside at the carbon of the CO_2 moiety in monoreduced NHC-CO_2-BCl_3 (**[1-BCl_3]$^{\bullet-}$-[8-BCl_3]$^{\bullet-}$**, Scheme 12). Spin density is also located at the carbenic carbon from the NHC ring. The nitrogen and the boron atoms do not seem to change. The use of more acidic boranes such as, BCl_3, exhibits a beneficial effect on the spin density on the CO_2 moiety. Within all studied monoreduced NHC-CO_2-BCl_3 compounds, **[1-BCl_3]$^{\bullet-}$** is the monoreduced adduct that presents the highest degree of spin density at CO_2 moiety (0.42) followed by **[5-BCl_3]$^{\bullet-}$** (0.30) (Figure 5). Nevertheless, there is only 0.17 and 0.09 of spin density at the carbon atom from the CO_2 moiety, respectively (Table 7).

N-Alkyl groups

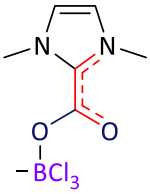

(**[1-BCl$_3$]$^{\bullet-}$**)

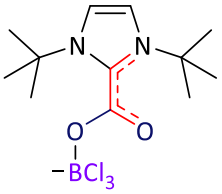

(**[2-BCl$_3$]$^{\bullet-}$**)

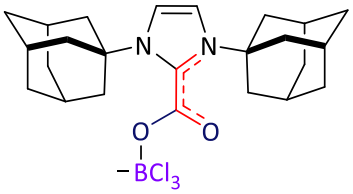

(**[3-BCl$_3$]$^{\bullet-}$**)

D(NHC-CO$_2$)	5.5	11.1	46.2

N-Aryl groups

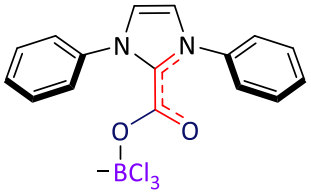

(**[4-BCl$_3$]$^{\bullet-}$**)

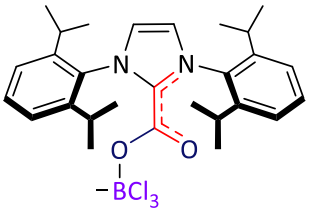

(**[5-BCl$_3$]$^{\bullet-}$**)

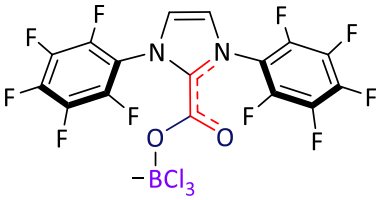

(**[6-BCl$_3$]$^{\bullet-}$**)

D(NHC-CO$_2$)	18.3	0.7	7.8

Enders and ^{Cy}CAAC-type NHCs

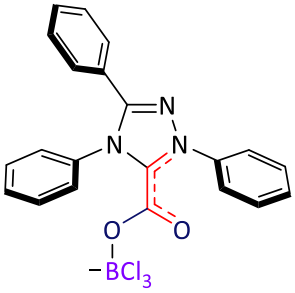

(**[7-BCl$_3$]$^{\bullet-}$**)

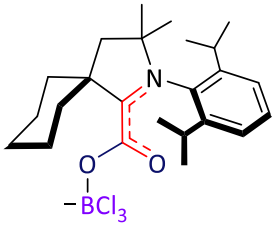

(**[8-BCl$_3$]$^{\bullet-}$**)

D(NHC-CO$_2$)	22.0	1.6

Scheme 12. Studied mononoreduced NHC-CO$_2$-BCl$_3$ adducts (**[1-BCl$_3$]$^{\bullet-}$**-**[8- BCl$_3$]$^{\bullet-}$**) and the torsion angles (D(NHC-CO$_2$)). The dihedral angles are expressed in degrees (°).

Table 7. Spin density distribution in monoreduced NHC-CO_2-BCl_3 adducts (**[1-BCl_3]$^{\bullet-}$-[8-BCl_3]$^{\bullet-}$**) in comparison to the free CO_2 radical anion.

Compounds	CO_2 moiety				NHC moiety		BR_3 moiety
	C	O (C=O)	O (C-O)	Total Spin density (CO_2)	Carbenic C	N	B
Free [CO_2]$^{\bullet-}$	0.81	0.19		1.00	-	-	-
[1-BCl_3]$^{\bullet-}$	0.17	0.21	0.04	0.42	0.20	0.30	-0.01
[2-BCl_3]$^{\bullet-}$	-0.18	0.17	0.03	0.02	0.55	0.34	0.00
[3-BCl_3]$^{\bullet-}$	0.05	0.15	0.02	0.22	0.42	0.33	0.01
[4-BCl_3]$^{\bullet-}$	0.08	0.17	0.01	0.26	0.35	0.23	0.01
[5-BCl_3]$^{\bullet-}$	0.09	0.20	0.01	0.30	0.34	0.34	0.01
[6-BCl_3]$^{\bullet-}$	0.03	0.18	0.02	0.23	0.41	0.22	0.01
[7-BCl_3]$^{\bullet-}$	0.08	0.17	0.03	0.28	0.35	0.33	0.01
[8-BCl_3]$^{\bullet-}$	0.01	0.20	0.00	0.21	0.56	0.28	0.00

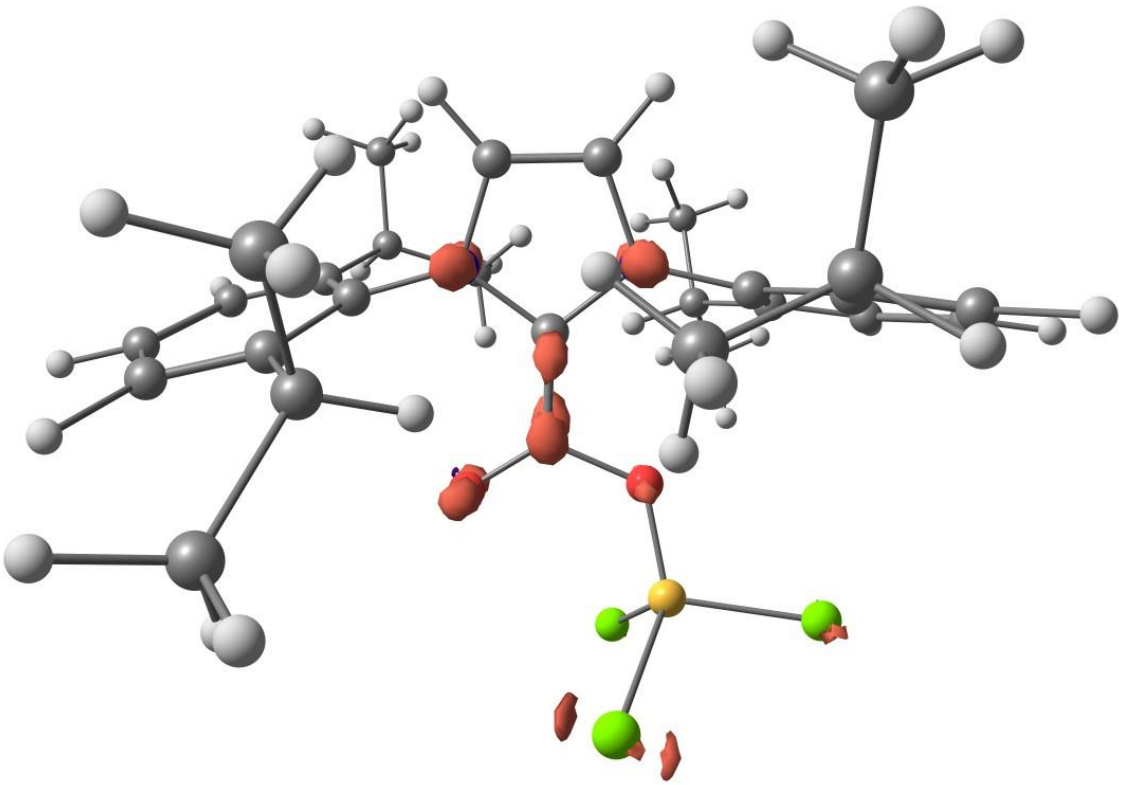

Figure 5. Spin density map of **[5-BH_3]$^{\bullet-}$** adduct. The isosurface value is 0.016.

4.3.2.3. Use of sterically hinder acidic boron Lewis acid and its impact on the spin density distribution of [NHC-CO_2-$B(C_6F_5)_3$]$^{\bullet-}$ adducts.

Using a more acidic and hindered Lewis acid respect to BH_3, $B(C_6F_5)_3$, we have access to more promising results in terms of spin density at the carbon atom of the CO_2 moiety. The adduct **[5-$B(C_6F_5)_3$]$^{\bullet-}$** exhibits 0.41 at that position, the highest value within all studied adducts (Table 9). As shown in Scheme 13, the CO_2 moiety set almost in a coplanar position respect to the NHC ring in adducts **[5-$B(C_6F_5)_3$]$^{\bullet-}$** which is translated into a higher amount of spin density at the C from the CO_2 (**[5-$B(C_6F_5)_3$]$^{\bullet-}$** (1.5 °, 0.41) and **[8-$B(C_6F_5)_3$]$^{\bullet-}$** (2.2 °, 0.33). In adduct **[5-$B(C_6F_5)_3$]$^{\bullet-}$**, more than the half of the spin density resides at the CO_2 moiety. It is followed by adduct **[1-$B(C_6F_5)_3$]$^{\bullet-}$** (0.46) and **[8-$B(C_6F_5)_3$]$^{\bullet-}$** (0.35). In the case of the nitrogen atom, there is no significant difference respect to monoreduced NHC-CO_2-BCl_3 adduct (Table 7).

N-Alkyl groups

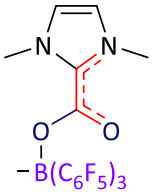

(**[1-B(C_6F_5)$_3$]$^{\bullet-}$**)

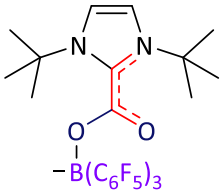

(**[2-B(C_6F_5)$_3$]$^{\bullet-}$**)

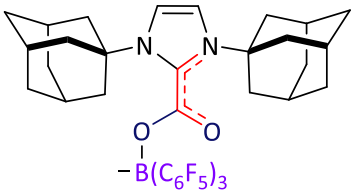

(**[3-B(C_6F_5)$_3$]$^{\bullet-}$**)

D(NHC-CO_2)	5.0	12.2	17.5

N-Aryl groups

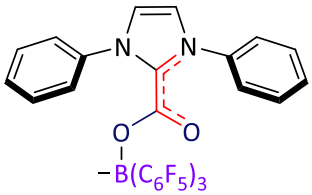

(**[4-B(C_6F_5)$_3$]$^{\bullet-}$**)

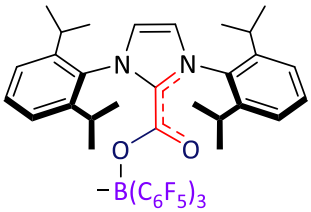

(**[5-B(C_6F_5)$_3$]$^{\bullet-}$**)

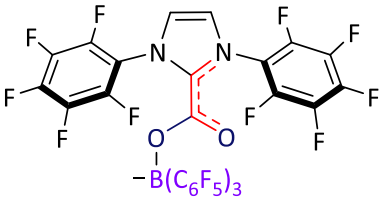

(**[6-B(C_6F_5)$_3$]$^{\bullet-}$**)

D(NHC-CO_2)	12.0	1.5	5.1

Enders and ^{Cy}CAAC-type NHCs

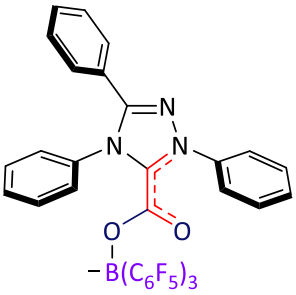

(**[7-B(C_6F_5)$_3$]$^{\bullet-}$**)

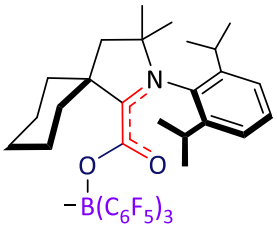

(**[8-B(C_6F_5)$_3$]$^{\bullet-}$**)

D(NHC-CO_2)	23.9	2.2

Scheme 13. Studied mononoreduced NHC-CO_2-B(C_6F_5)$_3$ adducts (**[1-B(C_6F_5)$_3$]$^{\bullet-}$-[8-B(C_6F_5)$_3$]$^{\bullet-}$**) and the torsion angle (D(NHC-CO_2)). The dihedral angles are expressed in degrees (°).

Table 8. Spin density distribution in monoreduced NHC-CO_2-$B(C_6F_5)_3$ adducts (**[1-$B(C_6F_5)_3]^{\bullet-}$-[8-$B(C_6F_5)_3]^{\bullet-}$**) in comparison to the free CO_2 radical anion.

Compounds	CO_2 moiety				NHC moiety		BR_3 moiety
	C	O (C=O)	O (C-O)	Total Spin density (CO_2)	Carbenic C	N	B
Free $[CO_2]^{\bullet-}$	0.81	0.19		1.00	-	-	-
[1-$B(C_6F_5)_3]^{\bullet-}$	0.22	0.18	0.06	0.46	0.22	0.30	0.06
[2-$B(C_6F_5)_3]^{\bullet-}$	0.13	0.14	0.04	0.31	0.30	0.33	0.00
[3-$B(C_6F_5)_3]^{\bullet-}$	0.01	0.11	0.05	0.17	0.35	0.33	-0.01
[4-$B(C_6F_5)_3]^{\bullet-}$	0.06	0.14	0.04	0.24	0.30	0.29	0.00
[5-$B(C_6F_5)_3]^{\bullet-}$	0.41	0.14	-0.04	0.51	0.57	0.17	0.02
[6-$B(C_6F_5)_3]^{\bullet-}$	0.08	0.16	0.05	0.29	0.38	0.22	0.02
[7-$B(C_6F_5)_3]^{\bullet-}$	-0.01	0.14	0.04	0.17	0.33	0.34	0.01
[8-$B(C_6F_5)_3]^{\bullet-}$	0.33	0.12	0.00	0.45	0.69	0.23	0.04

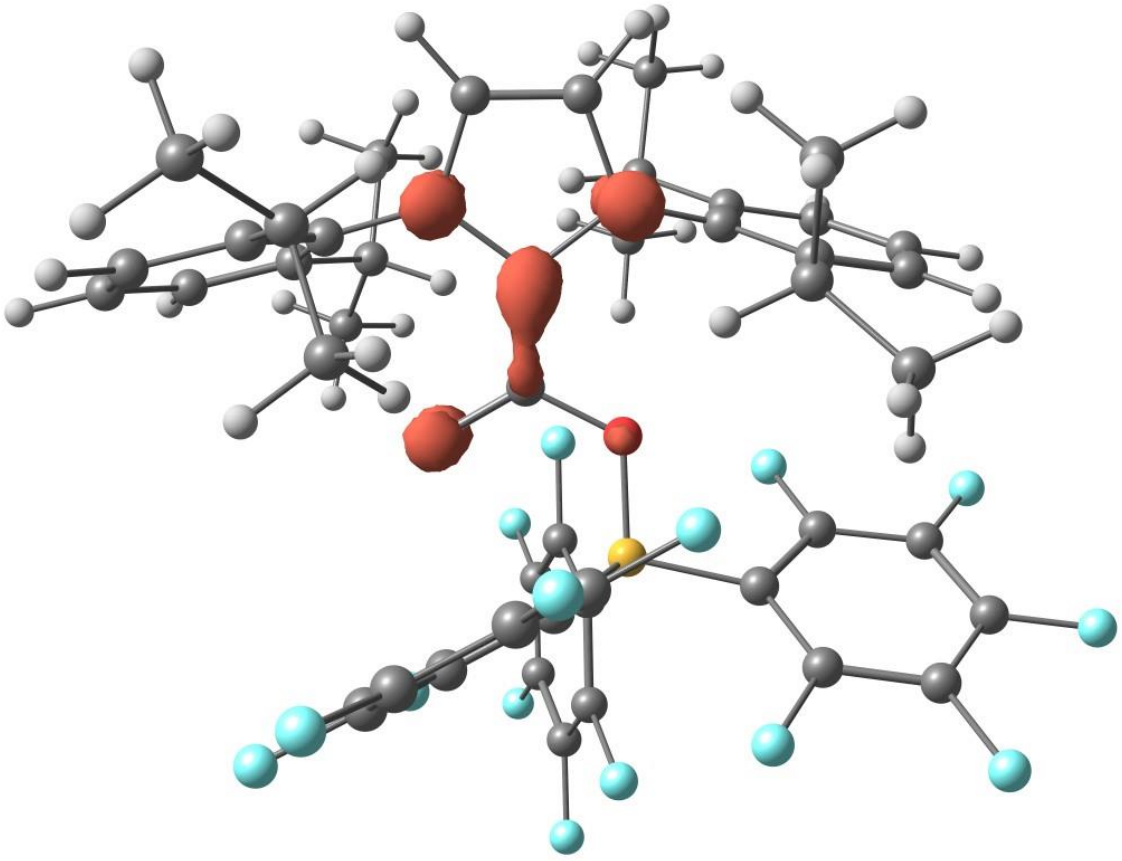

Figure 6. Spin density map of **[5-$B(C_6F_5)_3]^{\bullet-}$** adduct. The isosurface value is 0.016.

4.3.3. Spin population distribution and electron paramagnetic resonance (EPR)

In this section, we aimed at qualitatively correlating the spin population distribution of the radical anion and the hyperfine coupling constant associated with the nitrogen atom (a_N). The EPR is a technique which measures the absorption of microwave by paramagnetic centres with one or more unpaired electrons.[11] In our study, they are species originated from the one electron reduction of NHC-CO_2-based species. The final compound will solely exhibit one unpaired electron which interacts with the nitrogen nuclear moment as explained in the previous Chapter 3, section 3.3. "One electron reduction by chemical means: Synthesis and characterisation of monoreduced species." As a reminder, adducts **[8(K)]•** and **[8-B(C_6F_5)$_3$(K)]•** exhibit experimental coupling constants of 6.16 G and 6.01 G, respectively. With the addition of the borane (**[8-B(C_6F_5)$_3$(K)]•**), the coupling constant is slightly lower than in **[8(K)]•**. In the case of **[5-B(C_6F_5)$_3$(K)]•**, the coupling constant is 4.45 G which is lower than in both precedented adducts, **[8(K)]•** and **[8-B(C_6F_5)$_3$(K)]•**.

A lower value as coupling constant can be translated into a lower amount of spin density at an adjacent position to couple with the nitrogen atom, the carbenic carbon position. We preliminarily hypothesised that the spin density at the CO_2 might be increased if the spin density at the carbenic carbon is decreased (lower a_N value).

In Chapter 4, section 4.3. "Spin density distribution in monoreduced NHC-CO_2 and NHC-CO_2-BR_3 adducts.", we have previously observed that part of the spin density resides at the π-vacant orbital at the carbenic carbon of the NHC ring, among other parts. Depending on the spin density at that position, the spin coupling constant with the nitrogen atom (a_N) will be higher or lower. The coupling between the unpaired electron and the nitrogen nuclear moment will be enhanced with a higher amount of spin density at the carbenic carbon and, vice versa.

X-band EPR spectra were computed from the previously optimised structures via DFT means for the radical anions **[8]•⁻**, **[5-B(C_6F_5)]•⁻**, **[8-B(C_6F_5)$_3$]•⁻**. In our model, the adducts were considered as radical anions in the absence of the counterion (K^+). Despite not having considered the counterion for the calculation, the computed data relatively agrees with the experimental results. Firstly, we tested as a basis set EPR-III which has

been exclusively developed to simulate EPR spectra.[12] EPR-III is a triple-zeta basis set including diffuse functions, double *d*-polarisations, and a single set of *f*-polarisation functions. Nevertheless, only the simulated EPR spectrum for adduct **[8]•⁻** was obtained (g = 2.00302; a_N = 4.87 G using M06-2X). Despite several attempts we could not obtain the computed EPR spectra for adducts **[5-B(C_6F_5)]•⁻** and **[8-B(C_6F_5)]•⁻** as they could not be converged in the Self-Consistent Field (SCF) calculation. Inspired by a work from Garribba[13] and colleagues, we computed EPR spectrum **[8]•** following their methodology. It consisted of a triple-zeta with a polarisation function basis set, 6-311G(d,p), including SOMF(1X)[14] as an additional keyword that accelerated the calculations of integrals in the spin-orbit coupling calculation part (prior to the formal calculation of EPR parameters). The use of a smaller basis set instead of EPR-III is good alternative for large molecules.[15] We obtained similar results to the ones obtained with the basis set EPR-III along with a drastic reduction in computation time (from day to minutes) (**[8]•⁻**, g = 2.00347; a_N = 4.61 G using M06-2X) and more importantly, the EPR spectra for adducts **[5-B(C_6F_5)]•⁻** and **[8-B(C_6F_5)]•⁻** could be also computed. We also performed an exploratory study to determine which functional provides more accurate simulated EPR spectra. The functionals M06-2X and B3LYP show similar performance in the calculation of g-value. However, M06-2X provides a_N values significantly closer to the experimental ones (Table 9). For this reason, the EPR parameters obtained with the functional M06-2X were used to construct Figures 7-9.

Table 9. Experimental and theoretical EPR parameters calculated with the functionals M06-2X and B3LYP using 6-311G(d,p) as a basis set in tetrahydrofuran. The experimental values correspond to adducts **[5-B(C_6F_5)$_3$(K)]•**, **[8(K)]•** and **[8-B(C_6F_5)$_3$(K)]•**.

Density Functional	M06-2X	B3LYP-D3	Experimental
g-factor (**[5-B(C_6F_5)$_3$]•⁻**)	2.00407	2.00368	2.00375
a_N (**[5-B(C_6F_5)$_3$]•⁻**)	5.22	3.35	4.45
g-factor (**[8]•⁻**)	2.00345	2.00329	2.00253
a_N (**[8]•⁻**)	4.61	3.19	6.16
g-factor (**[8-B(C_6F_5)$_3$]•⁻**)	2.00388	2.00355	2.00347
a_N (**[8-B(C_6F_5)$_3$]•⁻**)	5.89	3.66	6.01

Table 10. Experimental and computed hyperfine coupling constant (a_N) for adducts **[8(K)]•**, **[5-B(C_6F_5)$_3$(K)]•** and **[8-B(C_6F_5)$_3$(K)]•** along with the spin population at the C of the CO_2 moiety, carbenic carbon and nitrogen atom. The experimental values correspond to adducts **[5-B(C_6F_5)$_3$(K)]•**, **[8(K)]•** and **[8-B(C_6F_5)$_3$(K)]•**.

Adducts	Spin Population			a_N/G	
	C (CO_2)	Carbenic C	N	Experimental	Simulation
[5-B(C_6F_5)$_3$]•⁻	0.42	0.30	0.29	4.45	5.22
[8]•⁻	0.00	0.61	0.22	6.16	4.61
[8-B(C_6F_5)$_3$]•⁻	0.33	0.69	0.23	6.01	5.89

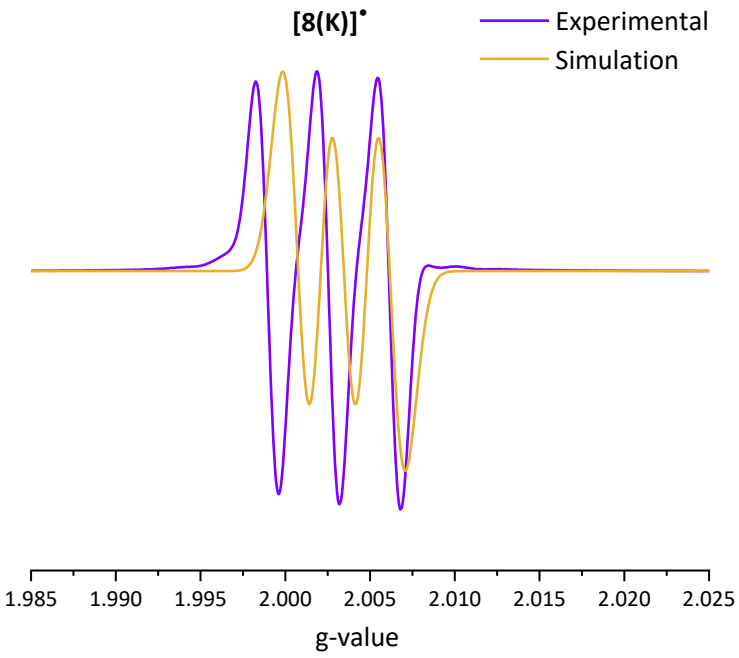

Figure 7. Experimental and calculated EPR spectra of adduct **[8(K)]•** in tetrahydrofuran.

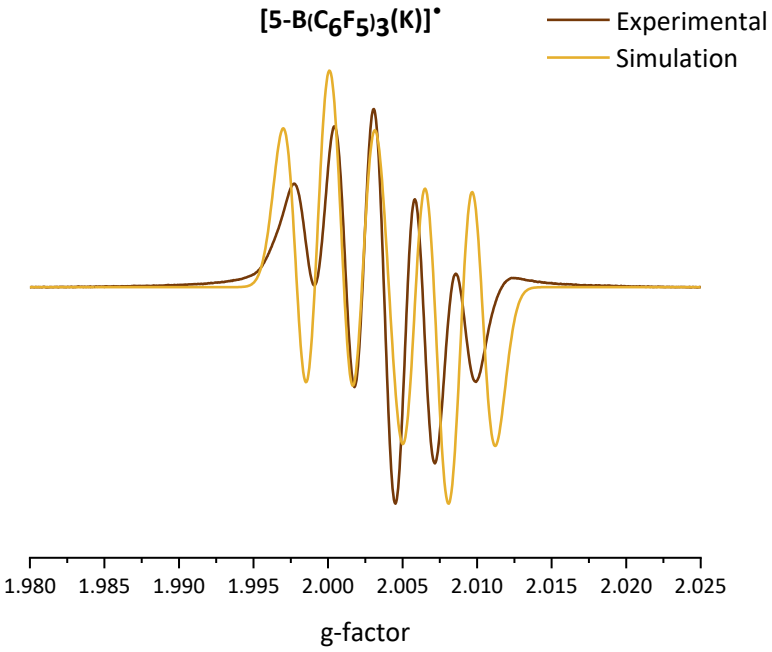

Figure 8. Experimental and calculated EPR spectra of adduct **[5-B(C$_6$F$_5$)$_3$]$^\bullet$** in tetrahydrofuran.

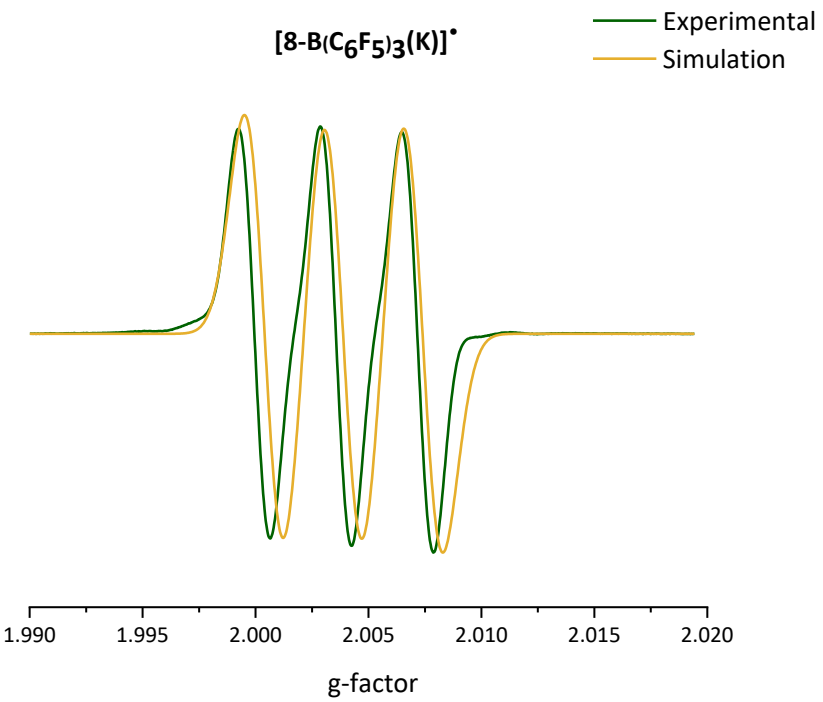

Figure 9. Experimental and calculated EPR spectra of adduct **[8-B(C_6F_5)$_3$]•** in tetrahydrofuran.

As shown in Table 10, the hyperfine coupling constant between the unpaired electron and the nitrogen atom indirectly is correlated to the spin population at the C of the CO_2 moiety. Further investigations will be carried out in the simulation of EPR spectra of adducts **[8(K)]•** (Figure 7) and **[5-B(C_6F_5)$_3$]•** (Figure 8) to improve the fitting with the experimental ones.

4.4. Orbital description of NHC-CO_2-based adducts.

In this section, the frontier orbitals of NHC-CO_2-based adducts will be described. In the case of the neutral adducts, the Highest Occupied Molecular Orbital (HOMO) and the Lowest Occupied Molecular Orbital (LUMO). Whereas in monoreduced species, only the Singly Occupied Molecular Orbital (SOMO) will be presented. In the case of LUMO (in neutral adducts) and SOMO (in monoreduced adducts) will be treated in the same section. These orbitals have been constructed via DFT means described in Chapter 2.

4.4.1. Localisation of the HOMO orbital in NHC-CO_2-based adducts and its energy.

In this subsection, the localisation of the HOMO and its energy for all adducts will be discussed. Firstly, NHC-CO_2 adducts will be treated followed by NHC-CO_2-BR_3 adducts as in previous discussions.

4.4.1.1. Localisation of the HOMO orbital in NHC-CO_2 adducts (1-8) and its energy.

As shown in Figure 10, the localisation of the HOMO orbital in the NHC-CO_2 adducts depends on the morphology of the NHC moiety. In the case of adducts **1**-**3**, the HOMO is localised in the core of the NHC ring (backbone, nitrogen atoms and carbenic carbon) and on both oxygen atoms of the CO_2 unit. The HOMO is not delocalised over the *N*-tethered groups (methyl (**1**), tert-butyl (**2**) and adamantyl (**3**)). In contrast to the latter, the HOMO in adducts **4**-**6** is mainly localised on the *N*-tethered aryl derivatives. Unlike **5** and **6**, part of the HOMO is localised at the nitrogen atoms in adduct **4**. As adducts **1**-**3**, part of the HOMO is also localised at the oxygen atoms (**4**-**6**). In the case of adducts **7** and **8**, the HOMO is not distributed as in previous examples. In adduct **7**, the HOMO is delocalised all over the molecule (core NHC, *N*-substituents and oxygen atoms) whereas it is focussed on the *N*-tethered aryl-based substituent in adduct **8**. Regarding the HOMO energies, they are from -8.72 eV to -8.02 eV (a difference of 0.70 eV). Within all studied adducts, the HOMO of adduct **6** is the most stable (-8.72 eV). This adduct presents as a *N*-substituents, highly electron-withdrawing groups which decrease the energy of the HOMO.

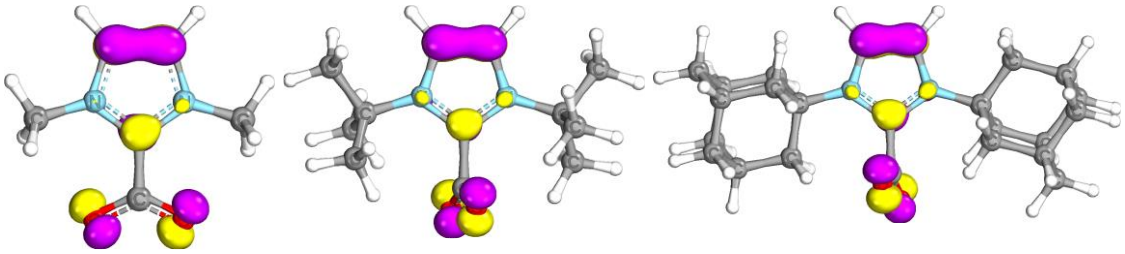

	(**1**)	(**2**)	(**3**)
E(HOMO)	-8.47	-8.12	-8.08

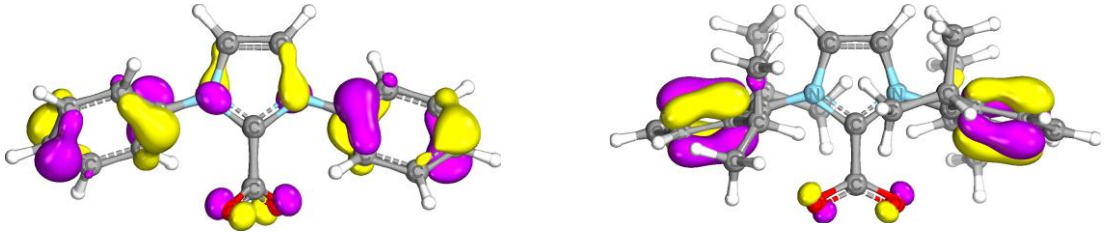

	(**4**)	(**5**)
E(HOMO)	-8.34	-8.03

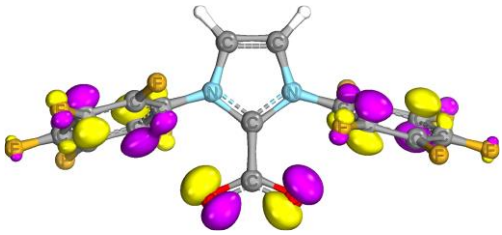

	(**6**)
E(HOMO)	-8.72

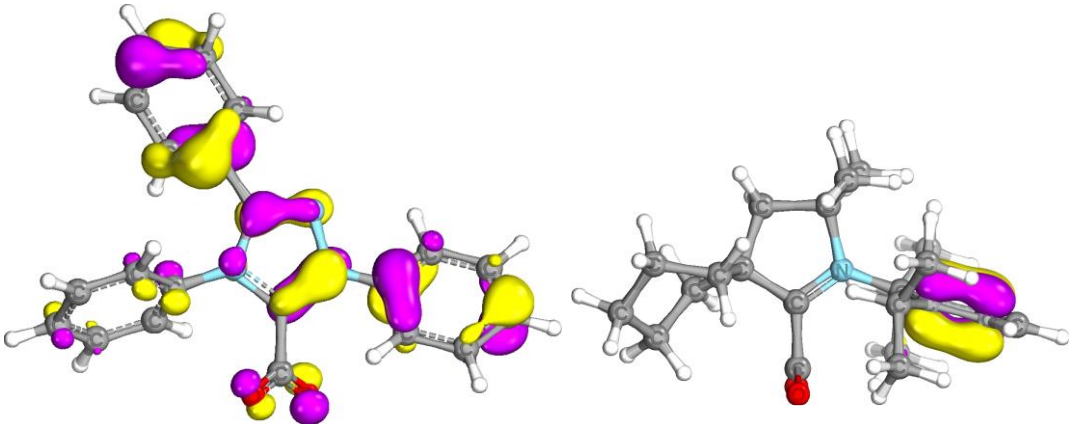

	(**7**)	(**8**)
E(HOMO)	-8.24	-8.02

Figure 10. Localisation of the HOMO in NHC-CO_2 adducts (**1**-**8**) and its energy expressed in electron-volts (eV). The isosurface threshold value is 45% and the resolution, 12/Å.

4.4.1.2. Localisation of the HOMO in NHC-CO_2-BH_3 adducts ((1-8)-BH_3) and its energy.

As in previous discussions in this chapter, the NHC-CO_2-based adducts with a BH_3 unit (NHC-CO_2-BH_3) were described at first instance in order to employ it as reference respect to others NHC-CO_2-BR_3 adducts (BR_3: $B(C_6F_5)_3$ and BCl_3) that will be described later. As shown in Figure 11, the HOMO in adducts whose *N*-substituents are alkyl groups ((**1**-**3**)-**BH_3**) is delocalised over the NHC ring (backbone, nitrogen atoms and carbenic carbon) and oxygen atoms as in their equivalents without borane (**1**-**3**). In adducts **1-BH_3** and **2-BH_3**, part of the HOMO is also localised at the B-H bonds. In adducts with aryl derivatives as *N*-tethered groups, (**4**-**6**)-**BH_3**, a clear trend cannot be observed. In the case of adduct **4-BH_3**, the HOMO is delocalised over all the adduct as in the absence of any borane (**4**), **5-BH_3** focalises the totality of the HOMO on one substituted aryl derivative group and **6-BH_3** on oxygen atoms and borane. Regarding the energies, as expected, the energy of the HOMO decreases with the addition of the borane. They range from -8.84 eV to -8.12 eV, a difference of 0.72 eV can be observed that does not differ from the difference of energies found in NHC-CO_2 adducts (0.72 eV). The addition of the borane to NHC-CO_2 adduct does not have a significant impact on the energy of the HOMO, only in adducts **2-BH_3** (0.58 eV) and **3-BH_3** (0.57 eV). In the rest of the adducts ((**1**, **4**-**8**)-**BH_3**)), the HOMO energy decreases between 0.21 eV to 0.09 eV respect to NHC-CO_2 adducts. The adduct **6-BH_3** is the one whose HOMO is the most stable (-8.84 eV) within all the studied NHC-CO_2-BH_3 adducts.

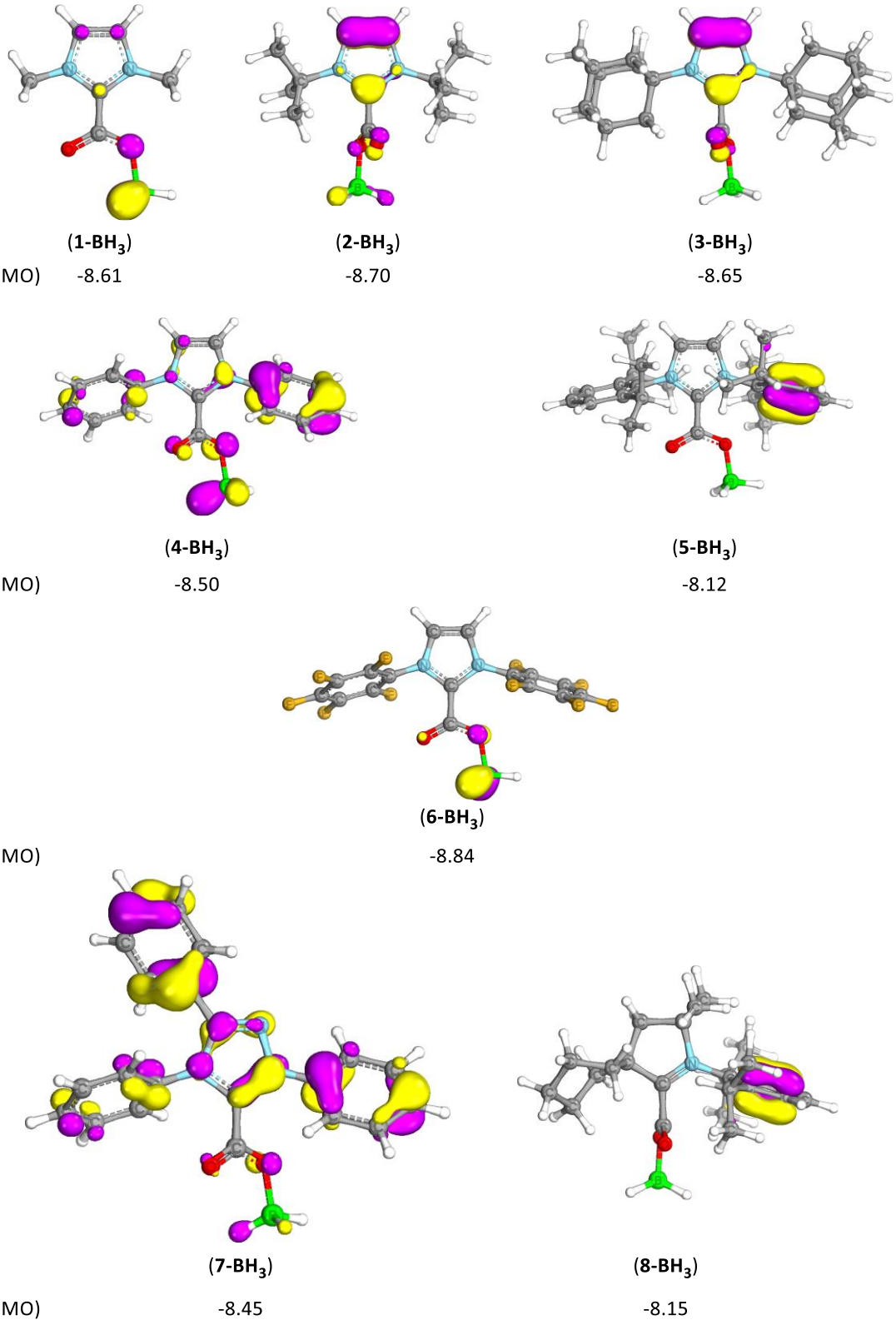

Figure 11. Localisation of the HOMO in NHC-CO_2-BH_3 adducts ((**1**-**8**)-**BH_3**) and its energy expressed in electron-volts (eV). The isosurface threshold value is 45% and the resolution, 12/Å.

4.4.1.3. Localisation of the HOMO in NHC-CO_2-BCl_3 adducts ((1-8)-BCl_3) and its energy.

Replacing the borane unit by a more acidic one, BCl_3, does not have significant impact on the localisation of HOMO on the adduct (Figure 12). In the case of adduct **1-BCl_3**, the HOMO is exclusively localised at the chlorine atoms from the borane unit. In adducts **2-BCl_3** and **3-BCl_3**, the HOMO is localised as in their respective equivalent NHC-CO_2 adducts (**2** and **3**). The HOMO is delocalised over the NHC ring (carbenic carbon, nitrogen atoms and backbone) and at the oxygen atoms from CO_2 moiety. In adducts whose *N*-substituents are aryl derivatives, (**4**-**6**)-**BCl_3**, there are slight differences between them. In the case of adduct **4-BCl_3**, the HOMO is delocalised all over the adduct except on the borane unit. Whereas the HOMO in adducts **5-BCl_3** and **6-BCl_3** only resides in one of the *N*-substituents. In adduct **7-BCl_3**, the HOMO is all over the adduct except on the CO_2 and BCl_3 moiety. IN adduct **8-BCl_3**, the addition of a more acidic borane does not affect the LUMO distribution respect to **8-BH_3**. The addition of a Lewis acid which exhibits a higher acidity enhances the stabilisation of the HOMO in all cases. The energies are from -8.94 eV to -8.12 eV (a difference of 0.72 eV). Compared to NHC-CO_2-BH_3 adducts, the energies are slightly lower than in the case of NHC-CO_2-BCl_3. The one that exhibits the lowest HOMO energy is as in previous cases, **6-BCl_3** whose *N*-substituents are perfluorinated aryl derivatives.

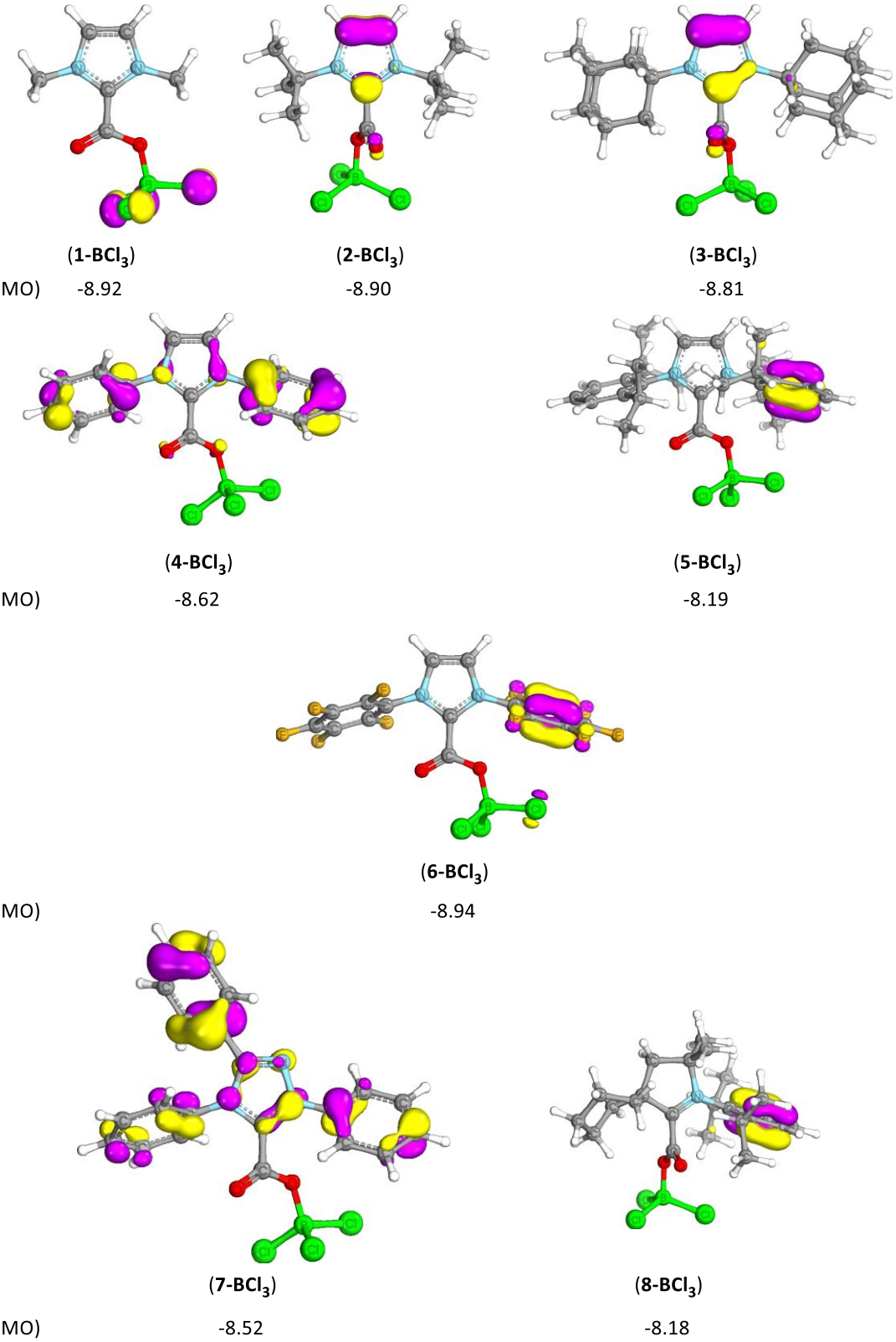

Figure 12. Localisation of the HOMO in NHC-CO_2-BCl_3 adducts ((**1**-**8**)-**BCl_3**) and its energy expressed in electron-volts (eV). The isosurface threshold value is 45% and the resolution, 12/Å.

4.4.1.4. Localisation of the HOMO in NHC-CO_2-$B(C_6F_5)_3$ adducts ((1-8)-$B(C_6F_5)_3$) and its energy.

As shown in Figure 13, the HOMO in NHC-CO_2-$B(C_6F_5)_3$ is mainly delocalised in the perfluorinated substituents of the borane moiety and in a lesser degree at the oxygen atoms. In adducts **5-$B(C_6F_5)_3$)** and **8-$B(C_6F_5)_3$**, part of the HOMO is also delocalised on the aryl derivatives. Surprisingly, replacing BH_3 by a more sterically hindered and acidic borane, $B(C_6F_5)_3$, negatively affects the stability of the HOMO. The energy of the HOMO orbital in NHC-CO_2-$B(C_6F_5)_3$ adducts goes from -8.17 eV to -8.05 eV (a difference of 0.12 eV). There are not significant changes in the HOMO energies within the NHC-CO_2-$B(C_6F_5)_3$ adducts. Instead of decreasing the energy of the HOMO, the replacement of BH_3 by $B(C_6F_5)_3$ increases the energy of the HOMO from 0.07 eV to 0.67 eV. It is the compound **6-$B(C_6F_5)_3$** the one that presents the most stable HOMO (-8.17 eV) and even so the one that suffers the highest destabilisation respect to its analogous **6-BH_3** (-8.84 eV).

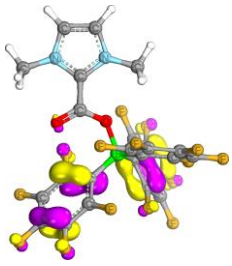

(**1**-**B**(C_6F_5)$_3$)

E(HOMO) -8.13

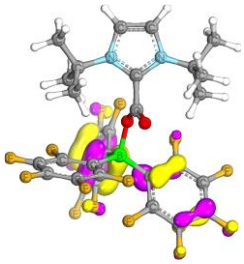

(**2**-**B**(C_6F_5)$_3$)

-8.13

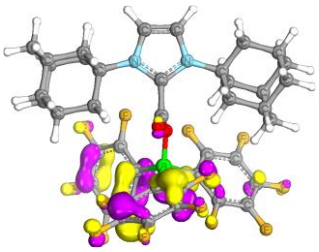

(**3**-**B**(C_6F_5)$_3$)

-8.12

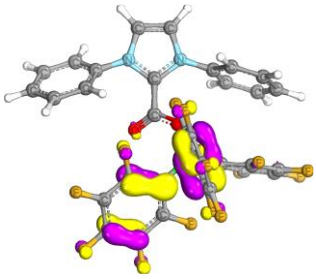

(**4**-**B**(C_6F_5)$_3$)

E(HOMO) -8.12

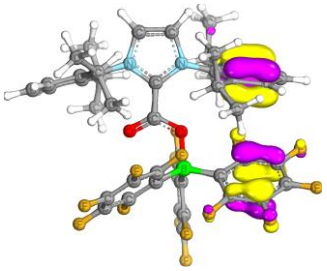

(**5**-**B**(C_6F_5)$_3$)

-8.05

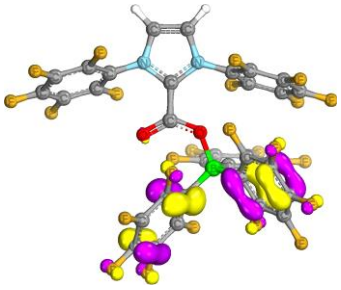

(**6**-**B**(C_6F_5)$_3$)

E(HOMO) -8.17

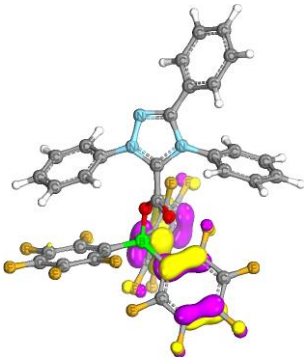

(**7**-**B**(C_6F_5)$_3$)

E(HOMO) -8.14

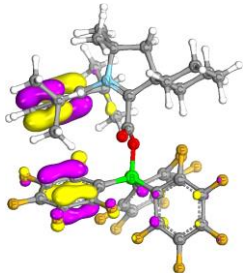

(**8**-**B**(C_6F_5)$_3$)

-8.06

Figure 13. Localisation of the HOMO in NHC-CO_2-B(C_6F_5)$_3$ adducts ((**1**-**8**)-**B**(C_6F_5)$_3$) and its energy expressed in electron-volts (eV). The isosurface threshold value is 45% and the resolution, 12/Å.

4.4.2. Localisation of the LUMO and SOMO orbital in NHC-CO_2-based adducts and their energy.

In this subsection, the localisation of the LUMO from neutral NHC-CO_2-based adducts along with its energy and the localisation of the SOMO (resulting orbital after the addition of one electron into the neutral adduct) and its energy from the monoreduced NHC-CO_2-based adducts will be treated together. It has been found that the localisation of the LUMO of neutral adducts is nearly identical to the SOMO in monoreduced NHC-CO_2-based adducts as it can be appreciated in Figures 14-21. Firstly, NHC-CO_2 adducts will be treated followed by NHC-CO_2-BR_3 as in previous discussions.

4.4.2.1. Localisation of the LUMO and SOMO orbitals in NHC-CO_2 adducts and its energy.

All studied adducts exhibit a common feature about the disposition of the LUMO and SOMO orbitals (except adduct **7** and **[7]**$^{\bullet-}$ that will be described later in this section). These orbitals are delocalised at the carbenic carbon, nitrogen and both oxygen atoms from the CO_2 moiety (Figures 14 and 15). Depending on the coplanarity of the CO_2 unit respect to the NHC ring, part of the LUMO/SOMO can also be observed at the carbon atom of the CO_2 unit. Part of the LUMO and SOMO can be also observed in a lesser degree on the *N*-tethered aryl groups. In the case of **7** and **[7]**$^{\bullet-}$, the LUMO and SOMO respectively, are only delocalised on the aromatic ring of the adducts and, at the nitrogen atoms in a lesser degree. No LUMO and SOMO is found either at the carbenic carbon or carbon from the CO_2 moiety in adducts **7** and **[7]**$^{\bullet-}$.

The energy of the LUMO is between -0.77 eV to 0.88 eV (a difference of 1.65 eV, a higher difference than in the case of the HOMO orbital previously discussed in section 4.4.1.1. in this chapter). The adduct that presents the lowest LUMO (more negative energy) is adduct **6**. In the case of the SOMO orbital, it ranges from -4.15 eV to -3.20 eV (a difference of 0.95 eV). The adduct that exhibits the SOMO lowest in energy is **[8]**$^{\bullet-}$ (-4.15 eV).

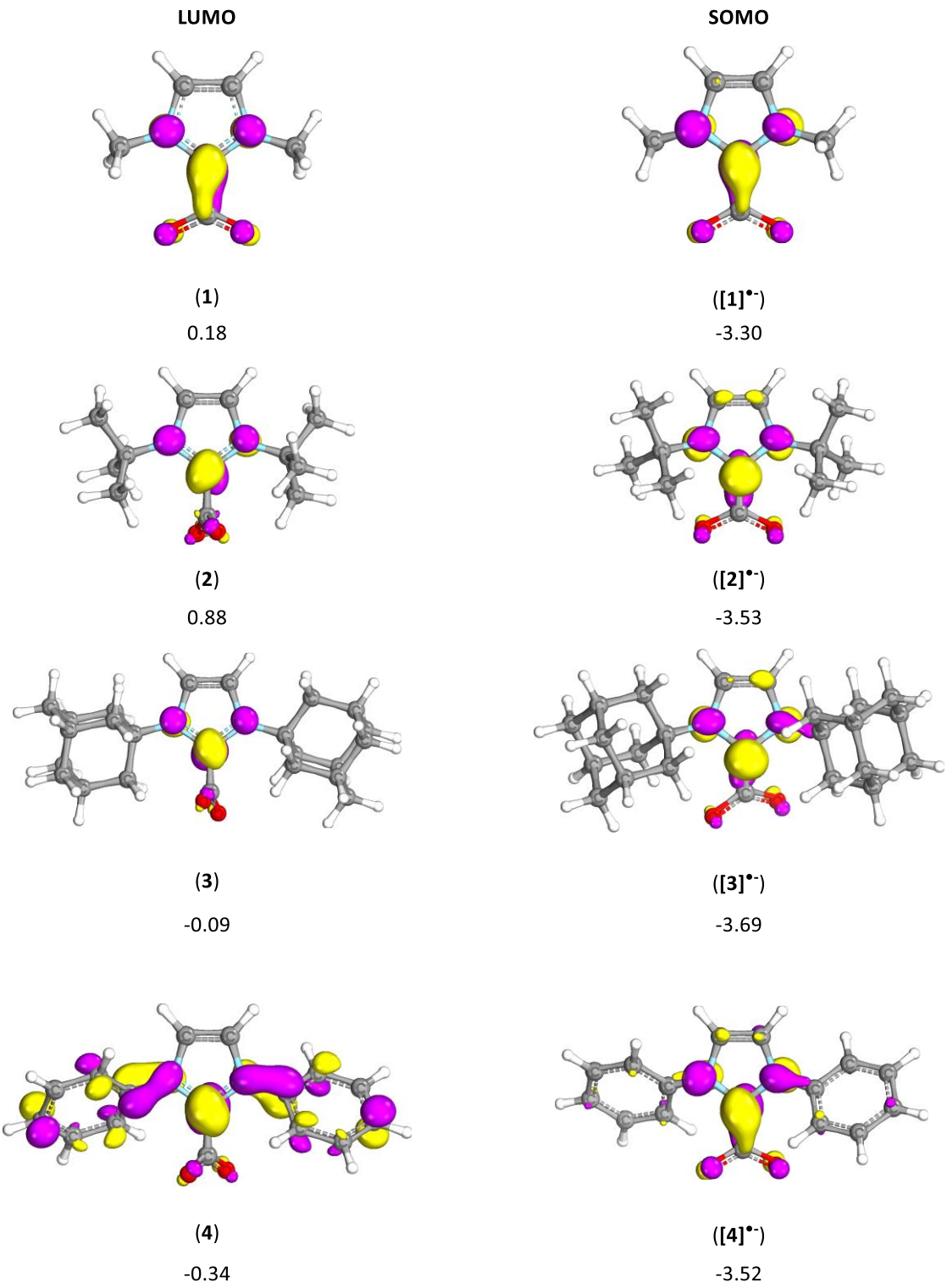

Figure 14. Localisation of the LUMO in NHC-CO_2 adducts (**1**-**4**) and its energy below (left) and localisation of the SOMO in monoreduced NHC-CO_2 adducts (**[1]**$^{\bullet-}$-**[4]**$^{\bullet-}$) and its energy below (right). The energies associated to each orbital was expressed in electron-volts (eV). The isosurface threshold value is 45% and the resolution, 12/Å.

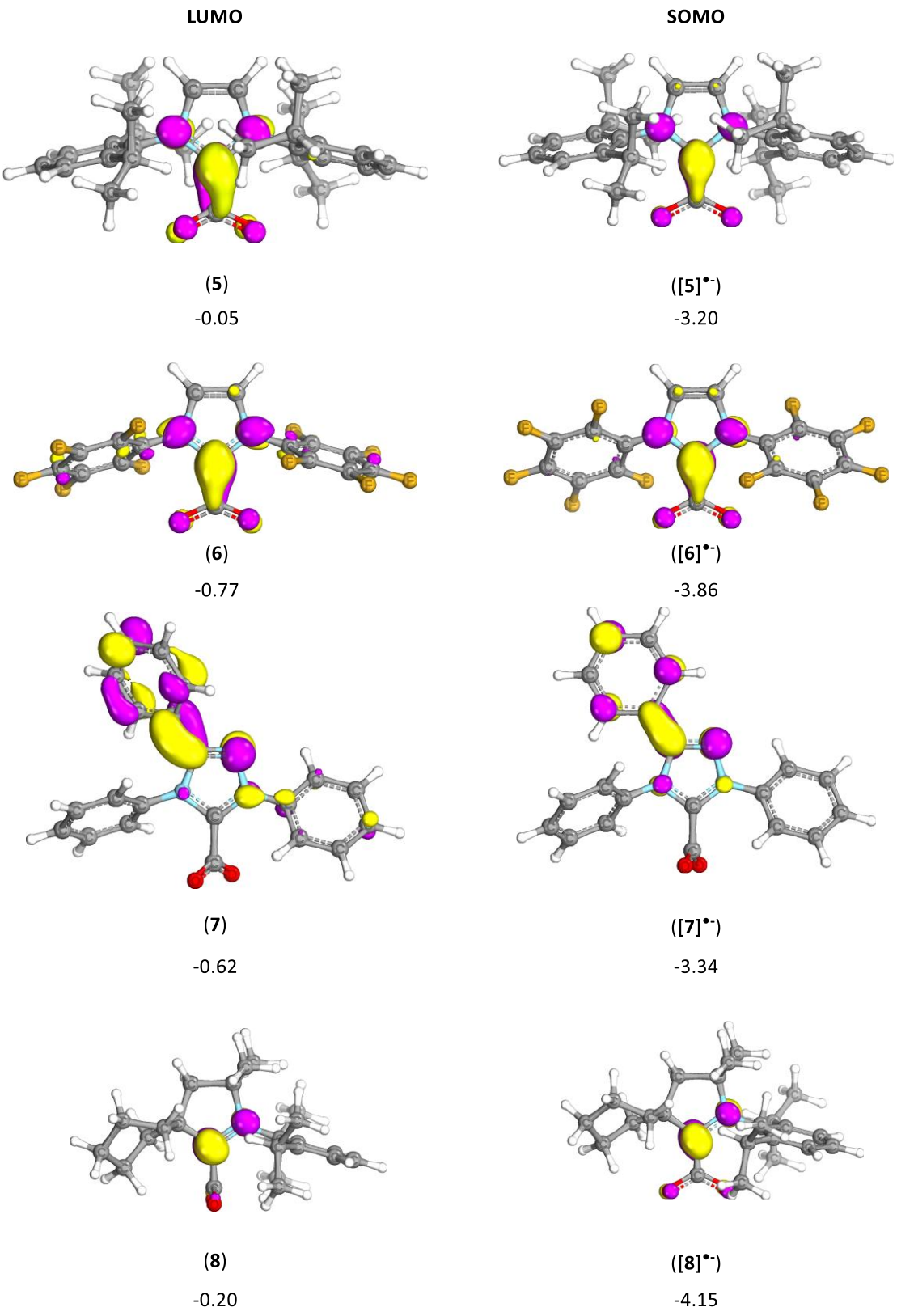

Figure 15. Localisation of the LUMO in NHC-CO_2 adducts (**5**-**8**) and its energy below (left) and localisation of the SOMO in monoreduced NHC-CO_2 adducts (**[5]**$^{\bullet-}$-**[8]**$^{\bullet-}$) and its

energy below (right). The energies associated to each orbital was expressed in electron-volts (eV). The isosurface threshold value is 45% and the resolution, 12/Å.

4.4.2.2. Localisation of the LUMO and SOMO orbitals in NHC-CO_2-BH_3 adducts and its energy.

In all NHC-CO_2-BH_3 adducts, as in NHC-CO_2 adducts, the LUMO and SOMO is distributed at the carbenic carbon, nitrogen and both oxygen atoms from the CO_2 moiety (Figures 16 and 17). Unlike in adduct NHC-CO_2 adducts, the addition of BH_3 to the NHC-CO_2 adducts makes possible the extension of the LUMO over the carbon of the CO_2 moiety regardless the torsion angle between the NHC ring and the CO_2 moiety (D(NHC-CO_2)). In the case of **7-BH_3** and **[7-BH_3]$^{\bullet-}$**, a remarkably difference respect to **7** and **[7]$^{\bullet-}$** can be noticed. The addition of the borane to **7** enables that part of the LUMO and SOMO occupy the carbenic carbon and, the carbon from the CO_2 moiety. In adduct **4-BH_3**, part of the LUMO also is delocalised through the B-H bonds.

In terms of energy, the LUMO ranges from -1.38 eV to 0.45 eV (a difference of 1.83 eV). The adduct that presents the lowest LUMO (more negative energy) is adduct **5-BH_3**. Surprisingly, the LUMO of adduct **3-BH_3** exhibits an energy at 0.45 eV followed by **2-BH3** at -0.04 eV. There is a large difference between them despite the fact of possessing a similar morphology. In the case of the SOMO orbital, it is from -4.73 eV to -3.67 eV (a difference of 1.06 eV). The adduct **[8-BH_3]$^{\bullet-}$** exhibits the SOMO with the lowest energy (more negative energy) at -4.73 eV within all [NHC-CO_2-BH_3]$^{\bullet-}$ adducts. The addition of the borane makes more stable the adduct, the SOMO of **[8-BH_3]$^{\bullet-}$** is 0.58 eV lower in energy than in adduct **[8]$^{\bullet-}$**.

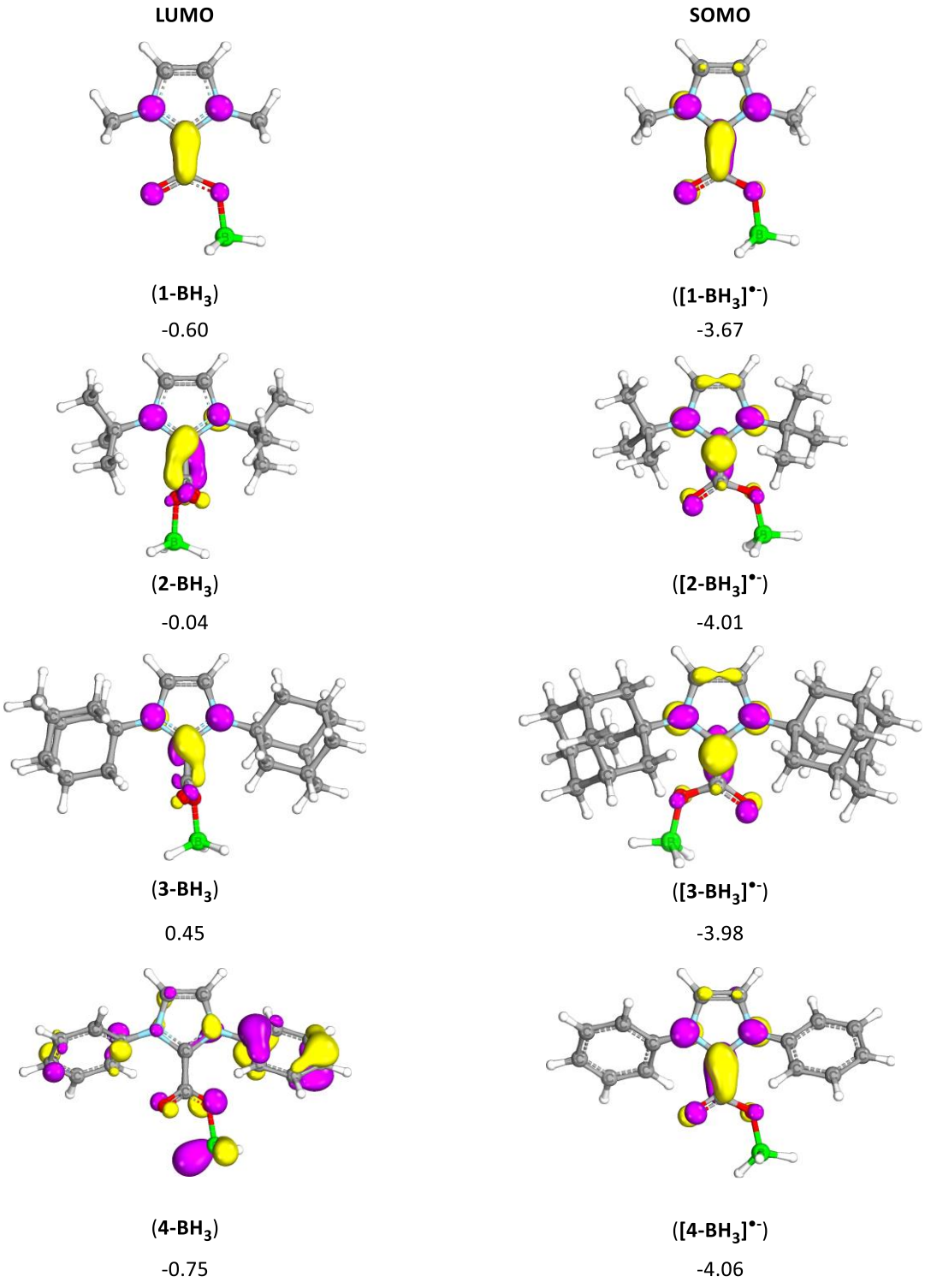

Figure 16. Localisation of the LUMO in NHC-CO_2-BH_3 adducts ((**1**-**4**)-**BH_3**) and its energy below (left) and localisation of the SOMO in monoreduced NHC-CO_2 adducts ((**[5]$^{\bullet-}$**-**[8]$^{\bullet-}$**)-**BH_3**) and its energy below (right). The energies associated to each orbital was expressed in electron-volts (eV). The isosurface threshold value is 45% and the resolution, 12/Å.

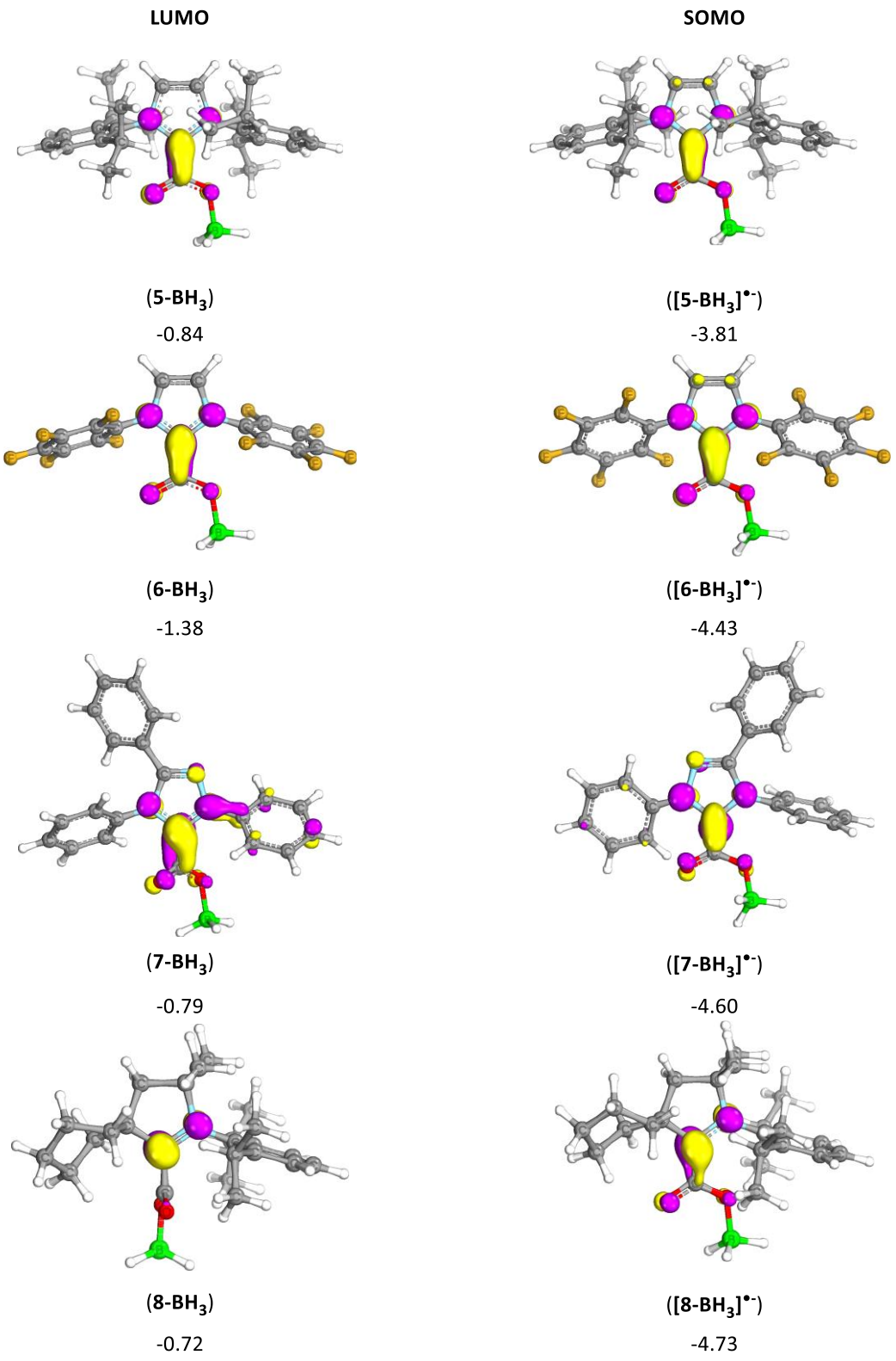

Figure 17. Localisation of the LUMO in NHC-CO_2-BH_3 adducts ((**5**-**8**)-**BH_3**) and its energy below (left) and localisation of the SOMO in monoreduced NHC-CO_2-BH_3 adducts ((**[5]$^{\bullet-}$**-**[8]$^{\bullet-}$**)-**BH_3**) and its energy below (right). The energies associated to each orbital was

expressed in electron-volts (eV). The isosurface threshold value is 45% and the resolution, 12/Å.

4.4.2.3. Localisation of the LUMO and SOMO orbitals in NHC-CO_2-BCl_3 adducts and its energy.

Replacing the borane unit by a more acidic one, BCl_3, does not significantly affect the localisation of LUMO and SOMO on the adduct respect to NHC-CO_2-BH_3 and [NHC-CO_2-BH_3]$^{\bullet-}$ adducts, respectively (Figures 18 and 19). A remarkable difference respect to previous adducts is that the LUMO and SOMO orbitals are not delocalised over the *N*-substituents in adducts which possess aryl derivatives on their structure. Only in **7-BCl_3**, in a lesser degree compared to other positions. The LUMO and SOMO orbitals are distributed over the NHC ring (carbenic carbon nitrogen atoms and backbone (this latter only the SOMO orbital) and on the CO_2 moiety. The energies of the LUMO range between -1.73 eV to 0.01 eV (a difference of 1.74 eV). Compared to NHC-CO_2-BH_3 adducts, the energies are rather lower. For instance, in adduct **1-BCl_3**, the fact of replacing BH_3 (**1-BH_3**: -0.60 eV) by BCl_3, stabilised the LUMO by 0.62 eV. The one that exhibit the lowest energy is as in previous cases, **6-BCl_3** whose *N*-substituents are perfluorinated aryl derivatives. In monoreduced species, the energies of the SOMO orbital are between -5.12 eV and -4.05 eV (a difference of 1.07 eV). Compared to [NHC-CO_2-BH_3]$^{\bullet-}$ adducts, it exists a stabilization of the SOMO orbital once the BH_3 is replaced by BCl_3 but in a lesser degree than in the LUMO orbital. For instance, the SOMO of adducts **[5-BCl_3]$^{\bullet-}$** and **[8-BCl_3]$^{\bullet-}$** are stabilised by 0.39 eV respect to **[5-BH_3]$^{\bullet-}$** (-3.81 eV) and **[8-BH_3]$^{\bullet-}$** (-4.73 eV). The adduct whose SOMO orbital presents the lowest energy is compound **[8-BCl_3]$^{\bullet-}$** (-5.12 eV).

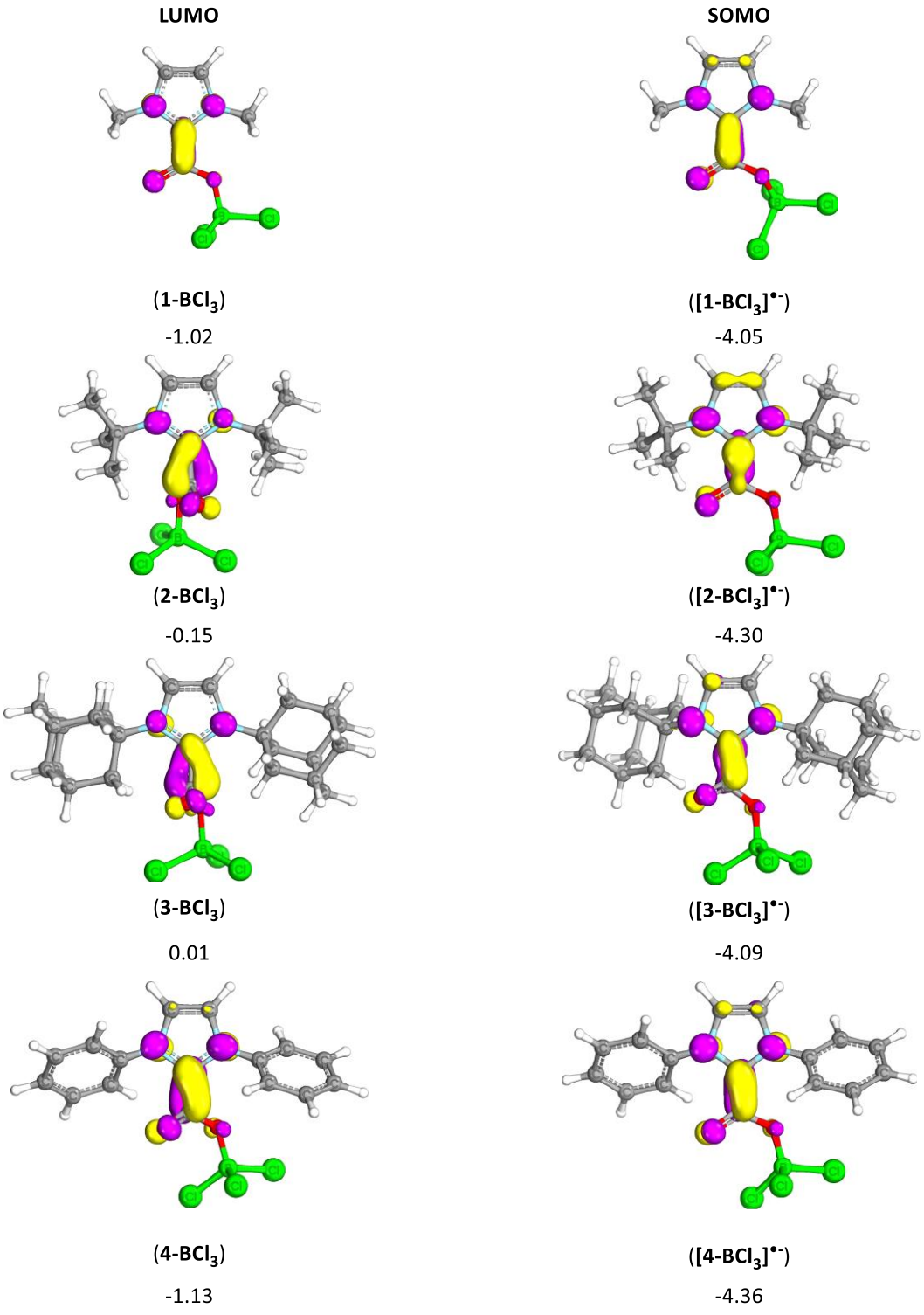

Figure 18. Localisation of the LUMO in NHC-CO_2-BCl_3 adducts ((**1**-**4**)-**BCl_3**) and its energy below (left) and localisation of the SOMO in monoreduced NHC-CO_2 adducts ((**[1]$^{\bullet-}$**-**[4]$^{\bullet-}$**)-**BCl_3**) and its energy below (right). The energies associated to each orbital was expressed in electron-volts (eV). The isosurface threshold value is 45% and the resolution, 12/Å.

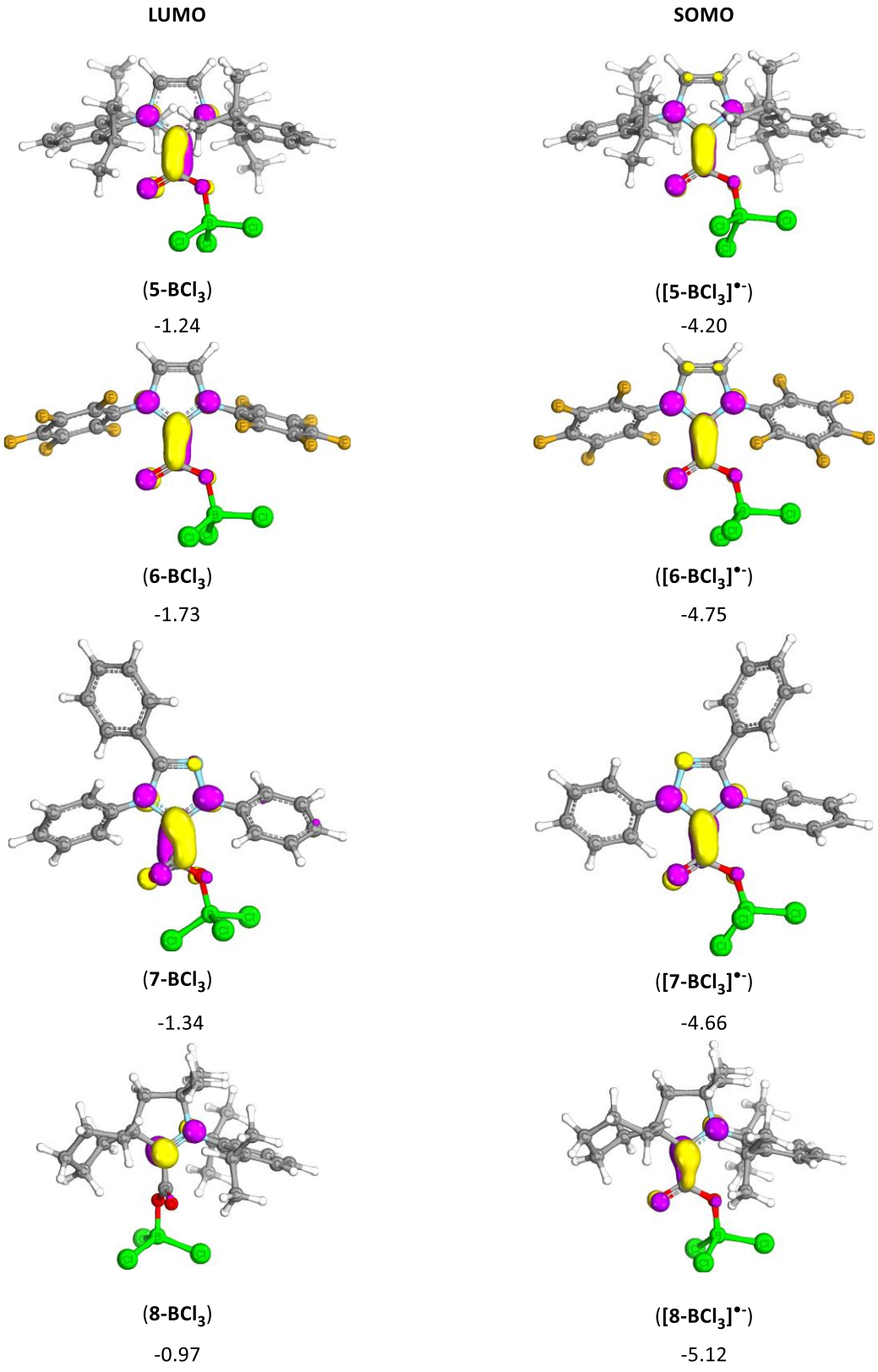

Figure 19. Localisation of the LUMO in NHC-CO_2-BCl_3 adducts (**(5-8)-BCl₃**) and its energy below (left) and localisation of the SOMO in monoreduced NHC-CO_2-BCl_3 adducts (**([5]•⁻-[8]•⁻)-BCl₃**) and its energy below (right). The energies associated to each orbital was

expressed in electron-volts (eV). The isosurface threshold value is 45% and the resolution, 12/Å.

4.4.2.4. Localisation of the LUMO and SOMO orbitals in NHC-CO_2-$B(C_6F_5)_3$ adducts and its energy.

As in NHC-CO_2-BCl_3 adducts, the LUMO and SOMO orbitals in NHC-CO_2-$B(C_6F_5)_3$ are mainly delocalised over the core of the NHC ring (nitrogen atoms, carbenic carbon and backbone (only in the SOMO orbital)) (Figures 20 and 21). The LUMO and SOMO can be also found on the CO_2 moiety. Surprisingly, in the case of adduct **3-$B(C_6F_5)_3$**, a large part of the LUMO is localised over the perfluorinated rings which belong to the $B(C_6F_5)_3$ moiety. In contrast to the HOMO, switching the BH_3 unity by $B(C_6F_5)_3$ presents a beneficial impact in the energy of the LUMO and SOMO. The energies of the LUMO orbitals are between -1.70 eV and -0.01 eV (a difference of 1.69 eV). A case to highlight is **3-$B(C_6F_5)_3$**, its LUMO exhibits an energy at -0.01 eV which is 0.46 eV lower than in **3-BH_3** (the highest difference between the energies of NHC-CO_2-BH_3 and NHC-CO_2-$B(C_6F_5)_3$ adducts). The LUMO which presents a lowest energy is **5-$B(C_6F_5)_3$**. In the case of the SOMO, the energy ranges from -5.02 eV to -3.98 eV (a difference of 1.04 eV). The adduct whose SOMO orbital is the most stable is **$[8\text{-}B(C_6F_5)_3]^{\bullet-}$**.

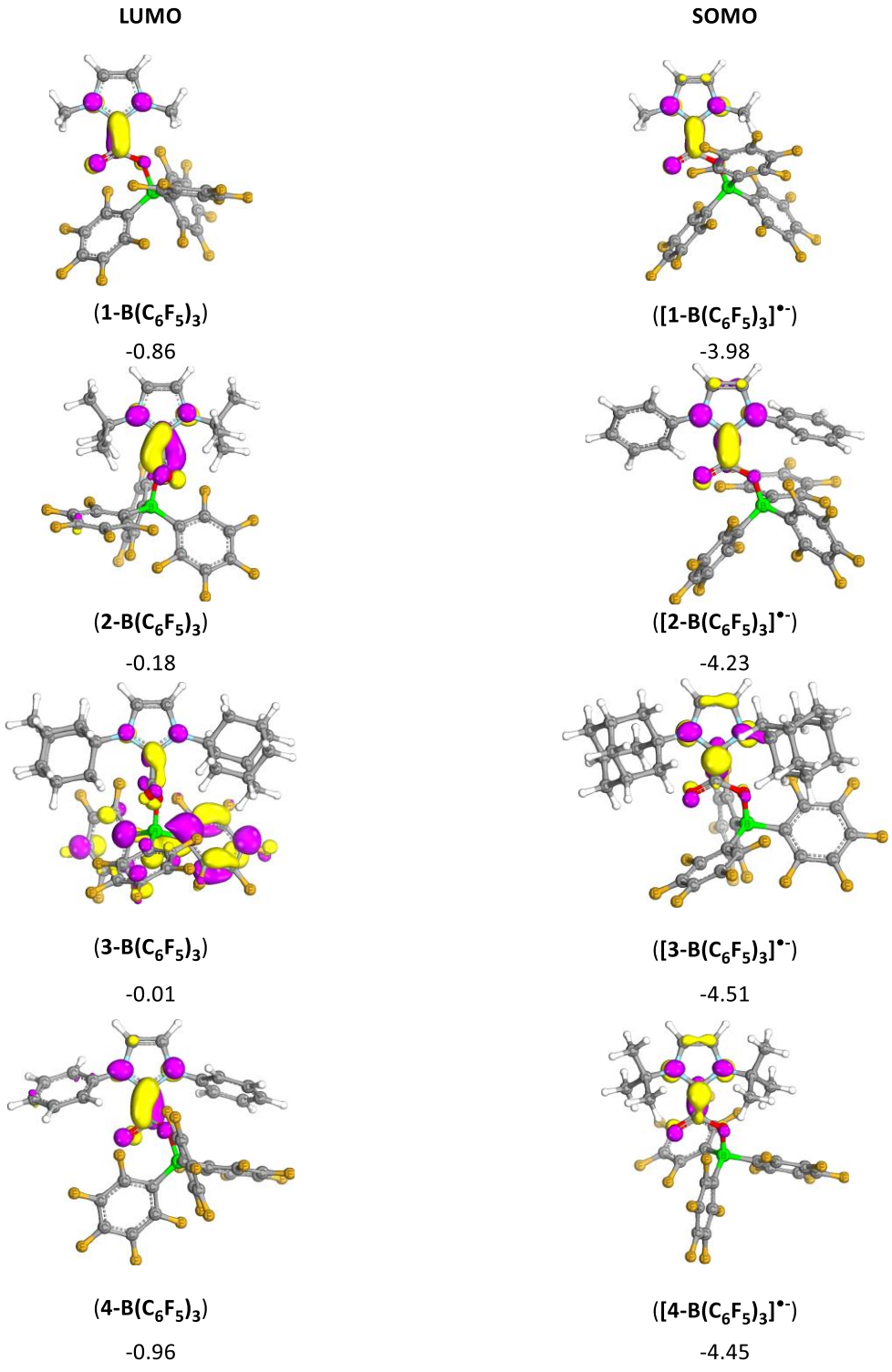

Figure 20. Localisation of the LUMO in NHC-CO_2-$B(C_6F_5)_3$ adducts ((**1**-**4**)-**B(C$_6$F$_5$)$_3$**) and its energy below (left) and localisation of the SOMO in monoreduced NHC-CO_2-BCl_3 adducts ((**[1]**$^{\bullet-}$-**[4]**$^{\bullet-}$)-**B(C$_6$F$_5$)$_3$**) and its energy below (right). The energies associated to each orbital was expressed in electron-volts (eV). The isosurface threshold value is 45% and the resolution, 12/Å.

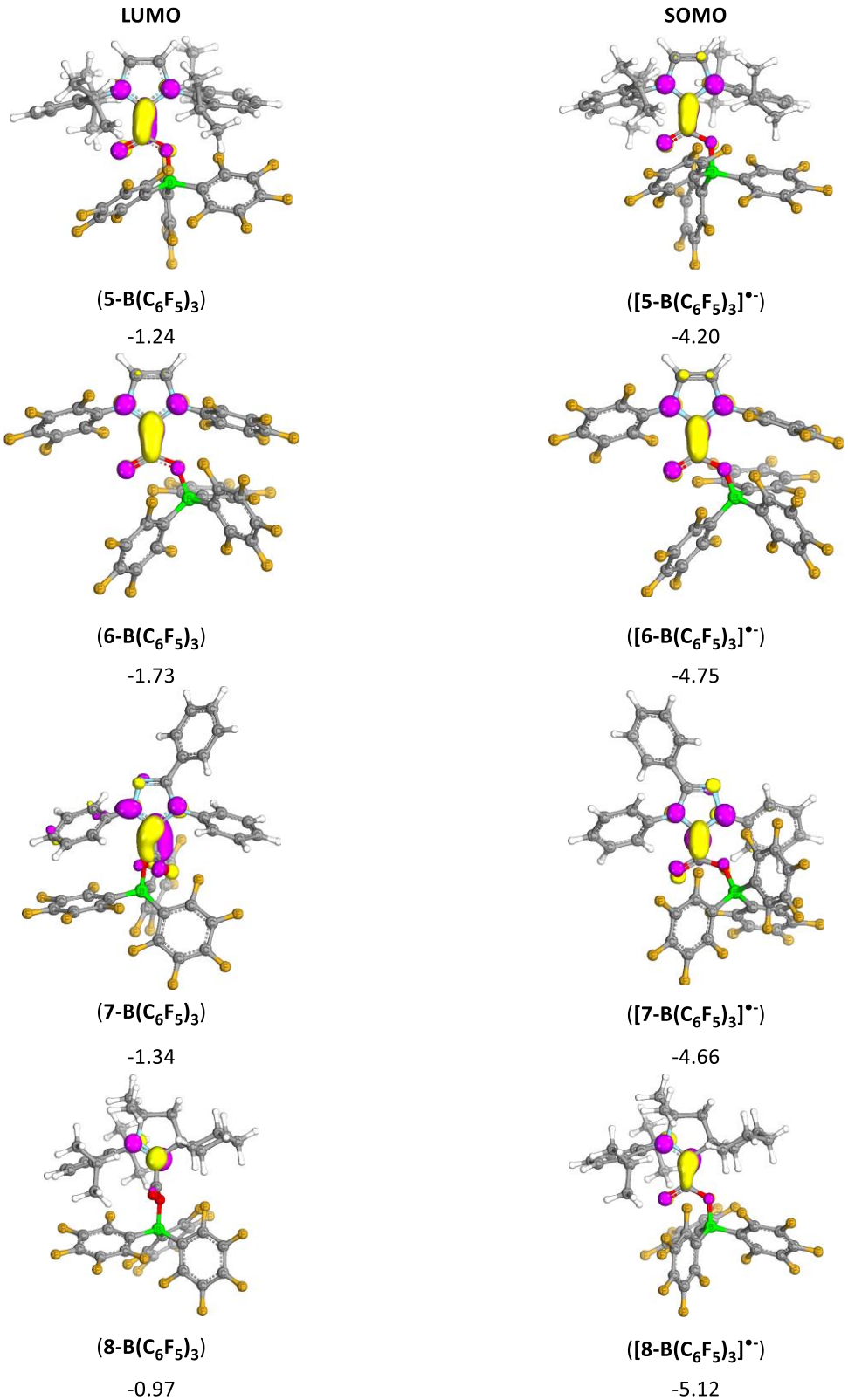

Figure 21. Localisation of the LUMO in NHC-CO_2-$B(C_6F_5)_3$ adducts ((**5**-**8**)-**B(C$_6$F$_5$)$_3$**) and its energy below (left) and localisation of the SOMO in monoreduced NHC-CO_2-BCl_3 adducts ((**[5]$^{\bullet-}$**-**[8]$^{\bullet-}$**)-**B(C$_6$F$_5$)$_3$**) and its energy below (right). The energies associated to each

orbital was expressed in electron-volts (eV). The isosurface threshold value is 45% and the resolution, 12/Å.

4.5. Natural charges analysis in NHC-CO_2-based adducts.

In this subsection, we performed a natural population analysis of the charges in NHC-CO_2-based adducts and in their monoreduced species. The discussion will be divided into two main parts: NHC-CO_2 and NHC-CO_2-BR_3 adducts (BR_3: BH_3, BCl_3 and $B(C_6F_5)_3$)).

4.5.1. Natural charges analysis in NHC-CO_2 and $[NHC\text{-}CO_2]^{\bullet-}$ adducts.

As shown in Table 11, the free CO_2 molecule exhibit a charge of 1.05 at the carbon atom and -1.05 between both oxygen atoms distributed equally. The free CO_2 molecule will be use as a reference in this subsection. In all cases, the coordination of a NHC towards free CO_2 molecule is associated to a gain of charge at the carbon and both oxygen atoms. Both oxygen atoms in NHC-CO_2 adducts were considered equivalent (the value which appears in Table 11 is the sum of the natural changes in both oxygens, the same for the nitrogen atoms). Within all studied adducts, the one in which the CO_2 moiety is the most negatively charged is compound **8** (-0.76) due to the strong σ-donation of cyclic(alkyl)(amino) carbene. Besides the latter fact, the charges on the coordinated CO_2 moity ranges from -0.69 to -0.76 (a difference of 0.07).

Table 11. Natural charge population in NHC-CO_2 adducts.

Compounds	CO_2 moiety			NHC moiety	
	C	O	Total Natural charge (CO_2)	Carbenic C	N
Free CO_2	1.05	-1.05	0	-	-
1	0.74	-1.48	-0.74	0.32	-0.55
2	0.75	-1.48	-0.73	0.35	-0.62
3	0.75	-1.48	-0.73	0.36	-0.63
4	0.74	-1.46	-0.72	0.37	-0.62
5	0.73	-1.46	-0.73	0.40	-0.67
6	0.75	-1.44	-0.69	0.38	-0.61
7	0.74	-1.43	-0.69	0.38	-0.73
8	0.72	-1.46	-0.76	0.46	-0.33

Upon reduction of the NHC-CO_2 adducts, the electronic density in the adduct is reorganised (Table 12). In all adducts, the electronic density on the CO_2 moiety does not significantly differ from each other and the free CO_2 molecule. The natural charge on the CO_2 moiety ranges between -0.73 and -1.02 (a difference of 0.29). The adducts that have placed more electronic density at the CO_2 moiety in respect to their neutral forms are **[1]**$^{\bullet-}$ and **[5]**$^{\bullet-}$. Within the CO_2 unit, the oxygen atoms have gained more electronic density than the carbon atom. Another important fact to mention is also the charge at the carbenic carbon, electronic density significantly increased at that position upon reduction except in adduct **[7]**$^{\bullet-}$ in respect to their neutral form.

Table 12. Natural charge population in [NHC-CO_2]$^{\bullet-}$ adducts.

Compounds	CO_2 moiety			NHC moiety	
	C	O	Total Natural charge (CO_2)	Carbenic C	N
[Free CO_2]$^{\bullet-}$	0.52	-1.52	-1.00	-	-
[1]$^{\bullet-}$	0.66	-1.68	-1.02	0.09	-0.74
[2]$^{\bullet-}$	0.70	-1.66	-0.96	0.09	-0.78
[3]$^{\bullet-}$	0.71	-1.64	-0.93	0.10	-0.82
[4]$^{\bullet-}$	0.68	-1.62	-0.94	0.14	-0.74
[5]$^{\bullet-}$	0.65	-1.67	-1.02	0.17	-0.84
[6]$^{\bullet-}$	0.69	-1.62	-0.93	0.17	-0.74
[7]$^{\bullet-}$	0.74	-1.47	-0.73	0.38	-0.94
[8]$^{\bullet-}$	0.68	-1.66	-0.98	0.09	-0.45

4.5.2. Natural charges analysis in NHC-CO_2-BH_3 and [NHC-CO_2-BH_3]$^{\bullet-}$ adducts.

As expected, the addition of BH_3 to the NHC-CO_2 adduct diminishes the negative charge at the CO_2 moiety as the borane withdraws part of the electronic density of the CO_2 moiety (Table 13). Nevertheless, it does not exit a significant impact on the charge at the carbon of the CO_2 moiety, the charge must be compensated by the NHC ring. The range at the CO_2 moiety ranges between -0.49 to -0.45 (a difference of 0.04). It seems that the electronic density at the CO_2 unit tends to the charge value -0.45 regardless the morphology of the NHC. The one that exhibits more electronic density at the CO_2 unit is adduct **8-BH_3** closely followed by the rest of NHC-CO_2-BH_3 adducts. The coordinated borane is slightly negatively charged (around -0.10).

Table 13. Natural charge population in NHC-CO_2-BH_3 adducts.

Compounds	CO_2 moiety				NHC moiety		BR_3 moiety
	C	O (C=O)	O (C-O)	Total Natural charge (CO_2)	Carbenic C	N	B
Free CO_2	1.05	-1.05		0.00	-	-	-
1-BH_3	0.77	-0.64	-0.61	-0.48	0.31	-0.51	-0.10
2-BH_3	0.79	-0.63	-0.62	-0.46	0.35	-0.58	-0.11
3-BH_3	0.79	-0.62	-0.63	-0.46	0.36	-0.59	-0.11
4-BH_3	0.78	-0.62	-0.61	-0.45	0.36	-0.57	-0.10
5-BH_3	0.77	-0.62	-0.61	-0.46	0.38	-0.62	-0.10
6-BH_3	0.78	-0.62	-0.61	-0.45	0.38	-0.57	-0.10
7-BH_3	0.78	-0.61	-0.60	-0.43	0.39	-0.56	-0.10
8-BH_3	0.76	-0.63	-0.62	-0.49	0.47	-0.30	-0.11

Upon the reduction of these adducts, the negative charge at the CO_2 moiety is enhanced respect to their neutral form (Table 13). The charge is between -0.79 and -0.65 (a difference of 0.14). In this case, the adduct that presents more electronic density at the CO_2 moiety is **[1-BH_3]$^{\bullet-}$** (-0.79). However, it is closely followed by the adduct **[5-BH_3]$^{\bullet-}$** (-0.77). With the addition of a BH_3 unit, the electronic density at the CO_2 moiety is lower in [NHC-CO_2-BH_3]$^{\bullet-}$ adducts than in their analogous [NHC-CO_2]$^{\bullet-}$ adducts. In [NHC-CO_2-BH_3]$^{\bullet-}$ adducts, the carbenic carbon exhibits less electronic density than in [NHC-CO_2]$^{\bullet-}$ adducts (the charge at the carbenic carbon in [NHC-CO_2-BH_3]$^{\bullet-}$ is more positive than in [NHC-CO_2]$^{\bullet-}$) , as expected by the presence of the borane that withdraws electronic density from the CO_2 unit.

Table 13. Natural charge population in [NHC-CO_2-BH_3]$^{\bullet-}$ adducts.

Compounds	CO_2 moiety				NHC moiety		BR_3 moiety
	C	O (C=O)	O (C-O)	Total Natural charge (CO_2)	Carbenic C	N	B
[Free CO_2]$^{\bullet-}$	0.52	-1.52		-1.00	-	-	-
[1-BH_3]$^{\bullet-}$	0.65	-0.75	-0.69	-0.79	0.14	-0.68	-0.08
[2-BH_3]$^{\bullet-}$	0.69	-0.74	-0.69	-0.74	0.14	-0.74	-0.09
[3-BH_3]$^{\bullet-}$	0.69	-0.74	-0.69	-0.74	0.14	-0.74	-0.09
[4-BH_3]$^{\bullet-}$	0.68	-0.71	-0.67	-0.70	0.17	-0.70	-0.09
[5-BH_3]$^{\bullet-}$	0.65	-0.74	-0.68	-0.77	0.21	-0.79	-0.08
[6-BH_3]$^{\bullet-}$	0.69	-0.71	-0.67	-0.69	0.20	-0.71	-0.09
[7-BH_3]$^{\bullet-}$	0.71	-0.70	-0.66	-0.65	0.15	-0.88	-0.09
[8-BH_3]$^{\bullet-}$	0.69	-0.72	-0.68	-0.71	0.12	-0.41	-0.09

4.5.3. Natural charges analysis in NHC-CO_2-BCl_3 and [NHC-CO_2-BCl_3]$^{\bullet-}$ adducts.

Replacing the BH_3 borane by BCl_3, the electronic density at the CO_2 moiety is very slightly decreased (Table 14). The total natural charge at the CO_2 moiety ranges from -0.56 up to -0.43 (a difference of 0.13). The adduct that keeps more electronic density at that location is adduct **6-BCl_3** (-0.56). Regarding the electronic densities at the carbon atom of the CO_2 unit, they are placed from 0.77 to 0.81. There is no significant difference within the NHC-CO_2-BCl_3 adduct, only 0.04. Electronegative chlorine atoms withdraw electronic density resulting in a boron atom with 0.40 as charge value.

Table 14. Natural charge population in NHC-CO_2-BCl_3 adducts.

Compounds	CO_2 moiety				NHC moiety		BR_3 moiety
	C	O (C=O)	O (C-O)	Total Natural charge (CO_2)	Carbenic C	N	B
Free CO_2	1.05	-1.05		0.00	-	-	-
1-BCl_3	0.79	-0.57	-0.68	-0.46	0.30	-0.49	0.41
2-BCl_3	0.80	-0.57	-0.69	-0.46	0.33	-0.56	0.41
3-BCl_3	0.81	-0.57	-0.69	-0.45	0.34	-0.58	0.41
4-BCl_3	0.79	-0.56	-0.67	-0.44	0.34	-0.55	0.41
5-BCl_3	0.78	-0.56	-0.68	-0.46	0.36	-0.60	0.41
6-BCl_3	0.79	-0.56	0.79	-0.56	0.37	-0.54	0.40
7-BCl_3	0.79	-0.55	-0.67	-0.43	0.37	-0.64	0.40
8-BCl_3	0.77	-0.57	-0.68	-0.48	0.45	-0.28	0.41

As shown in Table 15, upon reduction the electronic density is reorganised in the adduct. The electronic density ranges from -0.84 to -0.72 (a difference of 0.12). The adduct **[1-BCl_3]$^{\bullet-}$** is the most negatively charged at the CO_2 moiety, particularly, at the carbon atom (0.62). As expected, the monoreduced species exhibit more electronic density at the carbenic carbon (from 0.13 to 0.23) than NHC-CO_2-BCl_3 adducts at the neutral form. Upon reduction, the boron atom in monoreduced adducts exhibits less electronic density than their neutral form. As example, in the case of **8-BCl_3**, the chlorine atoms present a charge of -0.82 whereas in their monoreduced form (**[8-BCl_3]$^{\bullet-}$**), -0.97. The total charge in the borane unit stays almost invariable upon the reduction (**8-BCl_3**: -0.41 and **[8-BCl_3]$^{\bullet-}$**: -0.48). [NHC-CO_2-BCl_3]$^{\bullet-}$ adducts slightly exhibit more electronic density at the CO_2 unit than [NHC-CO_2-BH_3]$^{\bullet-}$ adducts (Table 13).

Table 15. Natural charge population in [NHC-CO_2-BCl_3]$^{\bullet-}$ adducts.

Compounds	CO_2 moiety				NHC moiety		BR_3 moiety
	C	O (C=O)	O (C-O)	Total Natural charge (CO_2)	Carbenic C	N	B
[Free CO_2]$^{\bullet-}$	0.52	-1.52		-1.00	-	-	-
[1-BCl_3]$^{\bullet-}$	0.62	-0.70	-0.76	-0.84	0.18	-0.66	0.50
[2-BCl_3]$^{\bullet-}$	0.67	-0.69	-0.75	-0.77	0.16	-0.72	0.49
[3-BCl_3]$^{\bullet-}$	0.69	-0.67	-0.75	-0.73	0.15	-0.74	0.49
[4-BCl_3]$^{\bullet-}$	0.66	-0.67	-0.74	-0.75	0.19	-0.69	0.48
[5-BCl_3]$^{\bullet-}$	0.63	-0.68	-0.75	-0.80	0.23	-0.67	0.50
[6-BCl_3]$^{\bullet-}$	0.67	-0.67	-0.74	-0.74	0.21	-0.70	0.47
[7-BCl_3]$^{\bullet-}$	0.67	-0.66	-0.73	-0.72	0.19	-0.84	0.48
[8-BCl_3]$^{\bullet-}$	0.68	-0.67	-0.75	-0.74	0.13	-0.39	0.49

4.5.4. Natural charges analysis in NHC-CO_2-$B(C_6F_5)_3$ and [NHC-CO_2-$B(C_6F_5)_3$]$^{\bullet-}$ adducts.

As shown in Table 16, the use of $B(C_6F_5)_3$ does not exhibit a significant impact in the charge at the CO_2 moiety respect to BH_3. The charges at that position range between -0.45 and -0.39 (a difference of 0.06). It is the adduct **1-$B(C_6F_5)_3$** closely followed by **8-$B(C_6F_5)_3$**, the one that exhibit more electronic density at the CO_2 moiety within all studied NHC-CO_2-$B(C_6F_5)_3$ adducts. Nevertheless, all adducts are positioned around the same value. At the carbon atom of the CO_2 moiety, there not a significant difference within the NHC-CO_2-$B(C_6F_5)_3$. The charge at the boron atom is set around 0.55 due to the strong withdrawing effect of its perfluorinated aryl derivatives.

Table 16. Natural charge population in NHC-CO_2-$B(C_6F_5)_3$ adducts.

Compounds	CO_2 moiety				NHC moiety		BR_3 moiety
	C	O (C=O)	O (C-O)	Total Natural charge (CO_2)	Carbenic C	N	B
Free CO_2	1.05	-1.05		0.00	-	-	-
1-$B(C_6F_5)_3$	0.79	-0.61	-0.63	-0.45	0.31	-0.50	0.55
2-$B(C_6F_5)_3$	0.81	-0.60	-0.63	-0.42	0.34	-0.57	0.56
3-$B(C_6F_5)_3$	0.82	-0.61	-0.63	-0.42	0.35	-0.58	0.56
4-$B(C_6F_5)_3$	0.79	-0.59	-0.62	-0.42	0.35	-0.52	0.55
5-$B(C_6F_5)_3$	0.80	-0.60	-0.62	-0.42	0.35	-0.58	0.56
6-$B(C_6F_5)_3$	0.80	-0.59	-0.62	-0.41	0.37	-0.55	0.56
7-$B(C_6F_5)_3$	0.80	-0.58	-0.61	-0.39	0.39	-0.66	0.55
8-$B(C_6F_5)_3$	0.78	-0.60	-0.63	-0.45	0.46	-0.29	0.56

Upon reduction, as in previous examples, the electronic density at the CO_2 moiety increases respect to their neutral form and ranges from -0.77 up to -0.63 as well as at the carbenic carbon which is between 0.13 and 0.20. The adduct that exhibit more electronic density at the carbon from the CO_2 moiety is **[5-$B(C_6F_5)_3$]$^{\bullet-}$** (0.66) followed by **[6-$B(C_6F_5)_3$]$^{\bullet-}$** (0.68) (Table 17). According to Table 17, adduct **[8-$B(C_6F_5)_3$]$^{\bullet-}$** possesses less electronic density at the carbon atom of the CO_2 unit, it is mainly placed at the carbenic carbon. The reduction does not exhibit a significant impact on the charge of the boron atom. Compared to BH_3 and BCl_3, the use of $B(C_6F_5)_3$ as a Lewis acid does not significantly improves the electron density either at the C from the CO_2 moiety.

Table 17. Natural charge population in [NHC-CO_2-$B(C_6F_5)_3$]$^{\bullet-}$ adducts.

Compounds	CO_2 moiety				NHC moiety		BR_3 moiety
	C	O (C=O)	O (C-O)	Total Natural charge (CO_2)	Carbenic C	N	B
[Free CO_2]$^{\bullet-}$	0.52	-1.52		-1.00	-	-	-
[1-$B(C_6F_5)_3$]$^{\bullet-}$	0.64	-0.72	-0.69	-0.77	0.17	-0.67	0.56
[2-$B(C_6F_5)_3$]$^{\bullet-}$	0.69	-0.73	-0.69	-0.72	0.16	-0.72	0.57
[3-$B(C_6F_5)_3$]$^{\bullet-}$	0.73	-0.72	-0.68	-0.67	0.14	-0.75	0.56
[4-$B(C_6F_5)_3$]$^{\bullet-}$	0.70	-0.68	-0.68	-0.66	0.16	-0.72	0.57
[5-$B(C_6F_5)_3$]$^{\bullet-}$	0.66	-0.71	-0.68	-0.73	0.20	-0.76	0.56
[6-$B(C_6F_5)_3$]$^{\bullet-}$	0.68	-0.69	-0.69	-0.70	0.20	-0.71	0.56
[7-$B(C_6F_5)_3$]$^{\bullet-}$	0.72	-0.68	-0.67	-0.63	0.15	-0.84	0.56
[8-$B(C_6F_5)_3$]$^{\bullet-}$	0.70	-0.70	-0.68	-0.68	0.13	-0.39	0.56

4.6. Evolution of the energy of the LUMO and reduction potentials depending on the torsion angle (D(NHC-CO_2)).

This section is divided into two parts. Firstly, the dependence of the energy of the LUMO in NHC-CO_2-based adducts with the torsion angle between the NHC ring and CO_2 moiety will be exposed. As the torsion angle is very sensitive with the reduction potential, we study how the reduction potential in NHC-CO_2-based adducts changes depending on the torsion angle. This discussion will be solely focussed on the neutral synthesised adducts in this work: **8**, **2-$B(C_6F_5)_3$**, **3-$B(C_6F_5)_3$**, **5-$B(C_6F_5)_3$** and **8-$B(C_6F_5)_3$**.

4.6.1. Dependence of the LUMO energy on torsion angle (D(NHC-CO_2)).

In this subsection, we investigated how much the energy of the LUMO in the synthesised adducts varies depending on the orientation of the CO_2 moiety respect to the NHC ring, the torsion angle (D(NHC-CO_2)). A clear tendency is observed for all adducts, the energy of the LUMO evolves following a quadratic function with the torsion angle between the NHC and the CO_2 adducts. The vertex of the function is the maximum of energy of the LUMO for all adducts and it localised close to 90 °. The minima of this function (lowest

energy values for the LUMO) are reached when the CO_2 moiety tends to be set closer to a coplanar position (close to 0 °) respect to the NHC ring (Figures 22-26).

The tendencies observed in the thermodynamic stability of NHC-CO_2-based adducts were already described in the section 4.2 of this chapter. In this subsection, we studied how the energy of the LUMO correlates with the energy of the synthesised adducts. As shown in Figure 22 and 23, **2-B(C_6F_5)$_3$** and **3-B(C_6F_5)$_3$** are more stable when the CO_2 is set at the perpendicular position due to the carbene high steric hindrance which matches up with the maximum of energy of the LUMO.

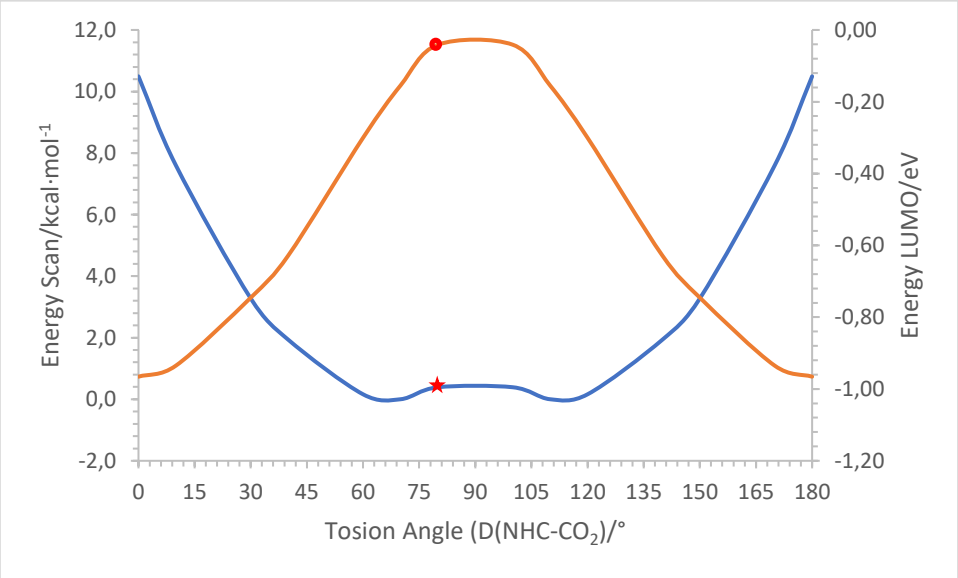

Figure 22. Conformation analysis of adduct **2-B(C_6F_5)$_3$** and its LUMO energy as function of the torsion angle between the NHC and the CO_2 moiety (D(NHC-CO_2)). The blue line corresponds to the evolution of the energy associated with each conformer respect to D(NHC-CO_2) and the orange one is related to the evolution of the energy of the LUMO with the torsion angle. The red circle and star correspond to the absolute minimum conformer.

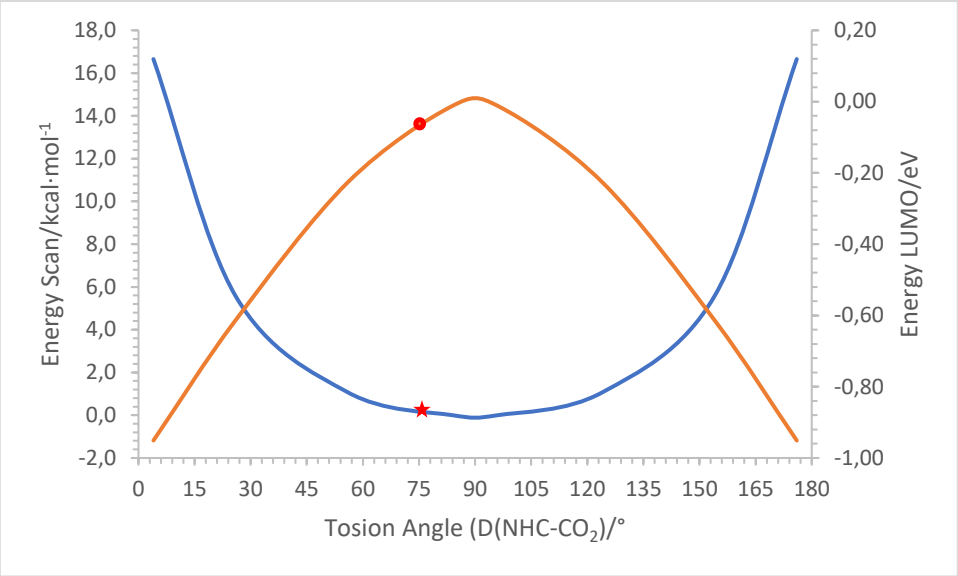

Figure 23. Conformation analysis of adduct **3-B(C_6F_5)$_3$** and its LUMO energy as function of the torsion angle between the NHC and the CO_2 moiety (D(NHC-CO_2)). The blue line corresponds to the evolution of the energy associated with each conformer respect to D(NHC-CO_2) and the orange one is related to the evolution of the energy of the LUMO with the torsion angle. The red circle and star correspond to the absolute minimum conformer.

In the case of **5-B(C_6F_5)$_3$**, it does not follow the precedented behaviour observed in adducts **2-B(C_6F_5)$_3$** and **3-B(C_6F_5)$_3$** (Figure 24). Adduct **5-B(C_6F_5)$_3$** is more stable when the CO_2 sets in a coplanar position respect to the NHC ring as its LUMO energy.

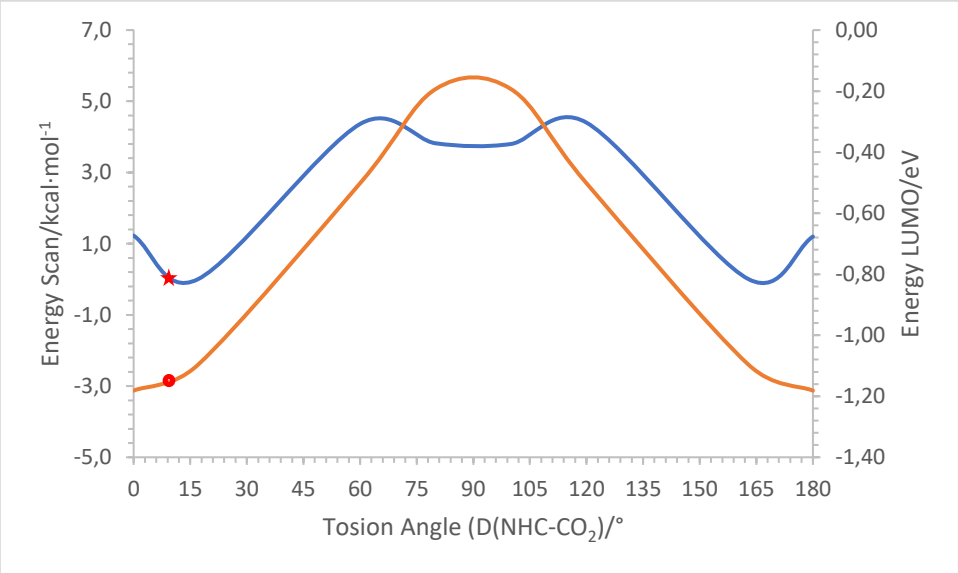

Evolution of the energy of the LUMO and reduction potentials depending on the torsion angle (D(NHC-CO_2)).

Figure 24. Conformation analysis of adduct **5-B(C_6F_5)$_3$** and its LUMO energy as function of the torsion angle between the NHC and the CO_2 moiety (D(NHC-CO_2)). The blue line corresponds to the evolution of the energy associated with each conformer respect to D(NHC-CO_2) and the orange one is related to the evolution of the energy of the LUMO with the torsion angle. The red circle and star correspond to the absolute minimum conformer.

In the case of the CAAC-type adduct, **8** (Figure 25) exhibits the same behaviour than adducts **2-B(C_6F_5)$_3$** and **3-B(C_6F_5)$_3$**. In adduct **8-B(C_6F_5)$_3$** (Figure 26), the energy of the LUMO increases with the torsion angle between the NHC ring and the CO_2 moiety up to 55 ° where it seems to exist a transition state (more information will be given in next subsection). Over 55 °, it falls into an energy well at 90 ° resulting in more stable conformer respect to the others. The LUMO energy does not seem to suffer a significant change with the torsion angle between 55 ° and 125 °.

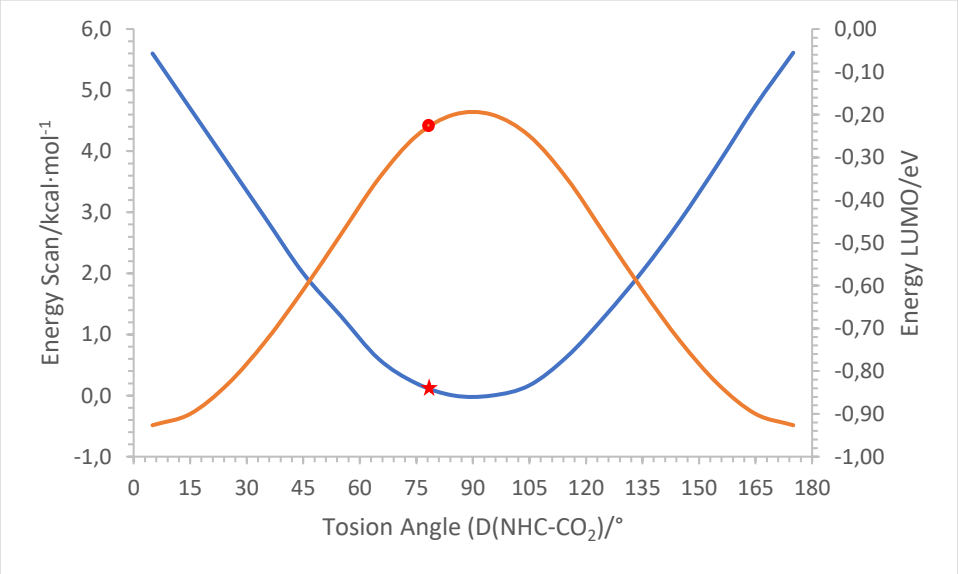

Figure 25. Conformation analysis of adduct **8** and its LUMO energy as function of the torsion angle between the NHC and the CO_2 moiety (D(NHC-CO_2)). The blue line corresponds to the evolution of the energy associated with each conformer respect to D(NHC-CO_2) and the orange one is related to the evolution of the energy of the LUMO with the torsion angle. The red circle and star correspond to the absolute minimum conformer.

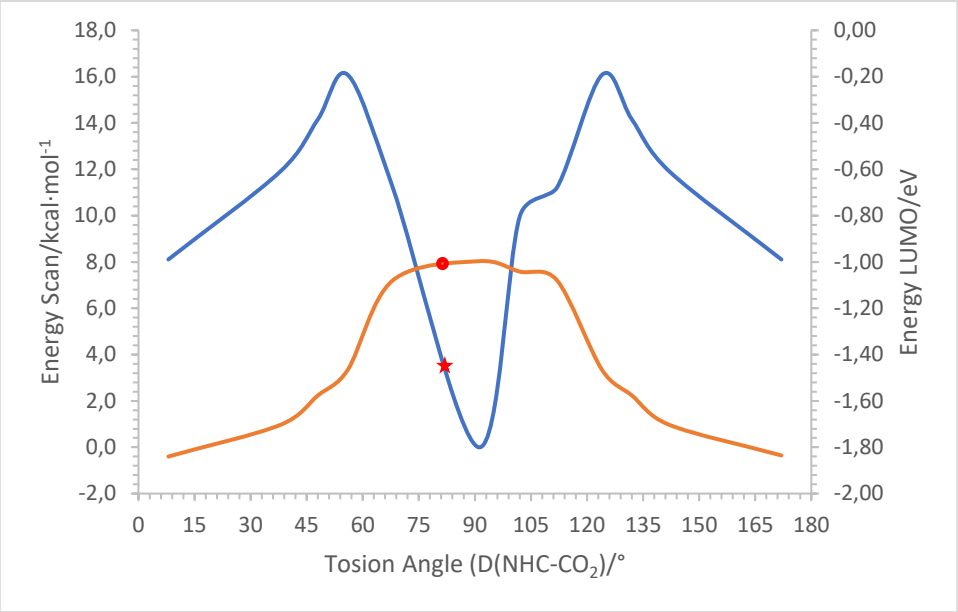

Figure 26. Conformation analysis of adduct **8-B(C_6F_5)$_3$** and its LUMO energy as function of the torsion angle between the NHC and the CO_2 moiety (D(NHC-CO_2)). The blue line corresponds to the evolution of the energy associated with each conformer respect to D(NHC-CO_2) and the orange one is related to the evolution of the energy of the LUMO with the torsion angle. The red circle and star correspond to the absolute minimum conformer.

4.6.2. Influence of the NHC-CO_2 torsion angle on the reduction potentials

In our study, we also interrogated how the torsion angle between the NHC ring and the CO_2 moiety (D(NHC-CO_2)) in neutral NHC-CO_2-based adducts impacts on their reduction potential. As a reminder, all synthesised adducts (**8**, **2-B(C_6F_5)$_3$**, **3-B(C_6F_5)$_3$** and **8-B(C_6F_5)$_3$**) exhibits a dihedral (torsion) angle which tends to set in a perpendicular position except **5-B(C_6F_5)$_3$** (Scheme 14 and Table 18).

Evolution of the energy of the LUMO and reduction potentials depending on the torsion angle (D(NHC-CO_2)).

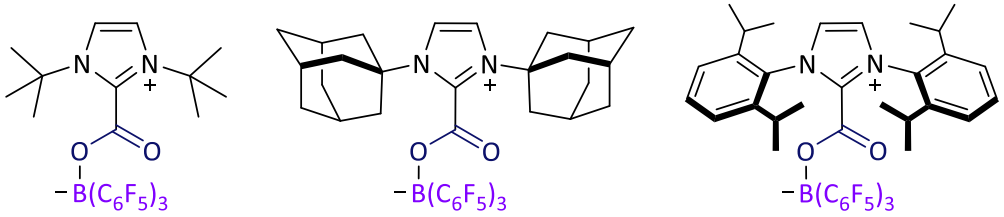

	2-B(C_6F_5)$_3$	**3-B(C_6F_5)$_3$**	**5-B(C_6F_5)$_3$**
D(NHC-CO_2)	80.5(2)	76.7(3)	7.3(2)

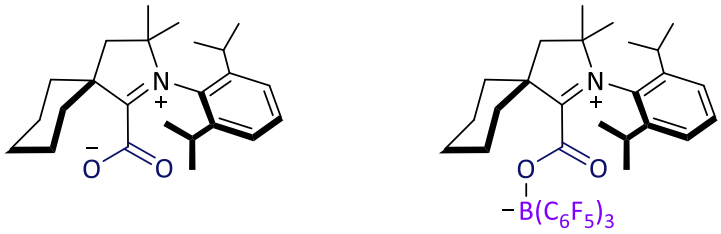

	8	**8-B(C_6F_5)$_3$**
D(NHC-CO_2)	77.9(4)	79.2(2)

Scheme 14. Synthesised NHC-CO_2-based adducts along with their torsion angles (D(NHC-CO_2) from the XRD analysis. The angles were expressed in degrees.

Table 18. Theoretical and experimental reduction potentials for all synthesised adducts (**8**, **2-B(C_6F_5)$_3$**, **3-B(C_6F_5)$_3$**, **5-B(C_6F_5)$_3$** and **8-B(C_6F_5)$_3$**) versus $Fc^{+/0}$ in volts (V).

Potentials	**Theoretical**	**Experimental**
$E_{1/2}$ (**2-B(C_6F_5)$_3$**)	-2.26	-2.27
$\lvert\Delta E_{1/2}\rvert$ (**2-B(C_6F_5)$_3$**)	0.01	-
$E_{1/2}$ (**3-B(C_6F_5)$_3$**)	-2.30	-2.41
$\lvert\Delta E_{1/2}\rvert$ (**3-B(C_6F_5)$_3$**)	0.11	-
$E_{1/2}$ (**5-B(C_6F_5)$_3$**)	-2.04	-2.08
$\lvert\Delta E_{1/2}\rvert$ (**5-B(C_6F_5)$_3$**)	0.04	-
$E_{1/2}$ (**8**)	-2.38	-2.13
$\lvert\Delta E_{1/2}\rvert$ (**8**)	0.25	-
$E_{1/2}$ (**8-B(C_6F_5)$_3$**)	-1.29	-1.34
$\lvert\Delta E_{1/2}\rvert$ (**8-B(C_6F_5)$_3$**)	0.05	-

In order to study how the reduction potentials change depending on the angle between the NHC ring and CO_2 moiety, we firstly studied the possibility of existence of any other local minima or in their absence, a transition state in the rotation process. This step is

fundamental because the estimation of theoretical reduction potentials can solely be performed on saddle points on the potential energy surface (PES) in which the calculation of frequencies is possible. In all adducts, rotation energy was estimated (Table 19). This rotation energy refers to the amount of energy that must be overcome for one full rotation. A transition state refers to the potential energy maximum at the saddle point[16] and it can be that the difference of Gibbs energies between the minimum and the transition state would result into the rotation energy of the adduct.

Table 19. Rotation energy of all studied adducts. The energy is expressed in kcal·mol^{-1} and the rate constant in s^{-1}.

Adducts	Rotation energy	Rate constant
2-B(C_6F_5)$_3$	13.5	8.2x10^2
3-B(C_6F_5)$_3$	16.5	5.3
5-B(C_6F_5)$_3$	4.6	2.6x10^9
8	6.7	7.2x10^7
8-B(C_6F_5)$_3$	11.8	1.4x10^4

As shown in Table 19, the adducts exhibit a rotation energy which ranges from 4.6 kcal·mol^{-1} up to 16.5 kcal·mol^{-1}. We can consider that CO_2 moiety freely rotates at room temperature in all species but adducts **2-B(C_6F_5)$_3$**, **3-B(C_6F_5)$_3$** and **8-B(C_6F_5)$_3$** present a higher hindrance to rotate (higher rotation energy). These adducts are more hindered which can be translated into a slower CO_2 rotation (Table 19).

Besides the minimum previously commented for the adduct **8-B(C_6F_5)$_3$**, two other local minima (conformers) were also obtained. As shown in Figure 27, half a turn of the CO_2 moiety respect to the ^{Cy}CAAC ring has been successfully recorded. The position of the borane either at the back (**8-B(C_6F_5)$_3$**) or at the front (**8-B(C_6F_5)$_3$-inverted**) of a fictional plane placed on the NHC-CO_2 bond exhibits a significant impact on the energy of the molecule and consequently also, on the estimated theoretical reduction potential. The choice of the right minimum is vital to have access to an accurate reduction potential in NHC-CO_2-based adducts (Table 20).

Evolution of the energy of the LUMO and reduction potentials depending on the torsion angle (D(NHC-CO_2)).

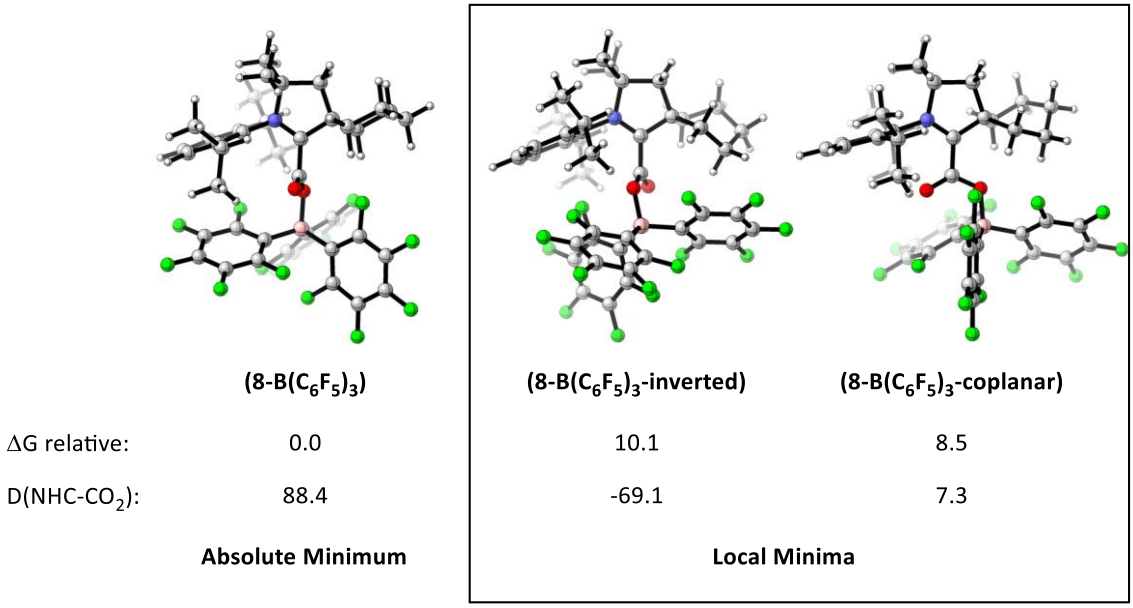

Figure 27. Absolute minimum and local minima for adduct **8-B(C_6F_5)$_3$** with their relative Gibbs energy respect to the absolute minimum (expressed in kcal·mol^{-1}) (ΔG relative) and the torsion angle between the NHC ring and the CO_2 moiety (D(NHC-CO_2)) expressed in degrees (°).

Table 20. Theoretical reduction potentials of **8-B(C_6F_5)$_3$** and its conformers (**8-B(C_6F_5)$_3$-inverted** and **8-B(C_6F_5)$_3$-coplanar**) versus $Fc^{+/0}$ in volts (V).

Potentials	Theoretical
$E^{1/2}_{red}$ (**8-B(C_6F_5)$_3$**)	-1.29
$E^{1/2}_{red}$ (**8-B(C_6F_5)$_3$-inverted**)	-0.86
$E^{1/2}_{red}$ (**8-B(C_6F_5)$_3$-coplanar**)	-0.92

The rotation rate constant for each synthesised adduct was also calculated using the Eyring equation expressed in Eq. 3. This equation relates the rate constant between the starting point and the transition state differing in energy by $\Delta G^{\ddagger}$,

$$k = \frac{k_b T}{h} e^{\frac{-\Delta G^{\ddagger}}{RT}} \qquad (Eq. 3)$$

where k_b is the Boltzmann's constant, h is the Planck's constant and R and T the ideal gas constant and temperature, respectively.

Then, we estimated how feasible is to transfer one electron into the adducts in the same conformation as in their respective transition state. The torsion angles between the NHC ring and the CO_2 moiety (D(NHC-CO_2)) of the respective transition states can be found in Figure 28. The transition states in this work are expressed with the symbol ascribed to the adduct in bracket followed by the Latin letter alveolar, ǂ, as superscript. For instance, the transition state found for adduct **2-B(C_6F_5)$_3$** will be expressed as **[2-B(C_6F_5)$_3$]‡**.

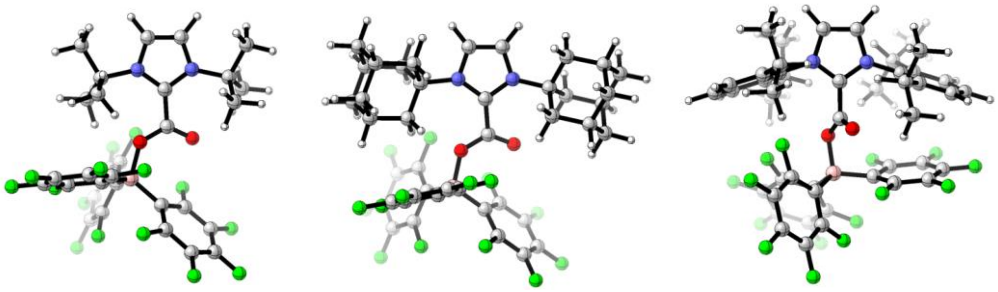

	[2-B(C_6F_5)$_3$]‡	**[3-B(C_6F_5)$_3$]‡**	**[5-B(C_6F_5)$_3$]‡**
D(NHC-CO_2)	12.2	8.6	55.7

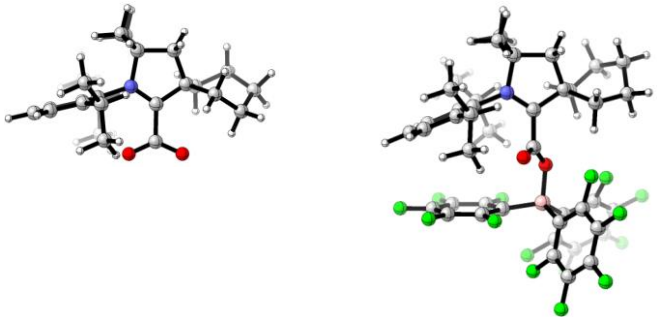

	[8]‡	**[8-B(C_6F_5)$_3$]‡**
D(NHC-CO_2)	6.8	60.4

Figure 28. Transition state of each adduct (**[8]‡**, **[2-B(C_6F_5)$_3$]‡**, **[3-B(C_6F_5)$_3$]‡**, **[5-B(C_6F_5)$_3$]‡** and **[8-B(C_6F_5)$_3$]‡**) along with the torsion angle (D(NHC-CO_2)) expressed in degrees (°).

As shown in Table 21, the reduction potential changes depending on the torsion angle between the NHC ring and CO_2 moiety. In almost all cases (**[2-B(C_6F_5)$_3$]‡**, **[3-B(C_6F_5)$_3$]‡**, **[8]‡** and **[8-B(C_6F_5)$_3$]‡**), the reduction potential is more accessible (less negative reduction potential) when the CO_2 moiety is set in a coplanar position in solution than in a perpendicular position. Surprisingly, in the case of **[8]‡** we observed a reduction

potential at -2.09 V which is significantly closer to the experimental reduction potential (-2.13, Table 1) than the theoretical potential firstly predicted, -2.38 V (Table 21).

Table 21. Theoretical reduction potential ($E^{1/2}_{red}$) of all synthesised adducts (from transition state) versus $Fc^{+/0}$ in volts (V). The energy associated to the one-electron reduction is expressed in kcal·mol^{-1} (ΔG_{red}).

Transition state	ΔG_{red}	$E^{1/2}_{red}$
[2-B(C_6F_5)$_3$]‡	-71.5	-1.68
[3-B(C_6F_5)$_3$]‡	-73.7	-1.58
[5-B(C_6F_5)$_3$]‡	-67.8	-1.84
[8]‡	-62.0	-2.09
[8-B(C_6F_5)$_3$]‡	-92.2	-0.78

Based on statistical mechanics, we assumed that there is a fraction of molecules that presents a dihedral angle equal to the one found in their respective transition states in one sample. We calculated how many molecules with the geometry dictated by the transition state (Figure 28) are present in solution respect to the ones with the geometry found on the solid state (Scheme 14), we calculated the relative population for each adduct based on the Boltzmann distribution (Eq. 4).

$$\frac{F_2}{F_1} = e^{\frac{-\Delta G^{\ddagger}}{k_b T}} \qquad (Eq. 4)$$

In Equation 4, F_2 corresponds to the molecules following the same geometry as the transition state and F_1, molecules whose geometry is identical than in the solid state. Other parameters are identical to the described ones in Equation 3.

Table 22. Relative population (F_2/F_1) for each adduct.

Adduct	F_2/F_1
2-B(C_6F_5)$_3$	$1.3x10^{-10}$
3-B(C_6F_5)$_3$	$8.4x10^{-13}$
5-B(C_6F_5)$_3$	$4.2x10^{-4}$
8	$1.2x10^{-5}$
8-B(C_6F_5)$_3$	$2.2x10^{-9}$
8-B(C_6F_5)$_3$-inverted	$8.5x10^{-13}$
8-B(C_6F_5)$_3$-coplanar	$5.5x10^{-7}$

As shown in Table 22, we can observe that adducts with a lower rotation energy will present a higher relative population than other examples whose rotation energy is higher. For instance, in the case of adduct **8** (rotation energy: 6.7 kcal·mol^{-1}) in solution present one molecule following the geometry of the transition state (**[8]‡**, D(NHC-CO_2): 6.8 °) over $1.2x10^5$ molecules whose geometry is dictated by **8**. In the case of **8-B(C_6F_5)$_3$**, there is one molecule whose geometry is identical to the transition state (**[8-B(C_6F_5)$_3$]‡**, D(NHC-CO_2): 8.6 °) over $2.2x10^9$ molecules with the geometry of **8-B(C_6F_5)$_3$**. If the local minima of the latter adduct are also considered, there is one molecule whose geometry is governed by the **8-B(C_6F_5)$_3$-inverted** and **8-B(C_6F_5)$_3$-coplanar** over $8.5x10^{13}$ and $5.5x10^7$ molecules of **8-B(C_6F_5)$_3$**, respectively.

Due to low rotation energy in adduct **8** (6.7 kcal·mol^{-1}), the CO_2 moiety in solution might tend to set in a coplanar position respect to the NHC ring favoured by the resonance stabilisation between both parts, the NHC ring and the CO_2 unit. In the case of **5-B(C_6F_5)$_3$**, the CO_2 moiety is already in a coplanar position respect to the NHC therefore, it does not rotate before the reduction. We suspect that the NHC-CO_2-based adducts whose rotation energy is extremely low ($\Delta G<10$ kcal·mol^{-1}) (**8**), they would make the CO_2 rotate to set it in a coplanar position (first the rotation process and then, the reduction). In those adducts with higher rotation energies (lower rotation rate constant) (**2-B(C_6F_5)$_3$**, **3-B(C_6F_5)$_3$** and **8-B(C_6F_5)$_3$**) they would get reduced before the rotation of the CO_2 occurs due to their high steric hindrance.

7.6. Conclusions

After calibrating the computational methodology, in an attempt to rationalise and predict how the NHC-CO_2-based adducts behave upon reduction, we presented a thorough computational study via density functional theory (DFT) calculations guided by the experimental data. After the theoretical analysis, some conclusions could be drawn.

1. Regarding the thermodynamic stability of NHC-CO_2-based adducts, all studied adducts are stable. The addition of a Lewis acid enhances the stability of the adducts. The stabilisation of these adducts is generally enhanced when the CO_2 moiety is set in a coplanar position respect to the NHC due to the resonance stabilisation of NHC ring and the CO_2 unit.
2. Upon reduction in NHC-CO_2-based adducts, the localisation of the spin density at the CO_2 moiety, particularly, at the carbon atom is governed by the torsion angle between the NHC and the CO_2 moiety. The presence of acidic borane Lewis acid (BCl_3 and $B(C_6F_5)_3$) in the NHC-CO_2-based adduct is fundamental to localise part of the spin density at the carbon atom of the CO_2 moiety. The adduct that exhibits more spin density at that position is **[5-$B(C_6F_5)_3$]$^{\bullet-}$** with 42% spin population at that position.
3. Regarding the frontier orbitals, the localisation of the LUMO of neutral adducts is nearly identical to the SOMO in monoreduced NHC-CO_2-based adducts. The addition of a Lewis acid to the NHC-CO_2 adducts enables the localisation of the LUMO and SOMO orbitals at the CO_2 unit in almost all cases regardless of the torsion angle and energetically stabilises the LUMO and SOMO orbitals. The adducts that exhibits the lowest LUMO energy were **8-BCl_3** (-0.97 eV) and **8-$B(C_6F_5)_3$** (-0.97 eV) which also presented the less negative reduction potentials, -1.38 V and -1.29 V respectively.
4. Based on a conformer analysis of the synthesised NHC-CO_2-based adducts as function of the torsion angle, the energy of the LUMO is maximum when the torsion angle is close to 90 ° and the minimum when the CO_2 moiety sets closer to a coplanar position (close to 0 °) respect to the NHC ring. The stabilisation energy of adducts **8**, **2-$B(C_6F_5)_3$**, **3-$B(C_6F_5)_3$**, and **8-$B(C_6F_5)_3$** varies opposite to the

LUMO energy whereas in adduct **5-B(C_6F_5)$_3$**, LUMO and stabilisation energy vary uniformly.

5. The torsion angle between the NHC and CO_2 moiety in the synthesised NHC-CO_2-based adducts (**8**, **2-B(C_6F_5)$_3$**, **3-B(C_6F_5)$_3$**, **5-B(C_6F_5)$_3$,** and **8-B(C_6F_5)$_3$**) have a significant impact on their reduction potentials.

7.7. References

(1) Elgrishi, N.; Rountree, K. J.; McCarthy, B. D.; Rountree, E. S.; Eisenhart, T. T.; Dempsey, J. L. A Practical Beginner's Guide to Cyclic Voltammetry. *J. Chem. Educ.* **2018**, *95* (2), 197–206. https://doi.org/10.1021/acs.jchemed.7b00361.

(2) Borioni, J. L.; Puiatti, M.; Vera, D. M. A.; Pierini, A. B. In Search of the Best DFT Functional for Dealing with Organic Anionic Species. *Phys. Chem. Chem. Phys.* **2017**, *19* (13), 9189–9198. https://doi.org/10.1039/C6CP06163J.

(3) Ree, N.; Andersen, C. L.; Kilde, M. D.; Hammerich, O.; Nielsen, M. B.; Mikkelsen, K. V. The Quest for Determining One-Electron Redox Potentials of Azulene-1-Carbonitriles by Calculation. *Phys. Chem. Chem. Phys.* **2018**, *20* (11), 7438–7446. https://doi.org/10.1039/C7CP08687C.

(4) Wang, Z.; Wang, F.; Xue, X. S.; Ji, P. Acidity Scale of N-Heterocyclic Carbene Precursors: Can We Predict the Stability of NHC-CO_2 Adducts? *Org. Lett.* **2018**, *20* (19), 6041–6045. https://doi.org/10.1021/acs.orglett.8b02290.

(5) Ausdall, B. R. V.; Glass, J. L.; Wiggins, K. M.; Aarif, A. M.; Louie, J. A Systematic Investigation of Factors Influencing the Decarboxylation of Imidazolium Carboxylates. *J. Org. Chem.* **2009**, *74* (20), 7935–7942. https://doi.org/10.1021/jo901791k.

(6) Allen, F. H.; Kennard, O.; Watson, D. G.; Brammer, L.; Orpen, A. G.; Taylor, R. Tables of Bond Lengths Determined by X-Ray and Neutron Diffraction. Part 1. Bond Lengths in Organic Compounds. *J. Chem. Soc. Perkin Trans. 2* **1987**, No. 12, S1. https://doi.org/10.1039/p298700000s1.

(7) Sivaev, I. B.; Bregadze, V. I. Lewis Acidity of Boron Compounds. *Front. Organomet. Chem. 2014* **2014**, *270–271*, 75–88. https://doi.org/10.1016/j.ccr.2013.10.017.

(8) Theuergarten, E.; Bannenberg, T.; Walter, M. D.; Holschumacher, D.; Freytag, M.; Daniliuc, C. G.; Jones, P. G.; Tamm, M. Computational and Experimental

Investigations of CO_2 and N_2O Fixation by Sterically Demanding N-Heterocyclic Carbenes (NHC) and NHC/Borane FLP Systems. *J. Chem. Soc. Dalton Trans.* **2014**, *43* (4), 1651–1662. https://doi.org/10.1039/c3dt52742e.

(9) Lieske, L. E.; Freeman, L. A.; Wang, G.; Dickie, D. A.; Gilliard, R. J.; Machan, C. W. Metal-Free Electrochemical Reduction of Carbon Dioxide Mediated by Cyclic(Alkyl)(Amino) Carbenes. *Chem. - Eur. J.* **2019**, *25* (24), 6098–6101. https://doi.org/10.1002/chem.201900316.

(10) Villamena, F. A.; Locigno, E. J.; Rockenbauer, A.; Hadad, C. M.; Zweier, J. L. Theoretical and Experimental Studies of the Spin Trapping of Inorganic Radicals by 5,5-Dimethyl-1-Pyrroline *N*-Oxide (DMPO). 1. Carbon Dioxide Radical Anion. *J. Phys. Chem. A* **2006**, *110* (49), 13253–13258. https://doi.org/10.1021/jp064892m.

(11) Eaton, G. R.; Eaton, S. S. 2.2 - Electron Paramagnetic Resonance Spectroscopy. In *Comprehensive Coordination Chemistry II*; McCleverty, J. A., Meyer, T. J., Eds.; Pergamon: Oxford, 2003; pp 37–48. https://doi.org/10.1016/B0-08-043748-6/01105-1.

(12) Barone, V. Structure, Magnetic Properties and Reactivities of Open-Shell Species From Density Functional and Self-Consistent Hybrid Methods. In *Recent Advances in Density Functional Methods*; Recent Advances in Computational Chemistry; WORLD SCIENTIFIC, 1995; Vol. Volume 1, pp 287–334. https://doi.org/10.1142/9789812830586_0008.

(13) Sciortino, G.; Lubinu, G.; Maréchal, J.-D.; Garribba, E. DFT Protocol for EPR Prediction of Paramagnetic Cu(II) Complexes and Application to Protein Binding Sites. *Magnetochemistry* **2018**, *4* (4), 55. https://doi.org/10.3390/magnetochemistry4040055.

(14) Neese, F.; Hansen, A.; Liakos, D. G. Efficient and Accurate Approximations to the Local Coupled Cluster Singles Doubles Method Using a Truncated Pair Natural Orbital Basis. *J. Chem. Phys.* **2009**, *131* (6), 064103. https://doi.org/10.1063/1.3173827.

(15) Hermosilla, L.; Calle, P.; García De La Vega, J. M.; Sieiro, C. Density Functional Theory Predictions of Isotropic Hyperfine Coupling Constants. *J. Phys. Chem. A* **2005**, *109* (6), 1114–1124. https://doi.org/10.1021/jp0466901.

(16) Minkin, V. I. Glossary of Terms Used in Theoretical Organic Chemistry. *Pure Appl. Chem.* **1999**, *71* (10), 1919–1981. https://doi.org/doi:10.1351/pac199971101919.

Chapter 5: Experimental section.

5.1. General procedures.

Manipulations were carried out following standard Schlenk line and glove box techniques using argon as the inert gas. Solvents were dried using a MBraun SPS column. Deuterated solvents were freeze-pump-thaw degassed and stored under Ar over 4Å molecular sieves. Quick Pressure Valve NMR tubes, a balloon fitted with a long needle adapter and Fisher-Porter flasks were used for the reactions with CO_2. NMR spectra were collected on Bruker machine: Avance III 400. All chemical shifts for ^{1}H and ^{13}C are relative to TMS. Chemical shifts are given in ppm, coupling constants in Hz. The following abbreviations are used: s, singlet; d, doublet; t, triplet; q, quartet sept, septet; m, multiplet.

Voltametric measurements were carried out with a potentiostat Autolab PGSTAT100 (ECO Chemie, The Netherlands) controlled by GPES 4.09 software. Experiments were performed in a homemade Schlenk three–electrode cell. The cell was prepared under argon in order to avoid the presence of moisture and air. The reference electrode consisted of a saturated calomel electrode (SCE) separated from the solution by a bridge compartment. The counter electrode was a platinum wire of ca 1cm² apparent surface. The working electrode was glassy carbon microdisk (1.0 mm of diameter, Bio-logic SAS). The supporting electrolyte (n-Bu_4N)[PF_6] (Fluka, 99% puriss electrochemical grade). It was dried under vacuum at 50°C for 12h. The solvent dichloromethane was collected from MBraun SPS column. The dichloromethane (pure for analysis – stabilized with amylene) was purchased from Carlo Erba. $B(C_6F_5)_3$ was purchased from Sigma Aldridge without any further purification.

5.2. Synthesis and characterisation of compounds.

5.2.1. I^{t}Bu-CO_2-$B(C_6F_5)_3$ (2-$B(C_6F_5)_3$).

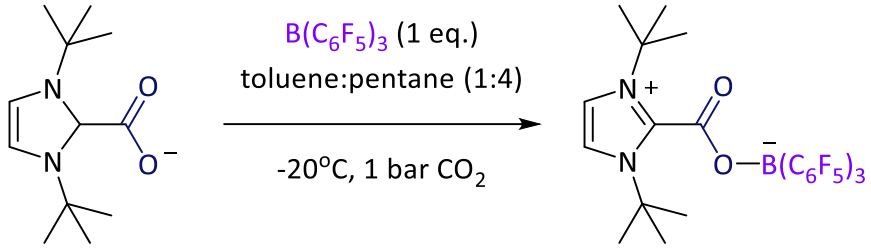

(**2**) (**2-$B(C_6F_5)_3$**) (20 %)

Following a similar synthesis procedure reported by Tamm et *al.*,[1] I^{t}Bu-CO_2 (**2**) (600 mg, 2.67 mmol) and $B(C_6F_5)_3$ (1369 mg, 2.67 mmol) were placed in a Schlenk at -20°C under argon. CO_2 was introduced in the flask via a balloon fitted with a needle adapter, which was purged 3 times with CO_2 prior to being filled. The Schlenk flask was purged with CO_2 for 1 min to ensure a CO_2 atmosphere in it. Under CO_2 at -20°C, toluene-pentane (1:4, 120 mL) was added and the mixture was stirred up for 1h. The white precipitate was filtered and washed 3 times with 5mL of pentane dried under vacuum. (1.36 g, 65%). The white solid was purified via crystallisation from a mixture of pentane-CH_2Cl_2 (414 mg, 20%).

^{1}H NMR (400 MHz, 298 K, CD_2Cl_2) δ 7.30 (s, 2H, CH) 1.61 (s, 18H, CH_3). ^{11}B NMR (128 MHz, 298 K, CD_2Cl_2) δ -4.0 (s). $^{13}C\{^1H\}$ NMR (100 MHz, 298 K, CD_2Cl_2) δ = 156.0 (NHC-*C*O_2), 148.5 (d, $^1J_{CF}$ = 241.8 Hz, o-C_6F_5) 140.0 (N_2C) 139.8 (d, $^1J_{CF}$= 254.5 Hz, p-C_6F_5) 137.1 (d, $^1J_{CF}$ = 247.4 Hz, m-C_6F_5) 120.9 (BC-ipso) 118.8 (C_2H_2) 64.8 (*C*$(CH_3)_3$) 30.0 ppm (CH_3). ^{19}F NMR (376 MHz, 298 K, CD_2Cl_2): δ −131.3 (d, $^3J_{FF}$= 19.9 Hz, 6F, o-C_6F_5) −160.3 (t, $^3J_{FF}$= 20.4 Hz, 3F, p-C_6F_5) −166.3 (t, $^3J_{FF}$ = 18.2 Hz, 6F, m-C_6F_5). FTIR (solid state): $\nu_{C=O}$ = 1714.3 cm^{-1}. E^p_{red} (vs. $Fc^{+/0}$) = -2.30 V.

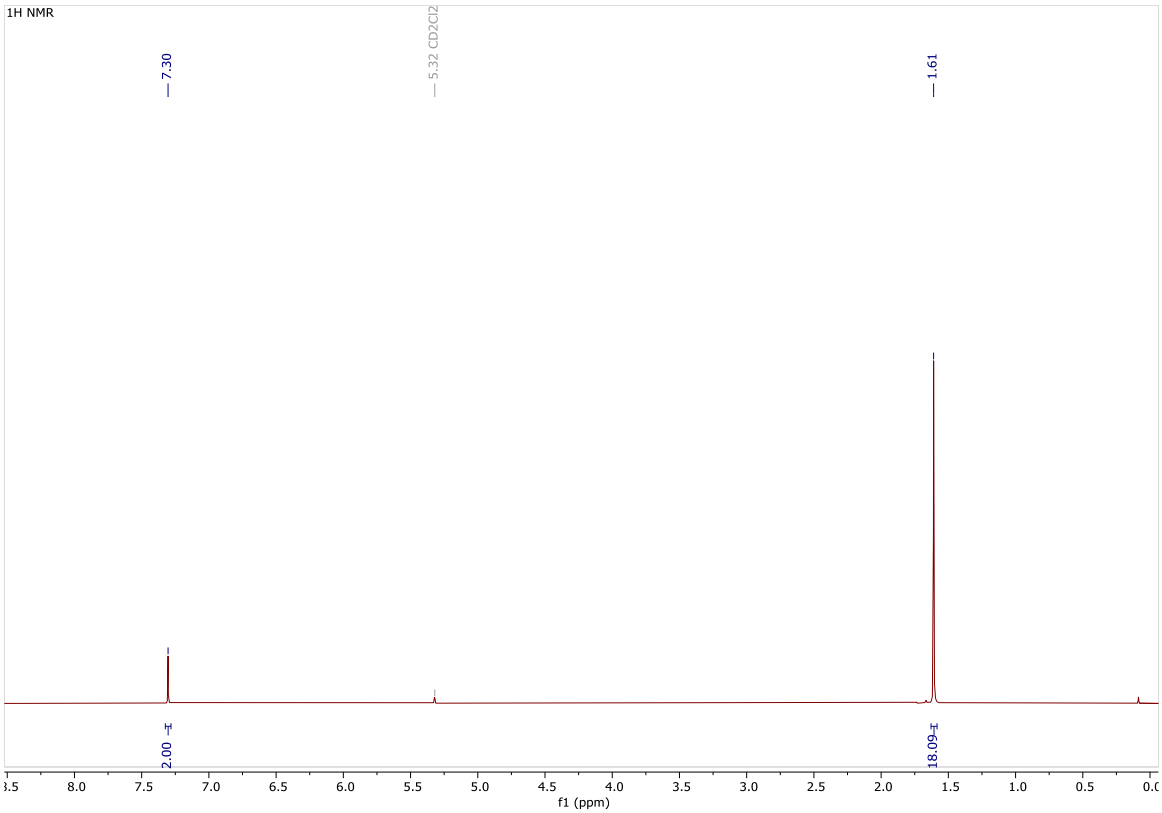

Figure S1. ^{1}H NMR spectrum of **2-B(C_6F_5)$_3$** in CD_2Cl_2 at 298 K.

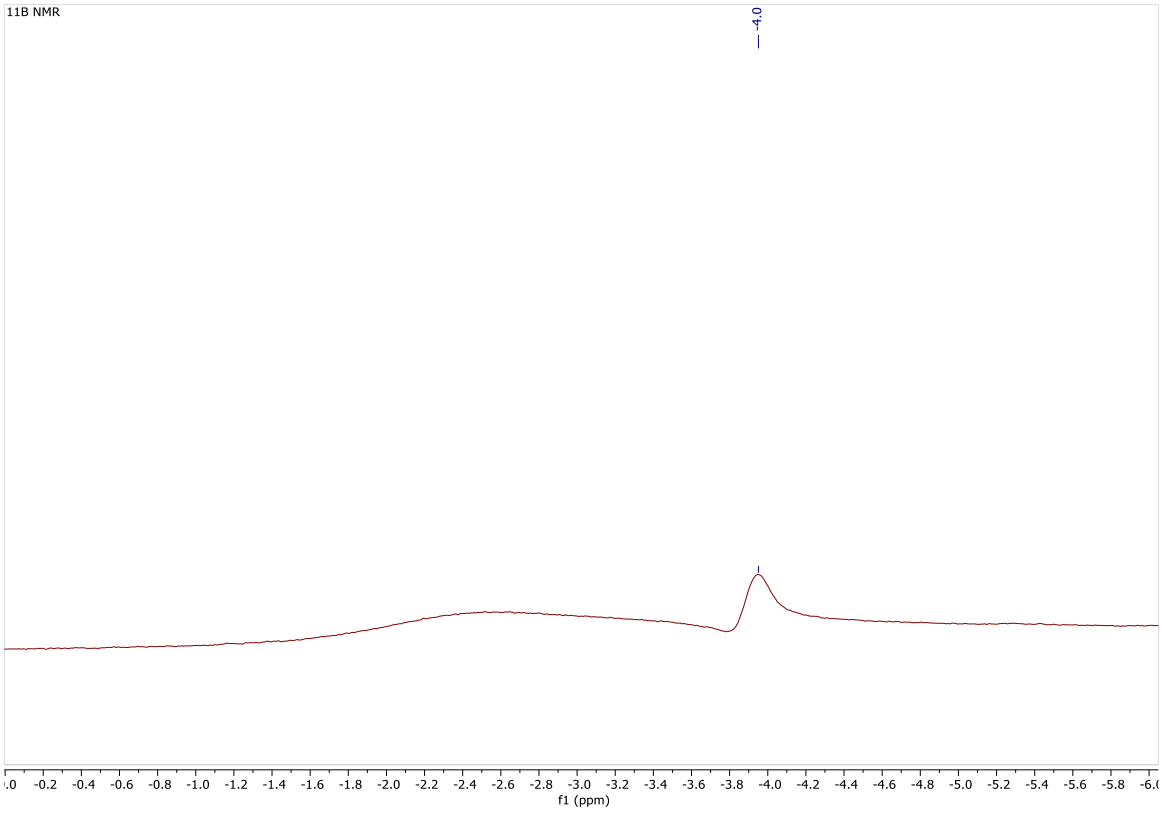

Figure S2. ^{11}B NMR spectrum of **2-B(C_6F_5)$_3$** in CD_2Cl_2 at 298 K.

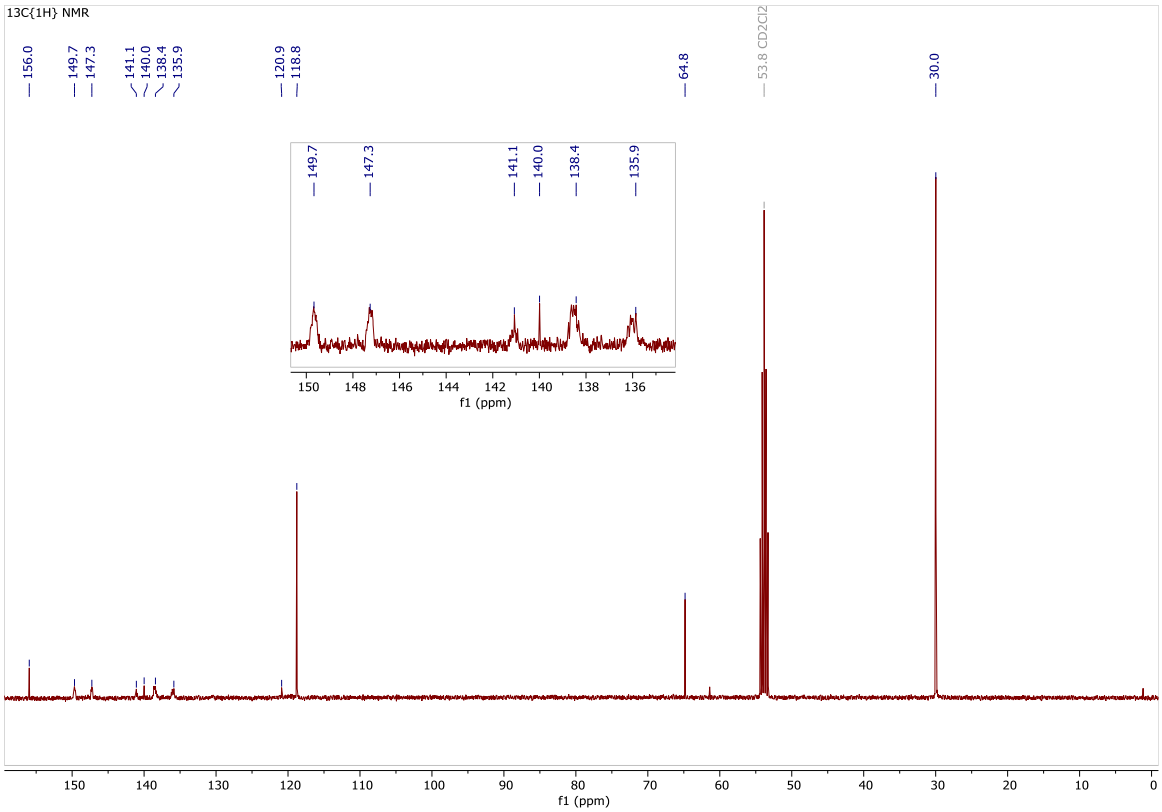

Figure 3. $^{13}C\{^{1}H\}$ NMR spectrum of **2-B(C_6F_5)$_3$** in CD_2Cl_2 at 298 K.

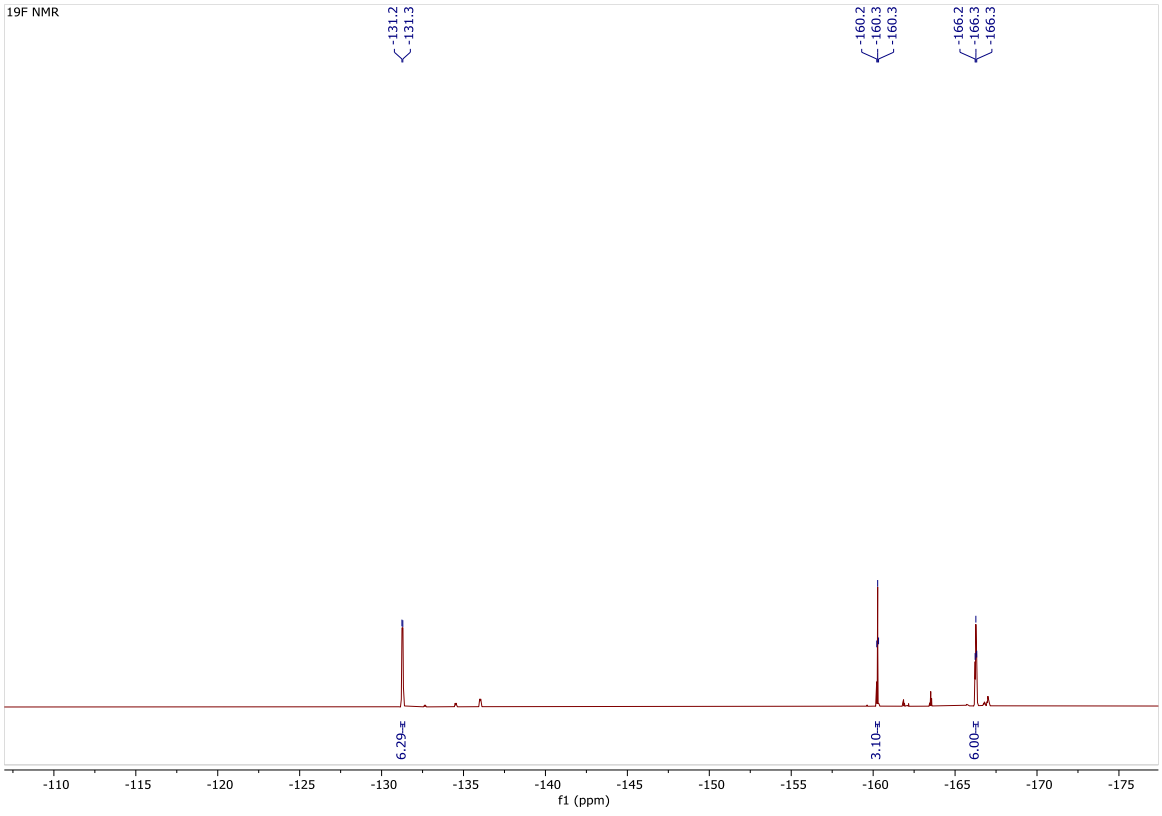

Figure S4. ^{19}F NMR spectrum of **2-B(C_6F_5)$_3$** in CD_2Cl_2 at 298 K.

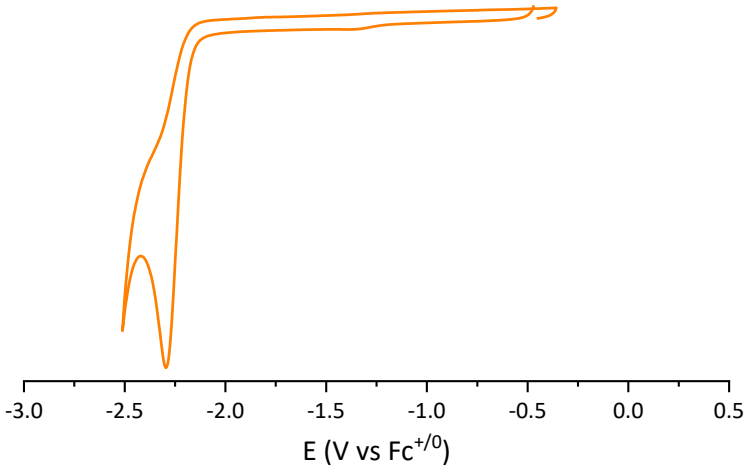

Figure S5. Normalised CV response of **2-B(C_6F_5)$_3$** at reducing potentials under Ar atmosphere in dichloromethane. Conditions: 5 mM compound **2-B(C_6F_5)$_3$** and 0.1 M [n-Bu_4N][PF_6], scan 200 mV/s.

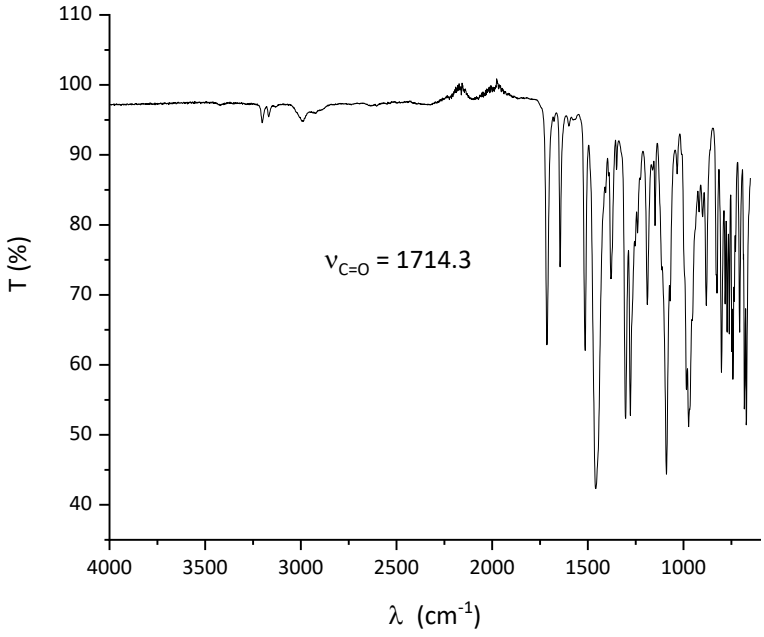

Figure S6. FTIR (solid state) of **2-B(C_6F_5)$_3$** at 298 K.

5.2.2. IAd-CO_2-$B(C_6F_5)_3$ (3-$B(C_6F_5)_3$).

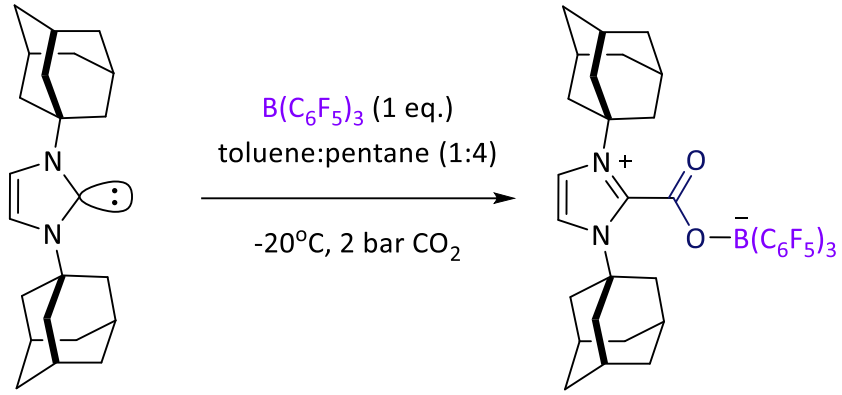

(**3'**) (**3-$B(C_6F_5)_3$**) (66 %)

IAd (**3'**) (150 mg, 0.45 mmol) and $B(C_6F_5)_3$ (236.8 mg, 0.44 mmol) were placed in a Fisher porter flask under argon. The flask was charged with 2 bar of CO_2 and three CO_2-vacuum cycles were performed. 10 mL of a mixture toluene-pentane (1:4) were then added and the flask placed at -20 °C under CO_2. The resulting white suspension was stirred for 1 h at -20 °C, after which the suspension was filtered and washed with pentane (3x5 mL) at room temperature. The resulting white residue was dried under vacuum and isolated as a white powder in 66% yield (265.5 mg).

^{1}H NMR (400.1 MHz, 298 K, $CDCl_3$) δ 7.42 (s, 2H, C_2H_2), 2.29 (s, 6H, CH-Ad) 2.15 (s, 12H, CH_2-Ad) 1.77 (q, $^{3}J_{HH}$ = 14.3 Hz, 12H, CH_2-Ad). ^{11}B NMR (128.4 MHz, 298 K, $CDCl_3$) δ -3.8 (s). $^{13}C\{^{1}H\}$ NMR (100.6 MHz, 297.9 K, $CDCl_3$) δ = 161.9 (NHC-*C*O_2), 148.1 (d, $^{1}J_{CF}$ = 240.1 Hz, m-C_6F_5), 139.1 (d, $^{1}J_{CF}$ = 234.9 Hz, p-C_6F_5), 136.6 (d, $^{1}J_{CF}$ = 237.9 Hz, o-C_6F_5), 130.7 (N_2C), 121.0 (BC-ipso), 118.9 (C_2H_2), 61.1 (C-Ad), 42.8 (CH_2-Ad), 35.3 (CH_2-Ad), 29.5 (CH-Ad). ^{19}F NMR (376.5 MHz, 298 K, CD_2Cl_2): δ −133.9 (d, $^{3}J_{FF}$ = 20.0 Hz, 6F, o-C_6F_5), −161.1 (t, $^{3}J_{FF}$ = 20.9 Hz, 3F, p-C_6F_5), −166.0 (t, $^{3}J_{FF}$ = 23.8 Hz, 6F, m-C_6F_5). Anal (%): Calcd for $C_{42}H_{32}BF_{15}N_2O_2.C_6H_5CH_3$: C, 59.77; H, 4.09; N, 2.85. Found: C, 59.27; H, 4.15; N, 3.70. FTIR (solid state): $\nu_{C=O}$ = 1715.2 cm^{-1}. E^{p}_{red} (vs. $Fc^{+/0}$) = -2.44 V.

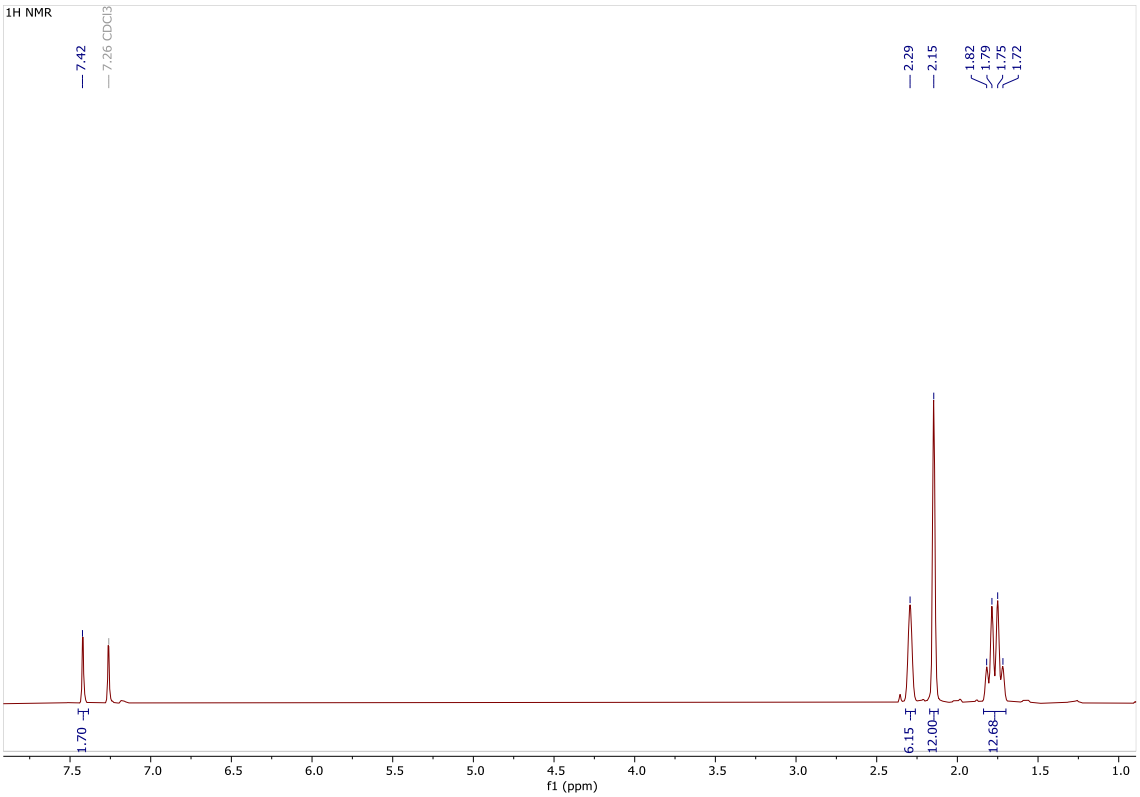

Figure S7. ^{1}H NMR spectrum of **3-B(C_6F_5)$_3$** in $CDCl_3$ at 298 K.

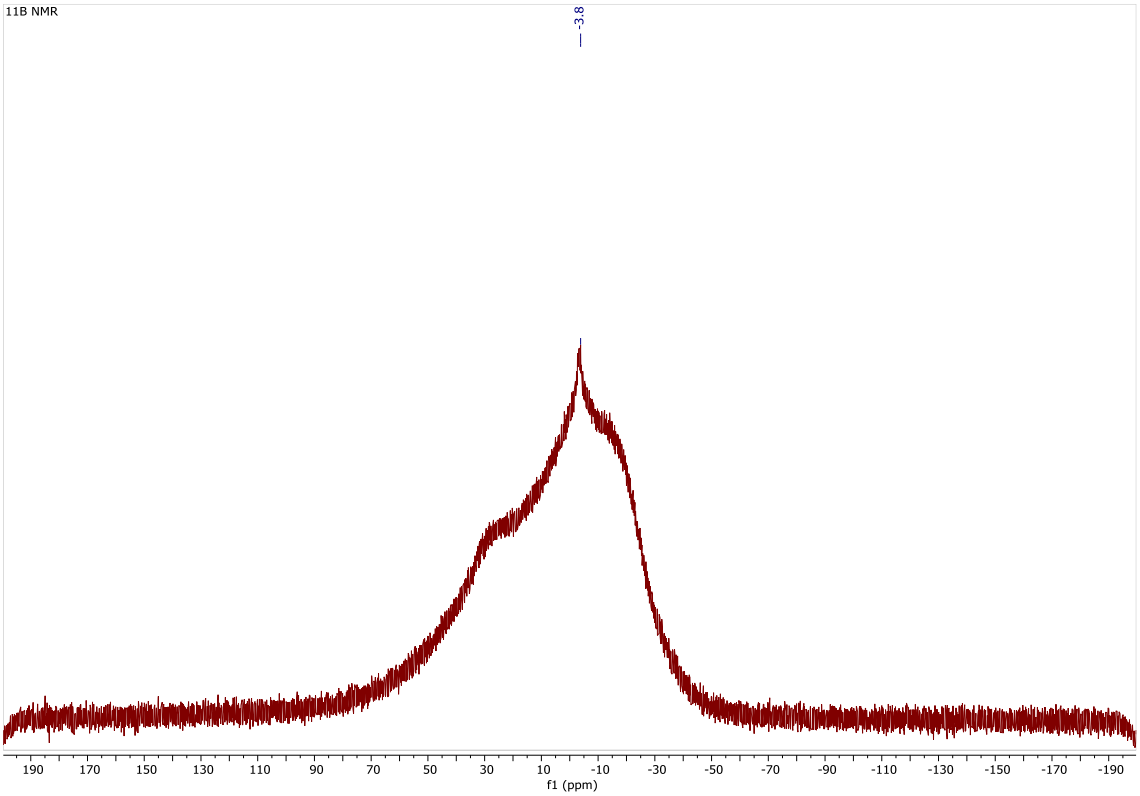

Figure S8. ^{11}B NMR spectrum of **3-B(C_6F_5)$_3$** in $CDCl_3$ at 298 K.

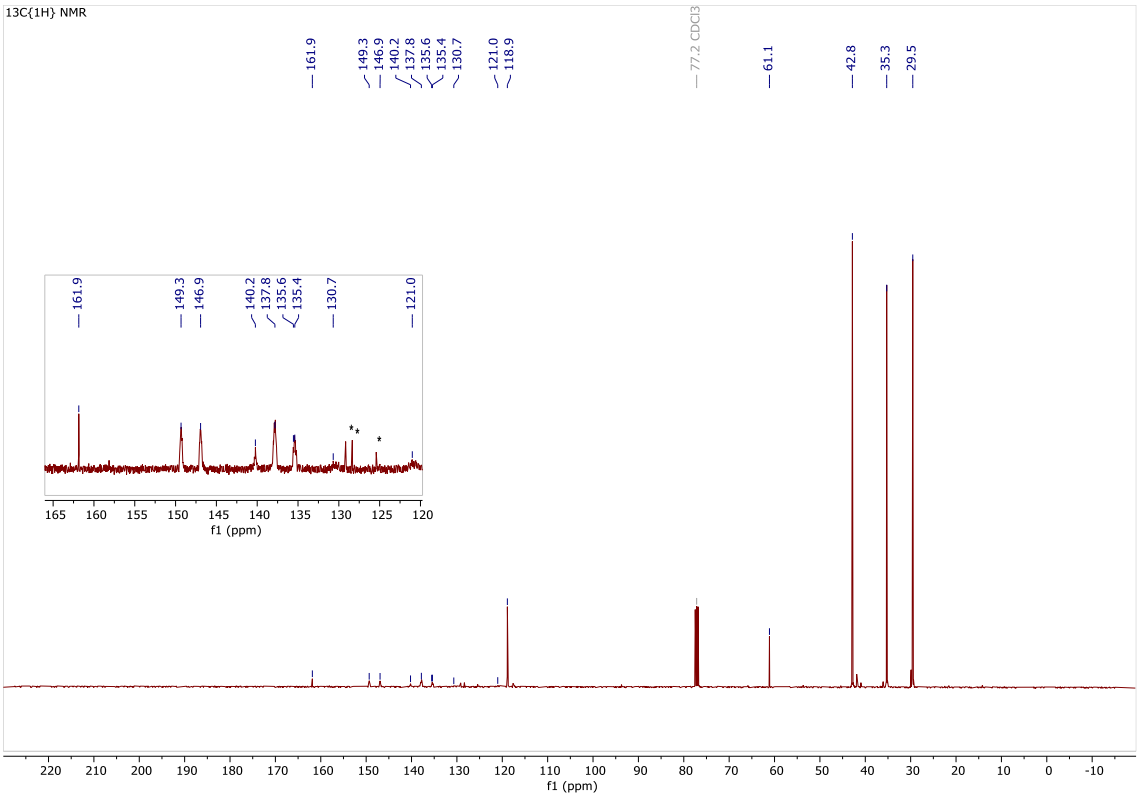

Figure S9. $^{13}C\{^{1}H\}$ NMR spectrum of **3-B(C_6F_5)$_3$** in $CDCl_3$ at 298 K. (* $C_6H_5CH_3$) 40 mg of **3-B(C_6F_5)$_3$**, ns = 8249.

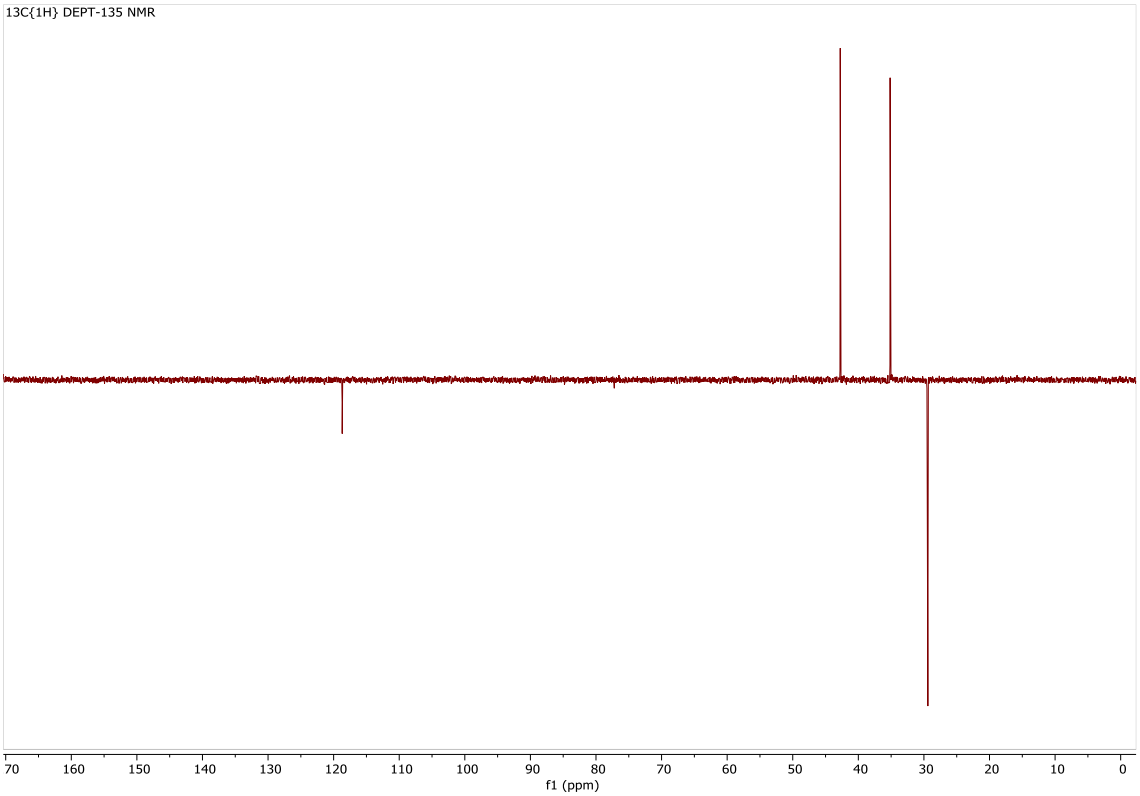

Figure S10. $^{13}C\{^{1}H\}$ DEPT-135 NMR spectrum of **3-B(C_6F_5)$_3$** in $CDCl_3$ at 298 K.

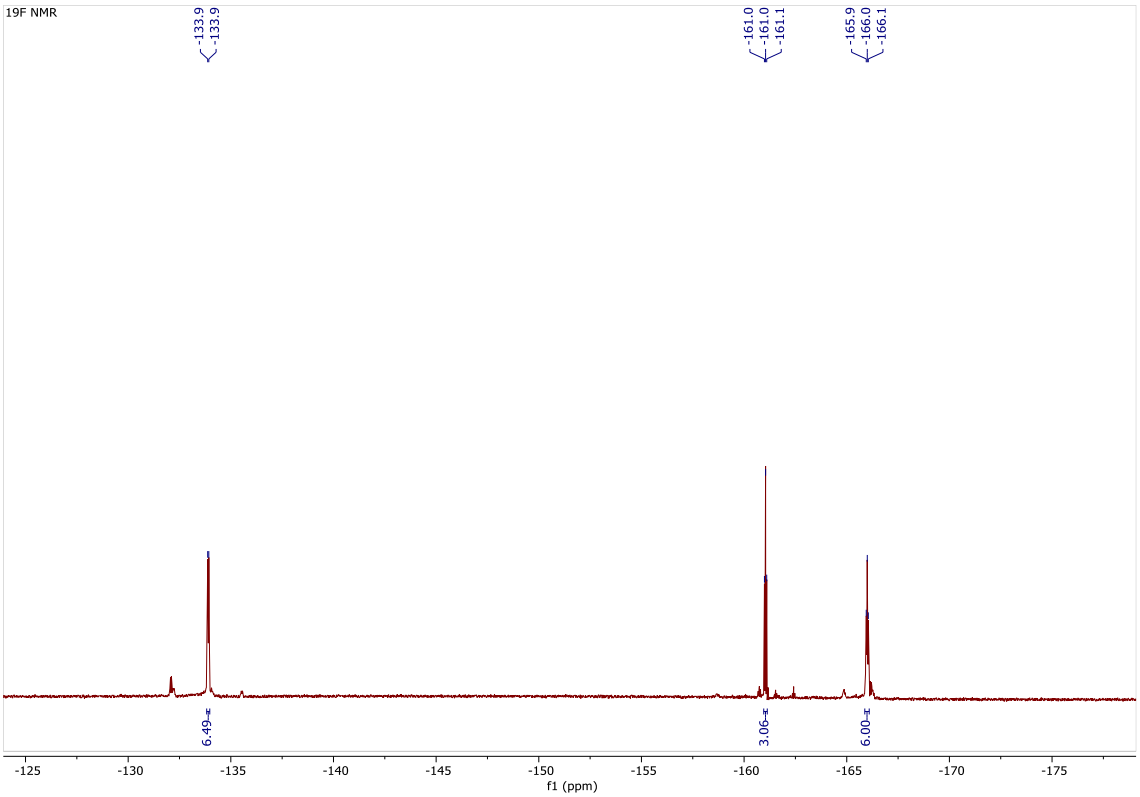

Figure S11. ^{19}F NMR spectrum of **3-B(C_6F_5)$_3$** in $CDCl_3$ at 298 K.

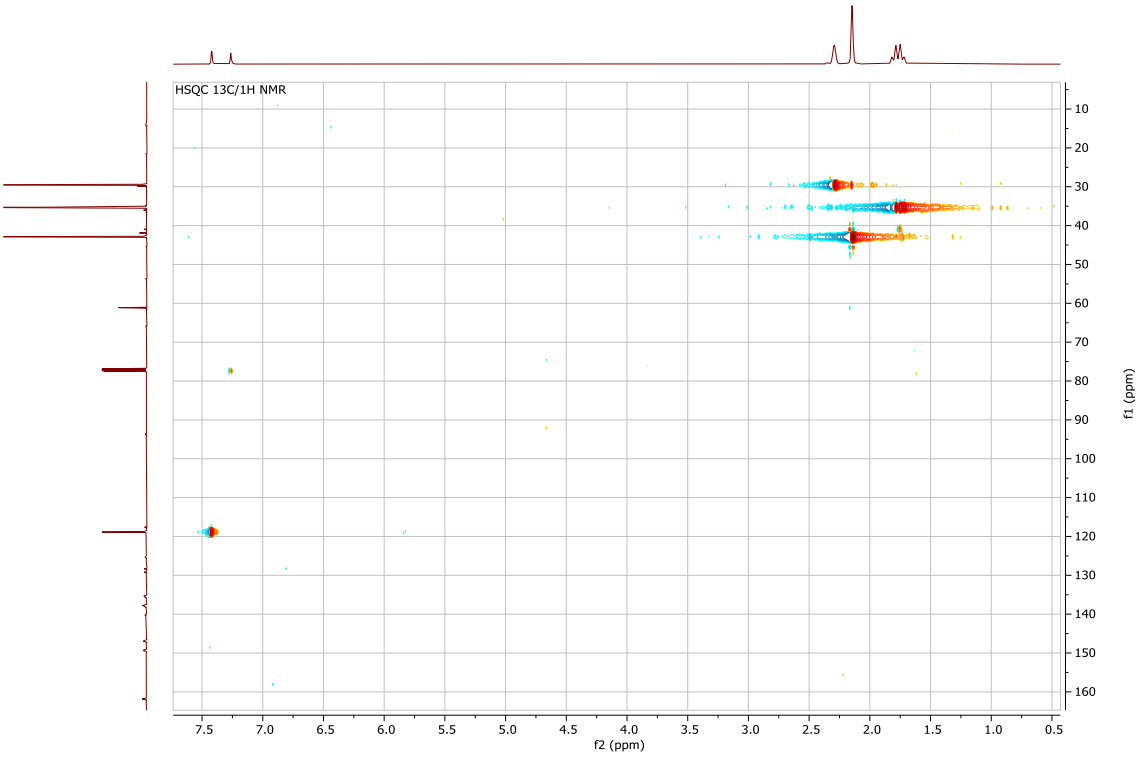

Figure S12. HSQC $^{13}C/^{1}H$ NMR spectrum of **3-B(C_6F_5)$_3$** in $CDCl_3$ at 298 K.

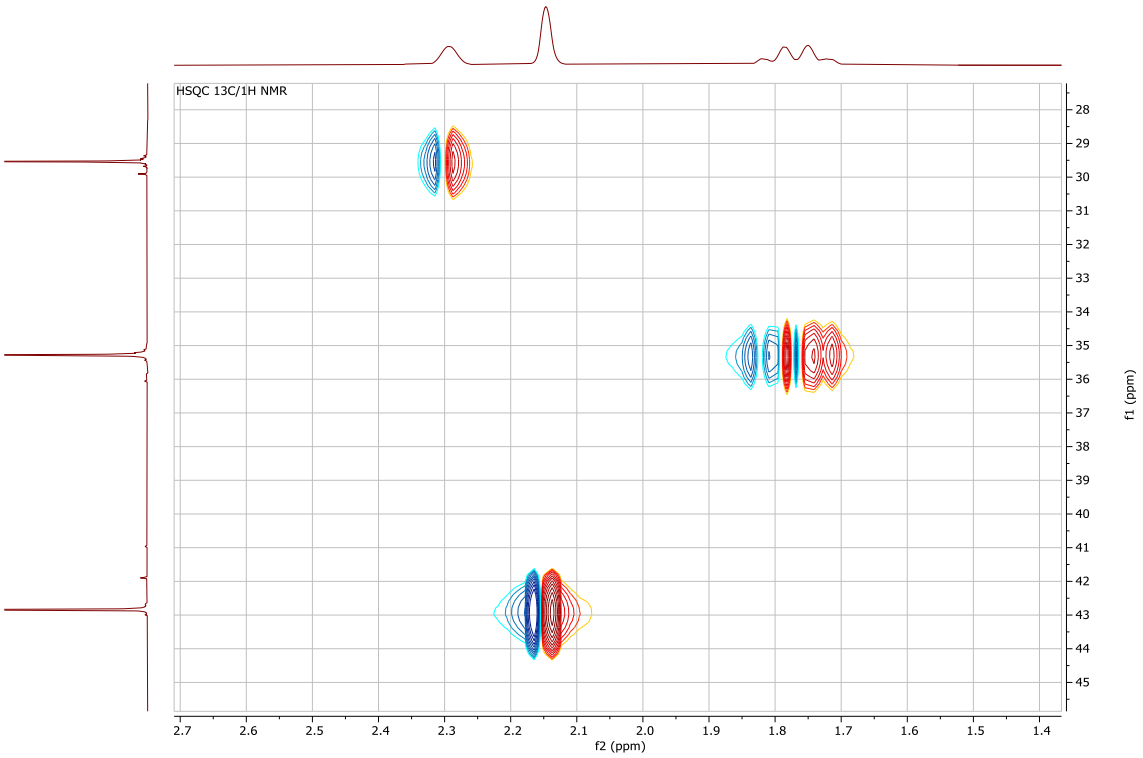

Figure S13. Zoom HSQC $^{13}C/^{1}H$ NMR spectrum of **3-B(C_6F_5)$_3$** in $CDCl_3$ at 298.1 K.

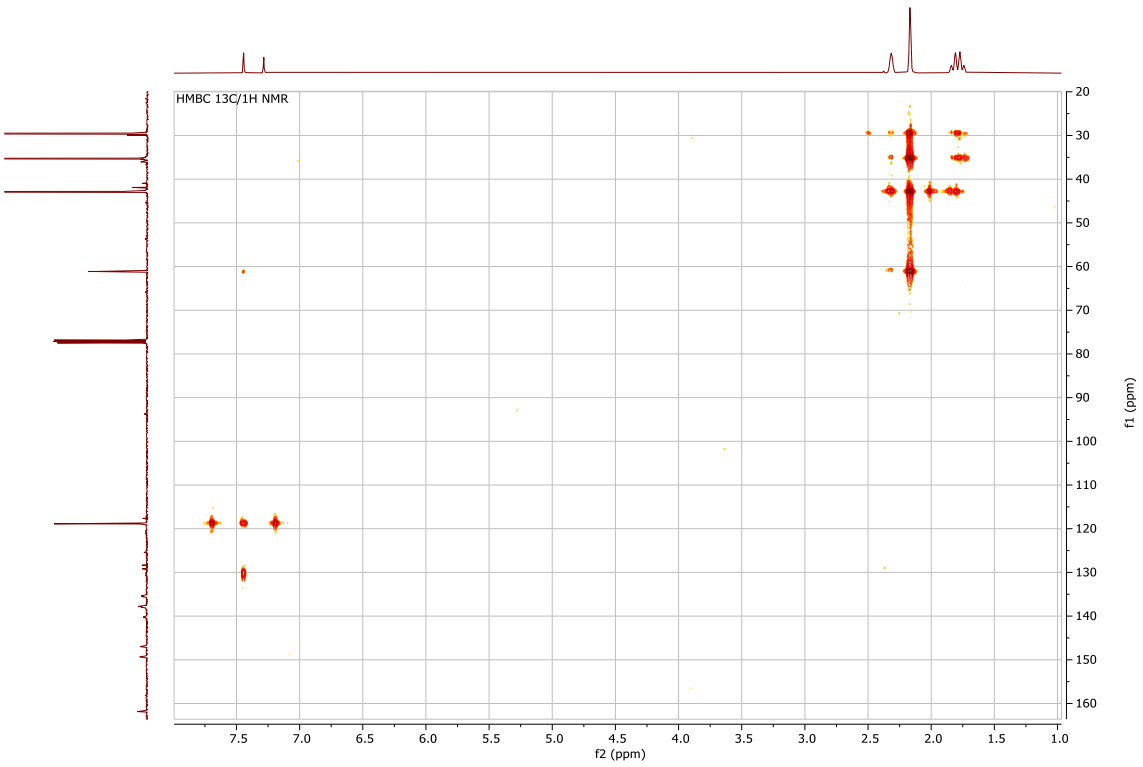

Figure S14. HMBC $^{13}C/^{1}H$ NMR spectrum of **3-B(C_6F_5)$_3$** in $CDCl_3$ at 298.1 K.

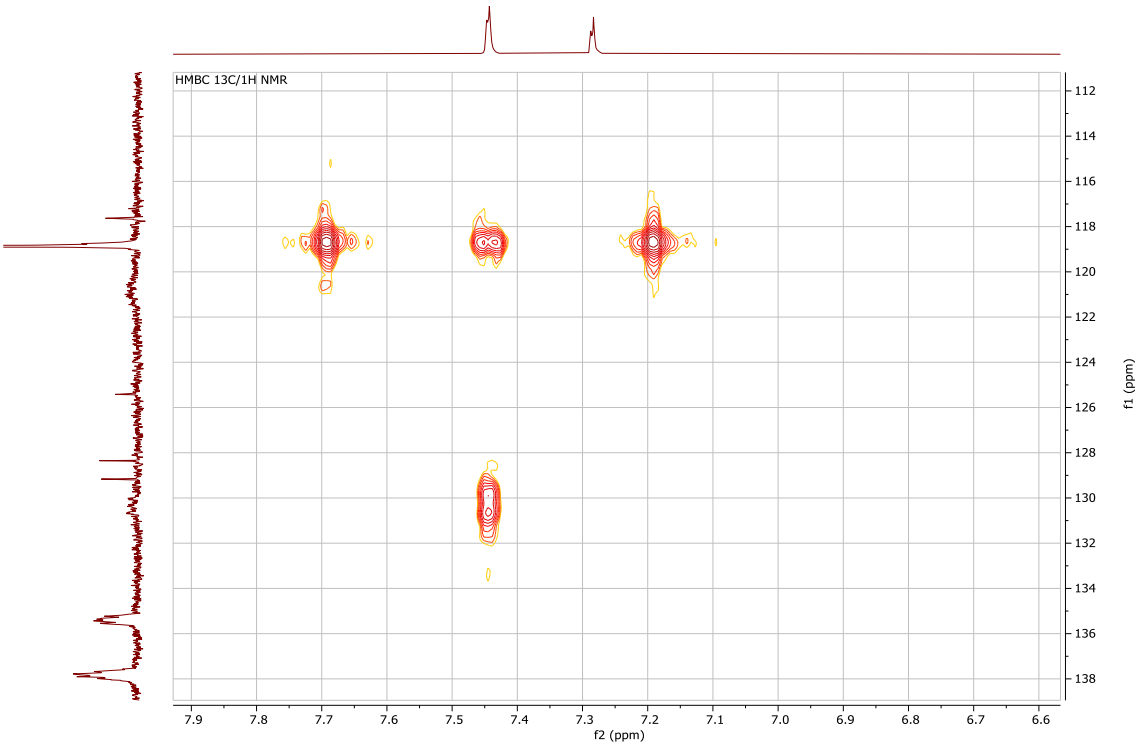

Figure S15. Zoom HMBC $^{13}C/^{1}H$ NMR spectrum of **3-B(C_6F_5)$_3$** in $CDCl_3$ at 298.1 K.

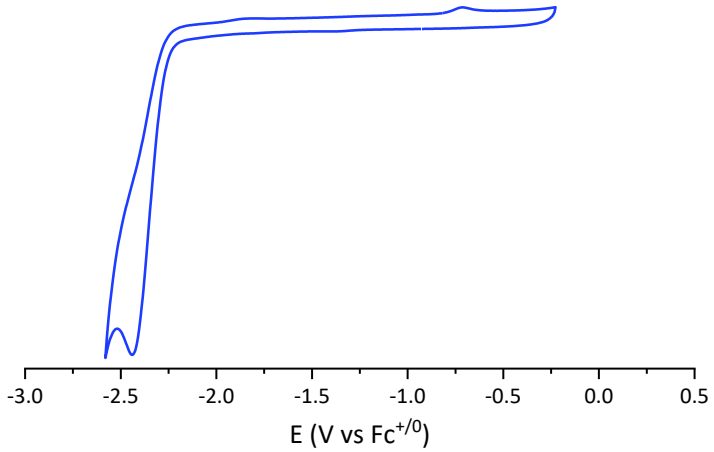

Figure S16. Normalised CV response of **3-B(C_6F_5)$_3$** at reducing potentials under Ar atmosphere in CH_2Cl_2. Conditions: 5 mM compound **3-B(C_6F_5)$_3$** and 0.1 M [n-Bu_4N][PF_6], scan 200 mV/s.

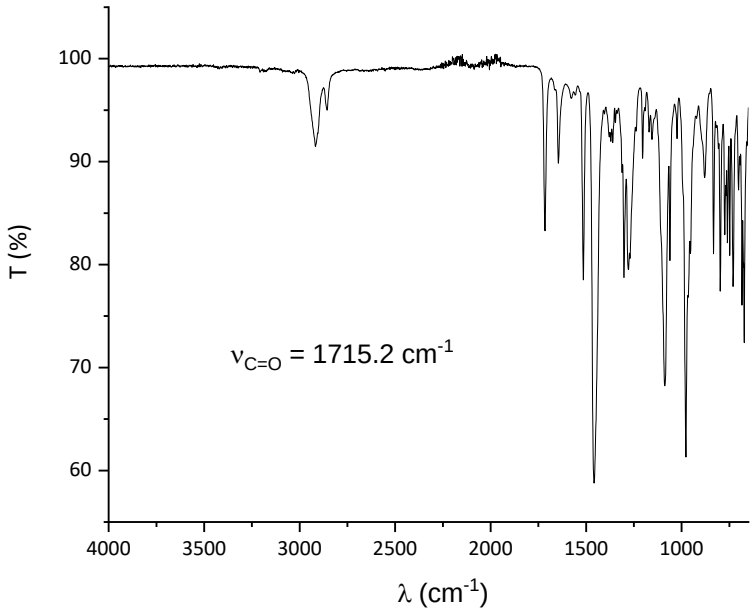

Figure S17. FTIR (solid state) of **3-B(C_6F_5)$_3$** at 298 K.

Crystallographic details of adduct 3-B(C_6F_5)$_3$.

Table S1. Crystal data.

$C_{42}H_{32}BF_{15}N_2O_2$	
M_r = 892.50	D_x = 1.597 Mg m^{-3}
Monoclinic, Cc	
Hall symbol: C -2yc	Cu Kα radiation, λ = 1.54184 Å
a = 11.4874 (2) Å	Cell parameters from 14591 reflections
b = 20.6397 (4) Å	θ = 4.3–79.4°
c = 15.6705 (3) Å	μ = 1.32 mm^{-1}
β = 92.130 (2)°	T = 100 K
V = 3712.85 (12) Å^3	Plate, colourless
Z = 4	0.18 × 0.10 × 0.03 mm
F(000) = 1816	

Table S2. Data collection.

XtaLAB Synergy, Dualflex, HyPix diffractometer	6206 independent reflections
Radiation source: micro-focus sealed X-ray tube, PhotonJet (Cu) X-ray Source	6074 reflections with $I > 2\sigma(I)$
Mirror monochromator	$R_{int} = 0.023$
Detector resolution: 10.0000 pixels mm^{-1}	$\theta_{max} = 80.5°$, $\theta_{min} = 4.3°$
	h = −14 14
Absorption correction: multi-scan	k = −18 26
CrysAlisPro 1.171.41.120a (Rigaku Oxford Diffraction, 2021) Empirical absorption correction using spherical harmonics, implemented in SCALE3 ABSPACK scaling algorithm.	
$T_{min} = 0.617$, $T_{max} = 1.000$	l = −19 18
18464 measured reflections	

Table S3. Refinement.

Refinement on F^2	Hydrogen site location: inferred from neighbouring sites
Least-squares matrix: full	H-atom parameters constrained
$R[F^2 > 2\sigma(F^2)] = 0.026$	$w = 1/[\sigma^2(F_o^2) + (0.035P)^2 + 1.8608P]$ where $P = (F_o^2 + 2F_c^2)/3$
$wR(F^2) = 0.069$	$(\Delta/\sigma)_{max} < 0.001$
$S = 1.06$	$\Delta\rho_{max} = 0.27$ e Å^{-3}
6206 reflections	$\Delta\rho_{min} = -0.18$ e Å^{-3}
561 parameters	Extinction correction: SHELXL-2018/3 (Sheldrick2018) $Fc^*=kFc[1+0.001xFc^2\lambda^3/\sin(2\theta)]^{-1/4}$
2 restraints	Extinction coefficient: 0.00033 (5)
Absolute structure parameter: 0.04 (8)	Absolute structure: Refined as an inversion twin.

5.2.3. IPr-CO_2-$B(C_6F_5)_3$ (5-$B(C_6F_5)_3$).

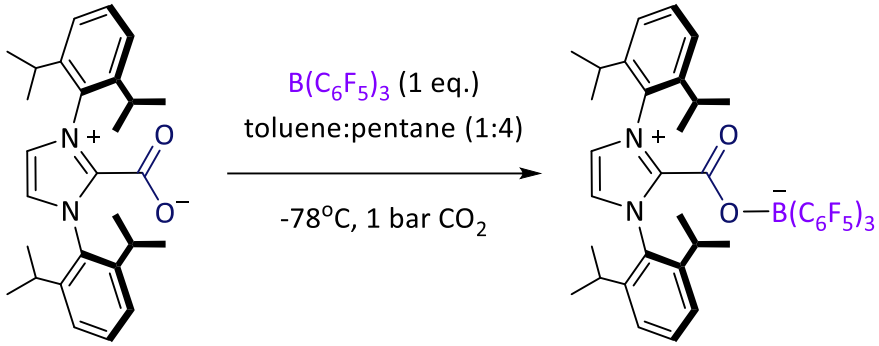

(**5**) (**5-$B(C_6F_5)_3$**) (29 %)

IPr-CO_2 (200 mg, 0.44 mmol) and $B(C_6F_5)_3$ (236.8 mg, 0.44 mmol) were placed in a Schlenk flask under argon. The flask was flushed with CO_2 via a balloon charged with this gas for 1 min. 10 mL of a mixture toluene-pentane (1:4) were then added and the flask placed at -78 °C under CO_2. The resulting white suspension was stirred for 1 h at -78 °C, after which the suspension was filtered and washed with pentane (3x5 mL) at room temperature. The resulting white residue was purified via crystallisation from a saturated solution of pentane-CH_2Cl_2. After filtration and drying under vacuum, the expected product was isolated as a white powder in 29% yield (122 mg).

^{1}H NMR (400.2 MHz, 298 K, CD_2Cl_2) δ 7.57 (t, $^3J_{HH}$ = 7.8 Hz, 2H, p-Ar) 7.36 (s, 2H, C_2H_2) 7.31 (d, $^3J_{HH}$ = 7.8 Hz, 4H, m-Ar) 2.40 (sept, $^3J_{HH}$ = 6.8 Hz, 2H, C*H*$(CH_3)_2$) 1.15 (d, $^3J_{HH}$ = 6.9 Hz, 12H, CH(C*H*$_3)_2$) 1.11 (d, $^3J_{HH}$ = 6.7 Hz, 12H, CH(C*H*$_3)_2$). ^{11}B NMR (128.4 MHz, 298 K, CD_2Cl_2) δ -3.4 (s). ^{13}C{^{1}H} NMR (100.6 MHz, 298 K, CD_2Cl_2) δ = 152.8 (NHC-*C*O_2), 148.1 (d, $^1J_{CF}$ = 241.0 Hz, m-C_6F_5) 144.5 (o-Ar) 139.5 (d, $^1J_{CF}$ = 247.3 Hz, p-C_6F_5) 139.3 (N_2C) 136.2 (d, $^1J_{CF}$ = 245.8 Hz, o-C_6F_5), 132.3 (ipso-Ar), 132.2 (p-Ar), 126.6 (C_2H_2), 125.0 (m-Ar), 120.0 (BC-ipso) 29.8 (*C*H$(CH_3)_2$) 25.4 (CH(*C*H$_3)_2$) 22.2 (CH(*C*H$_3)_2$). ^{19}F NMR (376.5 MHz, 298 K, CD_2Cl_2): δ −134.1 (d, $^3J_{FF}$ = 24.2 Hz, 6F, o-C_6F_5), −161.4 (t, $^3J_{FF}$ = 20.7 Hz, 3F, p-C_6F_5) −166.4 (t, $^3J_{FF}$ = 21.6 Hz, 6F, m-C_6F_5). HRMS (ESI+) m/z: Calcd for $C_{46}H_{37}BF_{15}N_2O_2$ [M+H$^+$]: 945.2620 found 945.2614. Anal (%): Calcd for $C_{46}H_{36}BF_{15}N_2O_2$: C, 58.49; H, 3.84; N, 2.97. Found: C, 58.41; H, 3.53; N, 2.83. FTIR (solid state): $\nu_{C=O}$ = 1717.0 cm^{-1}. $E^{1/2}_{red}$ (vs. $Fc^{+/0}$) = -2.08 V.

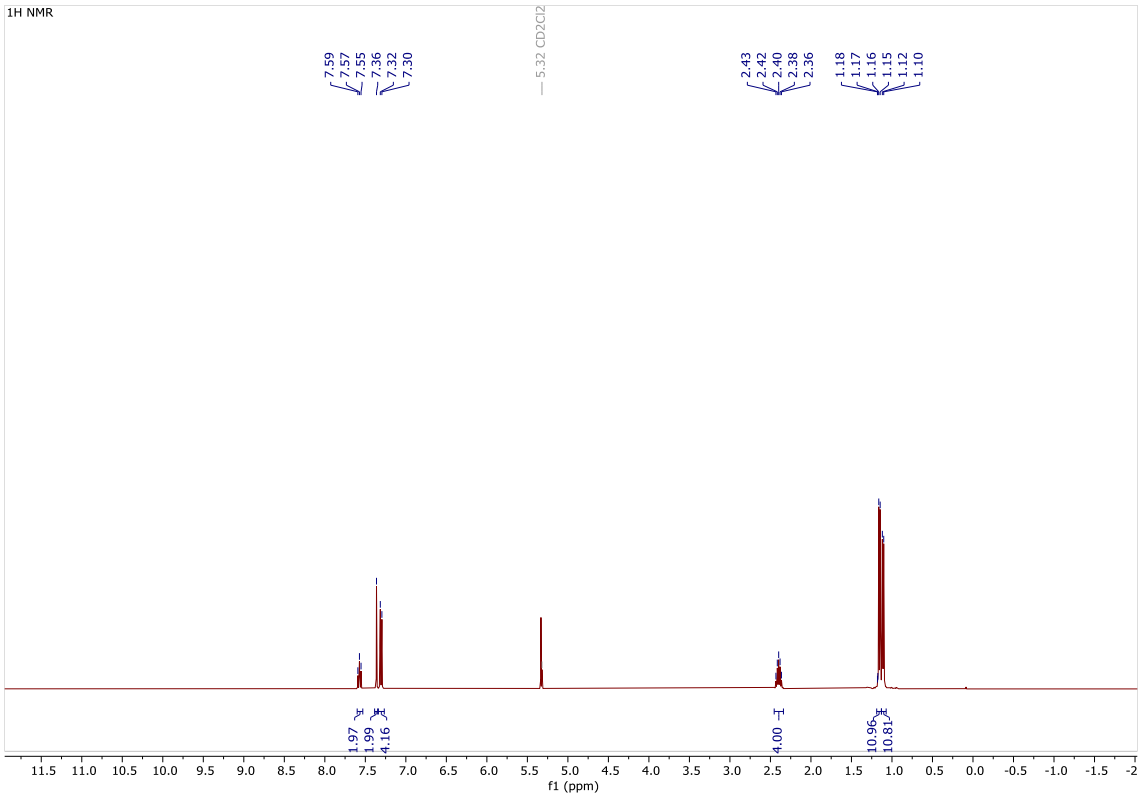

Figure S18. ^{1}H NMR spectrum of **5-B(C_6F_5)$_3$** in CD_2Cl_2 at 298 K.

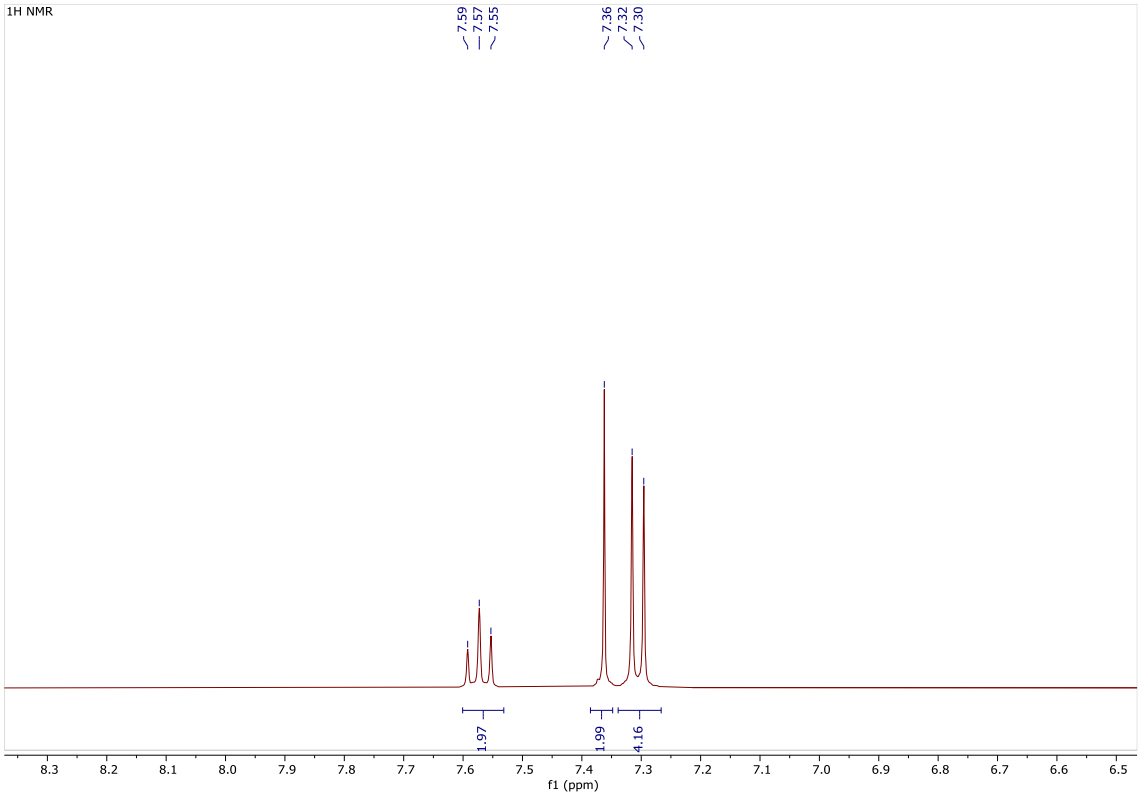

Figure S19. Zoom ^{1}H NMR spectrum of **5-B(C_6F_5)$_3$** in CD_2Cl_2 at 298 K between 8.3 and 6.5 ppm.

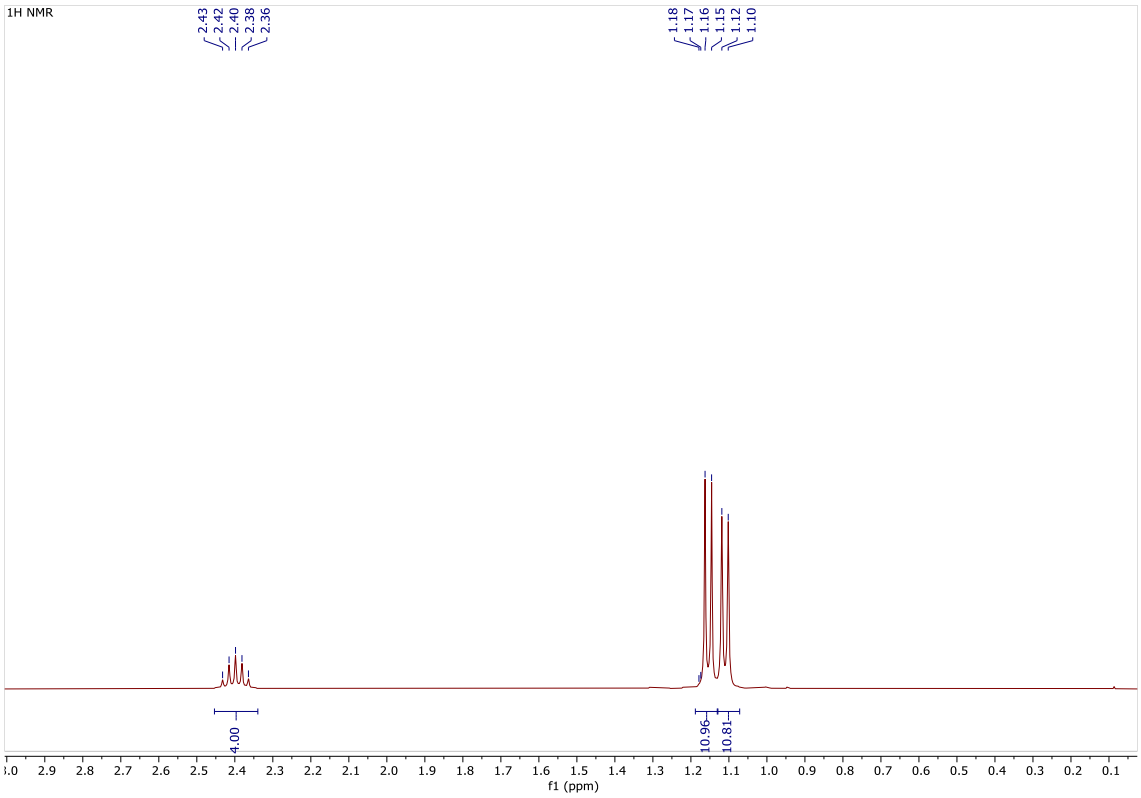

Figure S20. Zoom ^{1}H NMR spectrum of **5-B(C_6F_5)$_3$** in CD_2Cl_2 at 298 K between 2.9 and 0.1 ppm.

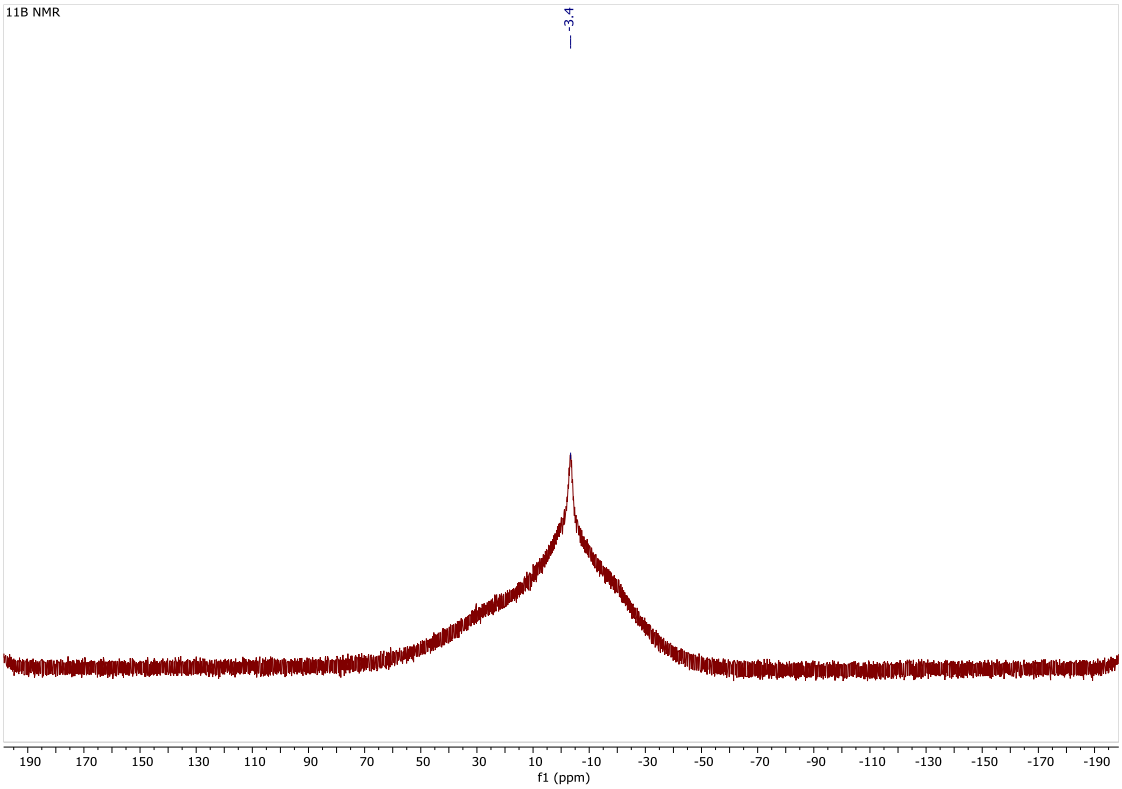

Figure S21. ^{11}B NMR spectrum of **5-B(C_6F_5)$_3$** in CD_2Cl_2 at 298 K.

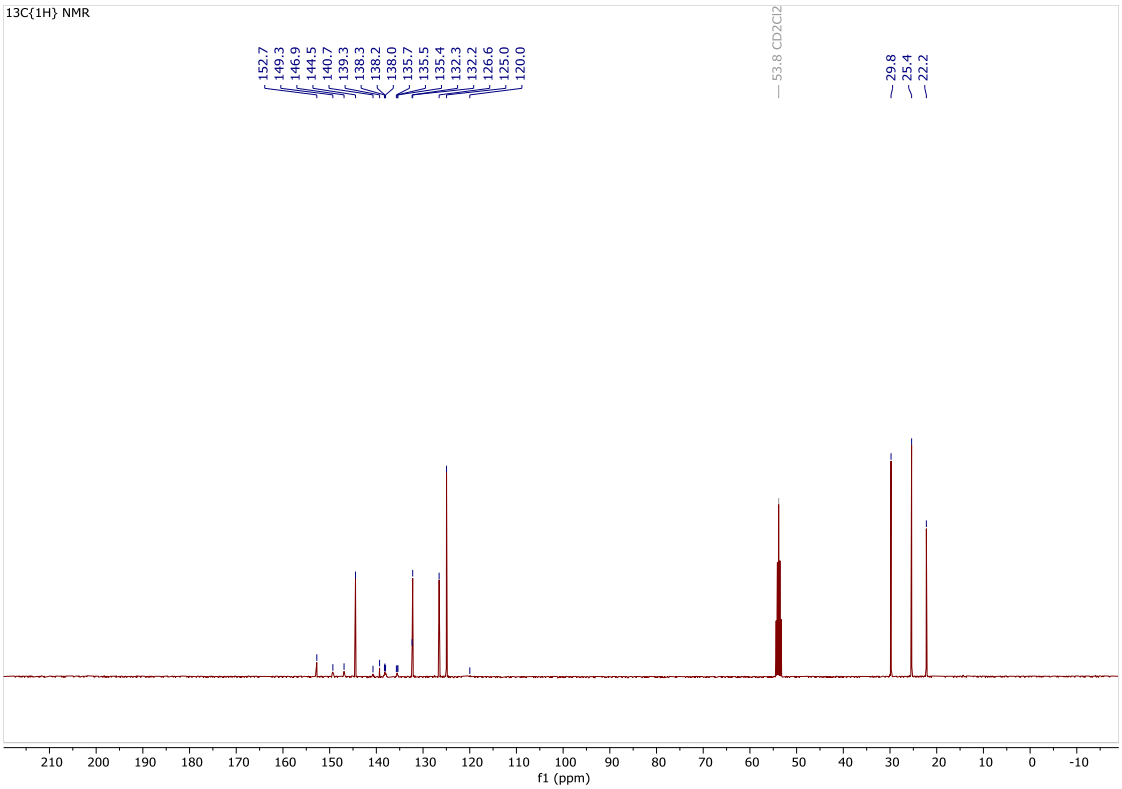

Figure S22. $^{13}C\{^{1}H\}$ NMR spectrum of **5-B(C_6F_5)$_3$** in CD_2Cl_2 at 298 K.

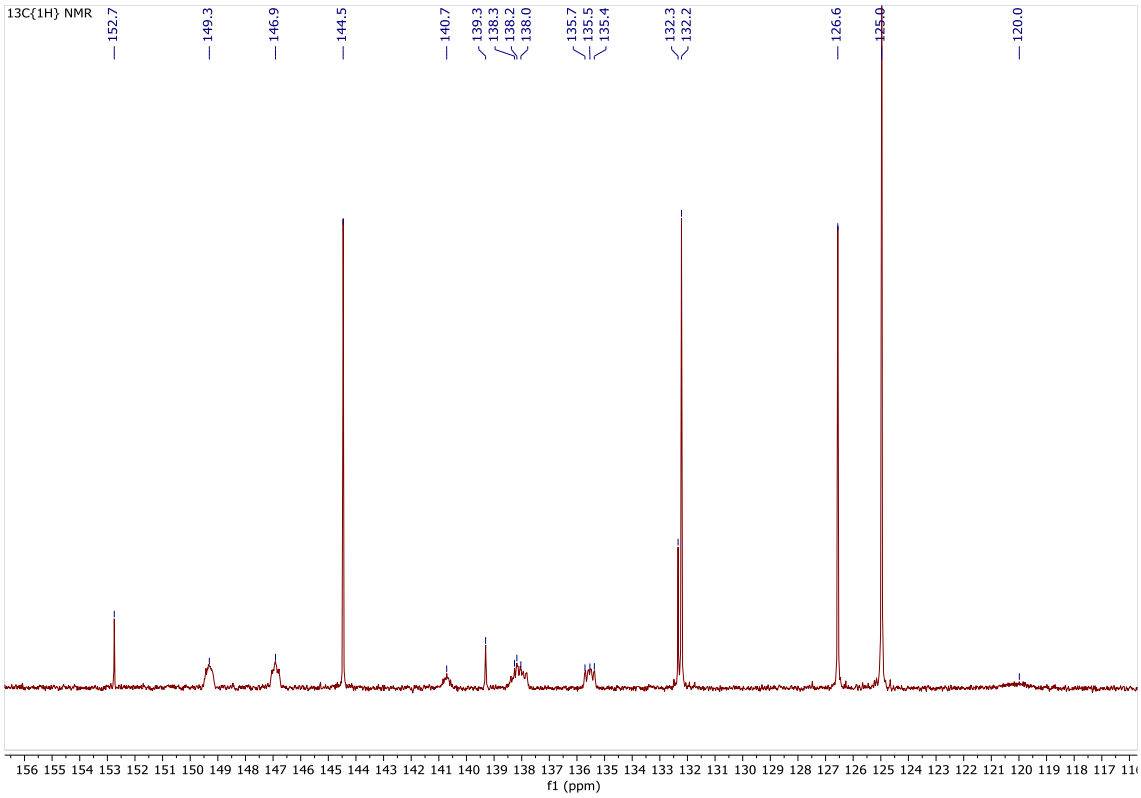

Figure S23. Zoom $^{13}C\{^{1}H\}$ NMR spectrum of **3** in CD_2Cl_2 at 298 K between 156 and 112 ppm.

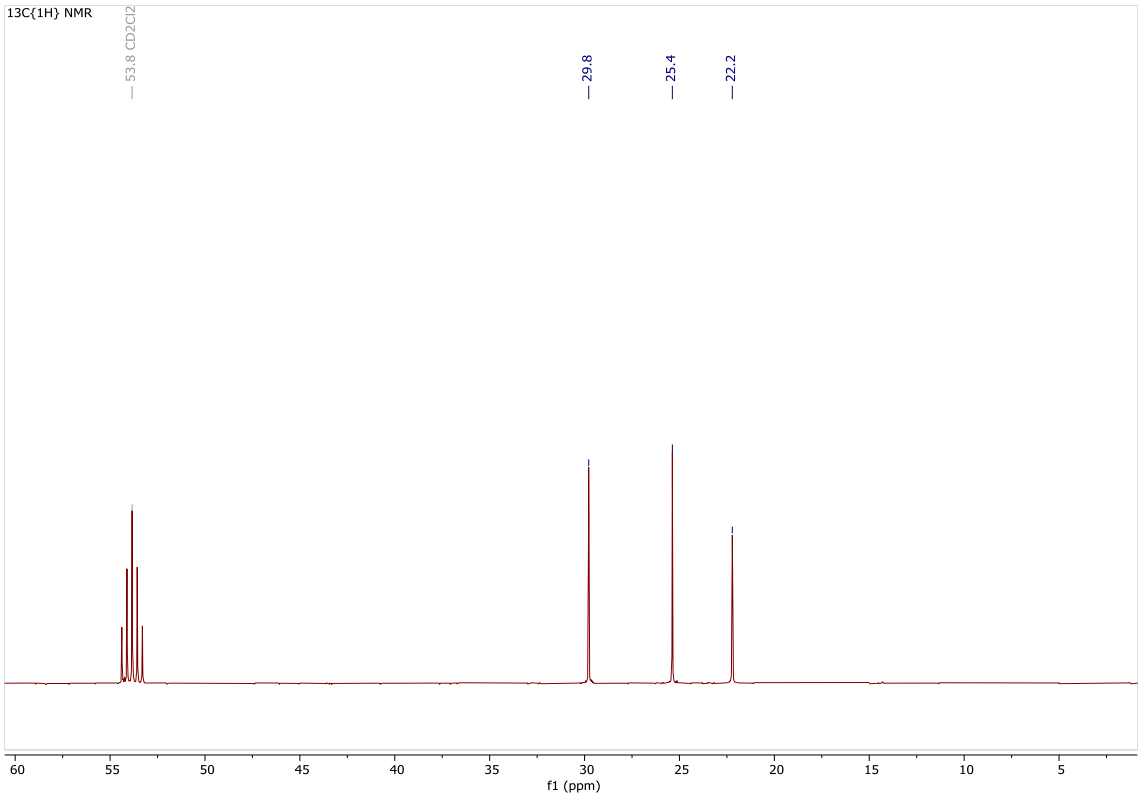

Figure S24. Zoom $^{13}C\{^{1}H\}$ NMR spectrum of **5-B(C_6F_5)$_3$** in CD_2Cl_2 at 298 K between 55 and 5 ppm.

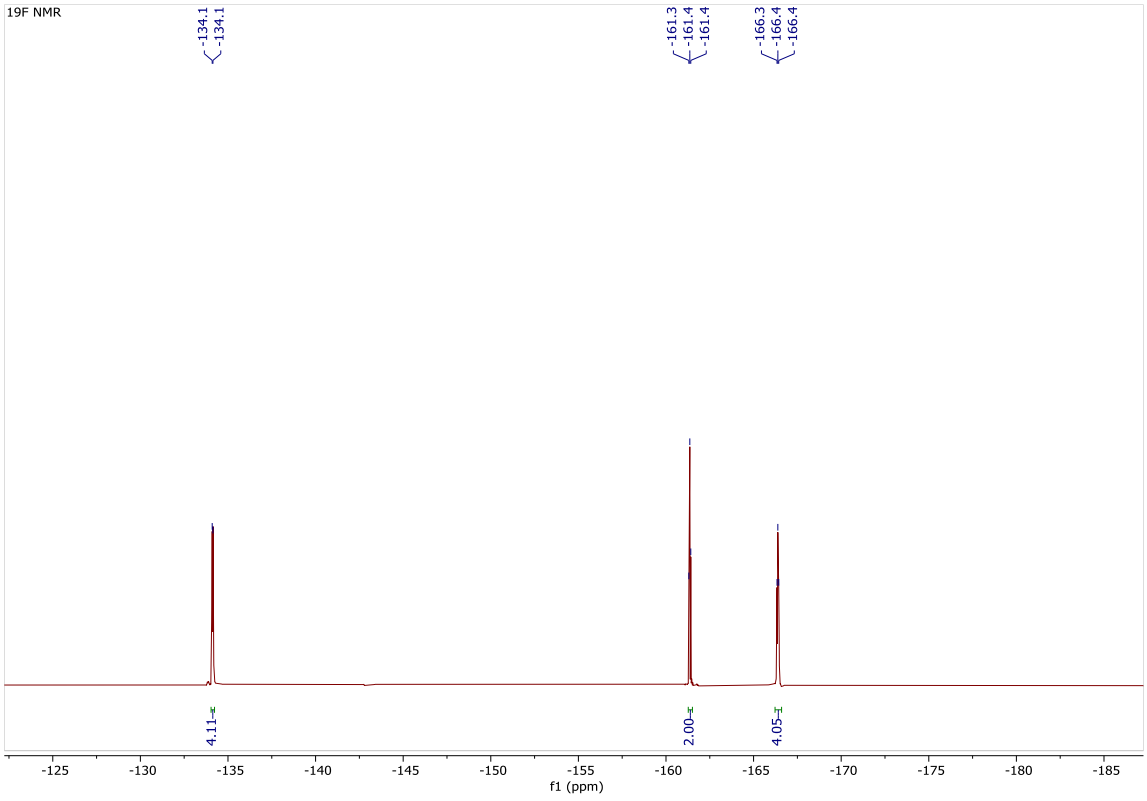

Figure S25. ^{19}F NMR spectrum of **5-B(C_6F_5)$_3$** in CD_2Cl_2 at 298 K.

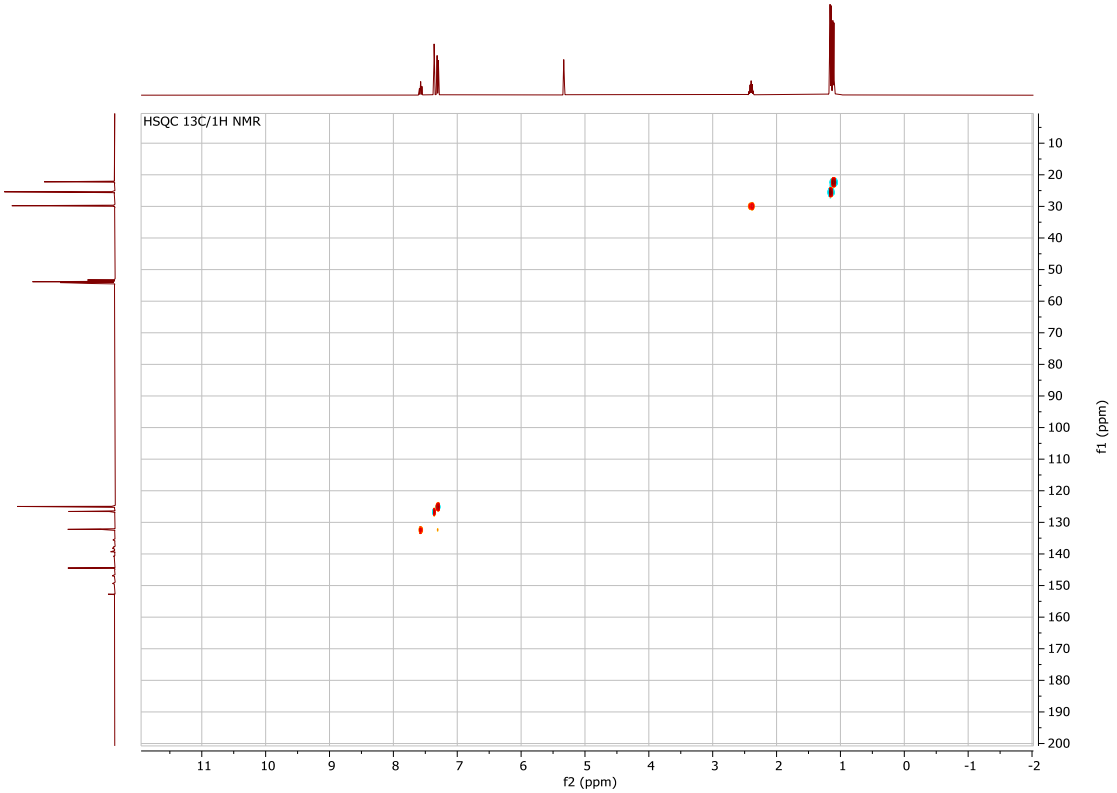

Figure S26. HSQC $^{13}C/^{1}H$ NMR spectrum of **5-B(C_6F_5)$_3$** in CD_2Cl_2 at 298 K.

Figure S27. Zoom HSQC $^{13}C/^{1}H$ NMR spectrum of **5-B(C_6F_5)$_3$** in CD_2Cl_2 at 298 K.

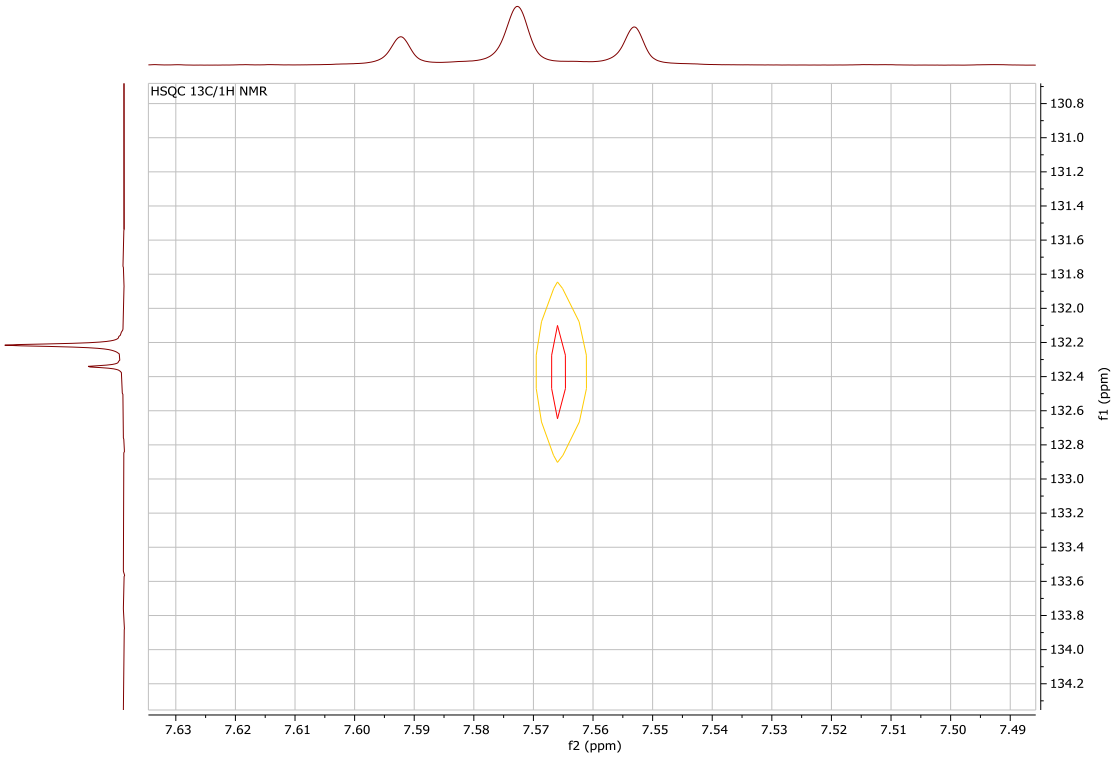

Figure S28. Zoom HSQC $^{13}C/^{1}H$ NMR spectrum of **5-B(C_6F_5)$_3$** in CD_2Cl_2 at 298 K.

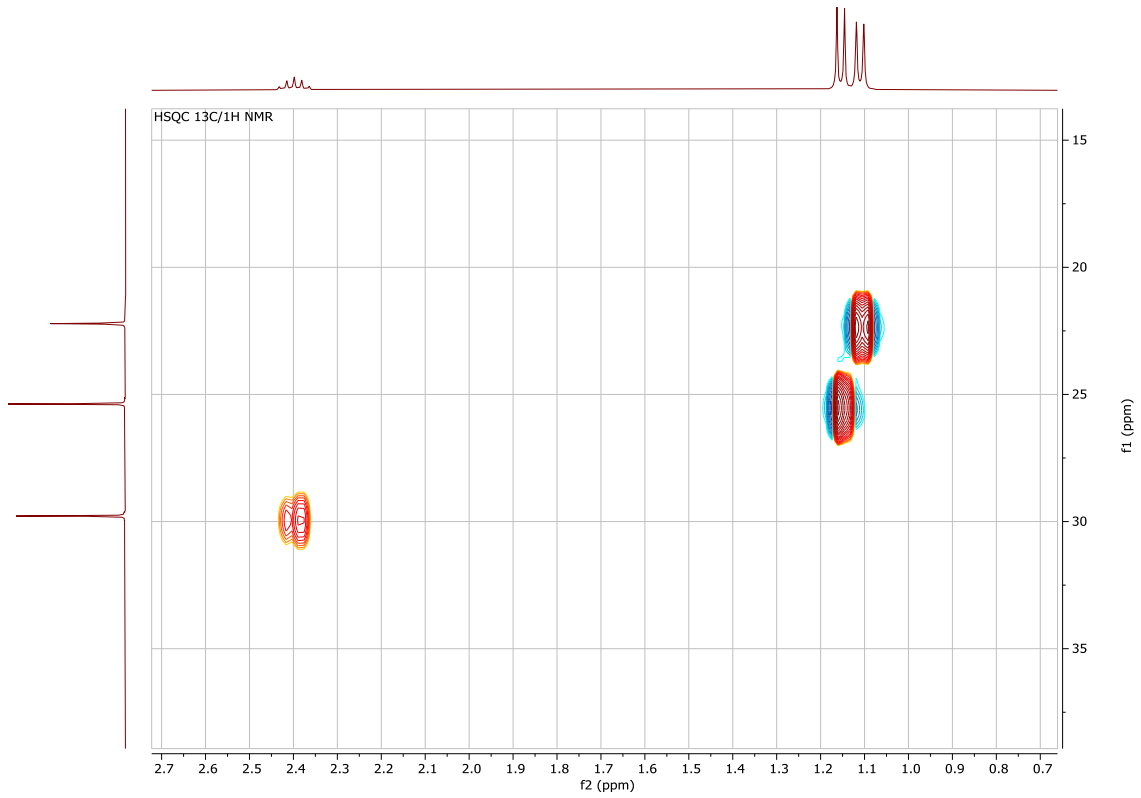

Figure S29. Zoom HSQC $^{13}C/^{1}H$ NMR spectrum of **5-B(C_6F_5)$_3$** in CD_2Cl_2 at 298 K.

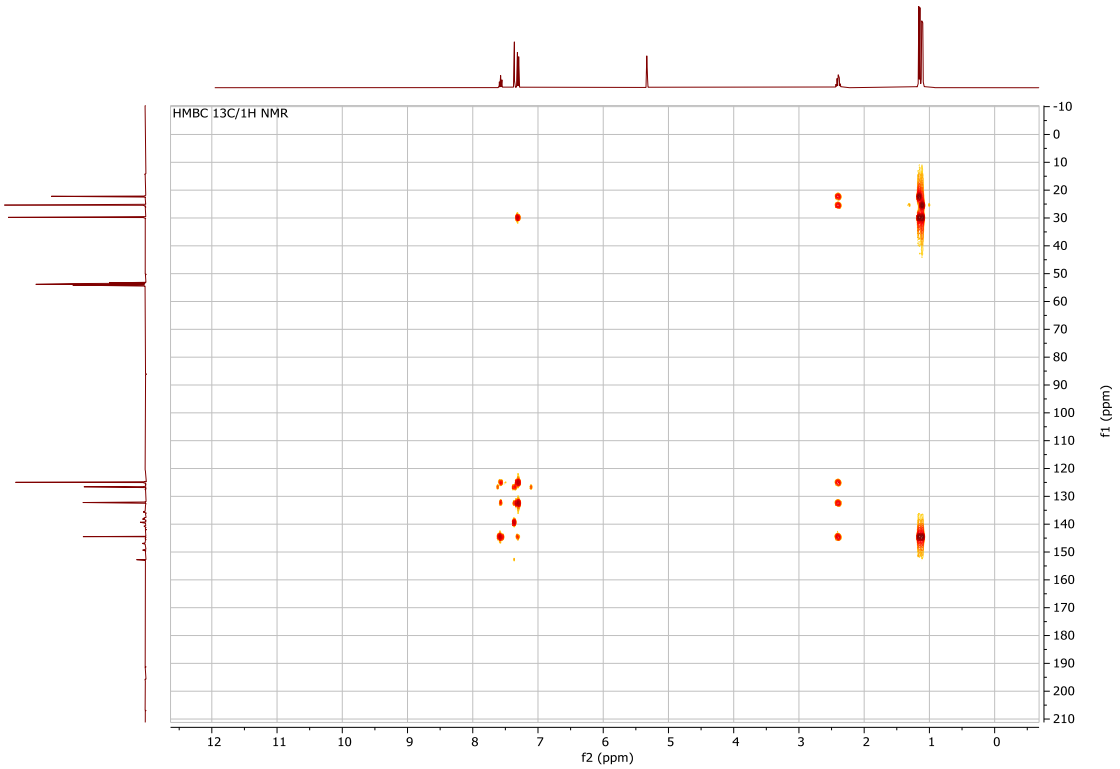

Figure S30. HMBC $^{13}C/^{1}H$ NMR spectrum of **5-B(C_6F_5)$_3$** in CD_2Cl_2 at 298 K.

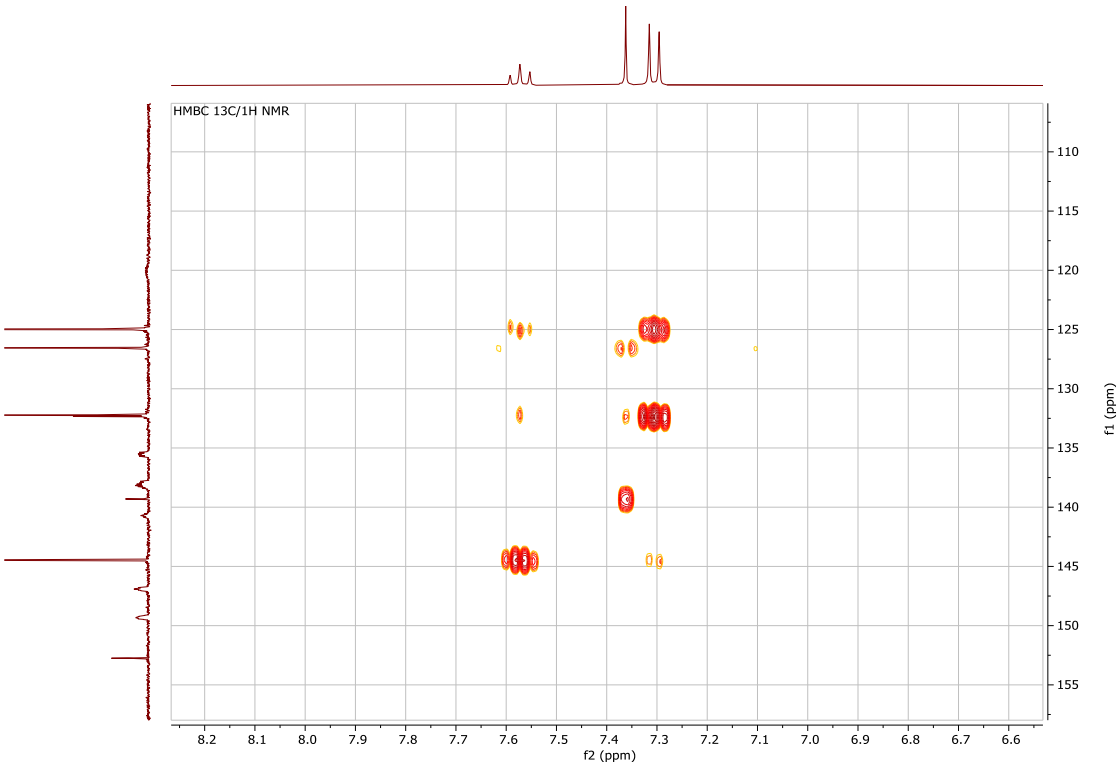

Figure S31. Zoom HMBC $^{13}C/^{1}H$ NMR spectrum of **5-B(C_6F_5)$_3$** in CD_2Cl_2 at 298 K.

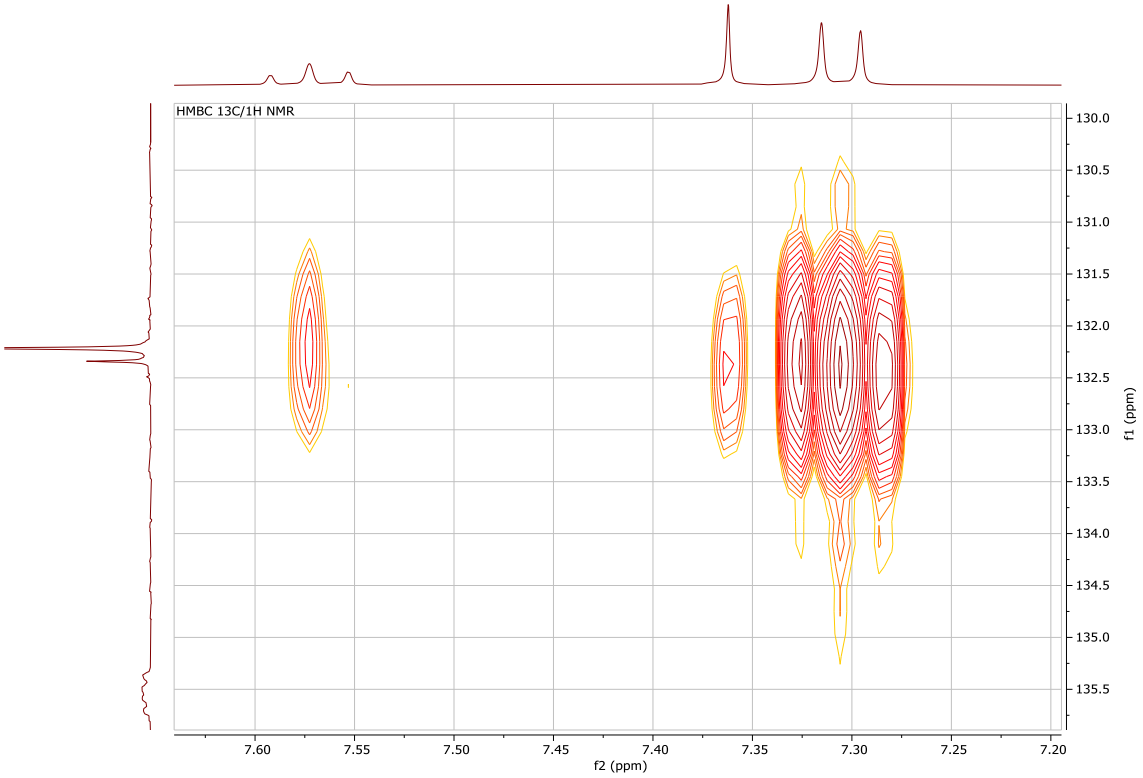

Figure S32. Zoom HMBC $^{13}C/^{1}H$ NMR spectrum of **5-B(C_6F_5)$_3$** in CD_2Cl_2 at 298 K.

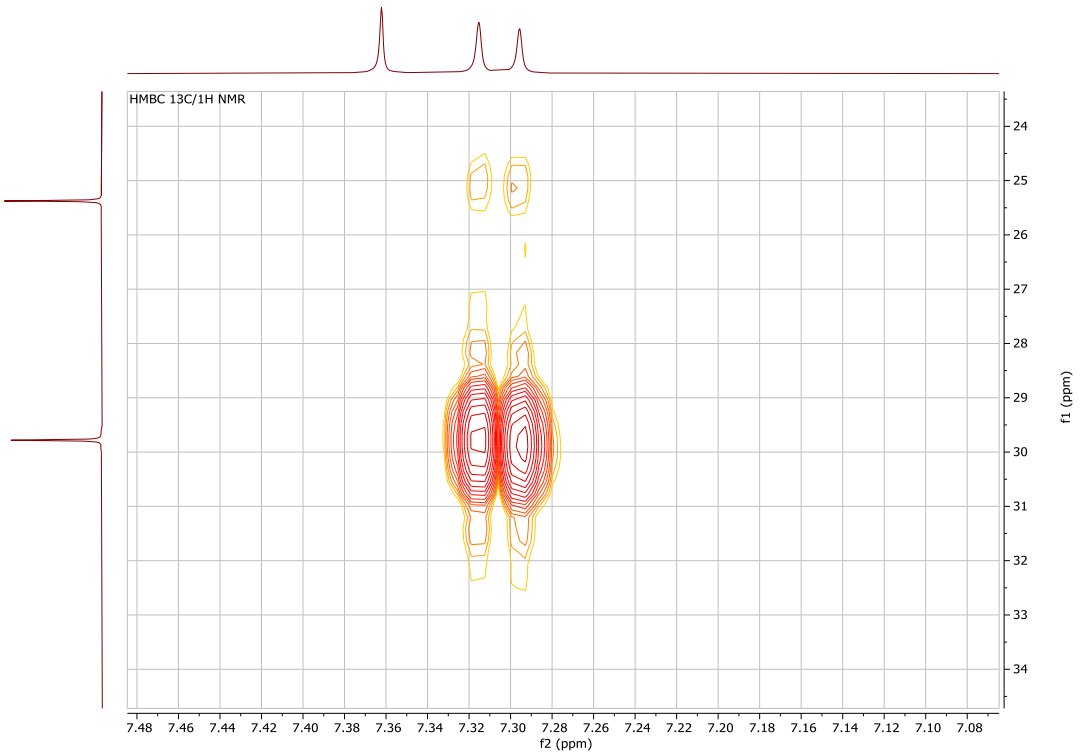

Figure S33. Zoom HMBC $^{13}C/^{1}H$ NMR spectrum of **5-B(C_6F_5)$_3$** in CD_2Cl_2 at 298 K.

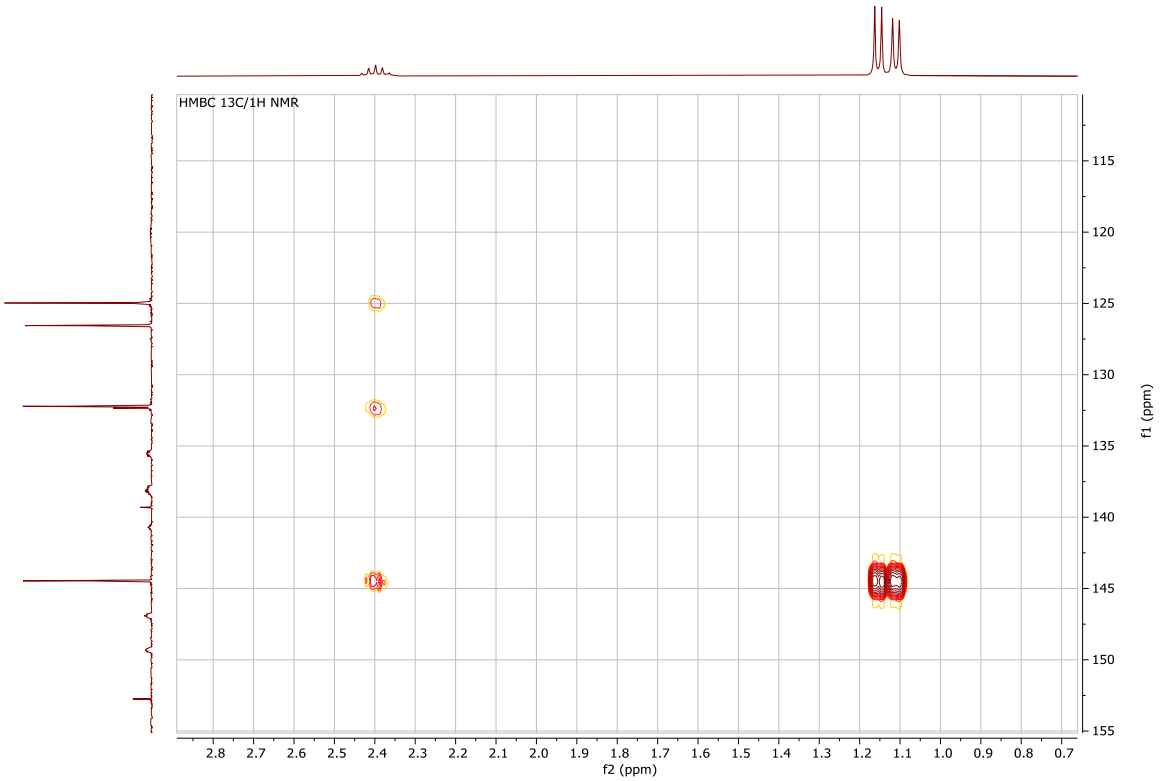

Figure S34. Zoom HMBC $^{13}C/^{1}H$ NMR spectrum of **5-B(C_6F_5)$_3$** in CD_2Cl_2 at 298 K.

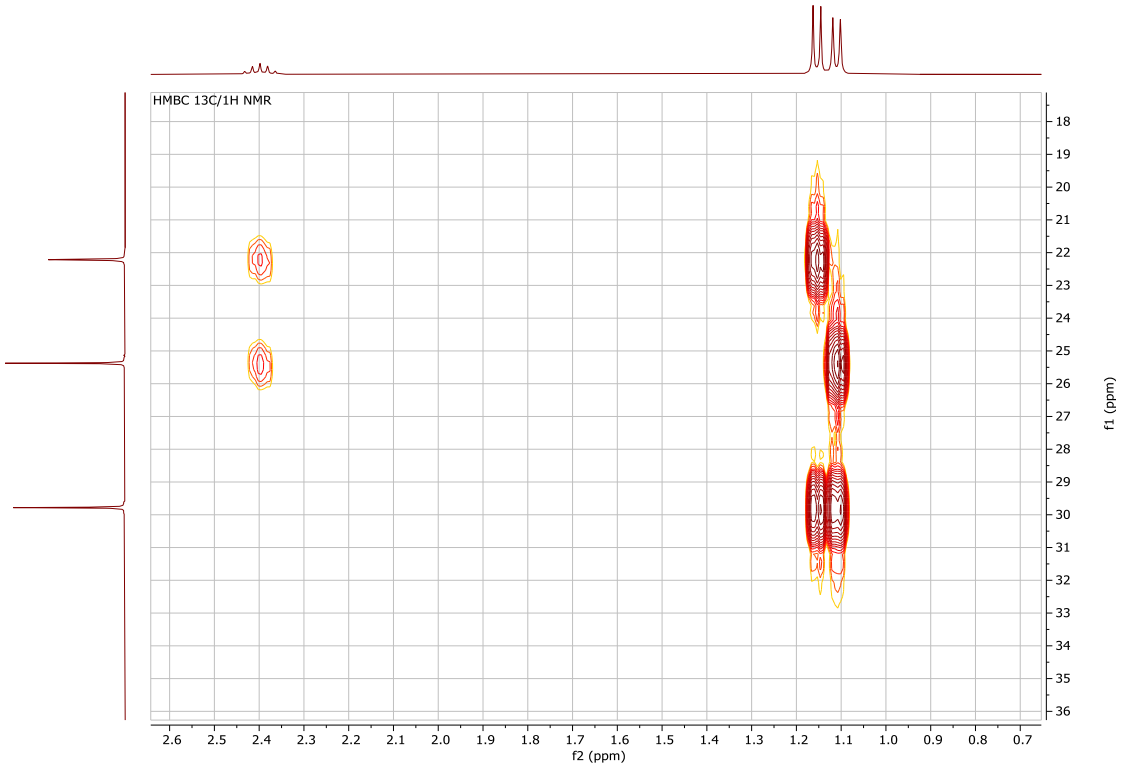

Figure S35. Zoom HMBC $^{13}C/^{1}H$ NMR spectrum of **5-B(C_6F_5)$_3$** in CD_2Cl_2 at 298 K.

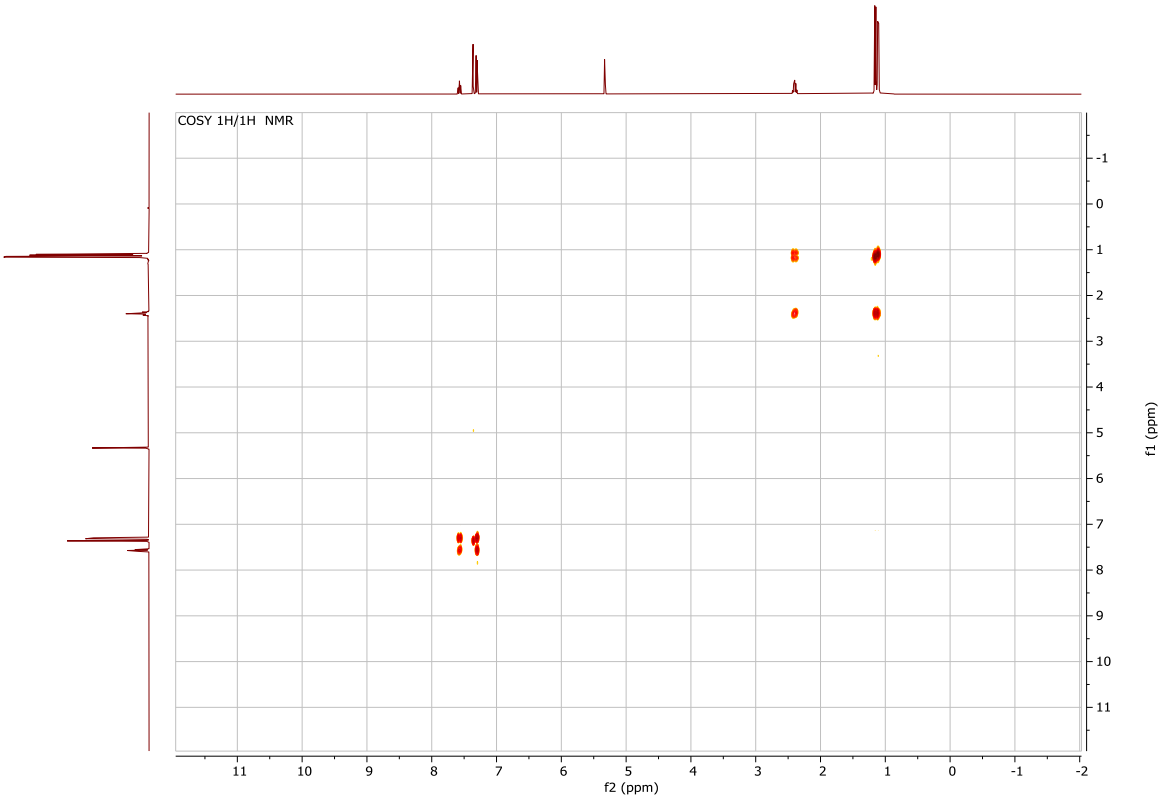

Figure S36. COSY $^{1}H/^{1}H$ NMR spectrum of **5-B(C_6F_5)$_3$** in CD_2Cl_2 at 298 K.

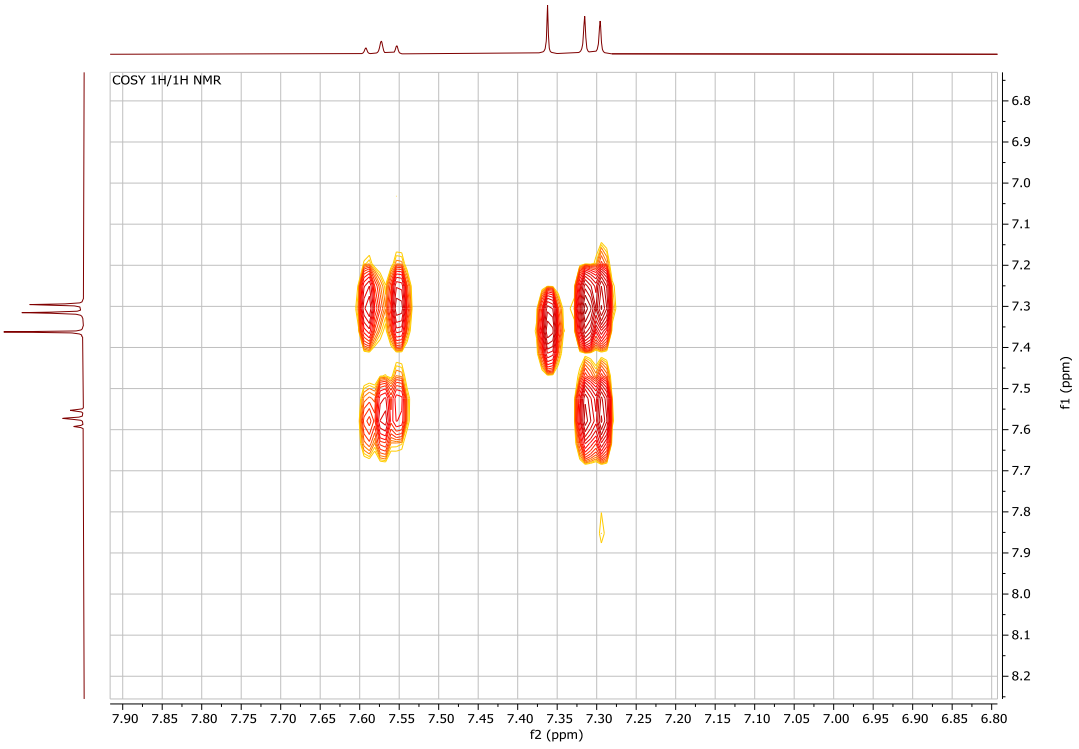

Figure S37. Zoom COSY $^{1}H/^{1}H$ NMR spectrum of **5-B(C_6F_5)$_3$** in CD_2Cl_2 at 298 K.

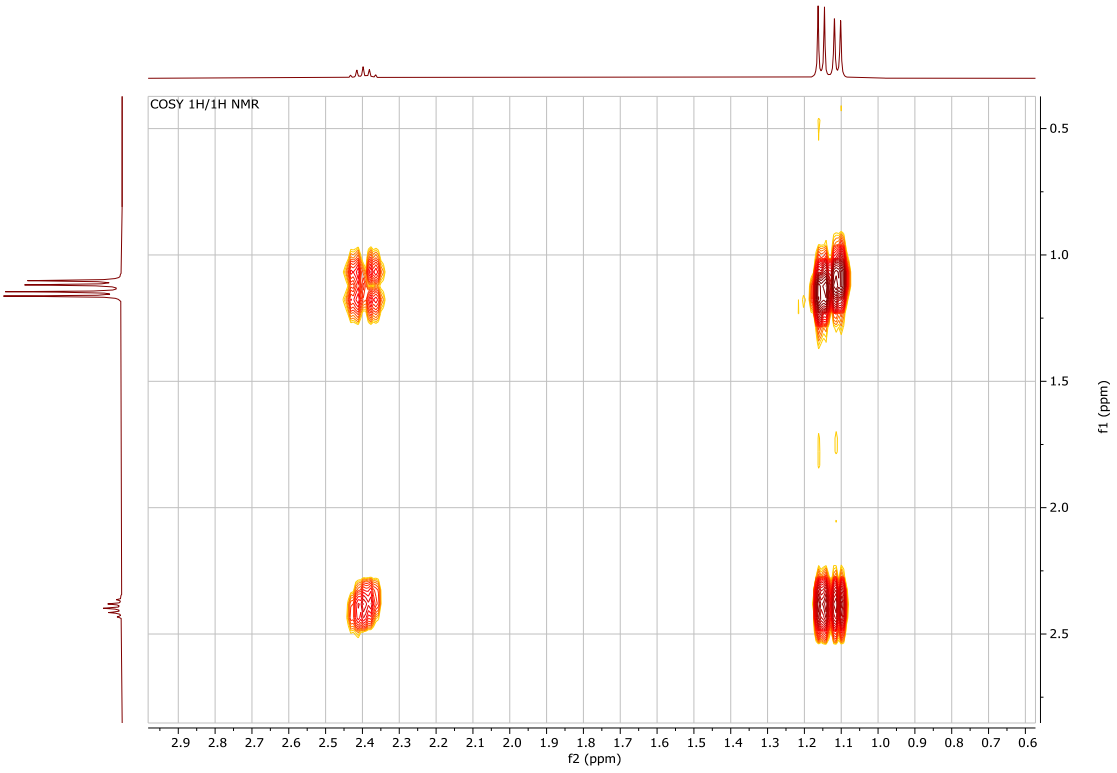

Figure S38. Zoom COSY $^{1}H/^{1}H$ NMR spectrum of **5-B(C_6F_5)$_3$** in CD_2Cl_2 at 298 K.

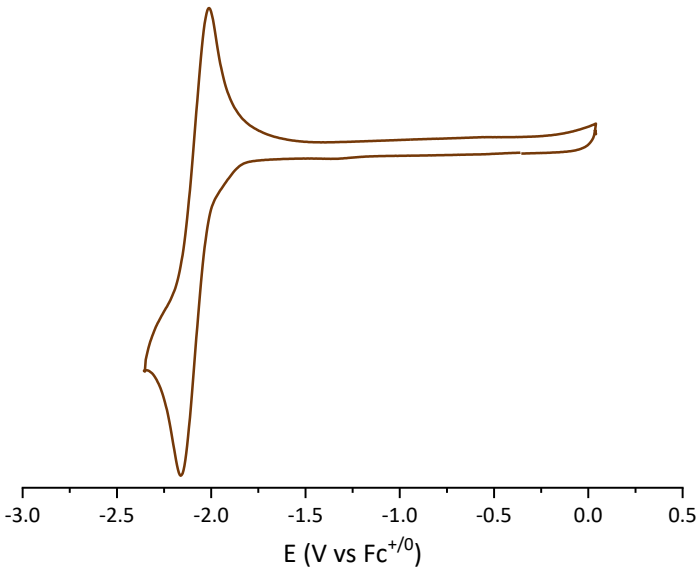

Figure S39. Normalised CV response of **5-B(C_6F_5)$_3$** at reducing potentials under Ar atmosphere in CH_2Cl_2. Conditions: 5 mM compound **5-B(C_6F_5)$_3$** and 0.1 M [n-Bu_4N][PF_6], scan 200 mV/s.

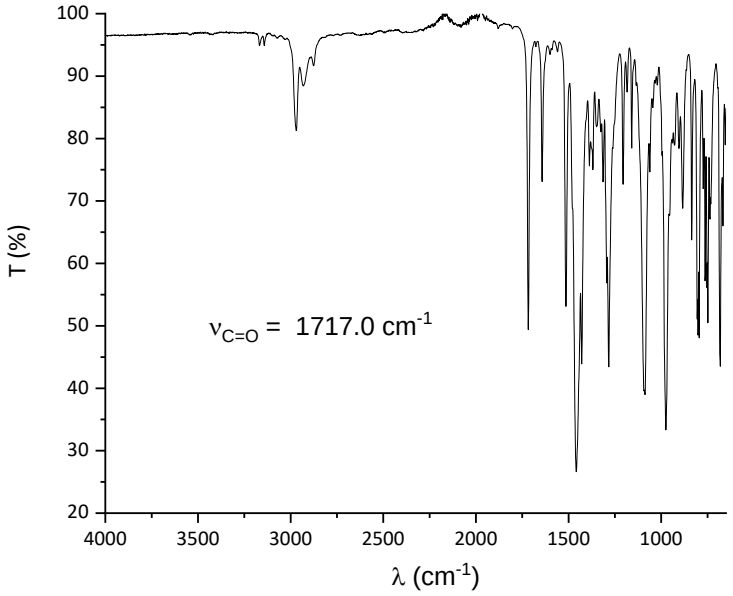

Figure S40. FTIR (solid state) of **5-B(C6F5)3** at 298 K.

Crystallographic details of adduct 5-B(C_6F_5)$_3$.

Table S4. Crystal data.

$C_{46}H_{36}BF_{15}N_2O_2$	
M_r = 944.58	D_x = 1.485 Mg m^{-3}
Monoclinic, $P2_1/n$	
Hall symbol: -P 2yn	Cu Kα radiation, λ = 1.54184 Å
a = 12.0583 (1) Å	Cell parameters from 33785 reflections
b = 16.6138 (1) Å	θ = 3.4–80.0°
c = 21.2222 (2) Å	μ = 1.20 mm^{-1}
β = 96.569 (1)°	T = 100 K
V = 4223.62 (6) Å^3	Platelet, colourless
Z = 4	0.12 × 0.08 × 0.02 mm
F(000) = 1928	

Table S5. Data collection.

XtaLAB Synergy, Dualflex, HyPix diffractometer	9171 independent reflections
Radiation source: micro-focus sealed X-ray tube, PhotonJet (Cu) X-ray Source	7764 reflections with I > 2.0σ(I)
Mirror monochromator	R_{int} = 0.044
Detector resolution: 10.0000 pixels mm^{-1}	θ_{max} = 80.5°, θ_{min} = 3.4°
	h = −15 13
Absorption correction: multi-scan CrysAlisPro (Rigaku Oxford Diffraction, 2017)	k = −21 20
T_{min} = 0.63, T_{max} = 0.98	l = −26 27
77348 measured reflections	

Table S6. Refinement.

Refinement on F^2	
Least-squares matrix: full	Hydrogen site location: difference Fourier map
$R[F^2 > 2\sigma(F^2)]$ = 0.038	H-atom parameters not refined
$wR(F^2)$ = 0.109	Method = Modified Sheldrick $w = 1/[\sigma^2(F^2) + (0.06P)^2 + 2.33P]$, where $P = (\max(F_o^2,0) + 2F_c^2)/3$
S = 0.98	$(\Delta/\sigma)_{max}$ = 0.001
9170 reflections	$\Delta\rho_{max}$ = 0.34 e $Å^{-3}$
595 parameters	$\Delta\rho_{min}$ = −0.31 e $Å^{-3}$
0 restraints	Extinction correction: None

5.2.4. ^{Cy}CAAC-CO_2 (8).

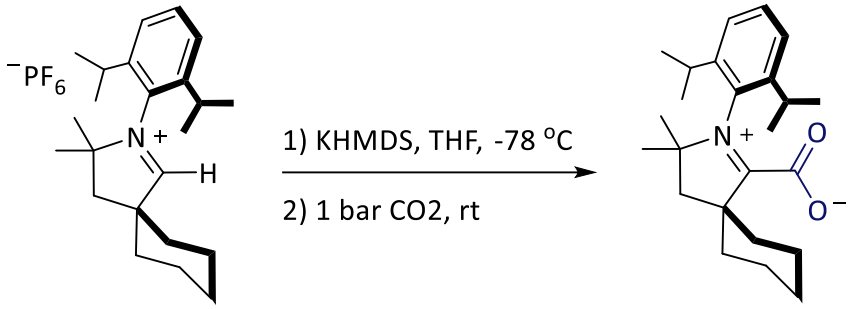

(^{Cy}CAACH·PF_6) (**8**) (85 %)

Following a similar synthesis procedure reported by Machan, Gilliard et *al.*,[2] ^{Cy}CAACH·PF_6 (150 mg, 0.32 mmol) and KHMDS (69.8 mg, 0.35 mmol) were placed in a Fischer-porter at -78°C. Under argon, THF (3mL) was added. The mixture was stirred for 1 hour resulting in a colourless solution at -78°C. Upon carbene generation, the solution was stirred under 1 bar of CO_2 (dynamic regime) for 1 hour at room temperature. The solvent was dried under vacuum and the resulting white solid was extracted with dichloromethane. It was washed once with diethyl ether (3 mL) and three times with pentane (3mL). After filtration and drying under vacuum, the expected product was isolated as a white powder in 85% yield (100.4 mg).

^{1}H NMR (400 MHz, 298 K, CD_2Cl_2) δ 7.44 (t, $^3J_{HH}$ = 7.81 Hz, 2H, p-Ar), 7.29 (d, $^3J_{HH}$ = 7.6 , 2H, m-Ar), 2.74 (sept, $^3J_{HH}$ = 6.4 Hz, 2H, C*H*$(CH_3)_2$), 2.33 (s, 2H, $(CH_2)_{backbone}$), 2.16 (td, J^3J_{HH} = 13.8 Hz, $^4J_{HH}$ = 3.8 Hz, 2H, $(CH_2)_{Cy}$)), 1.86 (m, 4H, $(CH_2)_{Cy}$)) 1.73 (d, $^3J_{HH}$ = 11.0 Hz, 1H, $(CH_2)_{Cy}$)), 1.46 (s, 6H, $(CH_2)_{backbone}$), 1.43 (m, 1H, $(CH_2)_{Cy}$), 1.39 (m, 2H, $(CH_2)_{Cy}$) 1.32 (d, $^3J_{HH}$ = 6.5 Hz, 6H, CH(C*H*$_3)_2$), 1.29 ppm (d, $^3J_{HH}$= 6.7 Hz, 6H, CH(C*H*$_3)_2$). ^{13}C{^{1}H} NMR (100.6 MHz, 298 K, CD_2Cl_2) δ 158.6 (NHC-*C*O2), 146.1 (o-Ar), 130.9 (p-Ar), 129.5 (ipso-Ar), 126.0 (m-Ar), 79.6 ($C_{backbone}$), 53.1 (C_{Cy}), 45.5 (($CH_2)_{backbone}$), 36.2 $(CH_2)_{Cy}$), 30.1 ((*C*H$(CH_3)_2$)), 29.6 (($CH_3)_{backbone}$), 26.5 (CH(*C*H$_3)_2$), 25.0 (CH$(CH_3)_2$), 24.5 (($CH_2)_{Cy}$) , 22.2 (($CH_2)_{Cy}$). $E^{1/2}_{red}$ (vs. $Fc^{+/0}$) = -2.13 V.

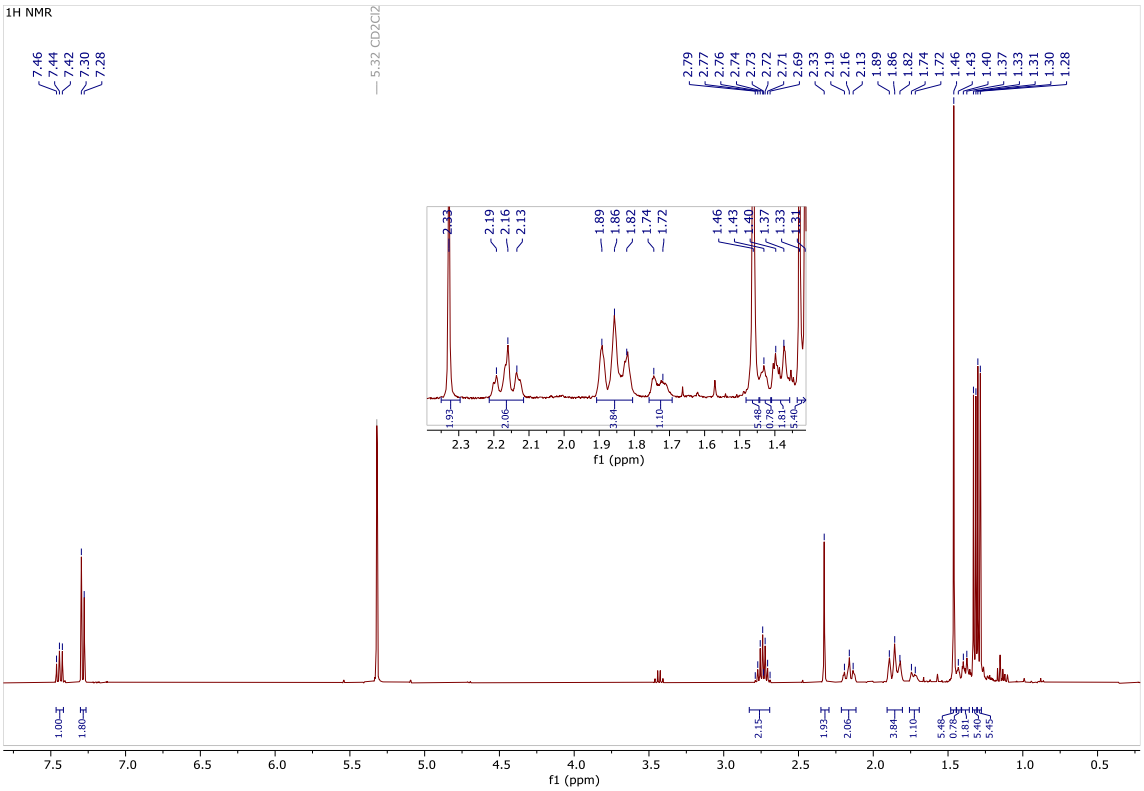

Figure S18. ^{1}H NMR spectrum of **8** in CD_2Cl_2 at 298 K.

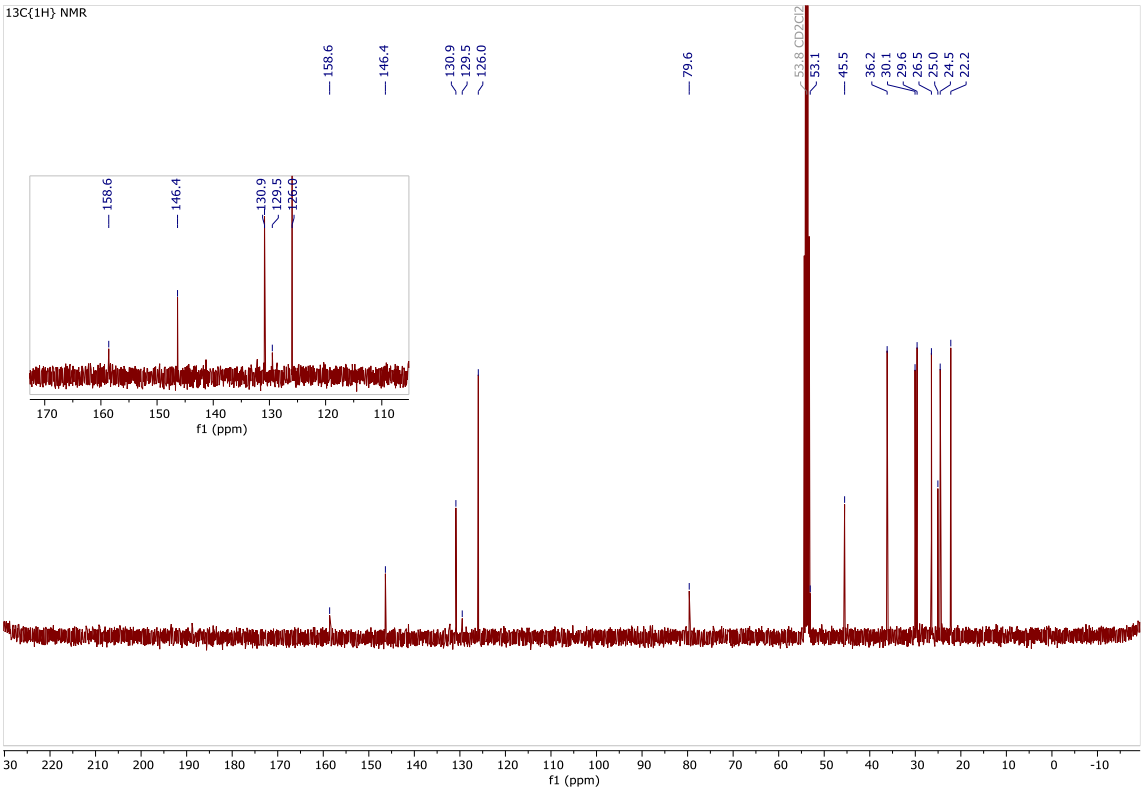

Figure S19. $^{13}C\{^{1}H\}$ NMR spectrum of **8** in CD_2Cl_2 at 298 K.

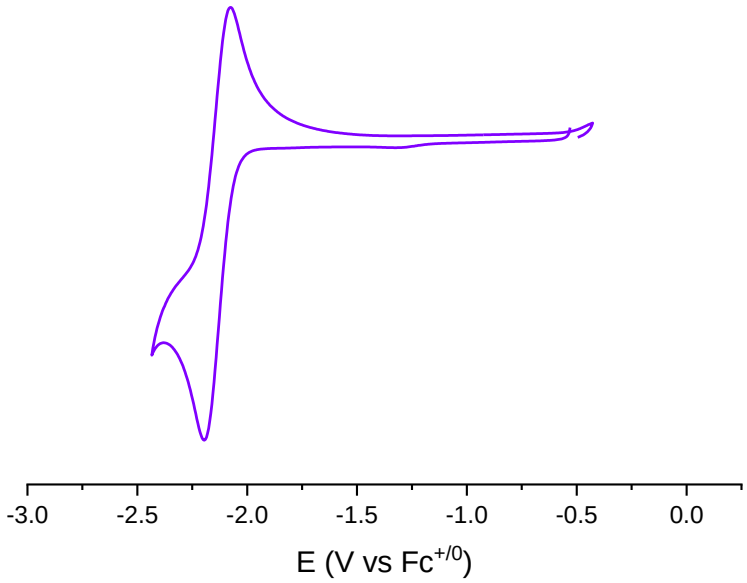

Figure S20. Normalised CV response of **8** at reducing potentials under Ar atmosphere in dichloromethane. Conditions: 5 mM compound **8** and 0.1 M [n-Bu_4N][PF_6], scan 200 mV/s.

5.2.5. ^{Cy}CAAC-CO_2-$B(C_6F_5)_3$ (8-$B(C_6F_5)_3$).

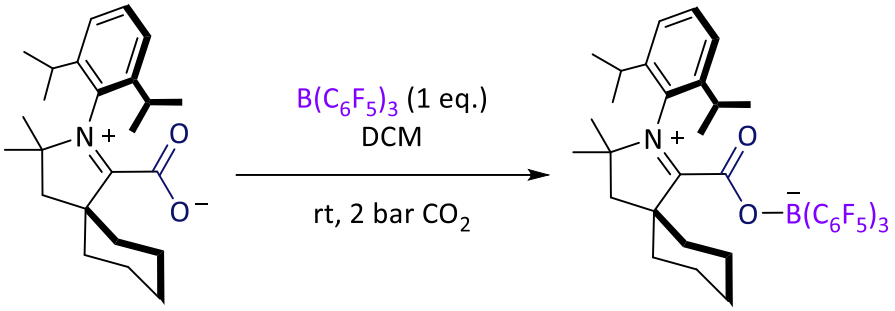

(**8**) (**8-$B(C_6F_5)_3$**) (89 %)

^{Cy}CAAC-CO_2 (**8**) (300 mg, 0.81 mmol) and $B(C_6F_5)_3$ (415.6 mg, 0.81 mmol) were placed in a Fischer-Porter at room temperature. Under 2 bar CO_2, dichloromethane (10 mL) was added, and the solution was stirred up for 1h. The solvent was removed under reduced pressure yielding a white solid in 89% (515.9 mg, 0.72 mmol).

^{1}H NMR (400.2 MHz, 298 K, CD_2Cl_2) δ 7.53 (t, $^3J_{HH}$ = 7.7 Hz, 1H, p-Ar), 7.21 (d, $^3J_{HH}$ = 7.9 Hz, 2H, m-Ar) 2.48 (m, 6H, C*H*$(CH_3)_2$, $(CH_2)_{backbone}$, $(CH_2)_{Cy}$), 1.97 (m, 2H, $(CH_2)_{Cy}$), 1.86 (m, 3H, $(CH_2)_{Cy}$) 1.52 (s, 6H, $(CH_3)_{backbone}$), 1.47 (m, 3H, $(CH_2)_{Cy}$), 1.21 (d, $^3J_{HH}$ = 6.6 Hz, 6H, CH(C*H*$_3)_2$) 0.74 (d, $^3J_{HH}$ = 6.6 Hz, 6H, CH(C*H*$_3)_2$). ^{11}B NMR (128.4 MHz, 298 K, CD_2Cl_2) δ -2.9 (s). ^{13}C{^{1}H} NMR (100.6 MHz, 298 K, CD_2Cl_2) δ = 188.4 (N_2C), 158.0 (NHC-*C*O_2), 148.1 (d, $^1J_{CF}$ = 243.3 Hz, m-C_6F_5) 144.9 (o-Ar), 139.6 (d, $^1J_{CF}$ = 245.8 Hz, p-C_6F_5), 137.0 (d, $^1J_{CF}$ = 243.0 Hz, o-C_6F_5), 132.4 (p-Ar), 128.1 (ipso-Ar), 126.5 (m-Ar), 119.9 (BC-ipso), 83.5 ($C_{backbone}$), 55.7 (C_{Cy}), 46.1 ($(CH_2)_{backbone}$), 34.0 ($(CH_2)_{Cy}$), 30.1 (*C*H$(CH_3)_2$), 30.0 ($(CH_3)_{backbone}$), 25.0 (CH(*C*$H_3)_2$), 24.4 (CH(*C*$H_3)_2$), 24.4 ($(CH_2)_{Cy}$), 22.0 ($(CH_2)_{Cy}$). ^{19}F NMR (376.5 MHz, 298 K, CD_2Cl_2): δ −133.0 (d, $^3J_{FF}$ = 24.0 Hz, 6F, o-C_6F_5), −161.1 (t, $^3J_{FF}$ = 20.3 Hz, 3F, p-C_6F_5), −166.1 (td, $^3J_{FF}$ = 24.2 Hz, 6F, m-C_6F_5). HRMS (ESI+) m/z: Calcd for $C_{42}H_{35}BF_{15}N_2O_2$ [M+H$^+$]: 882.2594 found 882.2610. Anal (%): Calcd for $C_{42}H_{34}BF_{15}N_2O_2.CH_2Cl_2$: C, 53.44; H, 3.86; N, 1.47. Found: C, 54.32; H, 3.64; N, 1.47. FTIR (solid state): $\nu_{C=O}$ = 1708.6 cm^{-1}. $E^{1/2}_{red}$ (vs. $Fc^{+/0}$) = -1.34 V.

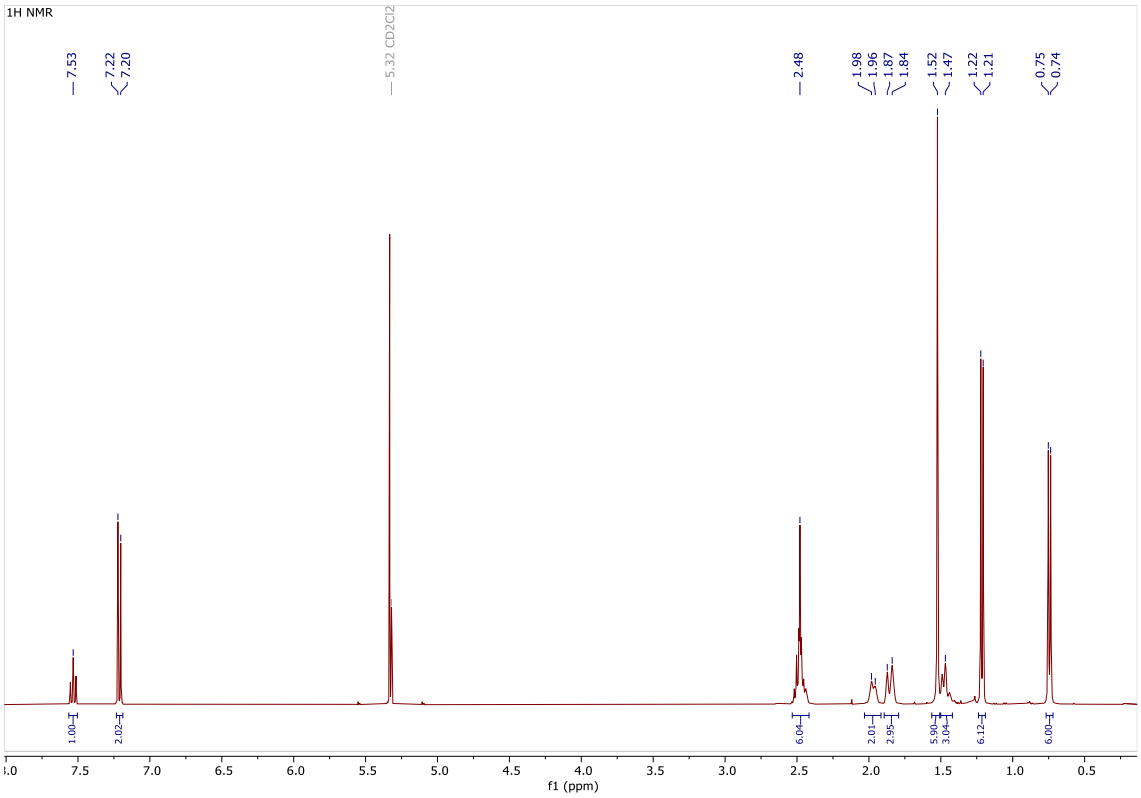

Figure S41. ^{1}H NMR spectrum of **8-B(C_6F_5)$_3$** in CD_2Cl_2 at 298 K.

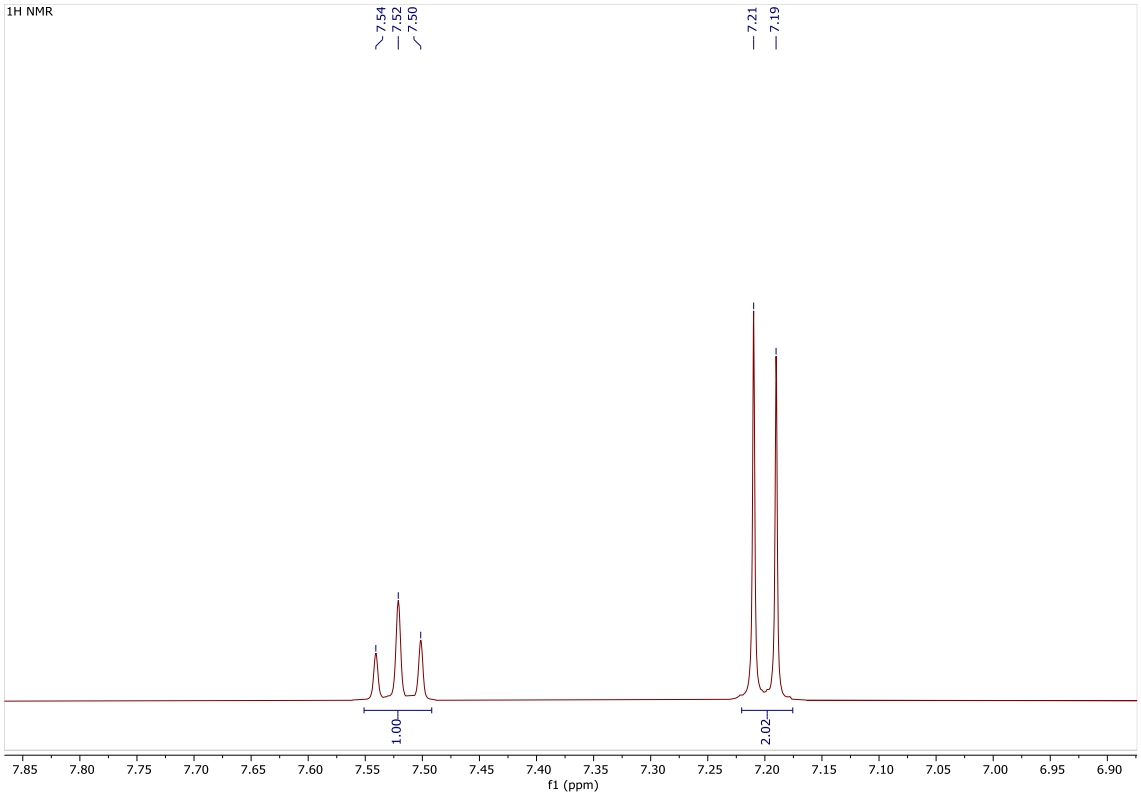

Figure S42. Zoom ^{1}H NMR spectrum of **8-B(C_6F_5)$_3$** in CD_2Cl_2 at 298 K between 7.85 and 6.90 ppm.

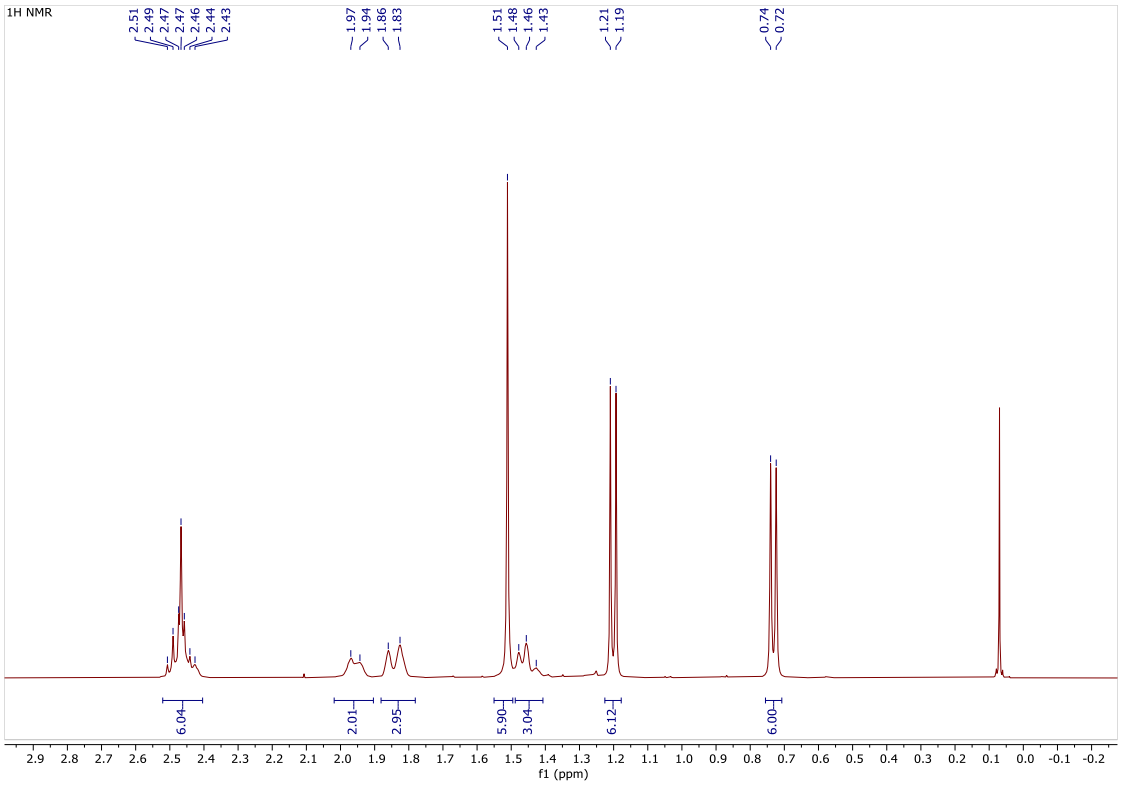

Figure S43. Zoom ^{1}H NMR spectrum of **8-B(C_6F_5)$_3$** in CD_2Cl_2 at 298 K between 2.9 and 0.0 ppm.

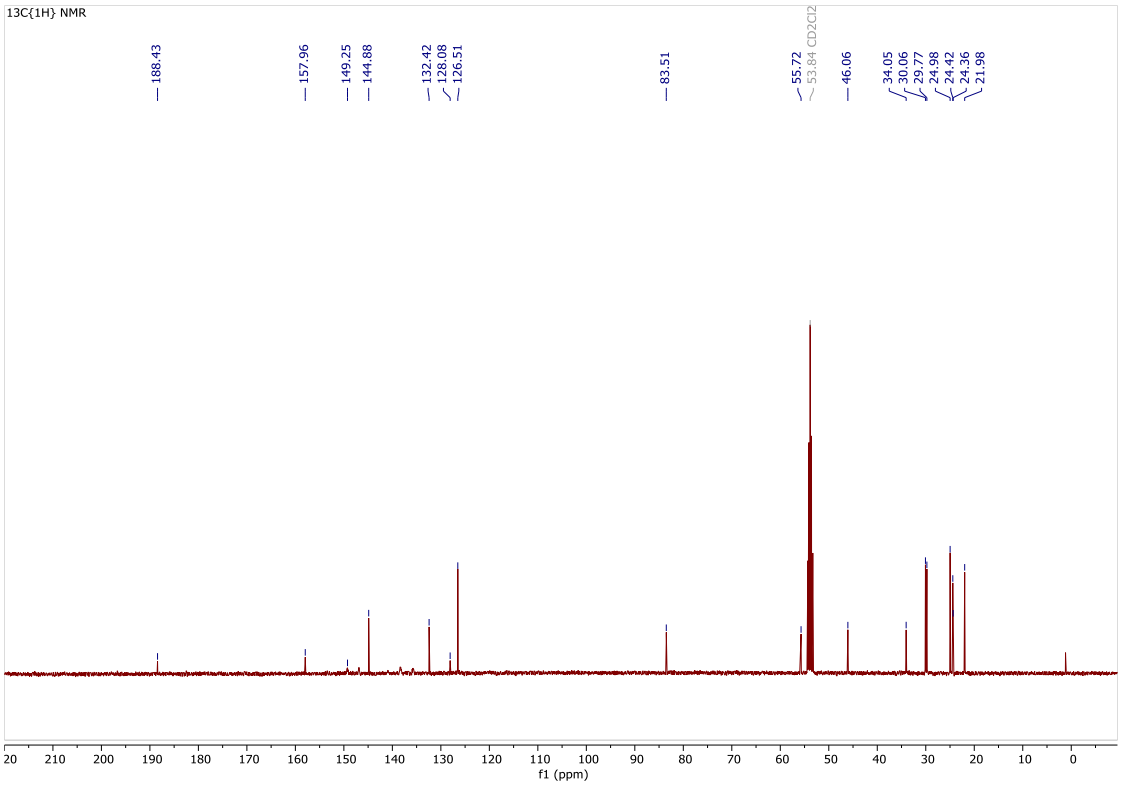

Figure S44. ^{13}C{^{1}H} NMR spectrum of **8-B(C_6F_5)$_3$** in CD_2Cl_2 at 298 K.

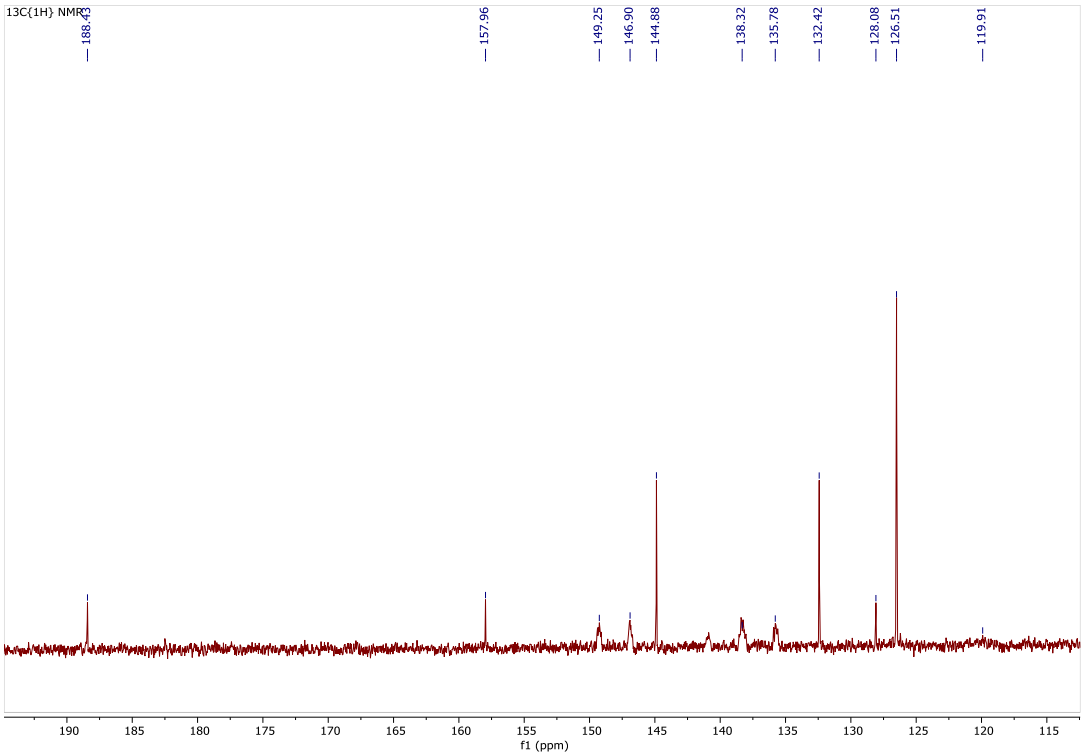

Figure S45. Zoom $^{13}C\{^{1}H\}$ NMR spectrum of **8-B(C_6F_5)$_3$** in CD_2Cl_2 at 298 K between 190 and 115 ppm.

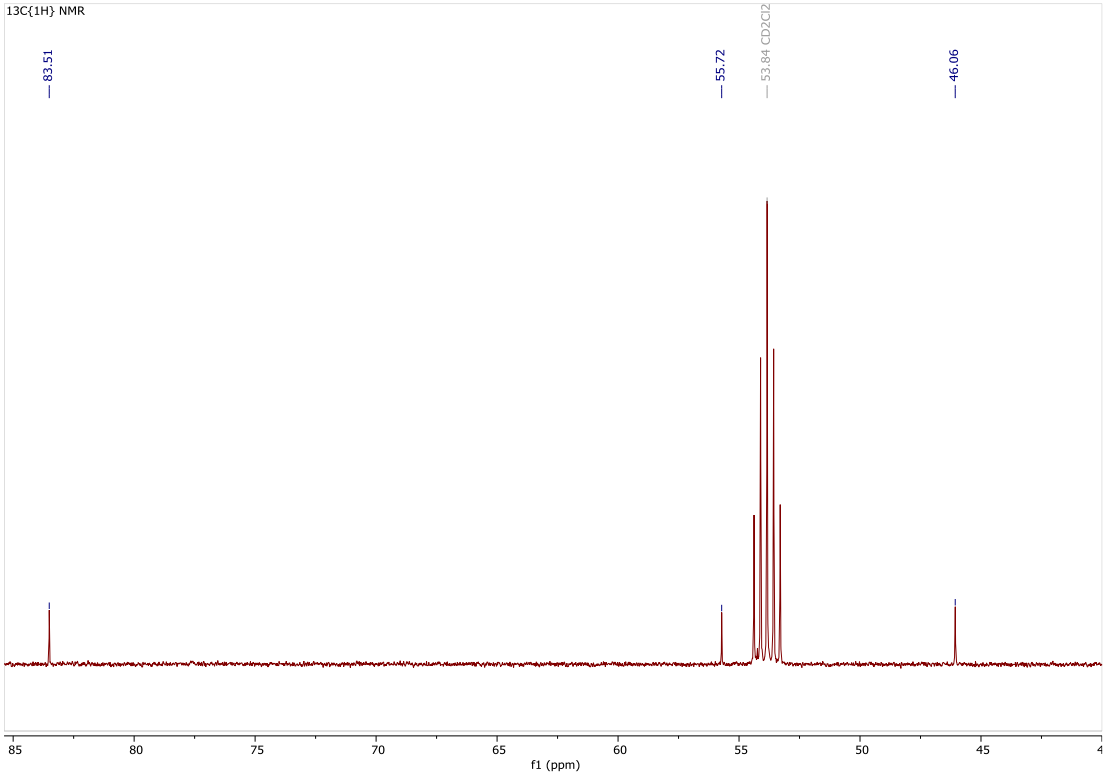

Figure S46. Zoom $^{13}C\{^{1}H\}$ NMR spectrum of **8-B(C_6F_5)$_3$** in CD_2Cl_2 at 298 K between 85 and 45 ppm.

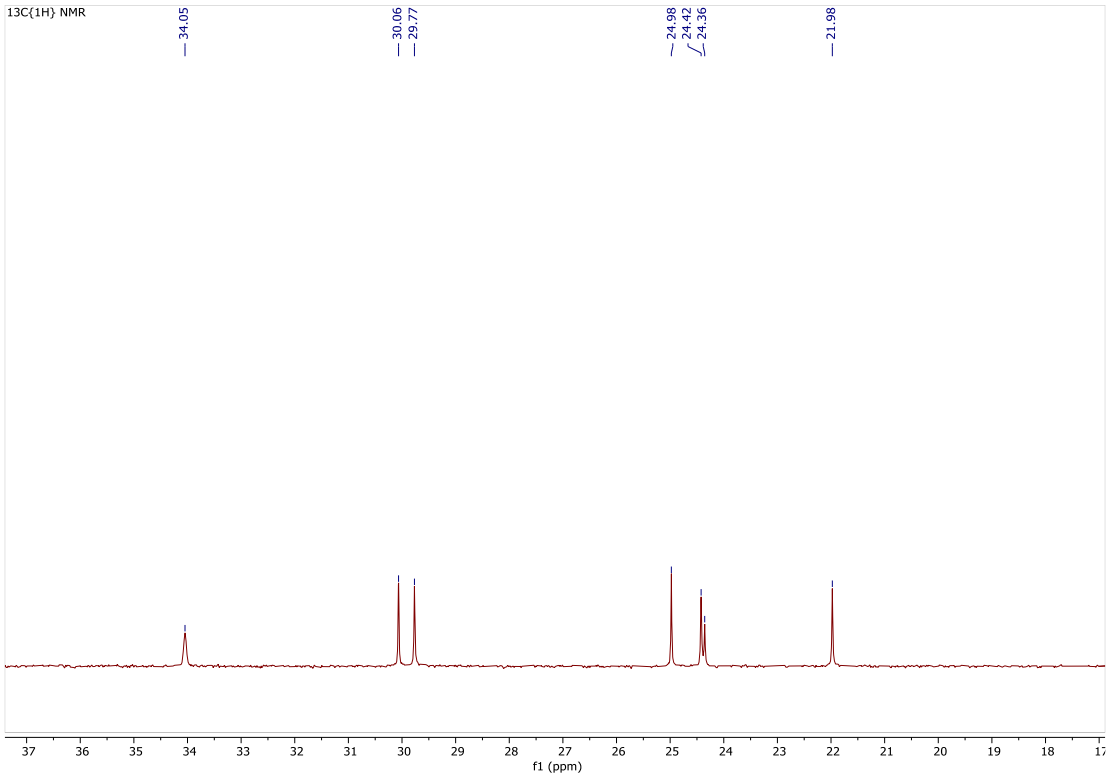

Figure S47. Zoom $^{13}C\{^{1}H\}$ NMR spectrum of **8-B(C_6F_5)$_3$** in CD_2Cl_2 at 298 K between 36 and 18 ppm.

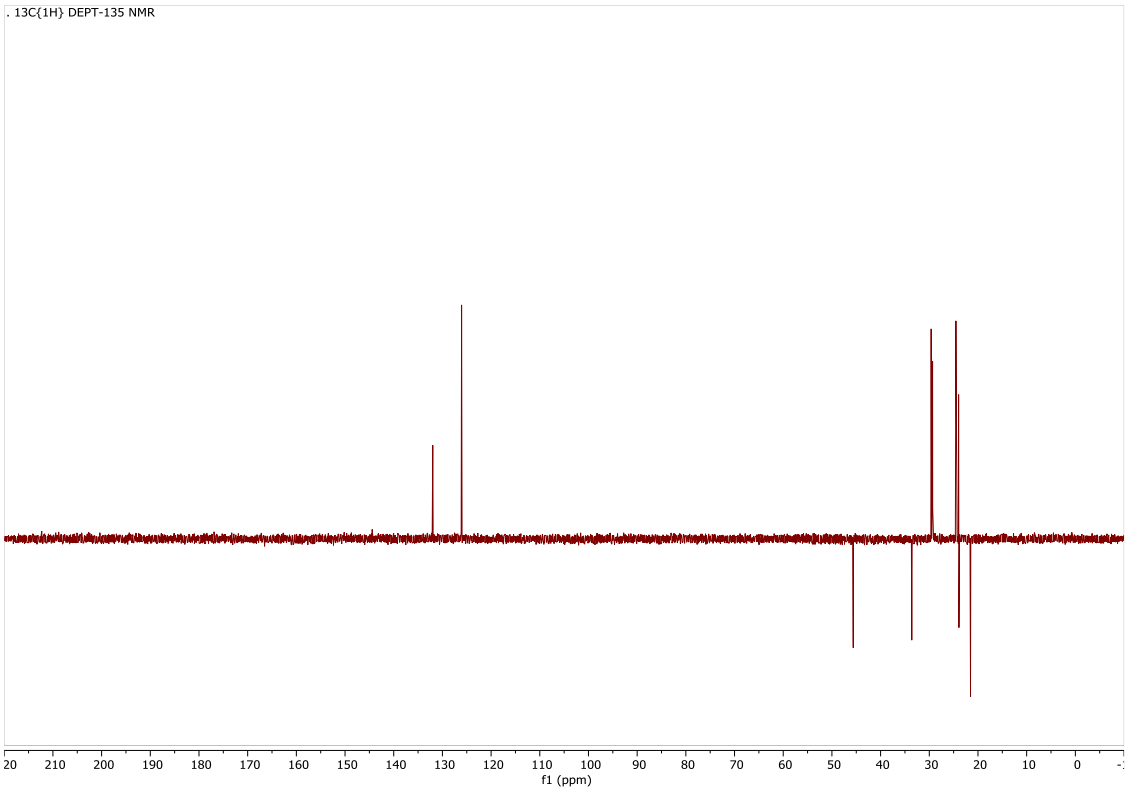

Figure S48. $^{13}C\{^{1}H\}$ DEPT-135 NMR spectrum of **8-B(C_6F_5)$_3$** in CD_2Cl_2 at 298 K.

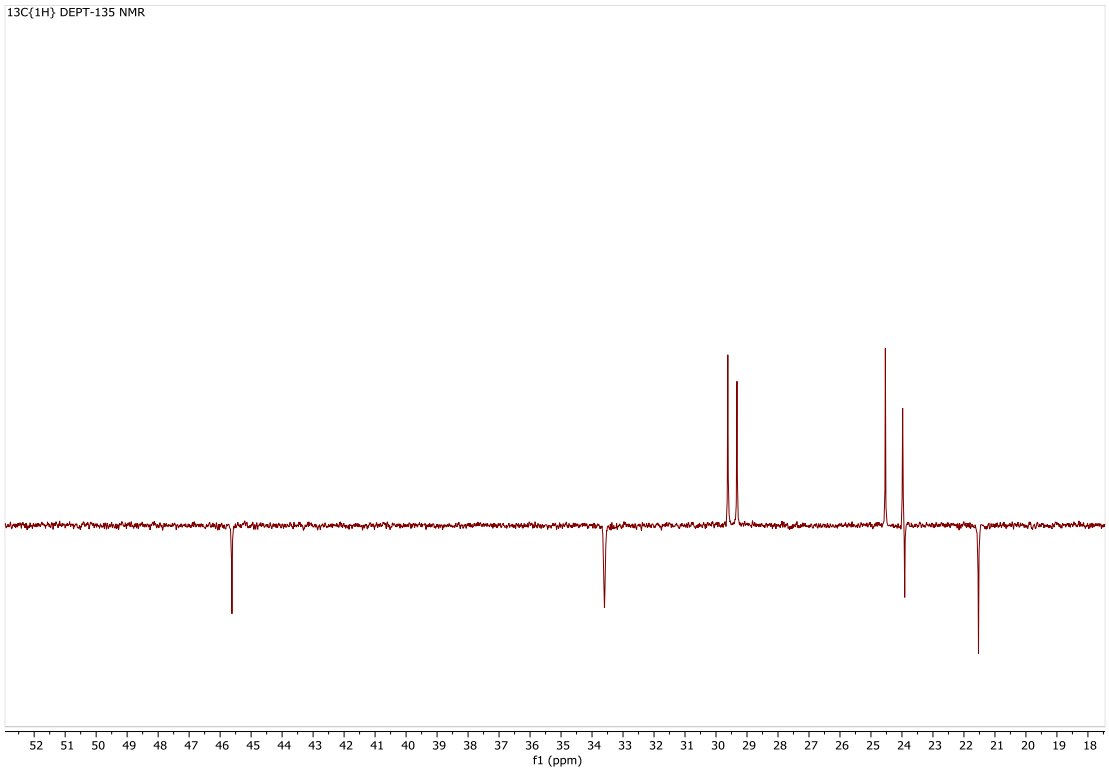

Figure S49. Zoom $^{13}C\{^{1}H\}$ DEPT-135 NMR spectrum of **8-B(C_6F_5)$_3$** in CD_2Cl_2 at 298 K between 52 and 19 ppm.

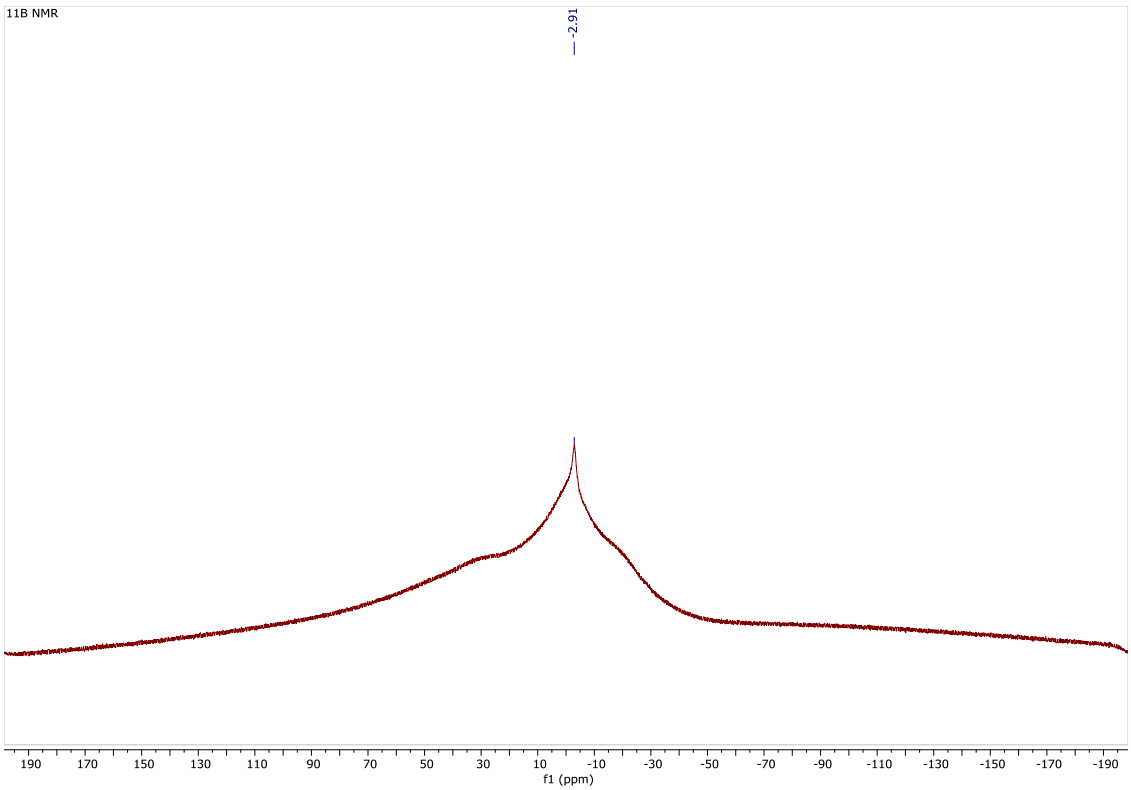

Figure S50. ^{11}B NMR spectrum of **8-B(C_6F_5)$_3$** in CD_2Cl_2 at 298 K.

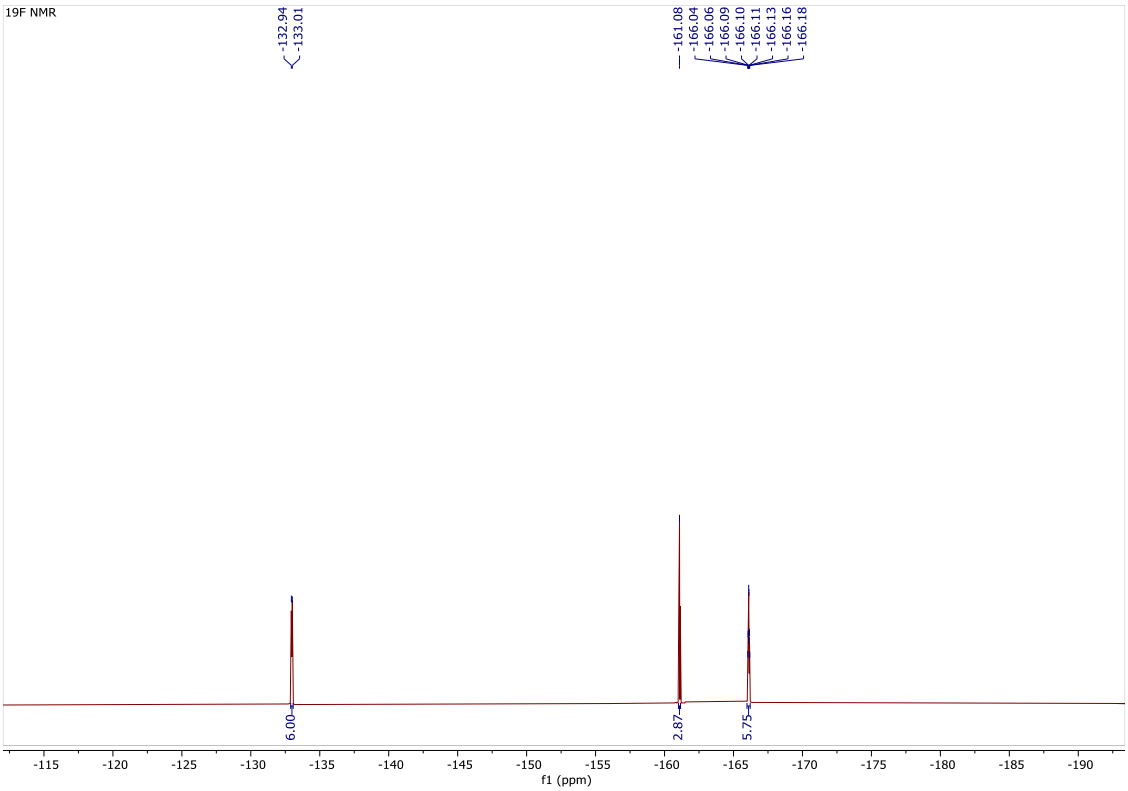

Figure S51. ^{19}F NMR spectrum of **8-B(C_6F_5)$_3$** in CD_2Cl_2 at 298 K.

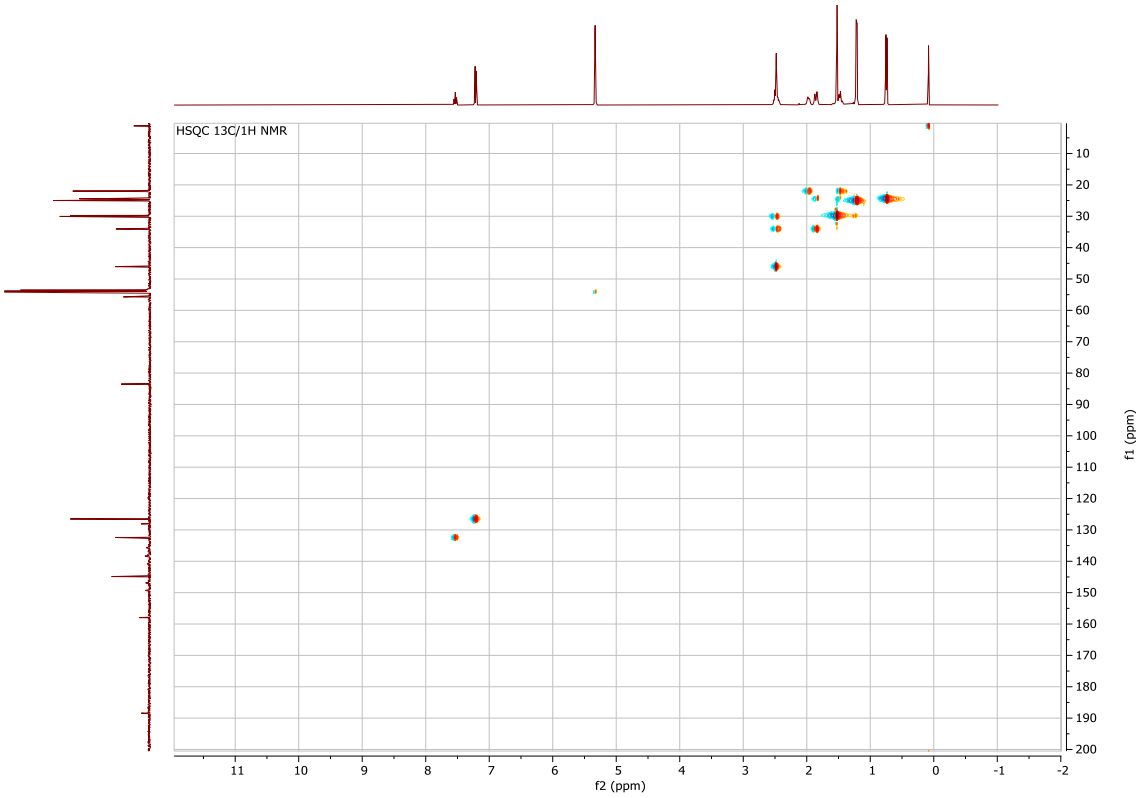

Figure S52. HSQC $^{13}C/^{1}H$ NMR spectrum of **8-B(C_6F_5)$_3$** in CD_2Cl_2 at 298 K.

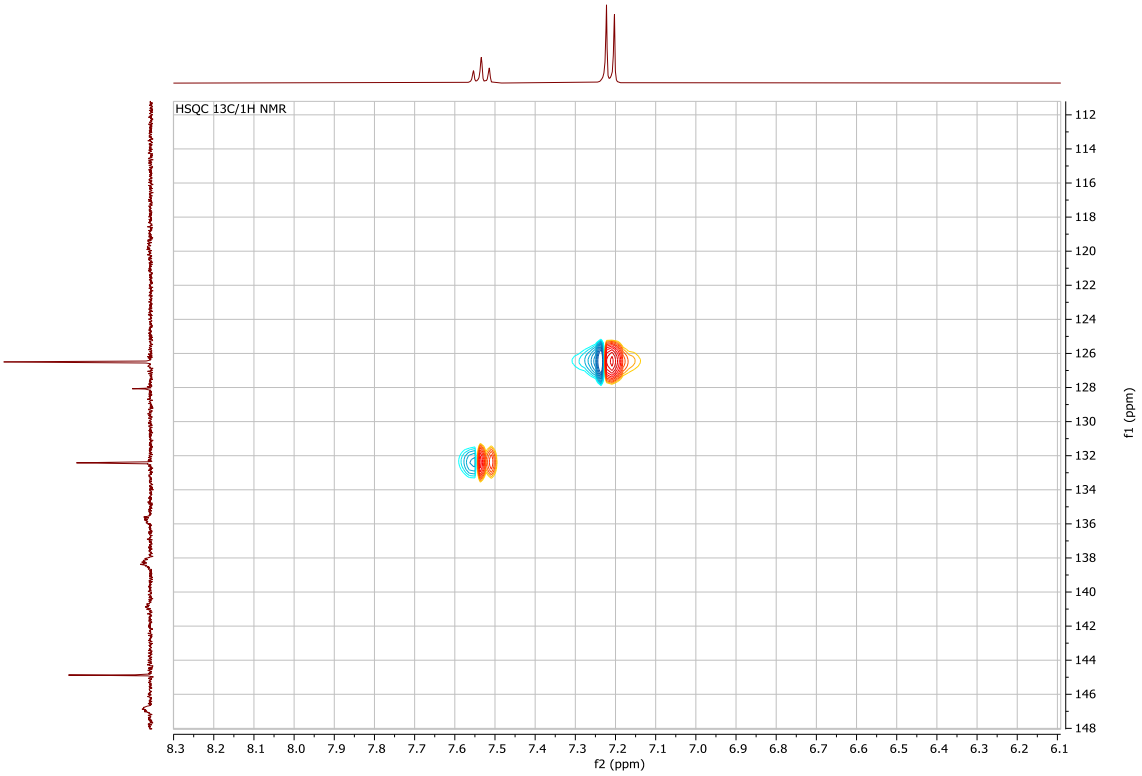

Figure S53. Zoom HSQC $^{13}C/^{1}H$ NMR spectrum of **8-B(C_6F_5)$_3$** in CD_2Cl_2 at 298 K.

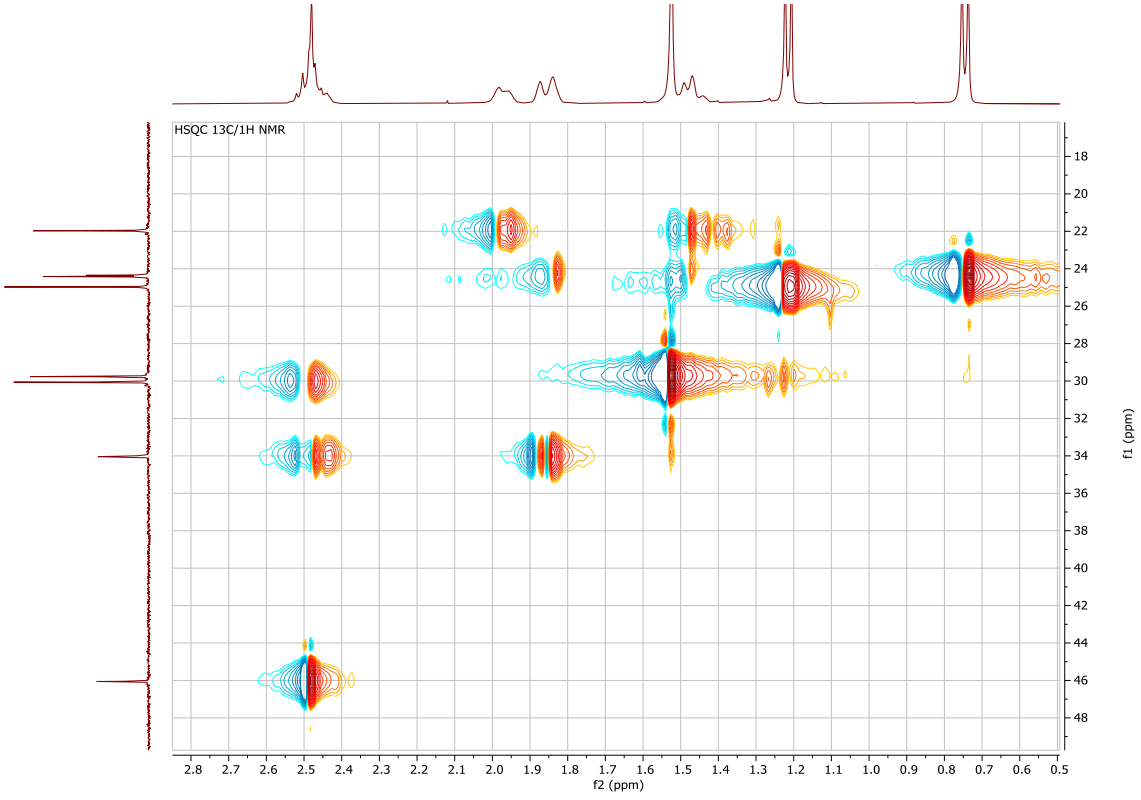

Figure S54. Zoom HSQC $^{13}C/^{1}H$ NMR spectrum of **8-B(C_6F_5)$_3$** in CD_2Cl_2 at 298 K.

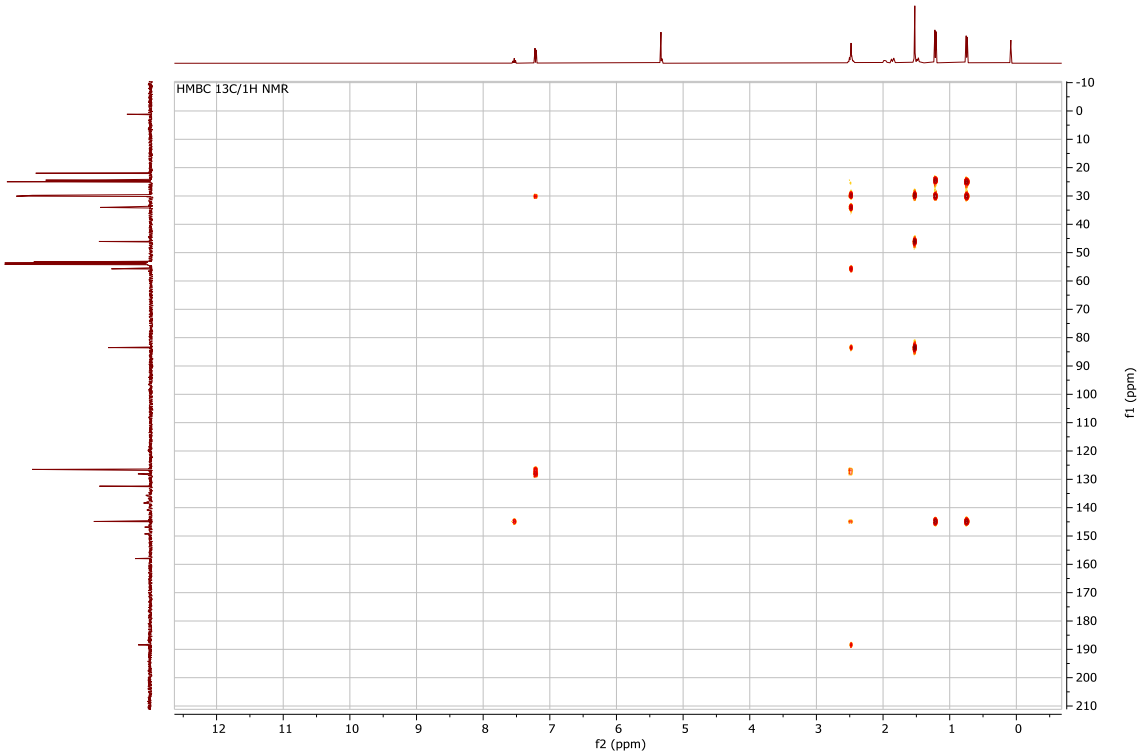

Figure S55. HMBC $^{13}C/^{1}H$ NMR spectrum of **8-B(C_6F_5)$_3$** in CD_2Cl_2 at 298 K.

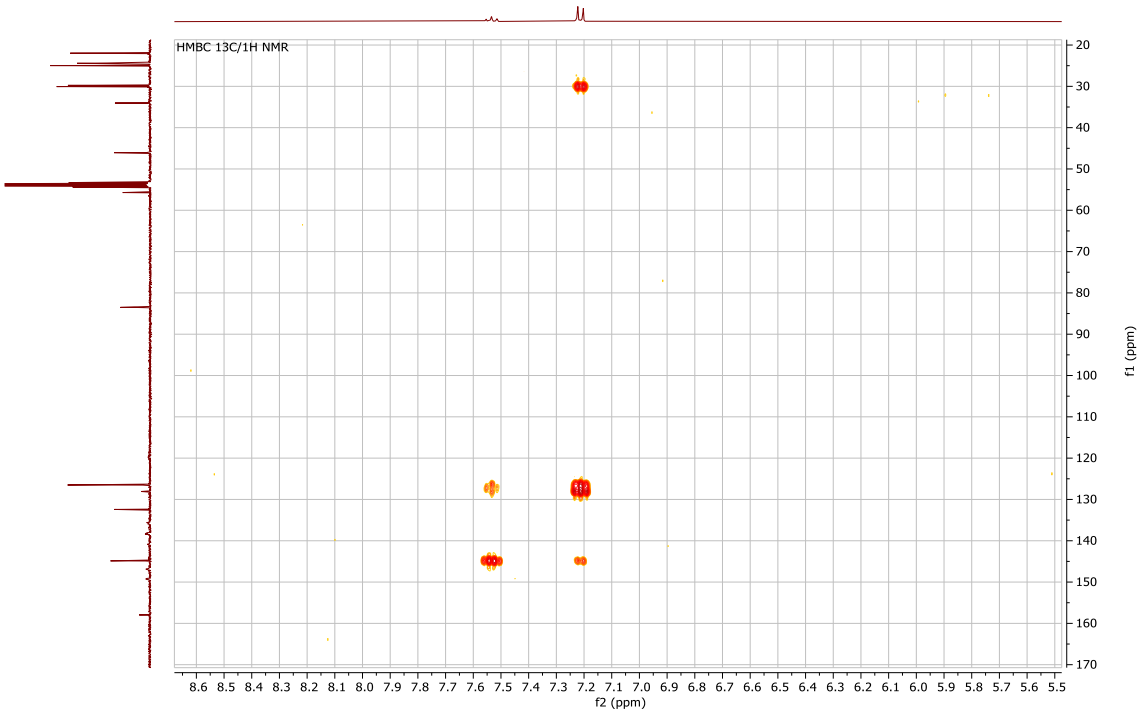

Figure S56. Zoom HMBC $^{13}C/^{1}H$ NMR spectrum of **8-B(C_6F_5)$_3$** in CD_2Cl_2 at 298 K.

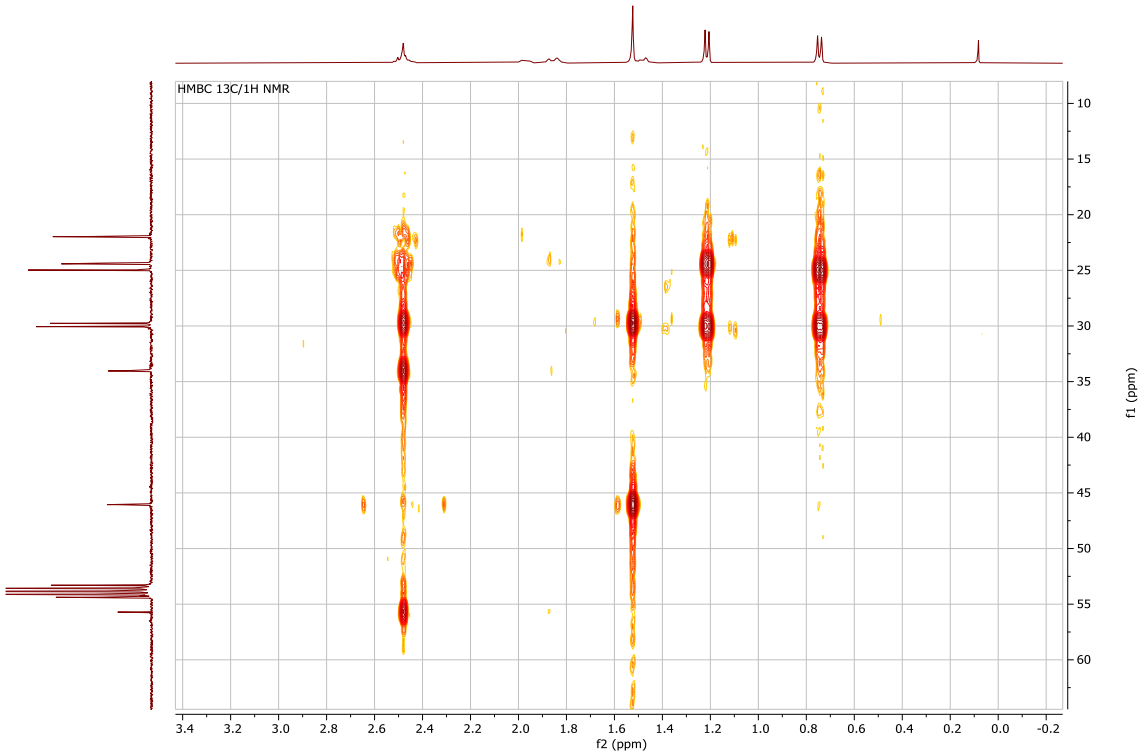

Figure S57. Zoom HMBC $^{13}C/^{1}H$ NMR spectrum of **8-B(C_6F_5)$_3$** in CD_2Cl_2 at 298 K.

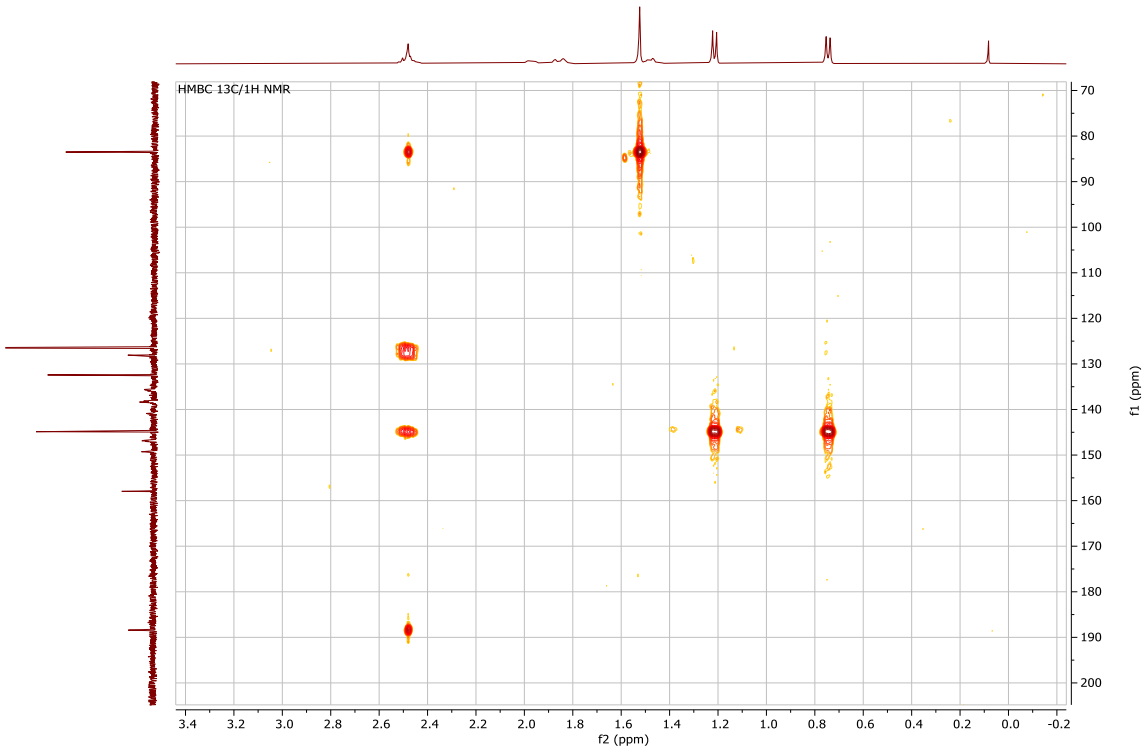

Figure S58. Zoom HMBC $^{13}C/^{1}H$ NMR spectrum of **8-B(C_6F_5)$_3$** in CD_2Cl_2 at 298 K.

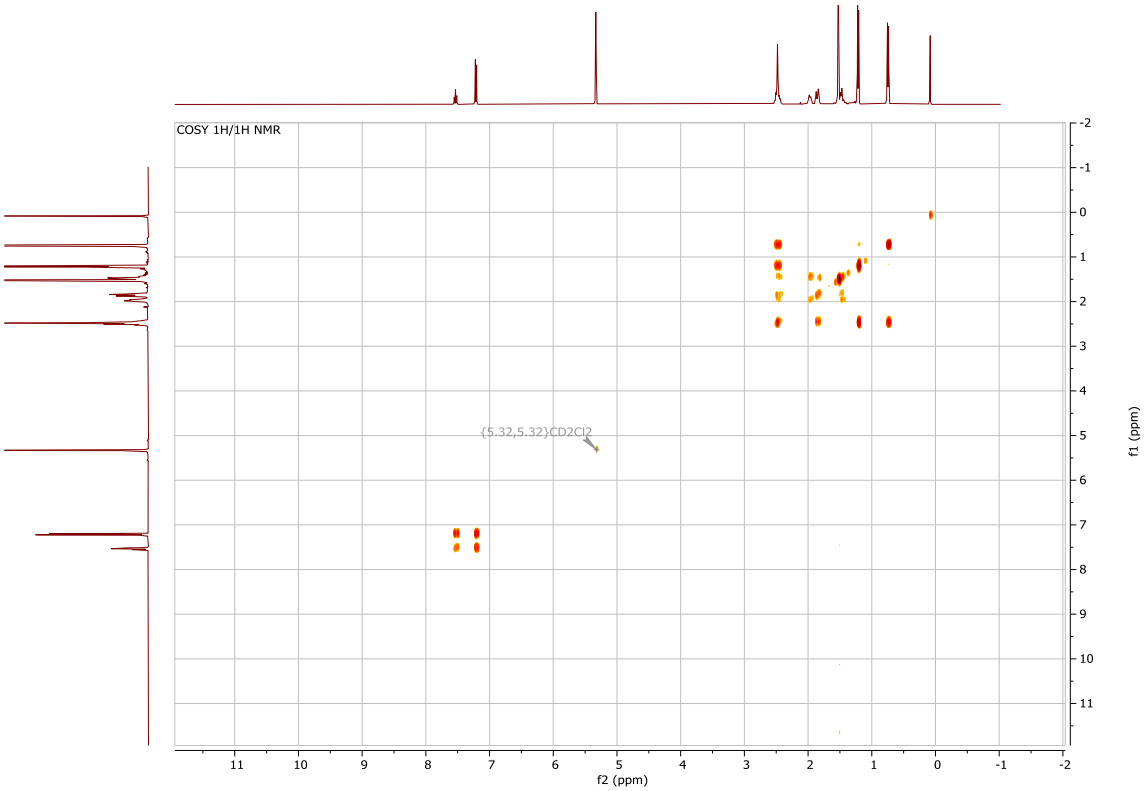

Figure S59. COSY $^{1}H/^{1}H$ NMR spectrum of **8-B(C_6F_5)$_3$** in CD_2Cl_2 at 298 K.

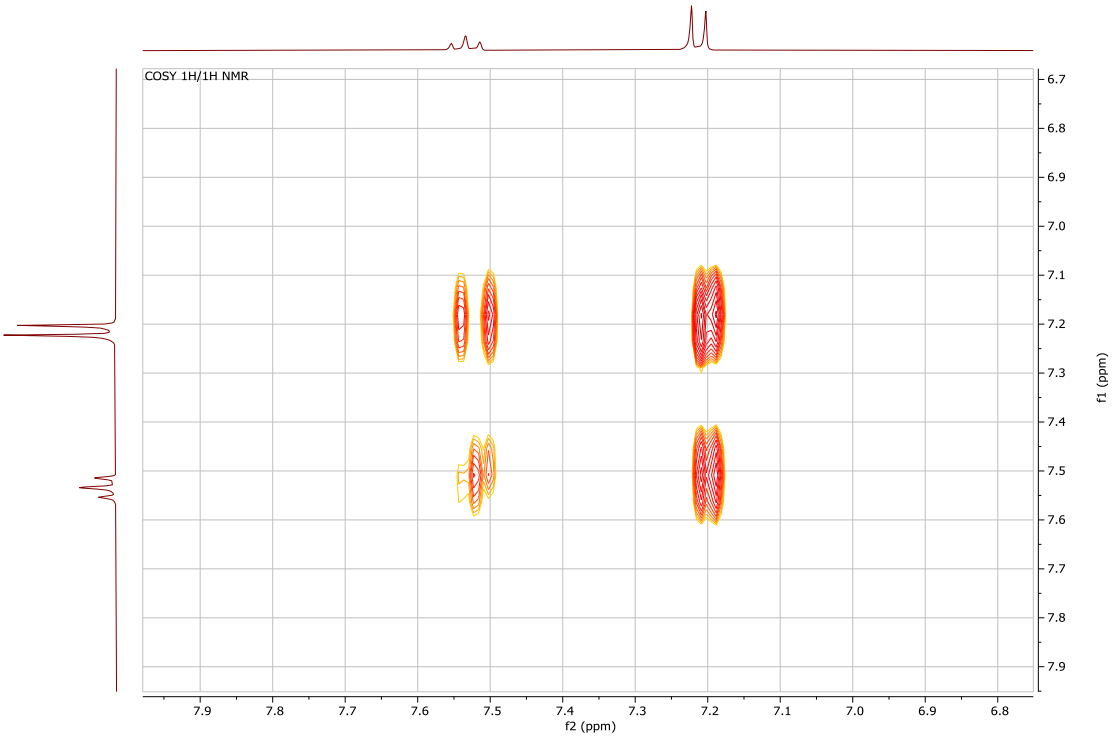

Figure S60. Zoom COSY $^{1}H/^{1}H$ NMR spectrum of **8-B(C_6F_5)$_3$** in CD_2Cl_2 at 298 K.

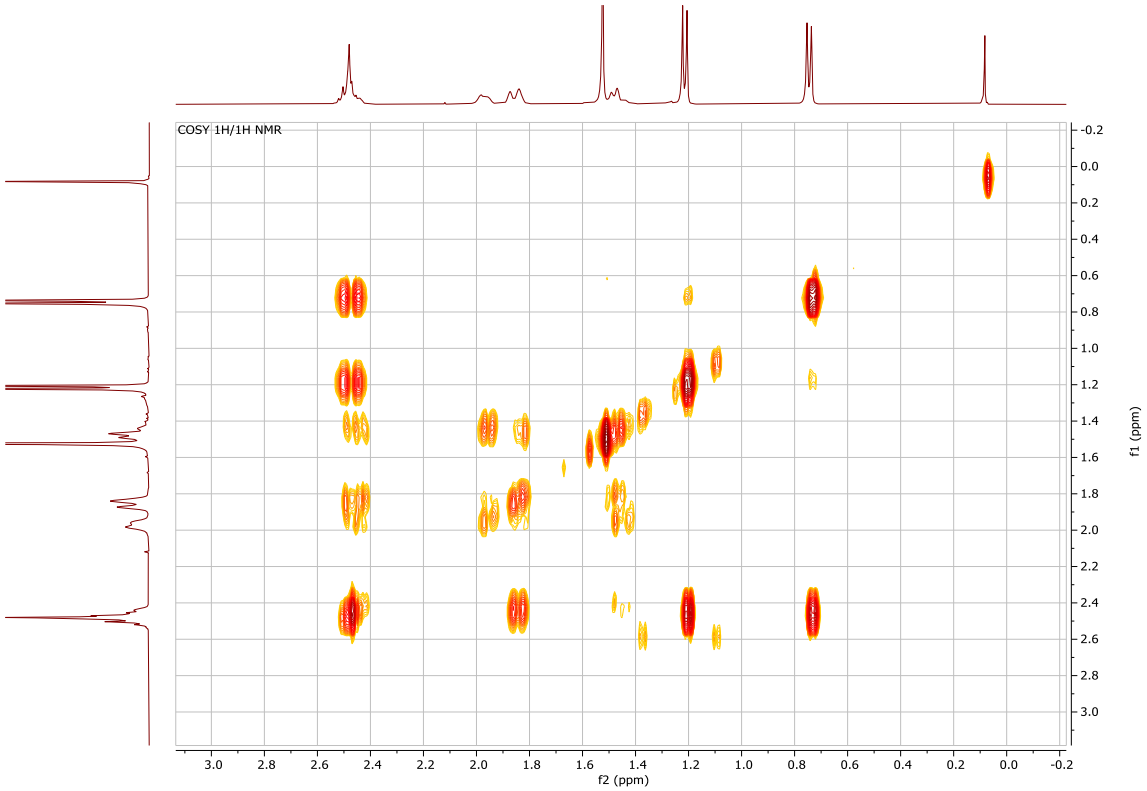

Figure S61. Zoom COSY $^{1}H/^{1}H$ NMR spectrum of **8-B(C_6F_5)$_3$** in CD_2Cl_2 at 298 K.

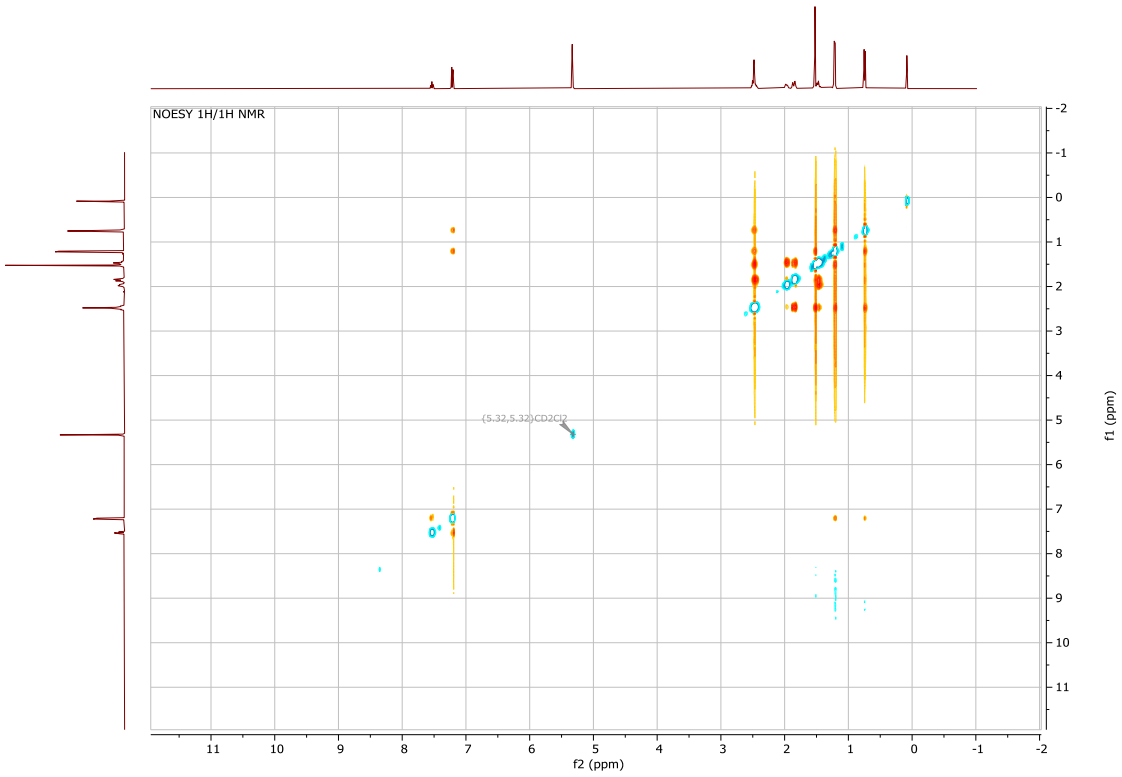

Figure S62. NOESY $^{1}H/^{1}H$ NMR spectrum of **8-B(C_6F_5)$_3$** in CD_2Cl_2 at 298 K.

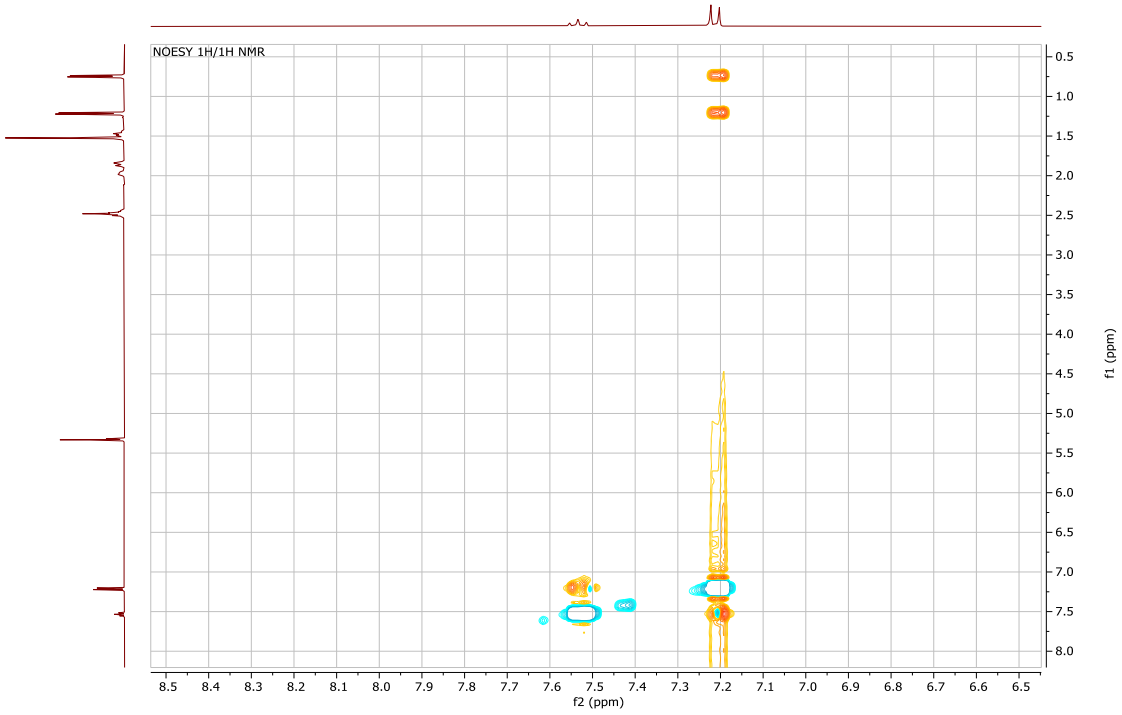

Figure S63. Zoom NOESY $^{1}H/^{1}H$ NMR spectrum of **8-B(C_6F_5)$_3$** in CD_2Cl_2 at 298 K.

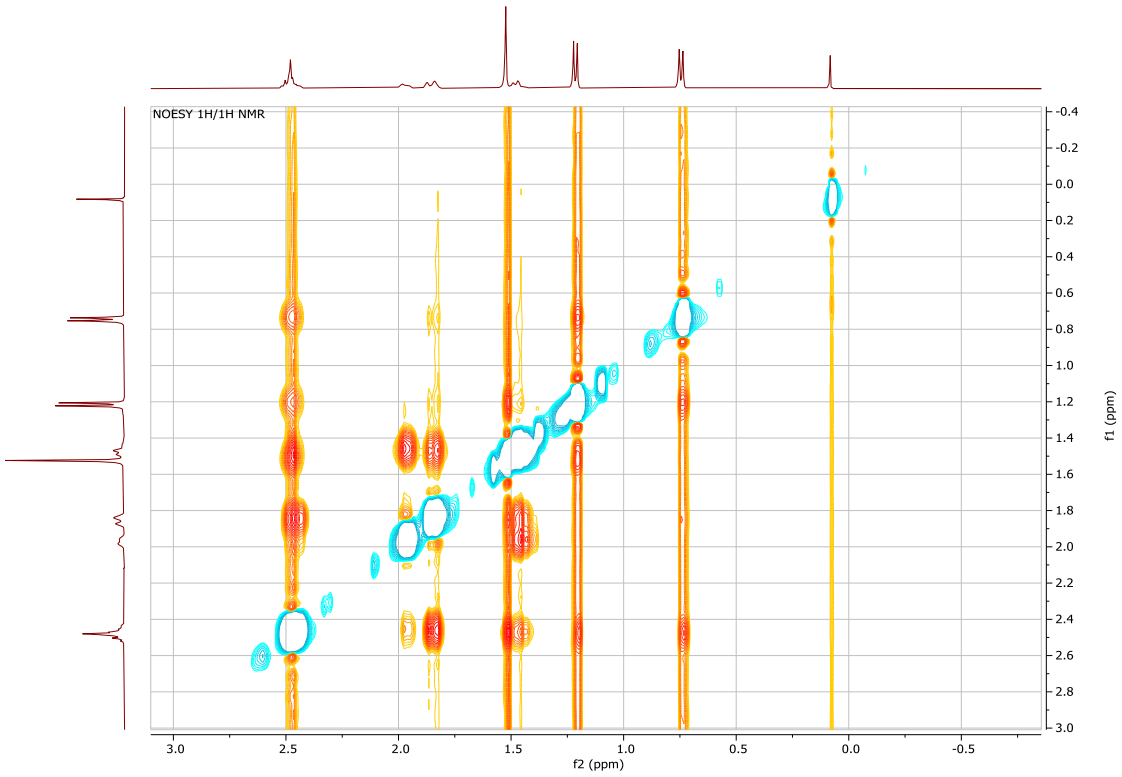

Figure S64. Zoom NOESY $^{1}H/^{1}H$ NMR spectrum of **8-B(C_6F_5)$_3$** in CD_2Cl_2 at 298 K.

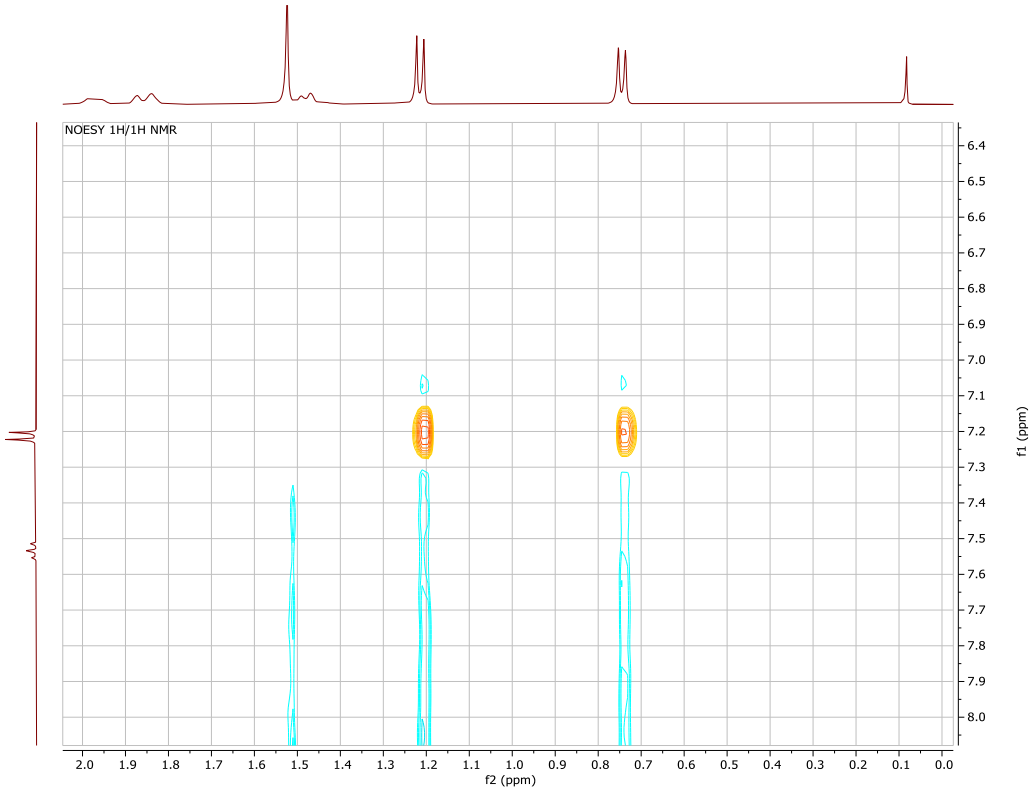

Figure S65. Zoom NOESY $^{1}H/^{1}H$ NMR spectrum of **8-B(C_6F_5)$_3$** in CD_2Cl_2 at 298 K.

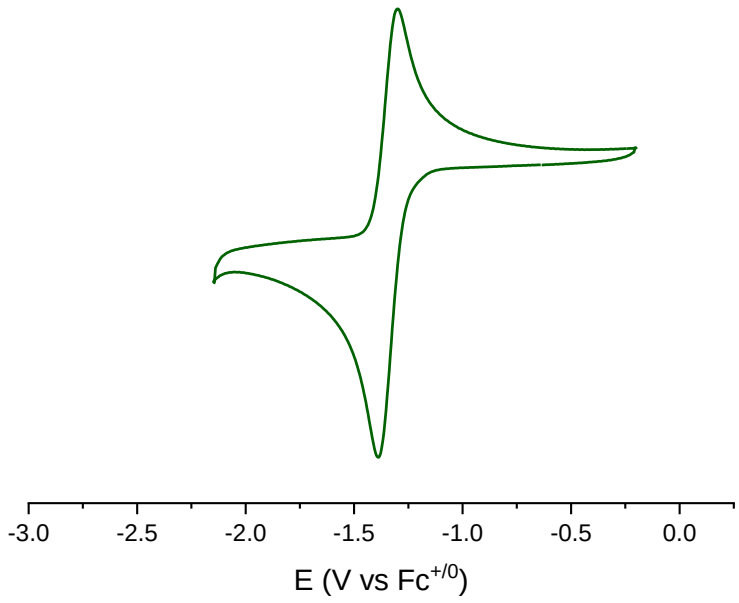

Figure S66. Normalised CV response of **8-B(C_6F_5)$_3$** at reducing potentials under Ar atmosphere in CH_2Cl_2. Conditions: 5 mM compound **8-B(C_6F_5)$_3$** and 0.1 M (n-Bu_4N)[PF_6], scan 200 mV/s.

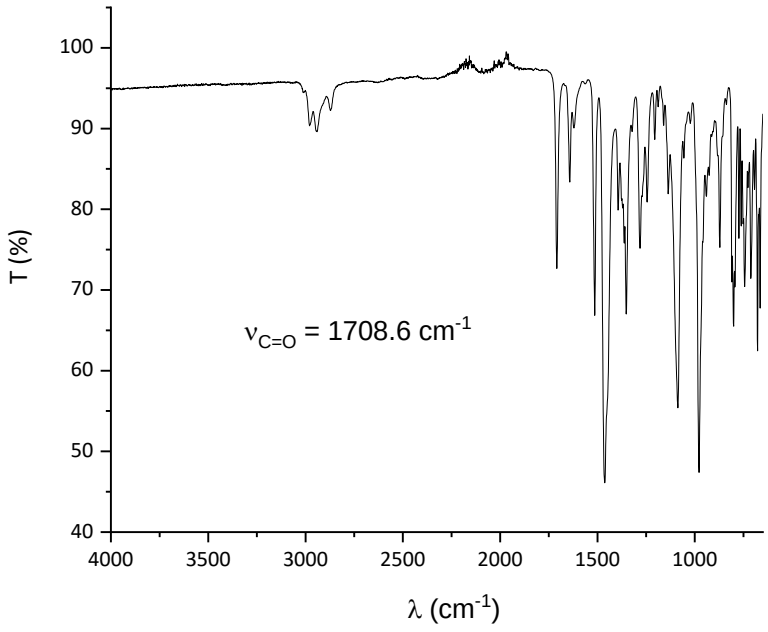

Figure S67. FTIR (solid state) of **8-B(C_6F_5)$_3$** at 298 K.

Crystallographic details of adduct 8-$B(C_6F_5)_3$.

Table S7. Crystal data.

$C_{42}H_{35}BF_{15}NO_2 \cdot CH_2Cl_2$	
M_r = 966.45	D_x = 1.561 Mg m^{-3}
Monoclinic, C2/c	
Hall symbol: -C 2yc	Mo Kα radiation, λ = 0.71073 Å
a = 32.364 (7) Å	Cell parameters from 8856 reflections
b = 11.022 (2) Å	θ = 2.6–30.4°
c = 23.039 (5) Å	μ = 0.27 mm^{-1}
β = 93.043 (10)°	T = 100 K
V = 8207 (3) $Å^3$	Plate, colourless
Z = 8	0.18 × 0.10 × 0.03 mm
F(000) = 3936	

Table S8. Data collection.

Bruker Kappa APEX II diffractometer	6944 reflections with I > 2σ(I)
Radiation source: fine-focus sealed tube	R_{int} = 0.062
Graphite monochromator	θ_{max} = 25.7°, θ_{min} = 1.8°
ω–ϕ scans	h = −39 39
Absorption correction: multi-scan	k = −13 13
[c.f. r.h. blessing, acta cryst. (1995), a51, 33-38]	
T_{min} = 0.723, T_{max} = 0.739	l = −28 28
176210 measured reflections	Standard reflections: 0
7795 independent reflections	

Table S9. Refinement.

Refinement on F^2	
Least-squares matrix: full	Hydrogen site location: inferred from neighbouring sites
$R[F^2 > 2\sigma(F^2)]$ = 0.032	H-atom parameters constrained
$wR(F^2)$ = 0.080	$w = 1/[\sigma^2(F_o^2) + (0.0286P)^2 + 14.3409P]$ where $P = (F_o^2 + 2F_c^2)/3$
S = 1.05	$(\Delta/\sigma)_{max}$ = 0.003
7795 reflections	$\Delta\rho_{max}$ = 0.40 e Å^{-3}
611 parameters	$\Delta\rho_{min}$ = −0.35 e Å^{-3}
0 restraints	Extinction correction: none

5.2.6. K^{Cy}CAAC-CO_2 ([8(K)]•).

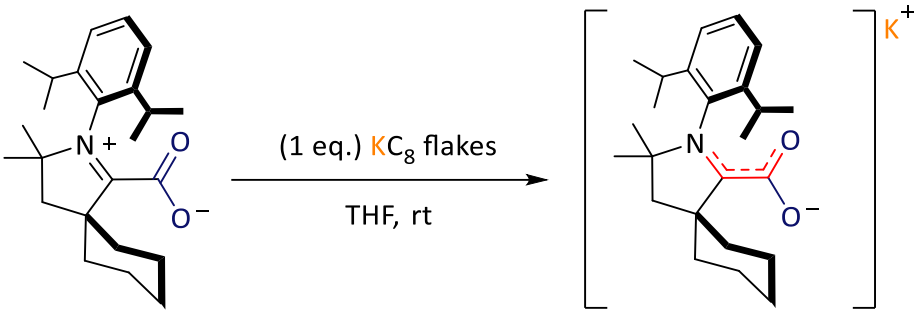

(**8**) ([**8(K)**]•)

Compound **8** (13.7 mg, 0.04 mmol) and KC_8 (5 mg, 0.04 mmol) were placed in a 4 mL vial inside an argon glovebox. Then, 1 mL of THF was added to the vial and stirred for one minute. The resulting dark solution was transferred into another vial and diluted by a factor 10 in order to perform the EPR measurement. EPR (CW, X-band) g = 2.00253 (a_N = 6.16 G).

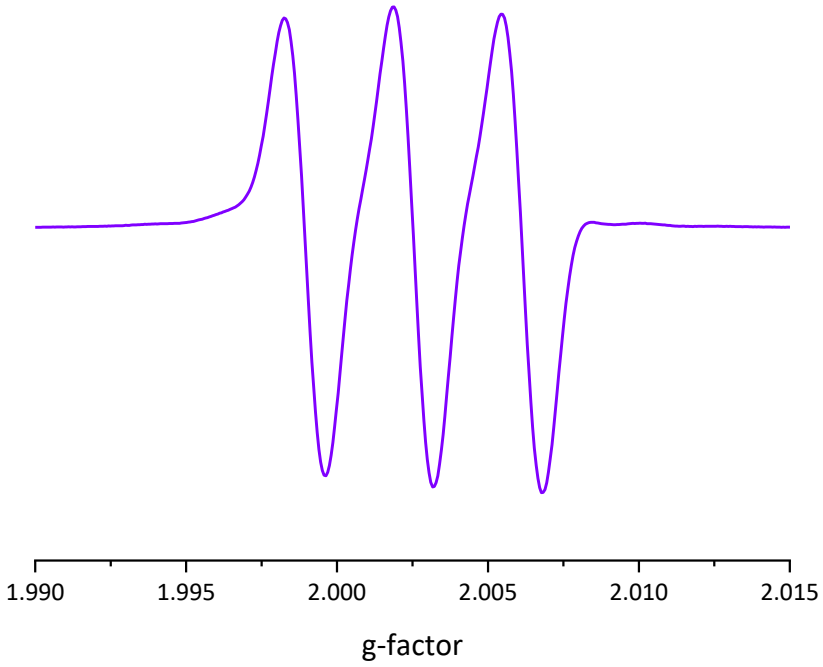

Figure S68. Continuous wave X-band EPR spectrum taken on a 4 mM **[8(K)]•** THF solution at room temperature.

5.2.7. K^{Cy}CAAC-CO_2-$B(C_6F_5)_3$.2THF ([8-$B(C_6F_5)_3$(K)]•).

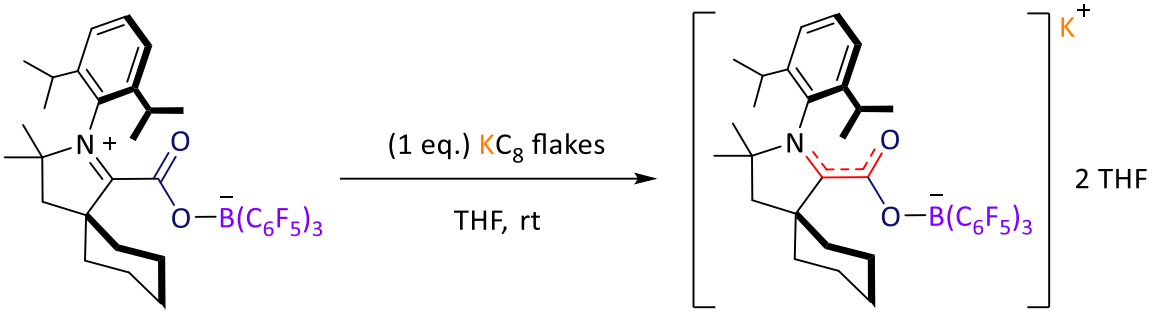

(8-$B(C_6F_5)_3$) ([8-$B(C_6F_5)_3$(K)]•)

Compound **8-$B(C_6F_5)_3$** (50 mg, 0.06 mmol) and KC_8 (7.7 mg, 0.06 mmol) were placed in a 4 mL vial inside an argon glovebox. Then, 0.5 mL of THF were added to the vial and stirred for one minute. The resulting dark yellow solution was transferred into another vial. To the precedent solution, 2 mL of pentane were added forming a double-layered solution, which was placed at -36°C. The expected product was isolated as orange crystals in 22% (11 mg). EPR (CW, X-band) g = 2.00347 (a_N = 6.01 G). Anal (%): Calcd for $C_{38}H_{32}BF_{15}KN_2O_4$: C, 57.04; H, 5.25; N, 1.28. Found: C, 56.80; H, 4.82; N, 1.47. FTIR (solid state): $\nu_{C=O}$ = 1595.6 cm^{-1}.

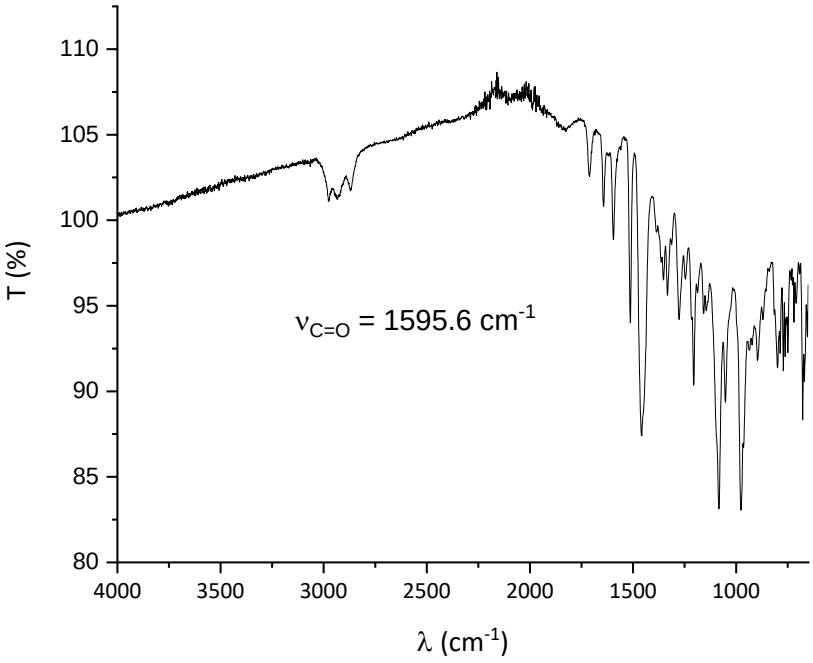

Figure S69. FTIR (solid state) of **[8-$B(C_6F_5)_3$(K)]•** at 298 K.

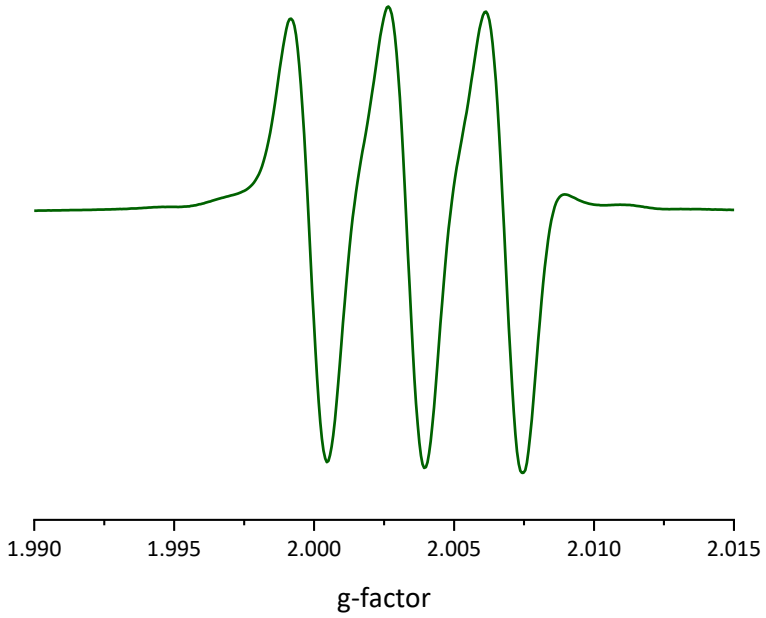

Figure S70. Continuous wave X-band EPR spectrum taken on a 6 mM **[8-B(C_6F_5)$_3$(K)]$^\bullet$** THF solution at room temperature.

Crystallographic details of adduct [8-B(C_6F_5)$_3$(K)]$^\bullet$.

Table S10. Crystal data.

$C_{50}H_{51}BF_{15}KNO_4$	
M_r = 1064.82	D_x = 1.334 Mg m^{-3}
Monoclinic, I2/a	
Hall symbol: -I 2ya	Cu Kα radiation, λ = 1.54184 Å
a = 23.8532 (3) Å	Cell parameters from 33823 reflections
b = 21.0638 (3) Å	θ = 2.8–76.9°
c = 21.3167 (3) Å	μ = 1.72 mm^{-1}
β = 97.970 (1)°	T = 100 K
V = 10606.9 (3) Å^3	Platelet, yellow
Z = 8	0.15 × 0.11 × 0.01 mm
F(000) = 4392	

Table 11. Data collection.

XtaLAB Synergy, Dualflex, HyPix diffractometer	9377 independent reflections
Radiation source: micro-focus sealed X-ray tube, PhotonJet (Cu) X-ray Source	8225 reflections with I > 2σ(I)
Mirror monochromator	R_{int} = 0.051
Detector resolution: 10.0000 pixels mm^{-1}	θ_{max} = 66.6°, θ_{min} = 2.8°
	h = −28 28
Absorption correction: multi-scan	k = −25 25
CrysAlisPro 1.171.41.120a (Rigaku Oxford Diffraction, 2021) Empirical absorption correction using spherical harmonics, implemented in SCALE3 ABSPACK scaling algorithm.	
T_{min} = 0.819, T_{max} = 1.000	l = −19 25
69963 measured reflections	

Table 12. Refinement.

Refinement on F^2	
Least-squares matrix: full	Hydrogen site location: inferred from neighbouring sites
$R[F^2 > 2\sigma(F^2)]$ = 0.053	H-atom parameters constrained
$wR(F^2)$ = 0.152	$w = 1/[\sigma^2(F_o^2) + (0.0909P)^2 + 15.0349P]$ where $P = (F_o^2 + 2F_c^2)/3$
S = 1.03	$(\Delta/\sigma)_{max}$ = 0.017
9377 reflections	$\Delta\rho_{max}$ = 0.77 e Å^{-3}
649 parameters	$\Delta\rho_{min}$ = −0.64 e Å^{-3}
5 restraints	Extinction correction: SHELXL-2018/3 (Sheldrick 2018) $Fc^*=kFc[1+0.001xFc^2\lambda^3/\sin(2\theta)]^{-1/4}$

5.2.8. [CoCp*$_2$]^{Cy}CAAC-CO$_2$-B(C$_6$F$_5$)$_3$ ([8-B(C$_6$F$_5$)$_3$(Co)]$^\bullet$).

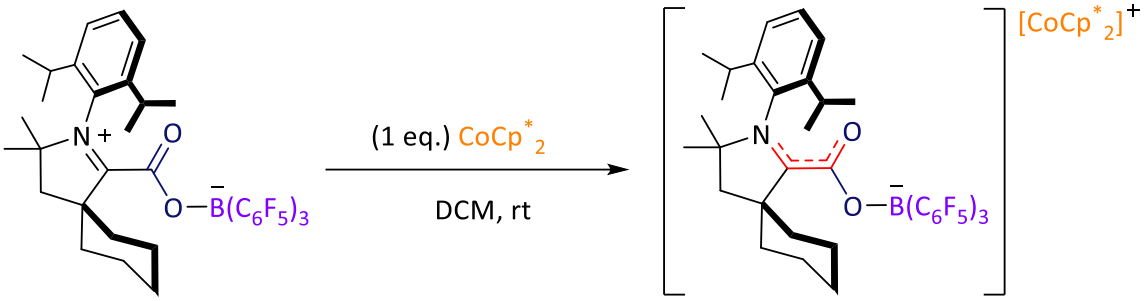

(**8-B(C$_6$F$_5$)$_3$**) (**[8-B(C$_6$F$_5$)$_3$(Co)]$^\bullet$**)

Compound **8-B(C$_6$F$_5$)$_3$** (13.4 mg, 0.02 mmol) and CoCp*$_2$ (5 mg, 0.02 mmol) were placed in a 4 mL vial inside an argon glovebox. Then, 1 mL of dichloromethane was added to the vial and stirred for one minute. The resulting dark solution was transferred into another vial and diluted by a factor 10 in order to perform the EPR measurement. EPR (CW, X-band) g = 2.00370 (a_N = 5.87 G).

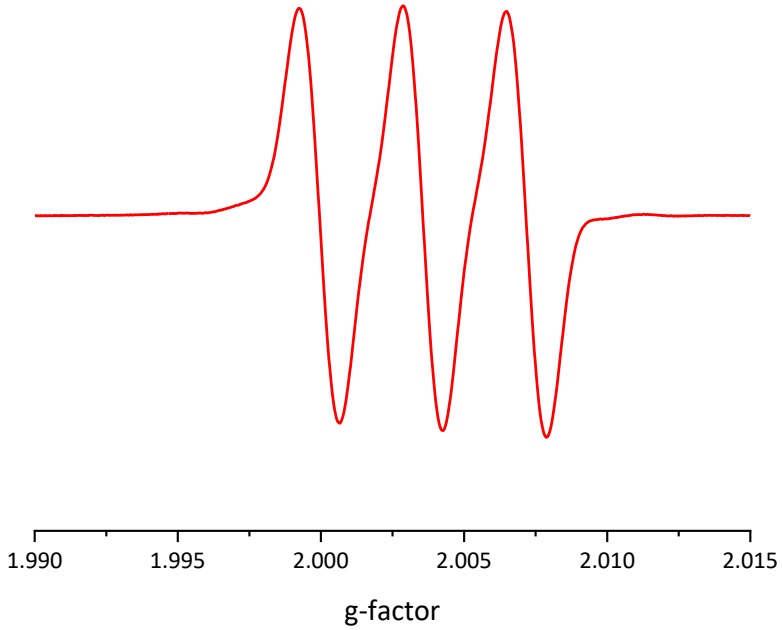

Figure S71. Continuous wave X-band EPR spectrum taken on a 2 mM **[8-B(C$_6$F$_5$)$_3$(Co)]$^\bullet$** dichloromethane solution at room temperature.

5.2.9. KIPr-CO_2-$B(C_6F_5)_3$ ([5-$B(C_6F_5)_3$(K)]•).

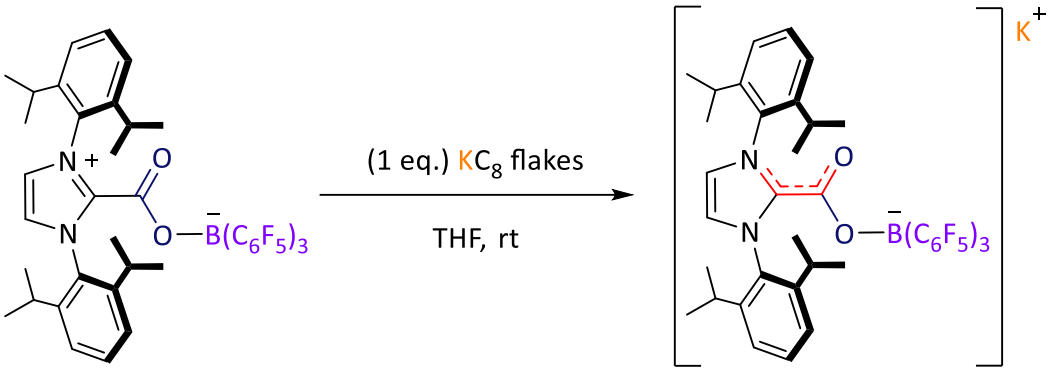

(**5-$B(C_6F_5)_3$**) (**[5-$B(C_6F_5)_3$(K)]•**)

Compound **5-$B(C_6F_5)_3$** (24 mg, 0.03 mmol) and KC_8 (3.2 mg, 0.03 mmol) were placed in a 4 mL vial inside an argon glovebox. Then, 1 mL of THF was added to the vial and stirred for one minute. The resulting dark solution was transferred into another vial and diluted by a factor 10 in order to perform the EPR and IR measurements. EPR (CW, X-band) g = 2.00375 (a_N = 4.45 G). IR (liquid state): $\nu_{C=O}$ = 1602.0 cm^{-1}.

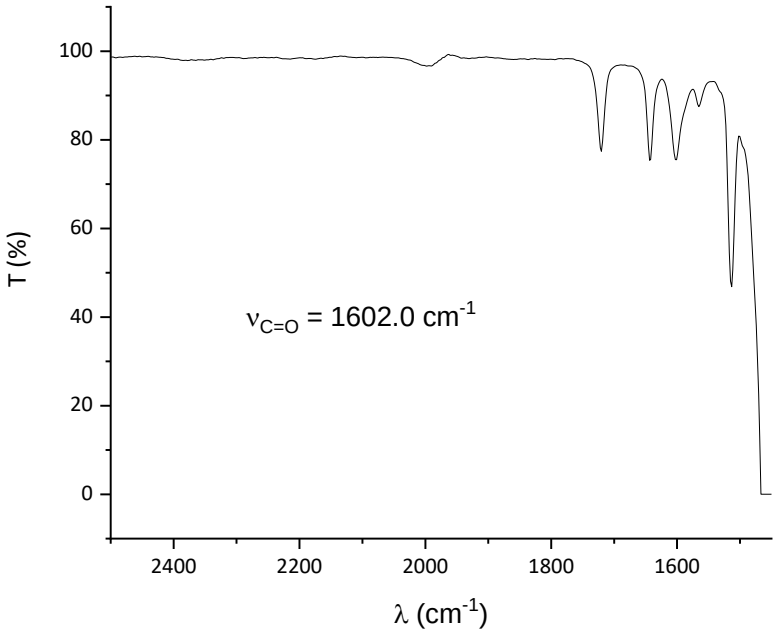

Figure S72. IR (liquid state) of **[5-$B(C_6F_5)_3$(K)]•** at 298 K.

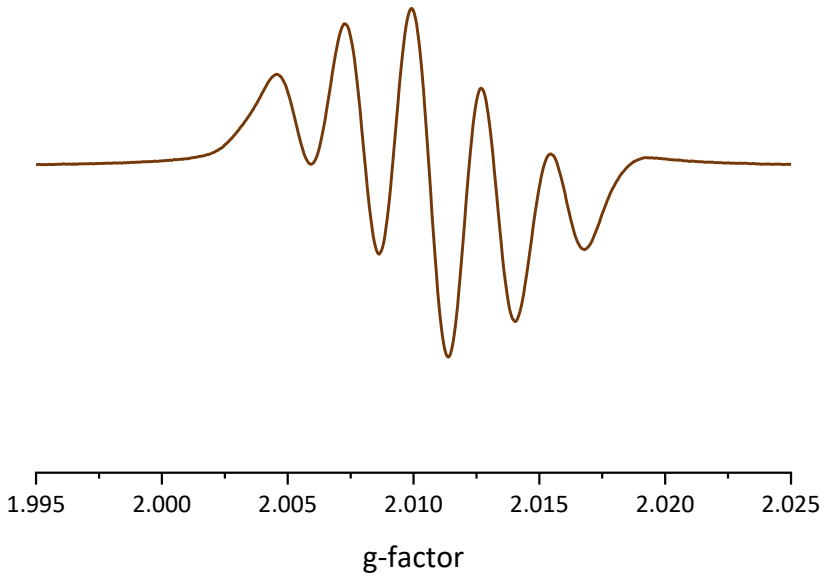

Figure S73. Continuous wave X-band EPR spectrum taken on a 3 mM **[5-B(C_6F_5)$_3$(K)]$^\bullet$** THF solution at room temperature.

5.3. References.

(1) Theuergarten, E.; Bannenberg, T.; Walter, M. D.; Holschumacher, D.; Freytag, M.; Daniliuc, C. G.; Jones, P. G.; Tamm, M. Computational and Experimental Investigations of CO_2 and N_2O Fixation by Sterically Demanding *N*-Heterocyclic Carbenes (NHC) and NHC/Borane FLP Systems. *J. Chem. Soc. Dalton Trans.* **2014**, *43* (4), 1651–1662. https://doi.org/10.1039/c3dt52742e.

(2) Lieske, L. E.; Freeman, L. A.; Wang, G.; Dickie, D. A.; Gilliard, R. J.; Machan, C. W. Metal-Free Electrochemical Reduction of Carbon Dioxide Mediated by Cyclic(Alkyl)(Amino) Carbenes. *Chem. - Eur. J.* **2019**, *25* (24), 6098–6101. https://doi.org/10.1002/chem.201900316.

General conclusions and perspectives.

1. The combination of an *N*-Heterocyclic Carbene (NHC) and a free CO_2 molecule result in the formation of NHC-CO_2 adducts. The presence of a borane (BR_3) leads to the formation of NHC-CO_2-BR_3 adducts, where the NHC and BR_3 parts are, respectively, the base and Lewis acid.
2. We can confirm that structural modifications of the NHC have a significant impact on the reduction potential of the NHC-CO_2 adducts in question.
3. Our approach, which combines experimental and theoretical methods, confirms that the addition of a borane to the NHC-CO_2 adducts results in reduction potentials less negative than in the case of NHC-CO_2 adducts and the free CO_2 molecule. Furthermore, a higher Lewis acidity of the borane translates to more accessible reduction potentials. The **8-B(C_6F_5)$_3$** adduct exhibits the least negative reduction potential at -1.34 V compared to $Fc^{+/0}$ in dichloromethane.
4. During the reduction of NHC-CO_2 adducts, the localisation of spin density in the CO_2 moiety, particularly on the carbon atom, is dictated by the electronic properties of the NHC. The presence of borane (BH_3, BCl_3, and $B(C_6F_5)_3$) allows for the localisation of spin density on the carbon atom of CO_2. The adduct with the highest spin density at this location is **[5-B(C_6F_5)$_3$]$^{\bullet-}$** with a spin population of 0.41.
5. The localisation of the LUMO in neutral adducts closely resembles the SOMO in their monoreduced form. The addition of a Lewis acid to NHC-CO_2 adducts enables the localization of LUMO and SOMO orbitals primarily in the CO_2 moiety in almost all cases, regardless of the torsion angle between the NHC and carbon dioxide. Additionally, this also results in a significant energy stabilization of the LUMO and SOMO orbitals. The adducts with the lowest LUMO energy are **8-BCl_3** (-0.97 eV) and **8-B(C_6F_5)$_3$** (-0.97 eV) and also exhibit the least negative reduction potentials, -1.38 V and -1.29 V, respectively. The energy of the LUMO in neutral species is correlated with their reduction potential.
6. Based on a conformation analysis of NHC-CO_2-based adducts synthesised as a function of the torsion angle, we have observed that the energy of the LUMO

reaches its highest point when the torsion angle is close to 90° and its lowest point when the CO_2 part tends to be closer to a coplanar orientation (near 0°) with respect to the NHC ring in all cases. The energy stabilisation of the **8**, **2-B(C_6F_5)$_3$**, **3-B(C_6F_5)$_3$** and **8-B(C_6F_5)$_3$** adducts behaves inversely to the LUMO energy, while in the **5-B(C_6F_5)$_3$** adduct, the LUMO energy and stabilisation energy change in a directly proportional manner. The torsion angle in NHC-CO_2-based adducts has a significant impact on their reduction potentials and LUMO energy.

The accessible reduction potentials found for NHC-CO_2-based adducts allow for the use of milder conditions to generate their reduced form than in the case of the CO_2 molecule. Additionally, the presence of spin density on the carbon atom of the CO_2 moiety in its reduced form is also one of the beneficial properties of these molecules that could make them ideal candidates as C1 synthons for building new C-C bonds.

Conclusiones generales y perspectivas.

1. La combinación de un Carbeno *N*-Heterocíclico (NHC) y una molécula libre de CO_2 resulta en la formación de aductos NHC-CO_2. La presencia de un borano (BR_3) da lugar a la formación de aductos NHC-CO_2-BR_3, donde la parte NHC y BR_3 son respectivamente la base y el ácido de Lewis.

2. Podemos confirmar que las modificaciones estructurales del NHC tienen un impacto significativo en el potencial de reducción de los aductos NHC-CO_2 en cuestión.

3. Nuestra aproximación, que combina métodos experimentales y teóricos, confirma que la adición de un borano a los aductos NHC-CO_2 resulta en potenciales de reducción menos negativos que en el caso de los aductos NHC-CO_2 y que en el caso de la molécula libre de CO_2. Además, una mayor acidez de Lewis del borano se traduce en potenciales de reducción más accesibles. El aducto **8-B(C_6F_5)$_3$** presenta el potencial de reducción menos negativo a -1.34 V respecto al $Fc^{+/0}$ en el diclorometano.

4. Durante la reducción de los aductos NHC-CO_2, la localización de la densidad de espín en la parte del CO_2, en particular en el átomo de carbono, está dictada por las propiedades electrónicas del NHC. La presencia del borano (BH_3, BCl_3 y $B(C_6F_5)_3$) permite la localización de una parte de la densidad de espín en el átomo de carbono del CO_2. El aducto que presenta la mayor densidad de espín en este lugar es **[5-B(C_6F_5)$_3$]$^{\bullet-}$** con una población de espín de 0.41.

5. La localización del LUMO en los aductos neutros se asemeja estrechamente al SOMO en su forma monorreducida. La adición de un ácido de Lewis a los aductos NHC-CO_2 permite la localización de las orbitales LUMO y SOMO principalmente en la parte del CO_2 en casi todos los casos, independientemente del ángulo de torsión entre el NHC y el dióxido de carbono. Además, esto también conlleva una significativa energía de estabilización de los orbitales LUMO y SOMO. Los aductos que presentan la menor energía LUMO son **8-BCl_3** (-0.97 eV) y **8-B(C_6F_5)$_3$** (-0.97 eV) y también presentan los potenciales de reducción menos negativos, -1.38 V

y -1,29 V respectivamente. La energía del LUMO en las especies neutras está correlacionada con su potencial de reducción.

6. Basándonos en un análisis de los confórmeros de los aductos basados en NHC-CO_2 sintetizados en función de diferentes ángulos de torsión, hemos observado que la energía de las LUMO alcanza su punto más alto cuando el ángulo de torsión está cerca de 90° y su punto más bajo cuando la parte del CO2 tiende a estar más cerca de una orientación coplanar (cerca de 0°) con respecto al anillo NHC en todos los casos. La energía de estabilización de los aductos **8**, **2-B(C_6F_5)$_3$**, **3-B(C_6F_5)$_3$** y **8-B(C_6F_5)$_3$** se comporta de manera inversa a la energía del LUMO, mientras que en el aducto **5-B(C_6F_5)$_3$**, el LUMO y la energía de estabilización cambian de manera directamente proporcional. El ángulo de torsión en los aductos basados en NHC-CO_2 tiene un impacto significativo en sus potenciales de reducción y en la energía del LUMO.

Los potenciales de reducción accesibles encontrados para los aductos basados en NHC-CO_2 permiten el uso de condiciones más suaves para generar su forma reducida que en el caso de la molécula de CO_2. Además, la presencia de densidad de espín en el átomo de carbono de la parte del CO_2 en su forma reducida es también una de las propiedades beneficiosas de estas moléculas que podría convertirlas en candidatos ideales como sintones C1 para construir nuevos enlaces químicos C-C.

Conclusions générales et perspectives.

1. La combinaison d'un Carbène *N*-Hétérocyclique (NHC) et d'une molécule libre de CO_2 conduit à la formation d'adduits NHC-CO_2. La présence d'un borane (BR_3) donne naissance à la formation d'adduits NHC-CO_2-BR_3 où la partie NHC et BR_3 sont respectivement la base et l'acide de Lewis.

2. Nous pouvons confirmer que les modifications structurales du NHC ont un impact important sur le potentiel de réduction des adduits NHC-CO_2 l'espèce en question.

3. Notre approche, qui combine des méthodes expérimentales et théoriques, confirme que l'ajout d'un borane aux adduits NHC-CO_2 conduit à des potentiels de réduction moins négatifs que dans le cas des adduits NHC-CO_2 et que dans le cas de la molécule de CO_2 libre. De plus, une plus grande acidité de Lewis du borane se traduit par des potentiels de réduction plus accessibles. L'adduit **8-$B(C_6F_5)_3$** présente le potentiel de réduction le moins négatif à -1.34 V par rapport à $Fc^{+/0}$ dans le dichlorométhane.

4. Lors de la réduction des adduits NHC-CO_2, la localisation de la densité de spin sur la partie CO_2, en particulier sur l'atome de carbone, est dictée par les propriétés électroniques du NHC. La présence de l'acide de Lewis borane (BH_3, BCl_3 et $B(C_6F_5)_3$) permet de localiser une partie de la densité de spin sur l'atome de carbone du CO_2. L'adduit qui présente le plus de densité de spin à cet endroit est $[5\text{-}B(C_6F_5)_3]^{\bullet-}$ avec 0.41 de population de spin.

5. La localisation des LUMO des adduits neutres ressemble étroitement au SOMO dans leur forme monoréduite. L'ajout d'un acide de Lewis sur les adduits NHC-CO_2 permet la localisation des orbitales LUMO et SOMO principalement dans la partie CO_2 dans presque tous les cas, indépendamment de l'angle de torsion entre le NHC et le dioxyde de carbone. De plus, cela entraîne également une énergie de stabilisation significative dans les orbitales LUMO et SOMO. Les adduits qui présentent la plus faible énergie LUMO sont **8-BCl_3** (-0.97 eV) et **8-$B(C_6F_5)_3$** (-0.97 eV) et possèdent également les potentiels de réduction moins

négatifs, -1.38 V et -1.29 V respectivement. L'énergie du LUMO dans les espèces neutres est corrélée à leur potentiel de réduction.

6. Basé sur une analyse des conformères des adduits basés sur NHC-CO_2 synthétisés en fonction de différents angles de torsion, nous avons observé que l'énergie des LUMO atteint son point le plus élevé lorsque l'angle de torsion est proche de 90° et le plus bas lorsque la partie du CO_2 tend à être plus proche d'une orientation coplanaire (proche de 0°) par rapport à l'anneau NHC dans tous les cas. L'énergie de stabilisation des adduits **8**, **2-B(C_6F_5)$_3$**, **3-B(C_6F_5)$_3$** et **8-B(C_6F_5)$_3$** se comporte de manière inverse à l'énergie du LUMO, tandis que dans l'adduit **5-B(C_6F_5)$_3$**, le LUMO et l'énergie de stabilisation changent de manière cohérente. L'angle de torsion dans les adduits basés sur NHC-CO_2 a un impact significatif sur leurs potentiels de réduction et l'énergie du LUMO.

Les potentiels de réduction accessibles trouvés pour les adduits basés sur NHC-CO_2 permettent l'utilisation de conditions plus douces pour générer leur forme réduite que dans le cas de la molécule du CO_2. De plus, la présence de densité de spin sur l'atome de carbone de la partie du CO_2 dans leur forme réduite est également l'une des propriétés bénéfiques de ces molécules qui pourrait en faire des candidats parfaits en tant que synthons C1 pour construire de nouveaux liaisons chimiques C-C.